

**Magnetic, Electrical and Surface  
Morphological Characterization of  
AuGe/Ni/Au Ohmic Contact Metallization on  
GaAs/AlGaAs Multilayer Structures**

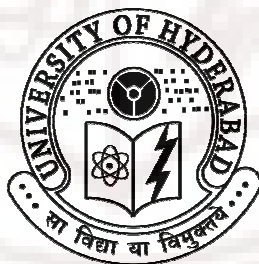
**A thesis submitted for the degree of**

**DOCTOR OF PHILOSOPHY**

**In  
PHYSICS**

**By**

**ABHILASH T. S  
(03PHPH19)**



**SCHOOL OF PHYSICS  
UNIVERSITY OF HYDERABAD  
CENTRAL UNIVERSITY P.O.  
HYDERABAD 500 046**

**JANUARY 2010**

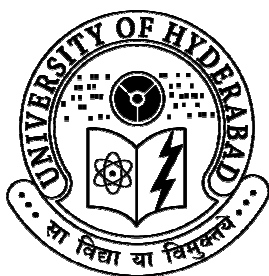
## **DECLARATION**

I here by declare that the matter embodied in this thesis titled “**Magnetic, Electrical and Surface Morphological Characterization of AuGe/Ni/Au Ohmic Contact Metallization on GaAs /AlGaAs Multilayer Structures**” submitted to University of Hyderabad for the award of **Doctor of Philosophy** in **Physics** is a record of original research work carried out by me under the supervision of **Prof. Guruswamy Rajaram**, School of Physics, University of Hyderabad. To the best of my knowledge, the thesis is not submitted for any degree in any University or institute.

Place: Hyderabad

(Abhilash T.S)

Date:



SCHOOL OF PHYSICS  
UNIVERSITY OF HYDERABAD  
CENTRAL UNIVERSITY P. O.  
HYDERABAD 500 046

---

## CERTIFICATE

This is to certify that the research work presented in this thesis titled “**Magnetic, Electrical and Surface Morphological Characterization of AuGe/Ni/Au Ohmic Contact Metallization on GaAs/AlGaAs Multilayer Structures**” for the award of **DOCTOR OF PHILOSOPHY** is an original work carried out by **Mr. Abhilash T.S** under my supervision at School of physics, University of Hyderabad, Hyderabad. This thesis work has not been submitted to this or any other university partially or fully for the award of any degree or diploma.

Date:

Prof. Guruswamy Rajaram

Place:

Thesis Supervisor

Dean

School of Physics

# ACKNOWLEDGEMENTS

First and foremost I would like to express my sincere and heartfelt gratitude to my supervisor **Prof. Guruswamy Rajaram** for his immeasurable kindness, immense help, wonderful guidance, constant support and encouragement during the entire span of my doctoral research.

I am grateful to my doctoral committee member, **Dr. M. Ghanashyam Krishna** for the discussions and comments, which helped to improve the scientific quality of this thesis.

I thank our Vice chancellors past and present. I thank the Dean and the faculty members of the School of Physics. In particular, I thank Prof. V. S. S. Sastry and Prof. S. N. Kaul, faculties and research scholars of electronics group and the administration.

I thank Prof. Govindacharyulu, Prof. B. M. Arora and Prof. D. N. Bose for the discussions and encouragement during my research work.

As part of my research, I have had the pleasure to collaborate with several renowned scientists from different laboratories. I would especially like to thank **Ms. Rita Saha** for helping me with micro-fabrication at IGCAR. I thank Dr. B. P. C. Rao, Dr. L. S. Vaidhyanathan, Dr. K. Gireesan, Dr. M. P. Janawadkar, Dr. T. Jayakumar and Dr. Baldev Raj, IGCAR, Kalpakkam. I also thank Dr. T. Geetha Kumary, IGCAR, Kalpakkam for the help in preparation of the AuGe alloy. I thank Dr. Sai Saravanan, GAETEC, for the discussion and encouragements.

I thank Dr. Balasubramanyam and group, SAC, Ahmedabad for helping me with the mask. I thank Dr. B. Sreedhar, IICT Hyderabad for helping me carry out the DSC measurements. I thank Prof. Mohan Rao, IISc Bangalore and Dr. Ravi Chandra, ARCI Hyderabad for the help provided with XPS and Cross sectional SEM measurements respectively. I thank Bruker Applied Physics laboratory, Germany for carrying out GIXRD measurements. I am grateful to Prof. T. P. Radhakrishnan and his research group for helping me with the current AFM measurements.

I thank the staff of the Central Instrument Laboratory, the PSO, Mr. C. S. Murthy, Dr. S. Manjunath, Mr. Nageshwara Rao and Mr. Pavan.



Many thanks are due to all my labmates over the years, Ch. Ravi Kumar, V. Yashaswini, B. Uday Bhaskar, B. Sandhya and L. Pushyami. The work presented in this dissertation would not have been possible without the help of **Mr. Ch. Ravi Kumar**. Special thanks to him for his immense help, friendship and good company.

Special thanks to Joji and Shinto, for being with me as wonderful friends over the years. I would like to thank other colleagues who have helped me, in particular A. Satish, V. Saravanan, G. Laksminarayana and Vasu.

Ajith and Sudheendan have been two friends whom I could always fall back on for any help I needed for which I am thankful to them. I would like to especially thank Juby, Daugthy and Tejal for their companionship. I always have pleasant memories of School of Physics. I thank Gnanavel, Yugandar, N. Sathish, Devaraju, Devendra, Ramudu, Venkaiah, Sultan, Brahma, Regina, Monisha, Geo, friends from MSc Physics and other friends. I always cherish the memories of the beautiful time I spend with my friends at NRS hostel: Biju, Rohith, K Rajesh, P. Rajesh, K.P. Rajesh, Anver, Azhar, Dinesh, Hashique, Yassar, Siraj, Sreeraj, Suraj, Ajith, Munir and Shihab. Special thanks to Santhosh and Shalina. I also remember the friendship I have with Lajna, Tintu, Neethu, Tresa, Sonia, Asha, Abin and Godwin. They have, directly or indirectly influenced the course of my work.

I acknowledge Mrs. Saramma, Mr. Abraham Mr. Vincent, Mr. Chandarapal, Mr. Poornachandra Rao, Mr. A. S. Reddy, Mr. Anil, Mr. Kurup, Mr. Koshy and Vijayan for their administrative and technical support.

I would like to thank my parents for their love and support throughout my life. It was their encouragement and love of learning that lead me to where I am today. I would also like to extend my gratitude to my elder brother Santhosh, Sneha, Anugraha and younger brother Sinjo, for their love and care throughout my life. A particular acknowledgement I owe to Neeraja who is going to be a part of my life.

I gratefully acknowledge the funding sources that made my thesis work possible: DAE/BRNS, IGCAR/DAE for the first four and a half years and CAS for the remaining term of my Ph.D. I also thank ACRHEM for the funding and Prof. S. P. Tiwari and Dr. A. K. Chaudhary for encouragement. I acknowledge the support of UGC (UPE), BRNS/DAE, IGCAR and DST (Centre for Nanotechnology) for support for facility development.

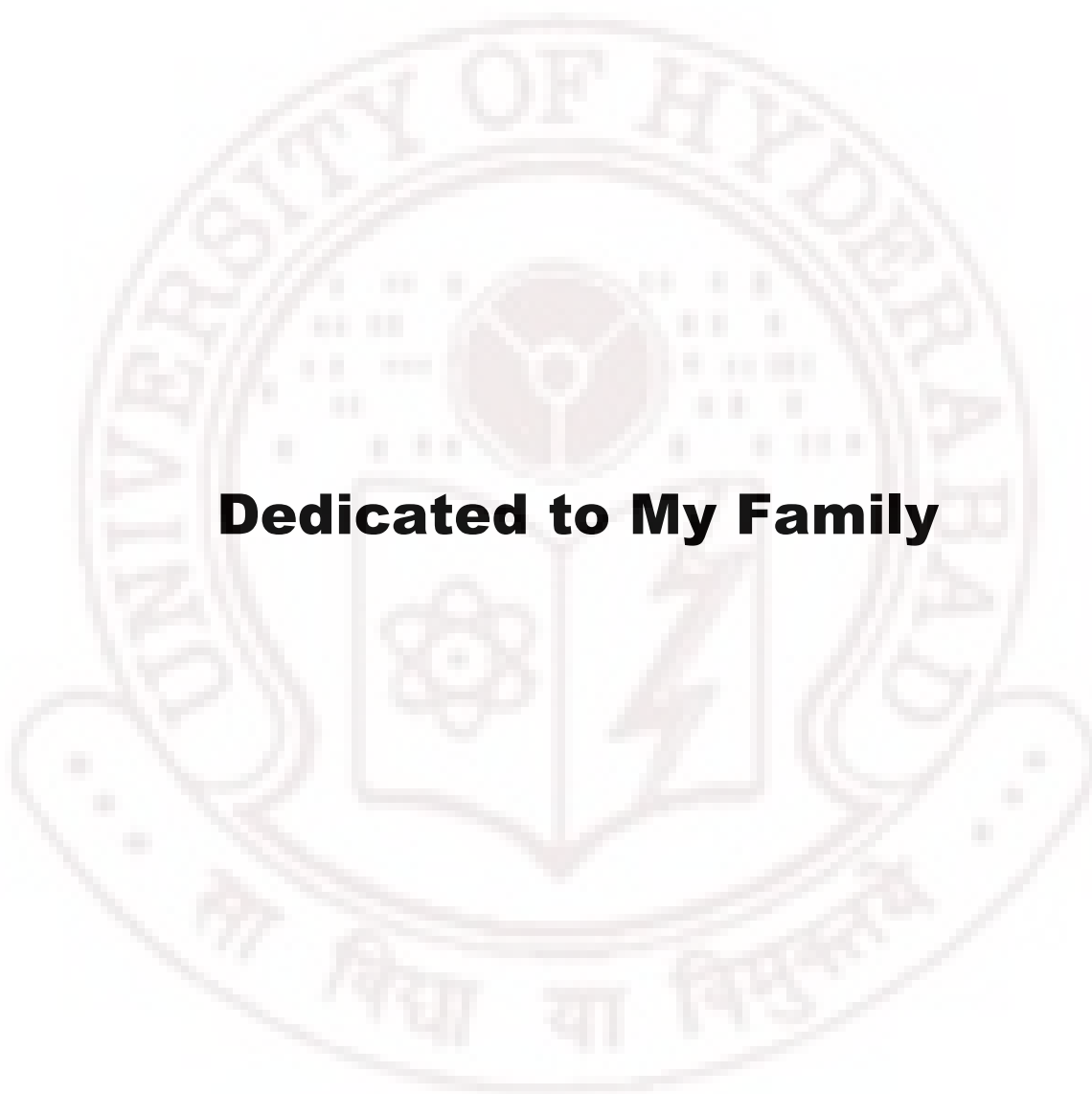


# Table of contents

## Chapter 1 Introduction

1.1	Introduction	1
1.1.1	GaAs crystal structure	1
1.1.2	Energy band structure	2
1.1.3	Heterostructures	3
1.1.4	GaAs/AlGaAs two dimensional electron gas	4
1.1.5	Scattering mechanisms and mobility	5
1.1.6	Hall sensor materials	7
1.1.7	Epitaxy growth techniques	8
1.1.7.1	Molecular Beam Epitaxy- MBE	8
1.1.7.2	Metal Organic Chemical Vapor Deposition- MOCVD	9
1.1.8	Other Heterostructures	9
1.2	Metal Semiconductor contacts- Ohmic contacts	10
1.2.1	Significance of Ohmic contacts	10
1.2.2	Ohmic contact theory	11
1.2.3	Charge transport mechanisms	12
1.2.4	Ohmic contact to GaAs/AlGaAs	14
1.2.4.1	Practical Ohmic contacts to GaAs and GaAs/AlGaAs	15
1.2.4.2	AuGe/Ni/Au Ohmic contact	16
1.2.4.3	Models of the Ohmic contact	18
1.2.4.4	Pd/Ge Ohmic contact	20
1.3	Specific contact resistance measurement	21
1.3.1	Transmission line/Transfer length model (TLM)	22
1.4	Motivation for this work	23
	References	25

## Chapter 2 Experimental Techniques

2.1	Introduction	29
2.2	GaAs/AlGaAs 2DEG wafer structure	29
2.3	Device Fabrication (TLM)	31
2.3.1	Mask Layout	31
2.3.2	Wafer Processing	33
2.3.2.1	Photo Lithography	33
2.3.2.2	Wet Etching	33
2.3.2.3	Lift off	33
2.3.3	Ohmic Contacts	34
2.3.3.1	AuGe alloy preparation by Arc melting	34
2.3.3.2	Photoresist Ashing/Descumming	35
2.3.3.3	Ohmic contact metal deposition	35
2.3.3.4	Surface profilometer: Etch depth and deposited Film thickness measurement	37
2.3.3.5	Rapid thermal annealing (RTA)	37
2.3.3.6	Probe station	39
2.3.3.7	Wire bonding	39
2.3.3.8	Device analyzer	40

2.4	Electrical Characterization	40
2.4.1	Contact resistance measurements by TLM	40
2.4.2	Temperature dependence of contact resistance measurements	42
2.5	Magnetic measurements	43
2.5.1	Vibrating Sample Magnetometer (VSM)	43
2.6	Differential Scanning Calorimetry	44
2.7	Surface morphology and Micro structure Analysis	45
2.7.1	Grazing Incidence XRD (GIXRD)	45
2.7.2	X-Ray Photoemission Spectroscopy (XPS)	46
2.7.3	Scanning Electron Microscopy (SEM) and Energy Dispersive Analysis of X-rays (EDAX)	46
2.7.4	Atomic Force Microscopy (AFM)	46
2.7.5	Conducting Probe Atomic Force Microscopy (C-AFM)	47
2.8	Adhesion Characterization	48
2.8.1	Nano scratch test	49
	References	51
<b>Chapter 3 Influence of Ni layer thickness on the contact resistance, magnetic properties and surface morphology</b>		
3.1	Introduction	52
3.2	Effect of Ti, Cr and Ni interlayer on AuGe/TM/Au Ohmic contacts	53
3.2.1	Electrical characteristics	54
3.2.2	Surface morphology	56
3.3	Influence of Nickel layer thickness on magnetic properties contact resistance and surface roughness	58
3.3.1	Electrical characteristics	58
3.3.2	Magnetic properties	63
3.3.3	Surface morphology	66
3.3.4	Influence of Ni-to-AuGe layer thickness ratio	69
3.3.5	Discussions	72
3.4	Conclusions	73
	References	75
<b>Chapter 4 Dependence of contact resistances, roughness and melting on Ge content in the AuGe alloy</b>		
4.1	Introduction	77
4.2	Dependence of contact resistance, roughness, magnetization and melting on Ge content in the AuGe alloy and Ni layer thickness	78
4.2.1	Experimental	78
4.2.2	Electrical characteristics	80
4.2.3	Surface roughness	83
4.2.4	Magnetic properties	85
4.2.5	Differential Scanning Calorimetry (DSC)	86
4.2.6	Structural Properties	87
4.2.7	Temperature dependence of contact resistance	88
4.3	Conclusions	93
	References	95

<b>Chapter 5 Ohmic Contact Formation: New Insights from Magnetization Measurements</b>	
5.1 Introduction	97
5.2 Changes in the metallization structure prior to alloying	98
5.3 Conductive Atomic Force Microscopy (C-AFM) – Characterizing conductivity variations in AuGe/Ni/Au alloyed contacts	113
5.4 X-ray photoemission spectroscopy analysis	115
5.5 Conclusions	119
References	120
<b>Chapter 6 Pd/Ge based Ohmic contacts</b>	
6.1 Introduction	121
6.2 Experimental	122
6.2.1 Electrical characteristics	123
6.2.2 Surface roughness	125
6.2.3 Differential Scanning Calorimetry (DSC)	126
6.2.4 Adhesion studies	127
6.3 Conclusions	129
References	130
<b>Chapter 7 Fabrication of Micro Hall Magnetic Sensors</b>	
7.1 Introduction	131
7.2 Hall sensors	131
7.2.1 Sensitivity	132
7.3 Micro Hall sensor fabrication	132
7.3.1 Choice of material	132
7.3.2 Hall magnetic sensor design	133
7.3.3 Hall sensor fabrication	133
7.3.4 Hall sensor process steps	135
7.4 Micro Hall magnetic sensor characteristics	135
7.5 Magnetic non destructive testing (NDT): Flux leakage measurement using 2DEG based Micro Hall Sensors	137
References	139
<b>Chapter 8 Thesis Summary and Future work</b>	
8.1 Results Summary	140
8.2 Future work	142

# OUTLINE

GaAs/AlGaAs heterostructures, incorporating the 2-dimensional electron gas (2DEG) layer, are used for the fabrication of High Electron Mobility Transistors (HEMTs) and devices such as IR sources and detectors. AuGe/Ni/Au based alloyed contacts are commonly used to obtain low resistance contacts to these structures. This recipe gives low contact resistance with moderate surface roughness which can be further improved by increasing Ni layer thickness. The 2DEG multilayer structures also have another application namely Hall effect based magnetic sensor. However, in this application any residual magnetism of Ni can distort the field at the active areas. Alternatives to Ni, such as Cr, Ti etc. are preferred. These alternatives however results in higher contact resistance and increased roughness. For implementing sensors and devices on the same substrate as well as for improved yield, magnetism of Ni containing layer needs to be investigated. The magnetization of alloyed Ohmic contact film structures of the form AuGe/Ni/Au deposited on GaAs/AlGaAs heterostructure substrate are investigated as functions of Ni layer thickness, alloying temperature and AuGe alloy composition. The results are correlated with contact resistance and surface morphology studies.

This thesis starts with an introduction **Chapter 1** of GaAs/AlGaAs heterostructures. Much of the work has been investigated for specific application of the fabricated Hall magnetic sensors using this structure. The second part of this chapter presents literature pertaining to Ohmic contacts to GaAs/AlGaAs 2DEG and characterization of the contact using Transmission Line model (TLM).

**Chapter 2** describes the samples and experimental techniques that are used for all of the experiments described in this thesis. The chapter starts with a brief overview of standard semiconductor processing for fabrication of Ohmic contacts, ends with measurement techniques employed for the electrical, magnetic and metallurgical characterization of the Ohmic contacts.

**Chapter 3** presents the study of influence of Ni layer thickness in the AuGe/Ni/Au Ohmic contact metallization on the residual magnetization of the processed Ohmic contact structure in the context of application to Hall magnetic field sensors along with contact resistance and roughness studies. The chapter begins with the possibility of

using alternate structures without the ferromagnetic Ni, namely, AuGe/Au, AuGe/Ti/Au and AuGe/Cr/Au. A comparative study of the contact resistance, surface roughness and surface composition in these metallization structures, after annealing treatments are carried out, is presented.

AuGe/Ni/Au metallization gives the lowest contact resistance and better surface morphology. However as-deposited Ni is magnetic, and the magnetization of the structure after alloying is of interest. Hence the dependence of magnetization hysteresis loops, surface roughness and the contact resistance of alloyed AuGe/Ni/Au contacts on the following process parameters: Ni layer thickness (for a fixed AuGe layer thickness of  $\sim 100\text{nm}$ ), anneal temperature and duration of post-deposition anneal are studied. Similar studies are undertaken on samples with three different AuGe layer thicknesses, but with the same Ni/AuGe thickness ratio.

**Chapter 4** discusses the influence of varying the Ge content in the AuGe alloy in the context of reducing surface roughness. Results of contact resistance, roughness studies and magnetization and also of melting in the metallization structure, as the Ge content in the AuGe alloy is lowered than that of the eutectic composition, are presented. Low temperature dependence of contact resistance of few structures is examined to study changes in the electrical contact mechanism and also in the context of low-temperature applications of the magnetic field sensor.

**Chapter 5** describes some insights into the changes in the metallization prior to alloyed contact formation from magnetization and DSC results as explained later. The chapter also discusses some results of Grazing Incidence XRD (GIXRD), cross-sectional SEM, current AFM, XPS and adhesion.

**Chapter 6** deals with Pd/Ge contacts. This contact structure has a low processing temperature. Also, an epi-Ge layer has been reported to form between the structures, on processing. Adhesion of the contact structure is of interest and has been performed and correlated with contact resistance and surface roughness.

**Chapter 7** describes for completion, the fabrication, characterization of micro Hall magnetic sensors using the GaAs/AlGaAs 2DEG structures and their application to magnetic flux leakage measurements.

**Chapter 8** ends with a brief summary of results and possible extension of work.



# Chapter -1

## Introduction

GaAs/AlGaAs heterostructures, with the two-dimensional electron gas (2DEG) layer, are useful for developing high speed, electronic and opto-electronic devices [1-3]. They are also used in fabrication of Hall-effect based magnetic field sensors [4, 5] in applications like magnetic phase diagram determination [6, 7], magnetic microscopy [8, 9] and non-destructive testing (NDT) [10, 11]. Contact resistances to the semiconductor, influence device parameters such as the transconductance and power dissipation in High electron mobility transistors and the output signal-to-noise ratio in magnetic field sensors. Film roughness of the contact metallization influences the minimum gate-drain separation that can be used in electronic devices when maximizing bandwidth.

### 1.1 Introduction

This chapter presents the formation of GaAs/AlGaAs two dimensional electron gas and summarizes the literature pertaining to Ohmic contacts to GaAs/AlGaAs 2DEG and Transmission Line model (TLM) used for characterizing the contacts.

#### 1.1.1 GaAs Crystal Structure

GaAs has a Zincblende structure. The crystal structure of GaAs (and AlAs) is shown in figure 1.1.1. It comprises of two interpenetrating face centered cubic lattices, one for Ga and another for As displaced from one another by  $(\frac{1}{4}, \frac{1}{4}, \frac{1}{4}) a$ , where 'a' is the lattice constant, which is  $\sim 5.66\text{\AA}$  [12].

$\text{Al}_x\text{Ga}_{1-x}\text{As}$  is a ternary alloy (abbreviated to AlGaAs) of AlAs and GaAs where the **Ga** atoms are randomly replaced by **Al** atoms but **As** sites are not altered. Since both GaAs and AlAs have the same crystal structure, the formation of solid solutions of **Al** in GaAs is easy and has the same crystal structure over a full range of **Al** substitution [13].



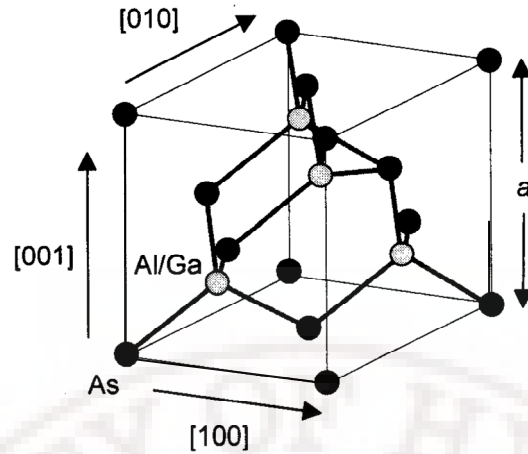


**Figure 1.1.1** GaAs (AlAs) crystal structure

### 1.1.2 Energy Band Structure

High-mobility carrier layers are generated in III-V semiconductor heterostructures, by engineering band-gap or electrical potential. These involve modifying the conduction and valence band configuration by varying composition and thickness of the layers. In this context, the band structure of GaAs and AlGaAs are reviewed.

GaAs has direct band gap structure while AlAs has indirect band gap. A general feature of the AlGaAs system, like in many III-V compound semiconductors, is that there are three valence bands whose maxima are situated at  $k = 0$  ( $\Gamma$  point). The conduction band has three minima: one at  $k = 0$  (the  $\Gamma$  point), another at the  $L$  on the Brillouin zone boundary along  $\langle 111 \rangle$  direction and at  $X$  point on the Brillouin zone boundary along  $\langle 100 \rangle$  [12]. As the composition (Al: Ga ratio) changes, relative positions and strengths of these minima change which determines the nature of the band gap.

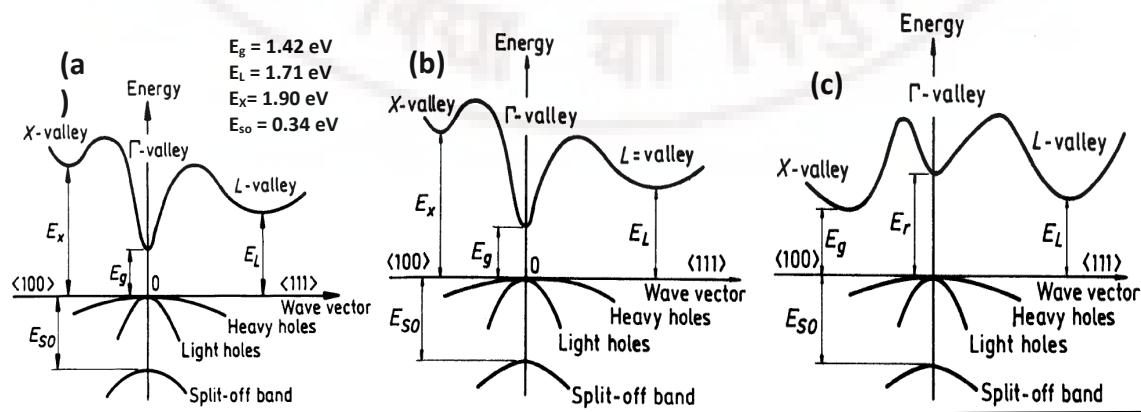


**Figure 1.1.2** Band structures of (a) GaAs (b)  $\text{Al}_x\text{Ga}_{1-x}\text{As}$  for  $x < 0.4$  (c)  $\text{Al}_x\text{Ga}_{1-x}\text{As}$  for  $x > 0.4$ .

GaAs has tetrahedral bonding between Ga and As and the character is partially ionic with large covalent character. The band gap is 1.42eV at 300K [12]. The energy difference between the various valleys of the conduction band and top of the valence band for GaAs and AlGaAs are also given in figure 1.1.2 a, b & c.

When the concentration of Al is less than 0.4, the band gap is direct. In this thesis, AlGaAs layer have  $x \sim 0.3$ . Valence band structure of GaAs and  $\text{Al}_x\text{Ga}_{1-x}\text{As}$  alloys has three bands: i) heavy hole band, ii) light hole band, and iii) split off band. The three valence bands have maxima at  $k=0$  as seen in Fig 1.1.2. The heavy and light hole bands are degenerate at  $k=0$ . In GaAs, the conduction band  $\Gamma$  valley is the lowest at  $k=0$  with electron effective mass  $\sim 0.067m_e$ . When the concentration of Al is more than 0.4, the band gap changes to indirect [13]. The energy gap of AlGaAs at 300K is given as

$$E_g \approx 1.424 + 1.247x \text{ eV } (x < 0.4) \quad \Gamma \text{ valley} \Rightarrow \text{direct gap}$$

$$E_g \approx 1.90 + 0.125x + 0.143x^2 \text{ eV } (x > 0.4) \quad X \text{ valley} \Rightarrow \text{indirect gap}$$

### 1.1.3 Heterostructures

Heterostructures contain more than one semiconductor, and in which the transition between the different semiconductors play a functional role in the operation of the device. Choice of materials in heterostructures used to engineer band gap is based on: Electrical or band structure properties and feasibility of fabricating the structure by structural properties. To successfully grow a crystalline material on another, lattice constant needs to be closely matched; other wise epitaxial layer will have large number of crystalline defects [14]. Fabrication of a desired structure is guided by the 'bible' of III-V heterostructure growth as shown in figure 1.1.3. GaAs and AlAs have almost the same lattice constant. The lattice constant of AlAs is only 0.15% larger than that for GaAs. [13].

When a junction is formed between two semiconductors whose band gaps are different is termed as heterojunction. There are three distinct cases of heterojunctions available. GaAs/AlGaAs interface, the heterojunction found is of the straddling type i.e. band gap of GaAs is completely contained in the band gap of the AlGaAs. In Staggered heterojunctions, the conduction band of one semiconductor lies below the valence band of the other, where as the band gaps of both semiconductors do not overlap are called the broken heterojunctions [14].

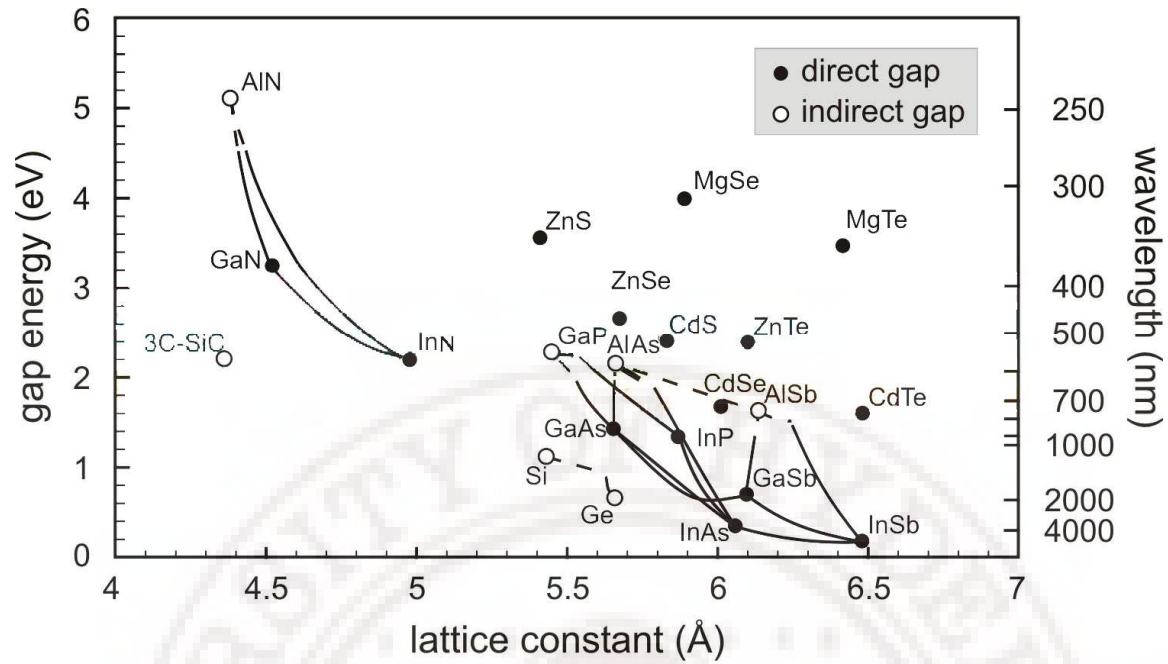


**Figure 1.1.3** Lattice constant and band gap energies for common III-V materials and their alloys

#### 1.1.4 GaAs/AlGaAs two dimensional electron gas

The low dimensional systems are classified corresponding to the confinement of charge carriers in one, two and all three dimensions as quantum wells (2D), quantum wires (1D) and quantum dots (0D). The interface between GaAs and AlGaAs alloys of different Al and Ga content can be used for confining electrons. A sketch of the band energies of this interface is shown in figure 1.1.4, where  $E_c$  and  $E_v$  are the conduction and valence band energies at the  $\Gamma$  point.

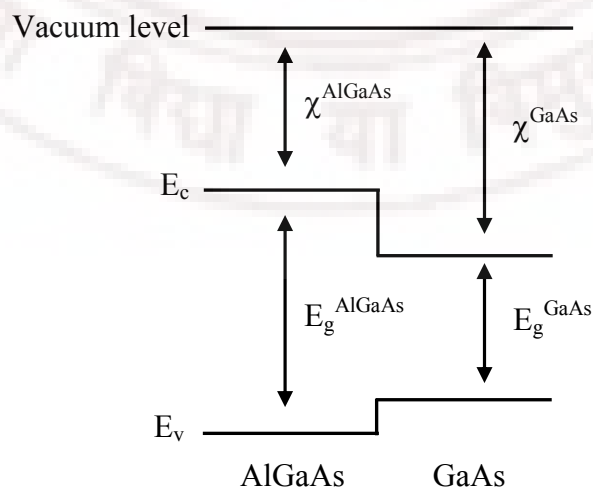


**Figure 1.1.4** GaAs-AlGaAs interface

The alignments of the conduction and valence bands are determined by the combination of the band gap  $E_g$  and electron affinity  $\chi$ . The difference between the conduction band energies at the interface between GaAs and  $\text{Al}_{0.3}\text{Ga}_{0.7}\text{As}$  is  $\Delta E_c = 0.23\text{eV}$ .

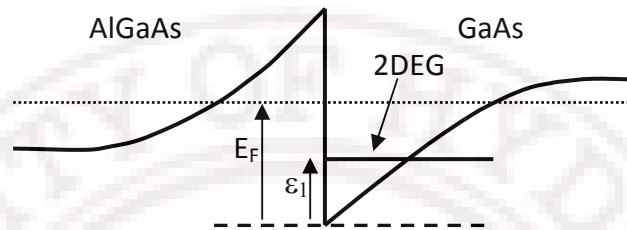


**Figure 1.1.5** Two dimensional electron gas (2DEG) in a AlGaAs/ GaAs

The GaAs/AlGaAs two dimensional electron gas layer (2DEG) is shown in figure 1.1.5. The 2DEG design is such that the conduction band forms a sheet of electrons at a GaAs/AlGaAs interface. Charge transfer between two materials take place as a result of alignment of Fermi levels. Electrons from AlGaAs donor layer move towards the interface between AlGaAs and GaAs due to lower conduction band energy in GaAs and form a two dimensional electron gas (also called modulation doping). This charge at the interface also forms a triangular quantum well as shown in figure 1.1.5. [15].

### 1.1.5 Scattering mechanisms and mobility

Carrier mobility and concentration are the two main parameters that determine the transport properties. The scattering mechanisms in bulk GaAs are well studied and an overview of various scattering mechanisms in bulk GaAs is presented in figure 1.1.6 [16].

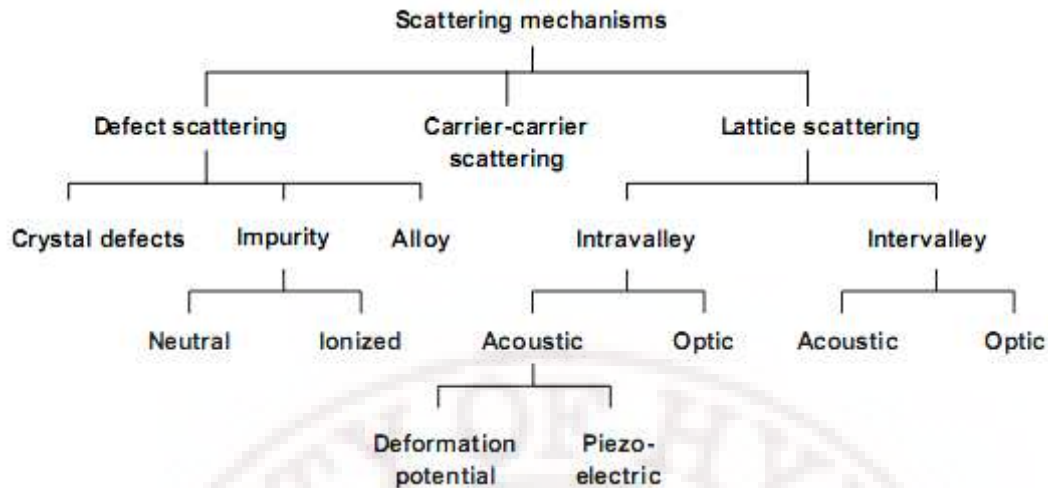


**Figure 1.1.6** The outline of different scattering mechanisms in bulk GaAs

For heterostructures some additional scattering mechanisms have to be accounted for: (i) interface roughness scattering (ii) inter-sub band scattering between the quantized states in the quantum well (iii) remote impurity scattering in the barrier material (iv) scattering on the barrier phonons (observed in GaAs/AlGaAs heterostructures) (v) scattering by alloy disorder when compound semiconductor are used as channel (vi) scattering by ionized impurity scattering. The influence of various scattering mechanisms on the mobility of the 2DEG is presented in figure 1.1.7[17].

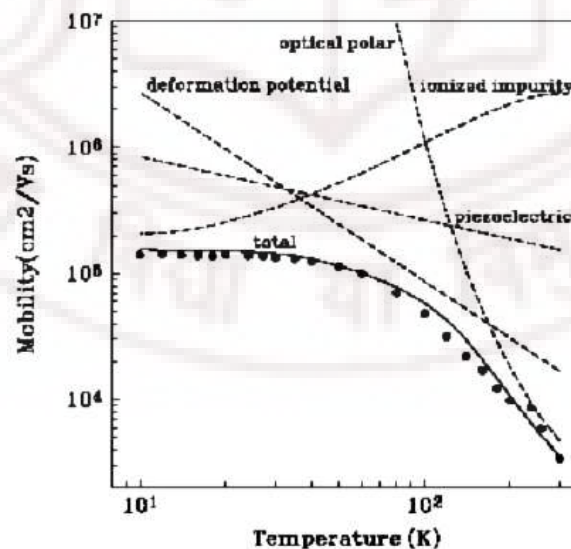


**Figure 1.1.7** Temperature variation of mobility due to various scattering mechanisms in 2DEG

The room temperature (RT) mobility of 2D electron gas (2DEG) is approximately  $8000 \text{ cm}^2/\text{Vs}$ . This is comparable with RT mobility values of electrons in high purity bulk GaAs. At low temperatures (77K), the 2DEG has mobility of around  $1, 40,000 \text{ cm}^2/\text{V.s}$ . The high mobility at low temperature is attributed to i) reduced thermal scattering and ii) absence of ionized impurity scattering due to modulation doping.

### 1.1.6 Hall sensor materials

The use of Hall magnetic sensors for applications like magnetic phase-diagram determination, flux leakage and microscopy (measurements of low magnetic fields) requires Hall sensors with high sensitivity, low noise and large signal to noise ratio. Most of the Hall devices are made of III-V compound semiconductors such as GaAs, InSb and InAs [18-21]. InSb in single crystal and thin-film form are popular Hall sensor materials [19]. The quantum well heterostructure semiconductors with the 2-Dimensional Electron Gas (2DEG) layer, grown by molecular beam epitaxy, are specially suited for fabrication of micro-Hall Sensors and sensor arrays since they consist of a thin carrier sheet of high mobility.

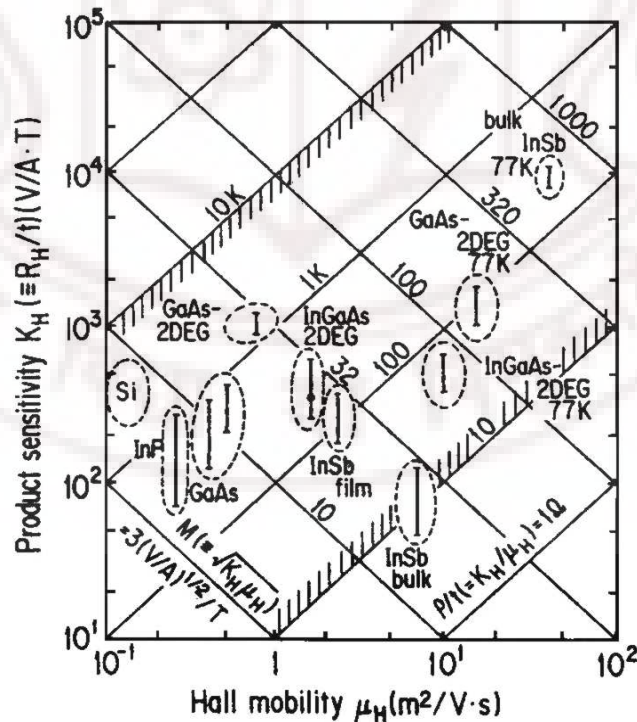


Figure 1.1.8 Magnetic sensitivity of Hall sensor [4]



Hall sensors made of GaAs/AlGaAs multilayer structures with the 2 dimensional electron gas (2DEG) layer have attracted increased interest in recent years because of the high electron mobility combined with moderate sheet carrier densities and good signal to noise ratio. They give sensitivities  $\sim 1000$  V/AT, which are comparable to InSb and three times larger than that of GaAs. They are particularly suited for use at low temperatures ( $<100$ K), where mobilities are enhanced by an order of magnitude from that at 300K and, more importantly, show a sensitivity that is nearly temperature independent ( $<100$ K) [4]. The suitability of various materials as Hall sensor materials with the resistance and magnetic sensitivity/allowed power dissipation as parameters is shown in figure 1.1.8.

Other III-V multilayer structures with the 2DEG, with extremely high mobility layers such as AlGaAs/InGaAs (pseudomorphic) are also possible [22]. The GaAs/AlGaAs based multilayer wafers with the 2DEG layers were the material used for the fabrication of Hall magnetic sensors in this thesis. These structures are also used in high speed, high bandwidth devices [22-24]. The detail of the wafer structure with the 2DEG layer used in this thesis is explained in chapter 2.

### **1.1.7 Epitaxy growth techniques**

For heterostructures to perform well, the interfaces must be abrupt and not suffer from defects. The most commonly used heterostructure growth techniques are molecular beam epitaxy (MBE) & metal organic chemical vapour deposition (MOCVD).

#### **1.1.7.1 Molecular Beam Epitaxy (MBE)**

In Molecular Beam Epitaxy (MBE), the molecular beams are produced by evaporation or sublimation from heated liquids or solids contained in crucibles. The GaAs/AlGaAs heterostructure wafer used in this thesis is grown via MBE [25].

The elements that compose heterostructure Ga, As and Al are vaporized in the furnaces with orifices directed towards the substrate. For a ultra high vacuum environment the chamber is pumped down to a pressure lower than  $10^{-10}$  Torr, and hence the mean free path of molecules is greater than size of the vacuum chamber. Flux

of each element can be controlled through the temperature of each furnace. Dopants are added by using additional cells. The physical and chemical properties of the film can be monitored in situ during MBE growth using Reflection High Energy Electron Diffraction (RHEED) and Auger Electron Spectroscopy (AES). MBE allows controlled growth of individual atomic layers. A typical growth rate is approximately one monolayer/second.

#### **1.1.7.2 Metal Organic Chemical Vapor Deposition (MOCVD)**

MOCVD involves the thermally activated chemical reaction of organometallic molecules containing the metal of interest, with other chemical gases. The alkyl precursor for the group III element and hydride precursor for group V element decompose in the 500°C to 800°C temperature range to form the III-V compound semiconductor. Requisite vapor is transported using carrier gases like H<sub>2</sub>. The common sources for As are AsH<sub>3</sub> while for Ga are trimethyl gallium (TMGa/Ga (CH<sub>3</sub>)<sub>3</sub>) and for Al are trimethyl Aluminum (TMAl/Al (CH<sub>3</sub>)<sub>3</sub>) respectively. Excellent uniformity in layer thickness, composition and carrier concentration is achieved over a large wafer area using MOCVD growth technique [42]. Quality is at present compatible to MBE along with high throughput.

#### **1.1.8 Other heterostructures**

In recent years, variety of semiconductor heterostructures have emerged since the advance in semiconductor heterostructure growth techniques. Semiconductor heterostructures show unique electronic properties compared to the bulk materials, such as the formation of a two-dimensional electron gas (2DEG) with enhanced mobility. As a result, heterostructures are used in numerous applications. Currently the most development has been observed in the field of nitride based semiconductors such as AlN, GaN, InN and their alloys. They are used for the development and fabrication of light emitters, photo detectors and high power high-frequency transistors for communication systems [26, 27].

The SiC and Diamond are another class of wide-band-gap materials. SiC based heterostructures are presently used in the fabrication of HEMTs. Diamond is a semiconductor material with a band gap of 5.45eV. Diodes and transistors based on



Diamond is the ideal candidate for high power and high temperature electronics [28, 29].

## **1.2 Metal Semiconductor contacts: Ohmic contacts**

Ohmic contacts are necessary to inject current from metal interconnect to semiconductor device and vice versa. By definition, a metal-semiconductor contact forms a Schottky junction and therefore under such circumstances constitutes a parasitic. This section reviews the metal semiconductor contact and the carrier transport mechanisms. Results presented in this thesis are part of research effort to fabricate and study Ohmic contacts to GaAs/AlGaAs multilayer structures with a GaAs cap layer, in the context of Hall-effect based magnetic field sensors for different applications and of high electron mobility transistors (HEMT).

### **1.2.1 Significance of Ohmic contacts**

Braun demonstrated metal semiconductor contact in 1874. The first widely accepted theory of the metal semiconductor contact was published by Schottky in the 1930s. Metal-semiconductor contacts can vary between two extremes, Schottky and Ohmic. Contacts with rectifying current - voltage characteristics are 'Schottky' type and non-rectifying contacts are said to be 'Ohmic'. The requirements for good Ohmic contacts are

- 1) Non- rectifying
- 2) Linear
- 3) Low contact resistance.

Other requirements indirectly influencing contact resistance parameters and processing are

- 1) Thermal stability during device fabrication and operation.
- 2) Smooth surface,
- 3) Strong adhesion between metal and semiconductor.
- 4) Shallow horizontal and vertical diffusion depth of the contact metal to semiconductor.
- 5) Reliability and reproducibility of the contacts [30-32].

### 1.2.2 Ohmic contact theory

Metal semiconductor Ohmic contact formation depends on potential barriers and current conduction mechanisms present at the junction. All practical metal-semiconductor contacts normally result in the formation of Schottky junction and they are rectifying to varying degrees.

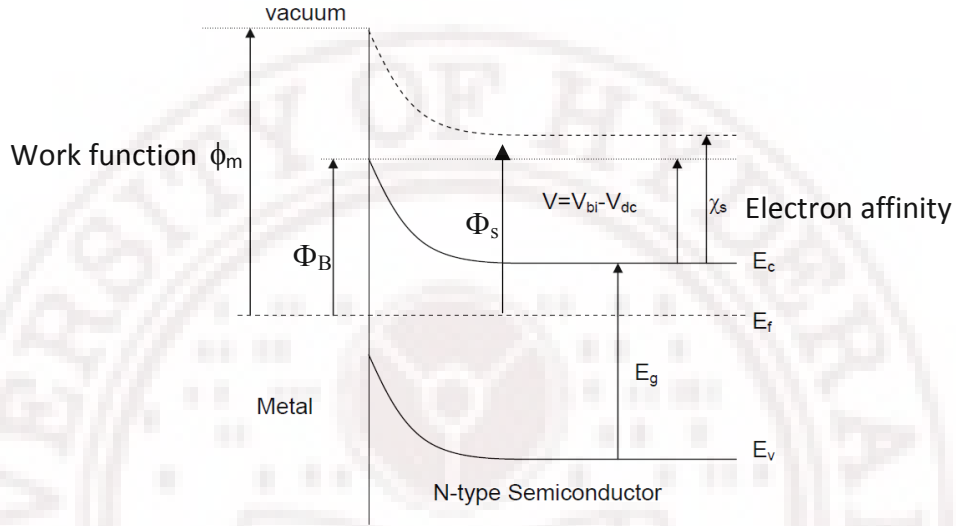


**Figure 1.2.1** Energy band diagram for metal semiconductor contact

Figure 1.2.1 gives the energy band diagram for a metal semiconductor contact at equilibrium with zero bias with the Fermi levels of metal and semiconductor lined up.

The Schottky potential barrier is  $\Phi_B = \Phi_m - \chi_s$

Potential barrier for electrons flowing from semiconductor to metal is  $\Phi_m - \Phi_s$  and potential barrier for electrons flowing from metal to semiconductor is  $\Phi_m - \chi_s$  and the junctions are rectifying.

If a large number of surface states exist on the semiconductor, the Fermi level is pinned and the barrier height is independent of the metal work function [33]. Even if  $\Phi_B$  becomes independent of metal work function due to domination of surface states, doping influences the depletion layer width ( $W$ ).

Under zero external bias, the depletion width is given by

$$W = \sqrt{[2\epsilon_s(V_0 - kT/q)/qN_D]} \text{ with } V_0 = \left( \frac{\Phi_m - \Phi_s}{q} \right)$$

$\epsilon_s$  is the relative permittivity of semiconductor,  $q$  is the electron charge,  $T$  is the temperature,  $V_o$  is the built in potential and  $k$  is the Boltzmann constant. The term  $\frac{kT}{q}$  arises from the contribution of the majority-carrier distribution. With the  $W$  being proportional to  $\frac{1}{\sqrt{N_D}}$ , higher doping will produce narrower  $W$ , thereby increasing tunneling probability [12].

### 1.2.3 Charge transport mechanisms

Current transport in metal semiconductor junction can be described by: thermionic emission (TE), field emission (FE) and combination of the two, thermionic field emission (TFE). This is shown in figure 1.2.2.

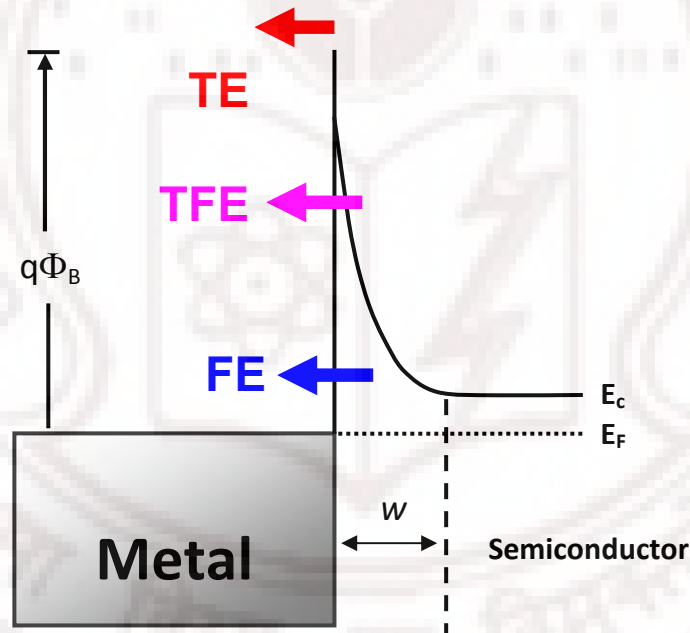


**Figure 1.2.2** Schematic band energy diagram of a metal semiconductor contact showing the three major current transport mechanisms.

**Thermionic emission:** This is the carrier transport over the Schottky barrier. When the depletion width is too large for tunneling to occur due to low doping concentration in the semiconductor, the dominant mechanism for conduction is thermal excitation over the barrier. At intermediate doping level the depletion region is reduced sufficiently to allow some tunneling through the barrier and both thermionic emission and tunneling

contribute to current density, (thermionic field emission, TFE). When the contact region is heavily doped, the depletion region is thin enough for the carriers to tunnel through the barrier and field emission (FE) is the dominant mechanism for current conduction [12, 34].

**Thermionic emission (TE):** The current density in case of TE is

$$J = J_s \exp\left(\frac{qV}{nkT}\right), \text{ for } V \gg \frac{kT}{q}, \quad J_s = A^{**} T^2 \exp\left(\frac{-q\Phi_B}{kT}\right)$$

$A^{**}$  is the effective Richardson constant.  $V$  is the forward voltage applied across the barrier,  $T$  is the absolute temperature,  $k$  - Boltzmann constant,  $n$  - ideality factor (values varying between 1 and 2). The value of  $n$  increases with increasing doping and barrier tends to be leaky Schottky barrier. The contacts operating by thermionic emission are usually rectifying to some degree and therefore not good Ohmic contacts. TE is characterized by an exponential dependence of the current density with forward bias and inverse temperature.

The specific contact resistance ( $\rho_c$ ) for TE is 
$$\rho_c = \left(\frac{\partial V}{\partial J}\right)_{V=0} = \frac{k}{qA^{**}T} \exp\frac{q\Phi_B}{kT}$$

**Field emission (FE):** The transmission probability  $P$  that electron energy  $E$  can successfully tunnel through a triangular shaped potential energy barrier with diffusion potential  $V_d$  is given by

$$P = \exp\left(\frac{-2(qV_d - E)^{3/2}}{3E_{oo}(qV_d)^{1/2}}\right)$$

The current density  $J \approx \exp\frac{-q\Phi_B}{E_{oo}}$ ,  $E_{oo}$  is the tunneling parameter,

and 
$$E_{oo} = \frac{q\hbar}{2} \left( \frac{\sqrt{N_d}}{\sqrt{\epsilon m^*}} \right)$$

$q$  is the electric charge,  $\hbar$  - Plank's constant,  $N_d$  is the donor concentration,  $\epsilon$  is the dielectric constant of the semiconductor and  $m^*$  is the effective mass of electron.

The specific contact resistance for FE is 
$$\rho_c = C \exp\left[\frac{q\Phi_B}{E_{oo}}\right]$$

In this case the  $\rho_c$  exhibit only a weak dependence on temperature.

**Thermionic field emission** (TFE) a mixture of both thermionic and tunneling mechanism is observed in intermediate doping concentration and the specific contact resistance is given by

$$\rho_c = C \exp \left[ \frac{q\Phi_B}{E_{oo} \coth \frac{E_{oo}}{kT}} \right]$$

The specific contact resistance depends on both temperature and transmission coefficient for tunneling.

#### 1.2.4 Ohmic contact to GaAs and GaAs/AlGaAs

Ohmic contacts can be achieved by lowering the barrier height ( $\Phi_B$ ) and/or increasing tunneling probability through the barrier. In view of decreasing sizes and hence contact areas into the sub micron range, optimizing Ohmic contact process for law specific contact resistance, reproducibility and low roughness is of increased importance.

The conventional Ohmic contact formation on GaAs involves deposition of a contact metal and subsequent annealing at elevated temperatures. Ohmic contact formations to GaAs fall into three broad categories [35].

- 1) Liquid phase reactions (AuGe/Ni/Au)
- 2) Solid phase reactions (Pd/Ge, Si/Ge, Ni/Ge)

Various types of Ohmic contacts to n-GaAs and GaAs/AlGaAs, InGaAs/AlGaAs studied in literature, some of the practical contacts are described in the table below. It can be seen that Germanium-based Ohmic contacts have extensively been used in the GaAs devices. It is believed that Ge plays either or both of two roles in reducing the contact resistance (i) increase of the doping concentration in the GaAs at the metal/GaAs interface (ii) reduction of the barrier height at the interface through forming an intermediate thin Ge layer between the metal and GaAs. Hence the presence of Ge is beneficial for the electrical properties of Ohmic contacts.

### 1.2.4.1 Practical Ohmic contacts to GaAs and GaAs/AlGaAs

Semiconductor	Metallization	Method of preparation	Anneal Temperature (°C)	Specific contact resistance ( $\Omega\text{-cm}^2$ )	Transfer contact resistance $\Omega\text{-mm}$	Reference
n-GaAs	AuGe/Ni/Au	Evaporation, RTA	410	$1.2 \times 10^{-6}$	-	[36]
	Ni/AuGe/Ni	evaporation, annealing	420	-	0.1	[37]
	Ge	MBE	-	$3 \times 10^{-6}$	-	[38]
	Ni/AuGe/Ag/Au	evaporation, annealing	450	$3.8 \times 10^{-5}$	-	[39]
	Pd/Ge	e-beam evaporation, annealing	325	$1\text{-}3 \times 10^{-6}$	-	[40]
	Pd/Si	e-beam evaporation, annealing	375	$1\text{-}3 \times 10^{-6}$	-	[41]
	Ni/Ge	e-beam evaporation, RTA	600	-	0.78	[42]
	Ni/Au/Ge	evaporation, RTA	450	-	0.18	[43]
GaAs/AlGaAs	AuGe/Ni/Au	evaporation, annealing	500	$5 \times 10^{-8}$	0.035	[44]
	Pd/Ge	e-beam evaporation, RTA	300	$3 \times 10^{-7}$	0.08	[45]
	Ni/AuGe/Ag/Au	evaporation, annealing	560	-	0.15	[46]
	Ni/Ge/Au	evaporation, annealing	460	-	0.1	[47]
	Ni/Ge/Au/Ni/Au	e-beam evaporation, RTA	420	-	$2\Omega$	[48]
AlGaAs/InGaAs	AuGe/Ni/Au	evaporation, RTA	430	-	0.048	[49]
	Pd/Ge	e-beam evaporation, RTA	325	$1.2 \times 10^{-7}$	-	[50]

Among these, AuGe/Ni/Au system is the most used Ohmic contact to GaAs and GaAs/AlGaAs 2DEG systems. Such contacts are the most preferred because (i) contacts are prepared by the conventional evaporation and lift-off (ii) they give relative low contact resistance by annealing at a relatively low temperature (iii) they have excellent reliability and reproducibility. Therefore, these contacts have become the industry standard. [51-60].

Pd/Ge systems are a relatively new class of Ohmic contacts to GaAs. They are an alternative to AuGe based contacts to compound semiconductors, where lower anneal temperatures are desired (300°C instead of 400°C) [61-66].

Ni/Ge system is the alternative for AuGe/Ni and Pd/Ge where higher anneal temperatures are required for the contact formation (~600°C) [47, 48].

AuGe/Ni/Au and Pd/Ge based Ohmic contacts were used for fabricating Ohmic contacts to GaAs/AlGaAs multilayer structures in this thesis which are described more detail below.

#### 1.2.4.2 AuGe/Ni/Au Ohmic contact

AuGe/Ni contacts were invented by Braslau et.al. in 1967 [51] and have been extensively used as n-type Ohmic contact materials for GaAs and GaAs/AlGaAs devices. Binary alloy contacts made using AuGe, were first used by Gunn in 1964 in his diodes [52].

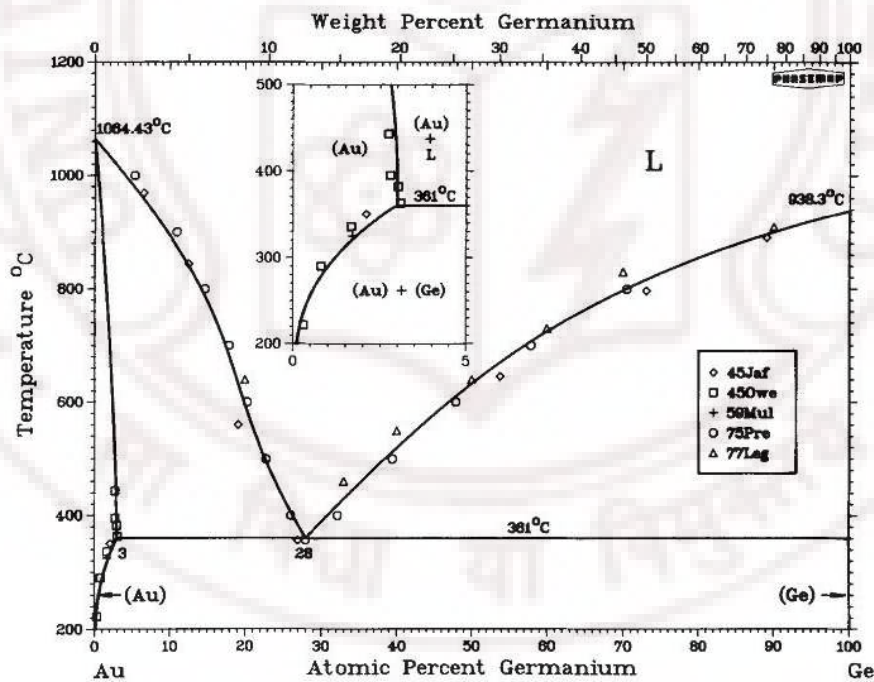


Figure 1.2.3 AuGe alloy phase diagram [67]

These contacts are usually based on the preparation of an evaporated eutectic alloy film of AuGe (88:12 wt %) followed by a rapid-thermal anneal to a temperature of ~ 400°C. The phase diagram of AuGe system is shown in figure 1.2.3. The binary alloy system has

a (bulk) deep eutectic at Ge: 12wt% with melting temperature of  $\sim 361^\circ\text{C}$  [67]. The use of eutectic composition of the AuGe alloy results in low contact resistance, presumably, due to enhanced diffusion of Ge into GaAs when the AuGe layer melts. This metallization, however, suffers from poor surface morphology on annealing. In addition to vertical diffusion, lateral spreading of the contact material takes place during annealing above the eutectic AuGe alloy melting temperature [53]. The addition of a Ni layer and a thick Au over-layer is found to reduce, to a considerable extent, the surface roughness during alloying [54] (see also chapter 3.2.2).

**Table 1.2.1** Schematic illustration of alloying sequence of AuGe/Ni/Au metallization.

Ni	AuGa	AuGa
AuGe	Ni <sub>3</sub> Ge	Ni <sub>2</sub> GeAs
n <sup>+</sup> GaAs	n <sup>+</sup> GaAs	n <sup>+</sup> GaAs
<b>As deposited</b>	<b>&lt; 400°C</b>	<b>&gt; 400°C</b>

Several studies have shown that, apart from the diffusion of various elemental components into GaAs, significant changes takes place in the metal film structure itself that could potentially influence electrical contact formation. For example, cross sectional TEM studies have shown the presence of binary and ternary compounds, Ni<sub>3</sub>Ge, Ni<sub>2</sub>GeAs and AuGa alloys after anneals [31, 36, 37]. Ni<sub>3</sub>Ge phase is seen after anneals close to the alloying temperature and Ni<sub>2</sub>GeAs phase is seen on heating well above the alloying temperatures (which are typically  $430^\circ\text{C}$ ) (table 1.2.1) [32, 33]. Moreover, Au reacted with GaAs forming low-melting-point AuGa phases. A correlation was reported between the formation of Ni<sub>2</sub>GeAs (between AuGa and GaAs layers) and low contact resistance [32].

In-situ x-ray diffraction studies on Au-Ge alloy layers deposited on GaAs wafers, after annealing [60] reveal the formation of AuGa compounds and the compounds formation appear to form when the AuGe alloy layer melts. The AuGa compounds have low melting temperatures ( $\sim 360^\circ\text{C}$ ) [60].

Glancing angle X-ray diffraction and back scattering studies of Ge/Au/Ni deposited on SiO<sub>2</sub> substrate and annealed at  $320^\circ\text{C}$  for 1 hour and  $450^\circ\text{C}$  for 5 minutes show the formation of AuGe layer and the inter-diffusion of Ge to Ni and the formation of NiGe. In a structure with the Au as top layer viz Au/Ni/Ge on SiO<sub>2</sub> substrate, formation of NiGe



compound layer was detected and the Au layer remained unaffected after annealing. When a thick Ni layer was used the formation of  $\text{Ni}_2\text{Ge}$  was detected [68].

Studies of Ge/Au/Ni deposited on GaAs substrate and annealing at  $350^\circ\text{C}$  for 6 minutes and  $450^\circ\text{C}$  for 5 minutes also showed the formation of AuGe and NiGe layers [69]. The Ni-Ge binary phase diagram is shown in figure 1.2.4. Four phases of  $\beta\text{-Ni}_3\text{Ge}$  (cubic),  $\text{Ni}_2\text{Ge}$  (orthorhombic),  $\text{Ni}_5\text{Ge}_3$  (monoclinic) and NiGe (orthorhombic) are the stable at room temperature and others are the stable at elevated temperatures. In situ XRD measurements during annealing of a 30nm thick Ni film deposited on Ge substrate detected the formation of  $\text{Ni}_5\text{Ge}_3$  at  $170^\circ\text{C}$  and of  $\text{Ni}_5\text{Ge}_3$  and NiGe at  $250^\circ\text{C}$ . The decrease of  $\text{Ni}_5\text{Ge}_3$  and increase of NiGe is observed at  $300^\circ\text{C}$  and finally completely converted to NiGe at  $380^\circ\text{C}$ . Ni has been identified as the moving species during these processes.

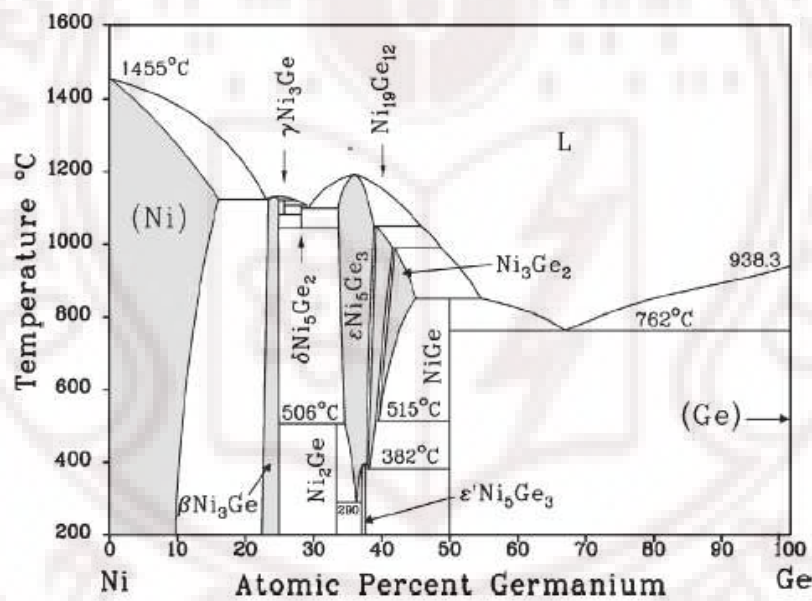


**Figure 1.2.4** Binary phase diagram for the Ni–Ge system [69]

### 1.2.4.3 Models of the Ohmic contact

According to the widely accepted model, at higher temperatures the Ge diffuse out of the Ni rich regions and heavily dope at the metal/GaAs interface making the depletion region narrow and allows tunneling of electrons through the barrier and results in low contact resistance [31].

Another model is that the contact resistance reduction was due to reduction of barrier height at the metal GaAs interface by the formation of thin Ge layer.

Braslau proposed a model for the alloyed contact and predicted a  $\frac{1}{N_d}$  dependence on contact resistance. The current flows through Ge rich islands, which are connected together through the overlying Au metal as shown in figure 1.2.5. The real area is a hemispherical region of radius  $r$  whose contact resistance  $r_c$  is less than that expected by tunneling. Emission is due to field enhancement at these penetrating points [70].

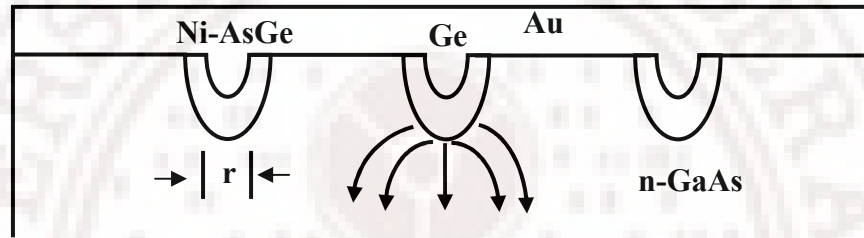


**Figure 1.2.5** Model of alloyed Ohmic contacts to GaAs<sup>[70]</sup>.

In the Ge poor regions, the conduction is smaller due to exponential dependence of tunneling current on underlying doping. They are however shorted by Au over-layer and Ge rich protrusions. Current flow is mainly through the regions of high conductance. The contact resistance can be written as

$$r_c = \langle a \rangle^2 \left[ \frac{\rho}{\pi \langle r \rangle} + \frac{r}{2f\pi \langle r \rangle^2} \right]$$

where  $\langle a \rangle$  is the mean separation of the protrusions and  $\langle r \rangle$  their mean radius;  $\rho$  is the resistivity of the region of doping  $N_d$ ; and  $f$  is the field enhancement factor which is  $\gg 1$ . For  $\rho > 10^{-3} \Omega\text{-cm}$ , the second term in the above relation ship is neglected. Thus the contact resistance is proportional to  $N_d^{-1}$ .

GaAs/AlGaAs 2DEG structures incorporate a  $n^+$  GaAs cap layer that is useful in the formation of Ohmic contacts. Backside Secondary Ion Mass Spectroscopy studies (SIMS) on AuGe/Ni/Au deposited on InGaAs/AlGaAs 2DEG structures with  $n^+$  GaAs cap layer and optimally annealed for low contact resistance (430°C-60s) samples detected Ge in

the  $n^+$  region with a concentration of  $10^{21}/\text{cm}^3$  and in the 2DEG channel with a concentration of  $3.5 \times 10^{20}/\text{cm}^3$  [49].

Cross sectional TEM studies of AuGe/Ni/Au deposited on GaAs/AlGaAs 2DEG and optimally annealed for low contact resistance show the penetration of Au grains and Ni grains, and the Ga in the Au rich grains and As in the Ni rich grains. The Ni rich phase absorbed most of Ge and Au rich grains did not contain Ge. Ge was detected down to the  $n^+$  AlGaAs supply layer. They conclude that Ge does not have to penetrate to the 2DEG layer to establish the contacts. Ni rich grains supply the Ge and Au rich grains resulting in large number of Ga vacancies in GaAs by forming AuGa, shows the importance of Ni and Ge in the metallization.

#### 1.2.4.4 Pd/Ge Ohmic contact

AuGe/Ni/Au metallization suffers from poor surface morphology when used with the eutectic AuGe composition and with optimized Ni layer thickness (for low contact resistance). Lateral spreading of the contact material takes place during annealing above the eutectic AuGe alloy melting temperature, a factor that influences the transistor gate fabrication. This translates into a need for contact structures that exhibit small lateral diffusion and provides smooth surface morphology in addition to good electrical properties. Hence, it is important to design a contact scheme with Ge and excluding liquid phase reactions for contact formations. Several attempts were made towards replacing Au with other metals in contact utilizing Ge but generally either the contact resistance increased or the thermal stability was poor.

A replacement for AuGe/Ni/Au alloy based Ohmic contacts is an Ohmic contact forming at  $\sim 300^\circ\text{C}$  through the solid phase reactions in a Pd/Ge metallization [61-65]. The Pd-Ge based Ohmic contact to GaAs/AlGaAs heterostructures has also been reported [66]. These studies of Pd/Ge on GaAs indicate that the optimum conditions are thickness of Pd and Ge layers for lowest contact resistance are 50nm and 100nm respectively [50]. It is observed that

- (a) Ge thickness  $\leq$  Pd thickness: no Ge growth at the GaAs surface and resulted in higher contact resistance.
- (b) Ge layer deposited first and then Pd layer: No Ohmic behaviour.

The contact scheme involves a metallic transport medium Pd, on to which a layer of Ge is grown. The thickness of Pd and Ge is chosen such that upon annealing, the entire Pd is consumed in the formation of a PdGe layer. The remaining amorphous Ge is transported through PdGe to re-grow epitaxially on the GaAs substrate. Early cross sectional TEM studies report that a solid state reaction between various layers and possibly with the substrate occurred as given in table 1.2.2. The subsequent studies confirm that an epitaxial layer of Ge with an over-layer of PdGe is formed. Alloying with the substrate is not so clear.

**Table 1.2.2** Schematic illustration of Pd/Ge contact formation [63]

Ge	Ge	Ge	Pd Ge	PdGe
pd	Pd	Pd		epi- Ge
GaAs	Pd <sub>4</sub> GaAs	Pd <sub>4</sub> GaAs (Ge)	n <sup>+</sup> - GaAs(Ge)	n <sup>+</sup> - GaAs(Ge)
As deposited	GaAs	GaAs	GaAs	GaAs
	100°C	200°C	250°C	300 °C above

DSC scans of Pd-20nm/Ge-150nm/Pd-50nm deposited on GaAs show several peaks at various temperatures. They also report Cross-sectional TEM results after anneals at temperatures corresponding to each of the peak positions. They have suggested that peaks correspond to solid state reactions in which various PdGe compounds are formed.

### 1.3 Specific contact resistance measurements

The quality of Ohmic contacts is characterized by its specific contact resistivity ( $\rho_c$ ). According to the direction of current flow in semiconductor, two types of contacts are possible, the vertical and the horizontal current flow geometry.

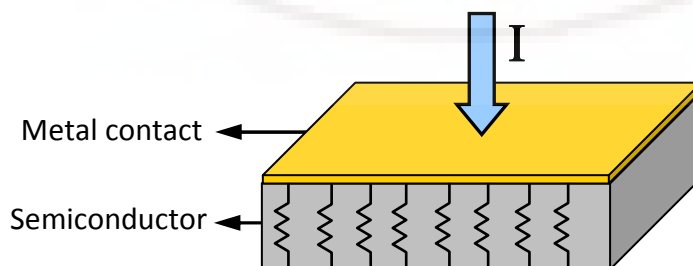


**Figure 1.3.1** Vertical contact geometry

Assuming that the current flow is uniform through the surface and the contact conductance is proportional to area  $A$  (figure 1.3.1), a contact conductance can be defined as conductance/Area or a specific contact resistance as  $\rho_c = R_c A$  given in  $\Omega\text{-cm}^2$ .

Transmission line or Transfer length model (TLM) model is used to assess the transfer contact resistance in horizontal or lateral current flow geometry [71, 72]. A brief description of TLM is given below.

### 1.3.1 Transmission line or transfer length model (TLM)

Transmission Line model or Transfer Length model (TLM) first introduced by Shockley and further advanced by Berger [73] and independently by Murmann and Widmann [74, 75]. Transfer length model uses a variable spacing between the metal pads on the test structure.

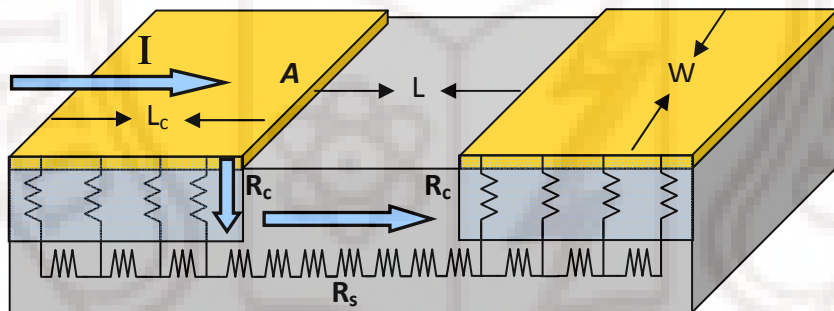


**Figure 1.3.2** Lateral/Horizontal contact geometry

In the horizontal flow case, current flows preferentially across the metal, then through the contacts and the semiconductor (figure 1.3.2). The current density is high at the edge of the metal  $A$ , and falls off away from the edge at a characteristic length '*transfer length*' determined by the ratio of the contact resistance to semiconductor sheet resistance. As long as the metallization '*length*' is much larger than the transfer length, the contact conductance is independent of the contact length (dimension in the direction of current flow), but scales with the contact width,  $W$ , (dimension perpendicular to current flow). The contacts can then be characterized by a conductance

per unit length perpendicular to current flow (i.e. width). The reciprocal of this quantity is the transfer contact resistance,  $R_{TC}$ , given in units of  $\Omega\text{-mm}$ .

According TLM the measured resistance is given as

$$R(L) = R_s \frac{L}{W} + \frac{2L_T}{W} R_s \coth \frac{L_c}{L_T}$$

where  $L$  is the contact spacing,  $L_c$  is the contact length,  $W$  is the contact width and  $L_T$  is defined as the transfer length. When  $L_c \gg L_T$  the  $\coth\left(\frac{L_c}{L_T}\right)$  term approaches unity so that  $R_s$  and  $L_T$  may be determined from a plot of total resistance versus contact spacing. In addition, extrapolation of the resistance versus gap spacing to zero gap spacing gives a value equal to twice the total contact resistance  $R_c$ . The y-axis intercept is  $R(L=0) = 2R_c$  and  $R_{TC} = R_c W$ . The x-axis intercept is  $2L_T$ . The slope gives  $R_s/W$  where  $R_s$  is the semiconductor sheet resistance. The specific contact resistance can be estimated from these quantities as  $\rho_c = R_s L_T^2$ . An assumption that the sheet resistance of the semiconductor below the contact pads is the same as that between the contact pads is made in this model.

TLM model is employed for measuring contact resistance in this study. The term ‘contact resistance’ with units specified as  $\Omega\text{-mm}$  means transfer contact resistance throughout the rest of the thesis.

#### 1.4 Motivation for this work

The use of Ni in Ohmic contact metallization, if magnetic after processing, may cause perturbation of the measured field in Hall magnetic field sensors. Despite the use of AuGe/Ni/Au Ohmic contacts to GaAs/AlGaAs for quite some time, systematic magnetic data of the contact structure are scarce in the literature. Sensor fabricators tend to use alternatives such as Cr, Ti etc. for the interlayer. However these formulations produce a rougher morphology after processing, as will be shown in chapter 3. The Ni based contacts are popularly used in active devices such as HEMTs where lateral roughness of the contacts near the gate needs to be minimized. Therefore, in the context of Hall magnetic field sensors with on-chip circuits, a process optimization needs to be carried

out wherein all three parameters- magnetization, contact resistance and roughness are considered. This is a primary objective of the work described in this thesis. The magnetization measurements have also provided some useful additional insights into changes occurring in the metallization layer early in the annealing process before alloying occurs.





## References

1. H. Lafontaine, A. M. Haghiri-Gosnet, Y. Jin, P. Crozat, R. Adde, M. Chaker, H. Pepin, F. Rousseaux and H. Lounois, *IEEE Trans. Electron Devices.*, **43** (1996) 175.
2. Jong Won Lim, Ho-Kyun Ahn, Hong-Gu Ji, Woo-Jin Chang, Jae-Kyoung Mun and Haecheon Kim, *Semicond. Sci. Technol.*, **19** (2004) 1416.
3. A. Köck, E. Gornik, G. Abstreiter, G. Böhm, M. Walther and G. Weimann, *Appl. Phys. Lett.*, **60** (1992) 2011.
4. Y. Sugiyama, *J. Vac. Sci. Technol., B* **13** (1995) 1075.
5. V. V. Khotkevych and S. J. Bending, *Journal of Physics: Conference Series*, **150** (2009) 012021.
6. Y. Abulafia, M. McElfresh, A. Shaulov, Y. Yeshurun, Y. Paltiel, D. Majer, H. Shtrikman, and E. Zeldov, *Appl. Phys. Lett.*, **72**, 22 (1998) 2891.
7. Y. Yamaguchi, G. Rajaram, N. Shirakawa, A. Mumtaz, H. Obara, T. Nakagawa and H. Bando, *Physical Review B.*, **63** (2000) 014504.
8. A. Sandhu, H. Masuda, A. Oral and S. J. Bending, *Jpn. J. Appl. Phys.*, **40** (2001) 4321.
9. P. D. Ye, D. Weiss, K. von Klitzing, K. Eberl and H. Nickel, *Appl. Phys. Lett.*, **67**, 10 (1995) 1441.
10. S. O. Connor, L. Clapham and P. Wild, *Meas. Sci. Technol.*, **13** (2002) 157.
11. K. Kosmas, Ch. Sargentis, D. Tsamakis and E. Hristoforou, *Journal of Materials Processing Technology*, **161** (2005) 359.
12. S.M. Sze, *Physics of semiconductor devices*, John Wiley, New York (1981).
13. S. Adachi, *J. Appl. Phys.*, **58** (1985) R1.
14. Zh. I. Alferov, *Semiconductors.*, **32** (1997) 1
15. John H. Davies, *The theory of Low dimensional semiconductors*, Cambridge University Press (1998).
16. W. Walukiewicz, H.E. Ruda, J. Lagowski and H.C. Gatos, *Phys. Rev. B.*, **30** (1984) 4571.
17. I. Y. Yanchev and S. K. Evtimova, *J. Phys. C: Solid State Phys.* **18** (1985) L377.
18. T. R. Lepkowski, G. Shade, S.P. Kwok, M. Peng, L. E. Dickens, D.L Laude and B. Schoendube, *IEEE Electron Device Letters.*, **EDL-7** (1986) 222.
19. A. Sandhu, H. Sanbonsugi, I. Shibasaki, M. Abe and H. Handa, *Jpn. J. Appl. Phys.*, **43** (2004) 868.



20. N. J. Gokemeijer, T.W. Clinton, T.M. Crawford, Mark Johnson, *Journal of Magnetism and Magnetic Materials.*, **290–291** (2005) 254.
21. A. Sandhu, *Jpn J Appl Phys.*, **43** (2004) 868.
22. A. Lepore, M. Levy, H. Lee, E. Kohn, *IEEE Trans. Electron Devices* **35** (1988) 2441.
23. Jin-Hee Lee, Hyung-Sup Yoon, Byung-Sun Park, Chul Soon Park, Sang-Soo Choi and Kwang-Eui Pyun, *ETRI*, **18** (1996) 171.
24. Kun-Ta Wu, P.H. Chang, S.T. Lien, N.C. Chen, Ching-An Chang, C.F. Shih, W.C. Lien, Y.H. Wu, Shang-Chia Chen, Y.H. Chang, C. T. Liang, *Physica E*, **32** (2006) 566.
25. The room temperature (RT) carrier mobility is  $\sim 7800 \text{ cm}^2/\text{V.s.}$  and at 77K is  $\sim 1.4 \times 10^5 \text{ cm}^2/\text{V.s.}$ , sheet carrier density is  $\sim 3.4 \times 10^{11} \text{ cm}^{-2}$  at RT and  $\sim 4.5 \times 10^{11} \text{ cm}^{-2}$  at 77K.
26. T. Wang, Y. H. Liu, Y. B. Lee, Y. Izumi, J.P. Ao, J. Bai, H.D. Li, S. Sakai, *Journal of crystal growth.*, **235** (2002) 177.
27. Y. Cordier, F. Semond, M. Hugues, F. Natali, P. Lorenzini, H. Haas, S. Chenot, M. Laugt, O. Tottereau, P. Vennegues, J. Massies, *Journal of Crystal Growth.*, **278** (2005) 393.
28. Xiaoliang Wang, Guoxin Hu, Zhiyong Ma, Junxue Ran, Cuimei Wang, Hongling Xiao, Jian Tang, Jianping Li, Junxi Wang, Yiping Zeng, Jinmin Li and Zhanguo Wang, *Journal of crystal growth.*, **298** (2007) 835.
29. R. J. Trew, J. B. Yan, P. M. Mock, *Proceedings of the IEEE.*, **79** (1991).
30. M. J. Howes and D. V. Morgan, *Gallium Arsenide Materials, Devices and circuits*, John Wiley & sons, Newyork (1985).
31. E.D. Marshall and M. Murakami, *Contacts to Semiconductors: Fundamentals and Technology.*, Noyes Publ., NJ (1993), 1
32. M. Murakami, *Science and Technology of Advanced Materials* **3** (2002) 1.
33. T. C. Shen, G. B. Gao and H. Morkoc, *J. Vac. Sci. Technol.*, **B 10** (1992) 2113.
34. M. S. Tyagi, *Introduction to semiconductor materials and devices*, John Wiley and sons (1991).
35. L. C. Wang, *J. Appl. Phys.*, **77** (1995) 1607.
36. T. S. Kuan, P. E. Batson, T. N. Jakson, H. Rupprecht and E. L. Wilkie *J. Appl. Phys.*, **54** (1983) 6952.

37. M. Murakami, K. D. Childs, J. M. Baker and A. Callegari, *J. Vac. Sci. Technol.*, B **4** (1986) 903.
38. R. A. Stall, C. E. C. Wood, K. Board, N. Dandekar, L. F. Eastman and J. Devlin, *J. Appl. Phys.*, **52** (1981) 4062.
39. Takashi Ehara, Naoki Shibata, Hirokazu Ohta, Tohru Nukui and Tadao Kazuno *Jpn. J. Appl. Phys.*, **34** (1995) 3051.
40. E. D. Marshall, W. X. Chen, C.S. Wu, S. S. Lau and T.F. Kuech, *Appl. Phys. Lett.*, **47** (1985) 298.
41. L. S. Yu, L. C. Wang, E. D. Marshall and S. S. Lau, *J. Appl. Phys.*, **65** (1989) 1621.
42. Kiwamu Tanahashi, H.J. Takata, A. Otuki and M. Murakami, *J. Appl. Phys.*, **72** (1992) 4183.
43. Hirotaka R. Kawata, Takeo Oku, Akira Otsuki and M. Murakami, *J. Appl. Phys.*, **75** (1994) 2530.
44. A. Ketterson, F. Ponse, T. Henderson, J. Klem, H. Morkoc, *J. Appl. Phys.*, **57** (1985), 2305
45. L. C. Wang, S. S. Lau, E. K. Hsieh and J. R. Velebir, *Appl. Phys. Lett.*, **54** (1989) 2677.
46. W. L. Jones, L. F. Eastman, *IEEE Transactions on electron devices.*, ED-**33** (1986), 712.
47. M. Furumai, T. Oku, H. Ishikawa, A. Ostuki, Y. Koide, T. Oikawa, M. Murakami, *J. Electron. Mater.*, **25** (1996) 1684.
48. H. J. Lee, M. S. Tse, K. Radhakrishnan, K. Prasad, J. Weng, S. F. Yoon, X. Zhou and H. S. Tan, *Mater. Sci. Eng. B.*, **35** (1995) 234.
49. G. Sai Saravanan, K. Mahadeva Bhat, K. Muraleedharan, H. P. Vyas, R. Muralidharan and A. P. Pathak, *Semicond. Sci. Technol.*, **23** (2008) 025019.
50. Jong-Lam Lee, Yi-Tae Kim, Jung-Woo Oh and Byung-Teak Lee, *Jpn. J. Appl. Phys.*, **40** (2001) 1188.
51. N. Braslau, J. B. Gunn, J. L. Staples, *Solid State Electron.* **10** (1967) 381.
52. J. B. Gunn, *IEEE Transactions of Electron Devices.*, ED **23** (1976) 705.
53. G.Y. Robinson, *Solid State Electron.*, **18** (1975) 331.
54. J. Gyalai, J. W. Mayer, V. Rodriguez, A. Y. C. Yu and H. J. Gopen, *J. Appl. Phys.*, **42** (1971) 3578.

55. R. P. Taylor, P.T. Coleridge, M. Davies, Y. Feng, J. P. McCaffrey, P. A. Marshall, *J. Appl. Phys.*, **76** (1994) 7966.
56. M. Kamada, T. Suzuki, F. Nakamura, Y. Mori, M. Arai, *Appl. Phys. Lett.*, **49** (1986) 1263.
57. A. G. Baca, F. Ren, J. C. Zolper, R. D. Briggs and S. J. Pearton, *Thin Solid Films* **308** (1997) 599.
58. V. Chabasseur-Molyneux, J. E. F. Frost, M. Y. Simmons, D. A. Ritchie and M. Pepper, *Appl. Phys. Lett.* **68** (1996) 3434.
59. R. V. Konakova, V. V. Milenin, M. A. Stovovoi, *Semiconductor Physics, Quantum Electronics and Optoelectronics.*, **2** (2002) 180.
60. T. Kim and D. D. L. Chung, *Thin Solid films.*, **147** (1986) 177.
61. E. D. Marshall, B. Zhang, L. C. Wang, P. F. Jiao, W. X Chen, T. Sawada and S. S Lau, *J. Appl. Phys.*, **62** (1987) 942.
62. F. Radulescu and J. M McCarthy, *J. Appl. Phys.*, **86** (1999) 995.
63. L. C. Wang, S. S Lau, E. K. Hsieh and J. R. Velebir, *Appl. Phys. Lett.*, **54** (1989) 2677.
64. C. J. Palmstrom, S.A. Schwarz, E. Yablonovitch, J. P. Harbison, C. L. Schwartz, L.T. Florez and T. J. Gmitter, *J. Appl. Phys.*, **67** (1990) 334.
65. Jiun-Tsuen Lai and Joseph Ya-Min Lee, *Appl. Phys. Lett.*, **64** (1994) 229.
66. D.A. Ahmari, M.L. Hattendorf, D.F. Lemmerhirt, Q. Yang, Q. J. Hartmann, J.E Baker and G.E Stillman, *Appl. Phys. Lett.*, **72** (1998) 3479
67. R. P. Elliott and F. A. Shunk, *Bulletin of Alloy Phase Diagrams* **2** (1981) 356.
68. M. Wittmer, R. Pretorius, J. W. Mayer and M. A. Nicolet, *Solid state electron.*, **20**, (1977) 433.
69. T.G. Finstad, *Thin solid films*, **47**, (1977) 279.
70. N. Braslau, *J. Vac. Sci. Technol.*, **19**, (1981) 803.
71. D. C. Look *J. Electrochem. Soc.*, **135** (1988) 2054.
72. D. C. Look, *Electrical Characterization of GaAs Materials and Devices.*, Wiley New York (1989) 138.
73. H.H. Berger, *Solid State Electron.*, **15** (1972) 145.
74. H. Murmann and D Widmann, *IEEE Trans. Electron Devices*, **ED-16** (1969) 1022.
75. H. Murmann and D. Widmann, *State Electron.*, **12** (1969) 879.

## Chapter -2

### Experimental Techniques

#### 2.1 Introduction

This chapter presents the experimental techniques used in the work for the thesis, especially the fabrication processes and characterization techniques. The processing steps involved in the fabrication of the transmission line pattern (TLM) for contact resistance measurement are discussed: Design of the mask pattern, photo lithography, wet etching of the mesa, Ohmic contact metallization and rapid thermal annealing.

Experimental techniques employed for the measurement of contact resistance and magnetic properties of the Ohmic contact film structures are presented. Scanning electron microscopy (SEM) and Atomic force microscopy (AFM) are used to study the morphology of the contact surface. In addition, X-ray photoelectron spectroscopy (XPS) is also used to get the chemical composition of the Ohmic contact layers before and after alloying. Grazing incidence XRD is used to observe structural evolution and changes in the metallization structure. Conducting probe Atomic Force Microscopy (C-AFM) is used to map the current distribution in the alloyed Ohmic contact surface, and the nano-scratch test is employed to study the adhesion properties of the Ohmic contact.

#### 2.2 GaAs/AlGaAs 2DEG wafer structure

The GaAs/AlGaAs multilayer structure used in this study is grown by Molecular Beam Epitaxy (MBE) and procured from IQE [1]. The structure is given in table 2.2.1. The potential diagram simulated using ID Poisson band diagram calculator is also given.

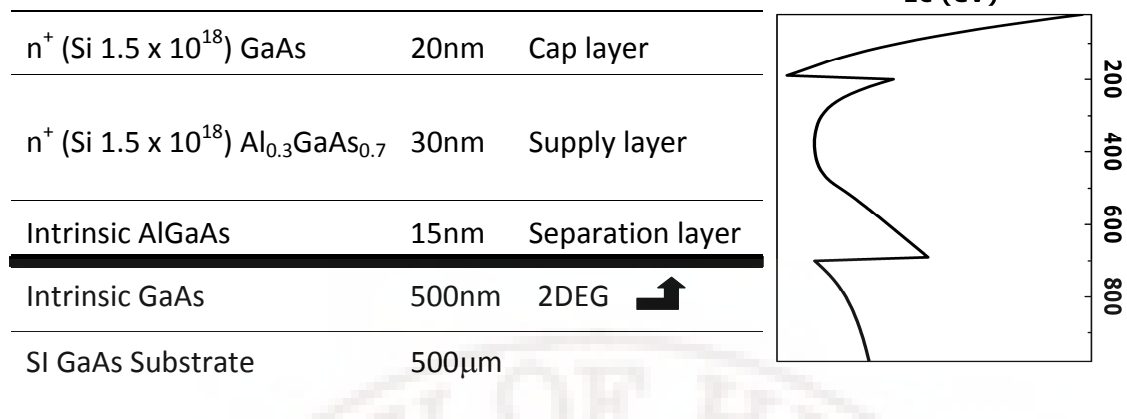


**Table 2.2.1** GaAs/AlGaAs wafer layer structure and the potential diagram

The epitaxial layers are grown on a semi-insulating GaAs substrate of 500  $\mu$ m thickness. A thick (500nm) buffer layer of GaAs is grown to reduce defects and impurities present on the wafer surface. The structure has one homogeneous junction ( $n^+$ AlGaAs/i-AlGaAs) and two heterogeneous-junctions ( $n^+$ GaAs/ $n^+$ AlGaAs, i-AlGaAs/i-GaAs). The 2DEG layer of ( $\sim 5$ -10nm thickness) is formed at the un-doped, intrinsic GaAs/AlGaAs interface. The supply layer is n-doped AlGaAs layer. The degenerately doped layer enables the availability of the carriers down to low temperatures. Electrons from the supply layer tunnel into the potential well at the interface of i-AlGaAs/i-GaAs and form a two dimensional electron gas layer. The effective width of the barrier for tunneling is controlled by width of the i-AlGaAs separation layer. The structures usually incorporate a silicon-doped  $n^+$  GaAs cap layer that is useful in the formation of Ohmic contacts and protects the AlGaAs from oxidation.

The sheet carrier density and electron mobility of the two dimensional electron gas are  $\sim 3.4 \times 10^{11} \text{ cm}^{-2}$  and  $\sim 7800 \text{ cm}^2/\text{V.s}$ , respectively, at 300K. The corresponding values at 77K are  $\sim 4.5 \times 10^{11} \text{ cm}^{-2}$  and  $\sim 1.4 \times 10^5 \text{ cm}^2/\text{V.s}$ . The etch pit density of the wafer are  $< 10000$ .

## 2.3 Device Fabrication (Transmission line pattern)

### 2.3.1 Mask layout

The geometric pattern drawn with CAD software (AUTOCAD) is used to create lithographic masks. The mask contains patterns for conductivity measurement, transmission line pattern (TLM) for contact resistance estimation, MESFET /HEMT and Hall sensors. The fabrication of the TLM involves a five mask processes. (i) device isolation by mesa etch (ii) deposition of Ohmic contact metallization and patterning by lift off (iii) deposition of Cr/Au layer for interconnect pads and patterning by lift off. Two additional trivial steps are used, deposition of Cr/Au alignment-marks at the beginning and a protection layer of hard baked photoresist at the end. The masks were fabricated at SAC Ahmedabad, using an electron-beam lithography system.

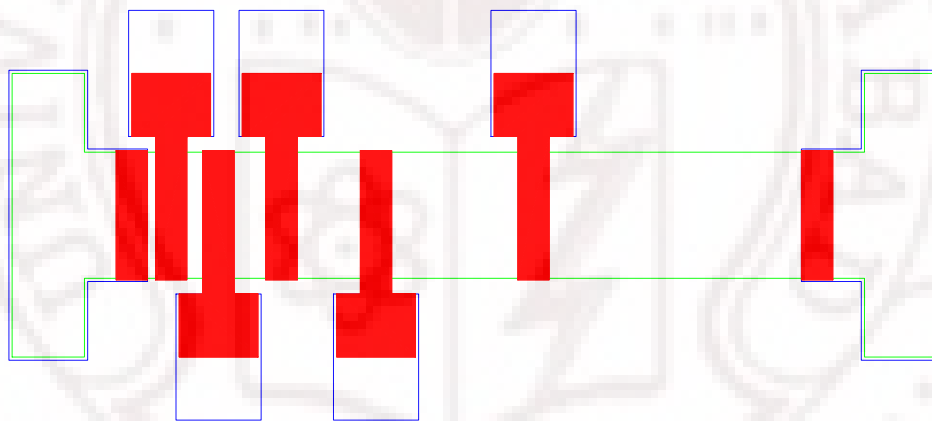


**Figure 2.3.1** Layout of the TLM configuration used for contact resistance measurement

The mask diagram of the TLM structure is shown in figure 2.3.1. Mesa etch mask is represented in green, Ohmic contact mask in red and interconnect mask in blue. The pad length of the Ohmic contact is 0.1mm and width is 0.4 mm. The spacing between the contact pad is varying as  $d = 0.025, 0.05, 0.1, 0.2, 0.4$  mm. Typically, wafer sizes that are processed at one time are 5 mm x 5mm. The processing sequence of a TLM pattern is shown in figure 2.3.2.

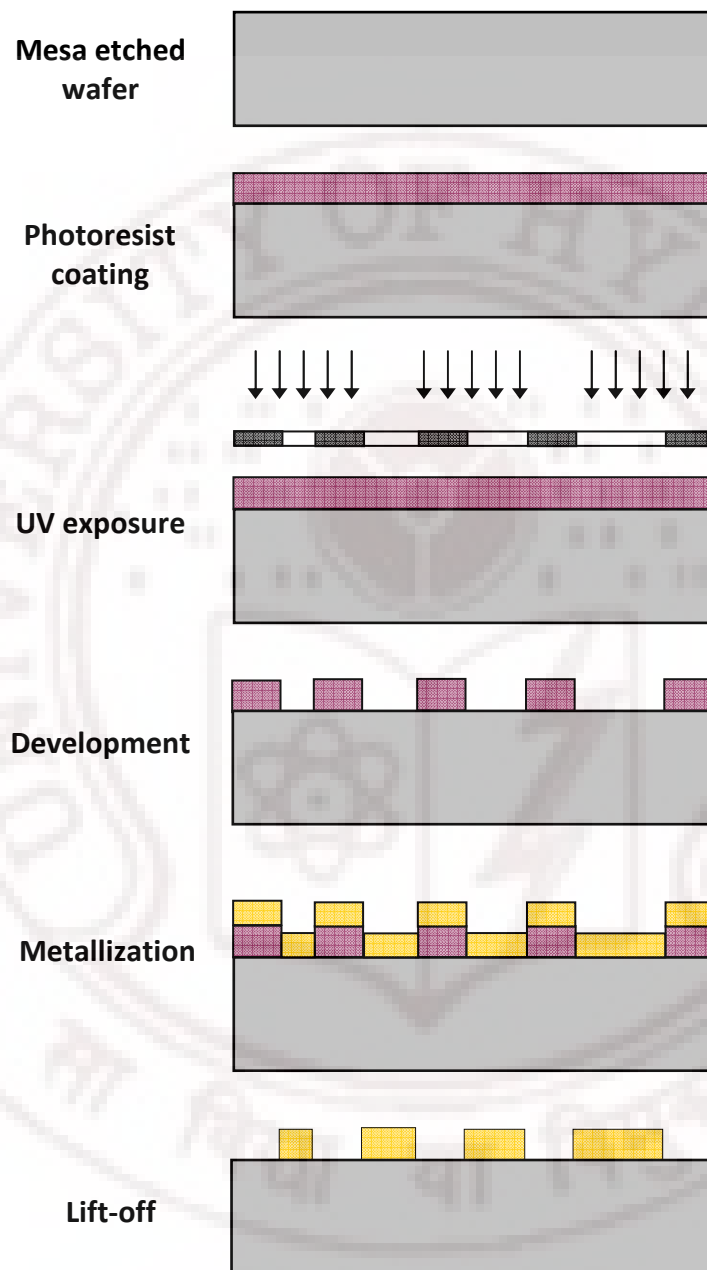


**Figure 2.3.2** Processing sequence of a TLM



### 2.3.2 Wafer processing

#### 2.3.2.1 Photo Lithography

The wafer surface is cleaned with acetone, propanol and De-ionized (DI)-water with ultrasonic agitation. The wafer is rinsed in running DI-water and water droplets are blown away with dry, filtered N<sub>2</sub> gas. The wafer is then dried at a temperature >100°C on a hot plate for about 20 minutes. UV photo lithography at a wavelength of 365nm (i-line) is used for patterning. For this, the wafer surface was spin coated with a positive photoresist (Fuji film OiR 620-10M) at a speed of 3000 rpm (typical resist thickness is 1µm), followed by soft baking. The wafer is then mounted in the mask aligner, aligned with the mask and exposed to UV light, After the development using developer (tetra-methyl ammonium hydroxide) the wafer is rinsed thoroughly with water. A Karl Suss MJB4 Contact Mask Aligner with Hg lamp UV light source and 4" beam diameter was used for defining the pattern.

#### 2.3.2.2 Wet Etching

Device isolation is achieved by lithographically patterning the wafer and etching down to the 2DEG everywhere except in a selected mesa region. The recipe used for mesa etch is wet etching with H<sub>3</sub>PO<sub>4</sub>:H<sub>2</sub>O<sub>2</sub>:H<sub>2</sub>O in the ratio 3:1:50. Calibration etch is performed during each fabrication run. The typical etch rate was 600Å<sup>o</sup>/minute. The etch depth is measured using a Diamond stylus profilometer after stripping the photoresist layer. In the present case, for isolation etch, the depth used is ~800Å<sup>o</sup> which is just below the 2DEG layer.

#### 2.3.2.3 Lift-off

Most of the deposited layers were patterned by lift off, as opposed to etching. Lift off is performed by dissolving the material in a photoresist stripper (acetone) there by lifting away the film deposited on top of the photoresist leaving only the film deposited on the substrate. In case of Shipley (S-1813) resists, monochloro- benzene (MCB) dip is used to harden the surface against development. This creates an overhang in the resist and

hence a distinct break between the material on top of the photoresist and that deposited on the exposed substrate. Some of the present work, photoresist used (Fuji film (OiR 620-10M) could not be hardened against development using MCB. However, the deposited layers up to 300nm could be patterned by lift-off using a 1 $\mu$ m photoresist thickness without using dual layer process.

### **2.3.3 Ohmic contacts**

Low resistance Ohmic contacts are essential for device applications. There is no universal process for Ohmic contact formation. A successful formation depends on the metal selection, annealing temperature, time and annealing atmosphere etc. The most common Ohmic contact metallization for GaAs and GaAs/AlGaAs heterostructure have been made by using AuGe/Ni/Au, Pd/Ge, and Ni/Ge [2-7] etc. These contacts are prepared usually by the evaporative deposition after patterning by lift-off techniques. This is usually followed by a rapid thermal anneal. Role of various metal layers in such metallization schemes are still a subject of investigation.

The subjects of present study are AuGe/Ni/Au and Pd/Ge based Ohmic contacts for which the process steps are described in more detail below.

#### **2.3.3.1 AuGe alloy Preparation by Arc Melting**

Eutectic AuGe (88:12 wt %) and off-eutectic AuGe (95:5, 97.3:2.7 wt %) alloys are prepared by arc melting. The Arc melting apparatus consists of tungsten cathode and water cooled copper anode crucibles. The chamber, cathode and anodes are thoroughly cleaned and pure Au (99.99%) and Ge (99.999%) are mounted in the crucible. The chamber is pumped down to  $10^{-6}$  mbar and flushed with Ar gas several times. A titanium gettering material is melted first to remove the residual oxygen present in the chamber or as impurity. The alloys are melted and re-melted after overturning few times to achieve a uniform composition. The uniformity of this alloy over size scales of 0.2mm (typical granule sizes used in evaporation) is confirmed using EDAX.

### 2.3.3.2 Photoresist Ashing / Descumming

Photoresist that have excellent adhesion to the surface, while desirable for lithography may leave extremely thin residual layers that are not etched by the developer. General cleanliness of the fabrication area may also introduce contaminants on the exposed substrate surface. This has potential for causing poor adhesion as well as reduced diffusion/alloying that are essential for Ohmic contact formation. Low power microwave and RF Oxygen plasmas can be used to remove the photoresist residues and carbon contaminants from the wafer. In the present study DC Oxygen plasma is used for the removal of photoresist residues. The evaporation chamber is initially pumped down to  $10^{-6}$  mbar using a turbo pump. Subsequently 99.99% Oxygen is introduced into the chamber and plasma sputter cleaning is performed at a DC power of 100W and at a chamber pressure of  $10^{-1}$  mbar. Typical duration for plasma cleaning that resulted in lower contact resistance is 20 minutes. At longer durations, the contact resistance increased probably due to plasma induced damage to the wafer. Hence for all subsequent processing the plasma cleaning is carried out for 20 minutes.

### 2.3.3.3 Ohmic contact Metal deposition

Two kinds of contact systems are studied and described in this thesis, one consisting of AuGe/Ni/Au and the other Pd/Ge deposited on GaAs/AlGaAs (figure 2.3.3). The deposition of Ohmic contact metallization is carried out in a vacuum evaporation system containing both e-beam and thermal evaporation. The system was pumped down to  $10^{-6}$  mbar with a turbo molecular pump backed by a mechanical pump. The pressure during evaporation was  $(2-4) \times 10^{-6}$  mbar.

For AuGe/Ni/Au metallization AuGe alloy (88:12 wt %) is deposited first using thermal evaporation, then Ni evaporated using e-beam evaporation and Au by thermal evaporation. The film thickness was calibrated by monitoring the growth rates of AuGe, Ni and Au films in-situ using a quartz crystal oscillator and verified using a surface profiler. A 0.1 gm of the material was deposited at a fixed current, vacuum ( $\sim 2-4 \times 10^{-6}$  mbar) and at constant deposition rate of  $\sim 3 \text{ \AA/s}$ . A thickness of  $\sim 700 \text{ \AA}$  is observed

in the quartz crystal oscillator which is verified using a surface profiler. Similarly AuGe and Au were weighed about 0.145 and 0.285 grams respectively for AuGe thickness of 1000Å and Au thickness of 2000Å. Tungsten boats are used for the evaporation. The TLM structures are patterned and sputter cleaned in O<sub>2</sub> plasma before deposition of the Ohmic contacts. For Pd/Ge metallization, Pd and Ge are deposited using e-beam evaporation.

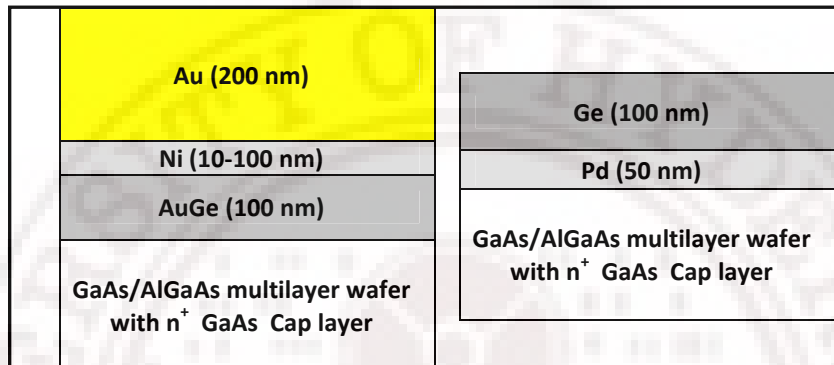


**Figure 2.3.3** Ohmic contact metallization

The mesa etched TLM structure, after AuGe/Ni/Au metallization and lift-off, is shown in figure 2.3.4.

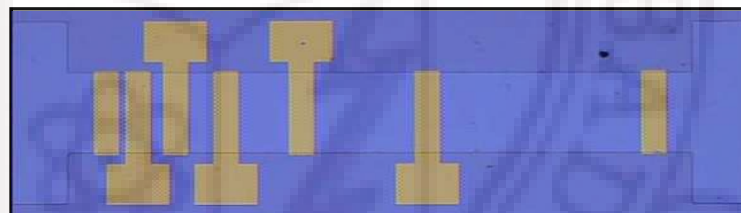


**Figure 2.3.4** Fabricated TLM pattern

The AuGe (88:12 wt %) alloy is prepared by arc melting. Reasonably good homogeneity is obtained as shown by the Differential Scanning Calorimetry (DSC) data on the bulk alloy sample (figure 2.3.5a). However, in evaporation processes, the film composition and homogeneity need not necessarily be the same as that of the source. To verify this, DSC runs were made on films deposited on Al foil in the same runs as the processed wafers and these do show sharp transitions close to the alloy eutectic temperature (figure 2.3.5b). When thin layers of material are deposited, the film's conformal surface coverage may not be uniform. This could cause additional agglomeration on processing.

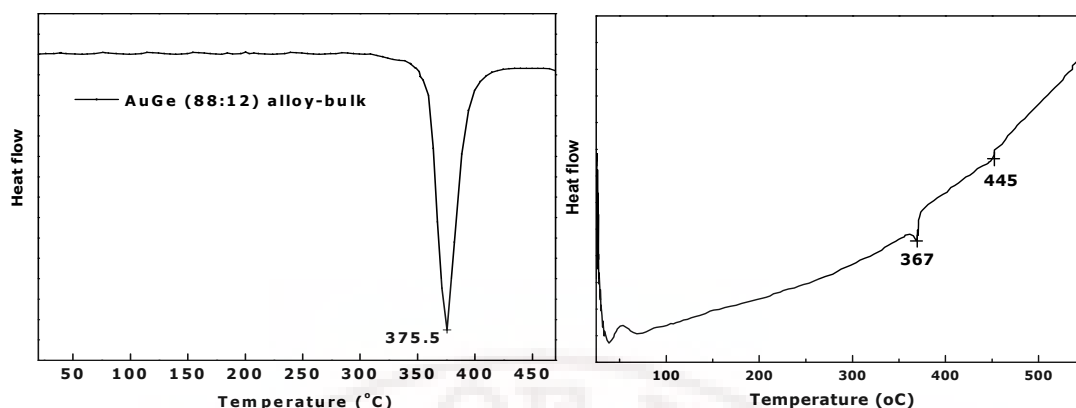


**Figure 2.3.5** DSC scans for samples with (a) eutectic (88:12 wt %) AuGe bulk alloy (b) eutectic AuGe alloy deposited on Al foil.

#### 2.3.3.4 Surface Profilometer: Etch depth and deposited film thickness measurement

The diamond stylus profilometer AMBIOS technology XP1 series is used to measure both roughness and step height/etch depth. The radius of the stylus tip is about 2 microns and the measurement edge profiles would be influenced by the tip size. This system measures the step height from 10 Å to 100 μm with a manufacturer specified vertical resolution of 1 Å at 10 μm. The profiler incorporates an optical deflection height measurement mechanism and magneto static force control system capable of a low force of about 0.05 mg. A diamond stylus is made to contact with the sample surface, and then moved laterally across the sample for a specified distance and with a specified contact force. The vertical reflection measures the changes in the step height and the displacement is recorded. The measurements are performed after calibrating with a standard sample.

#### 2.3.3.5 Rapid thermal Annealing (RTA)

Ohmic contacts require an annealing step to make electrical contact to the 2DEG. A rapid thermal annealing apparatus is set up in-house (figure 2.1.6). Halogen lamps were used for achieving rapid heating. The system is pumped down to  $10^{-3}$  mbar and flowing  $N_2$  gas is used as ambient.

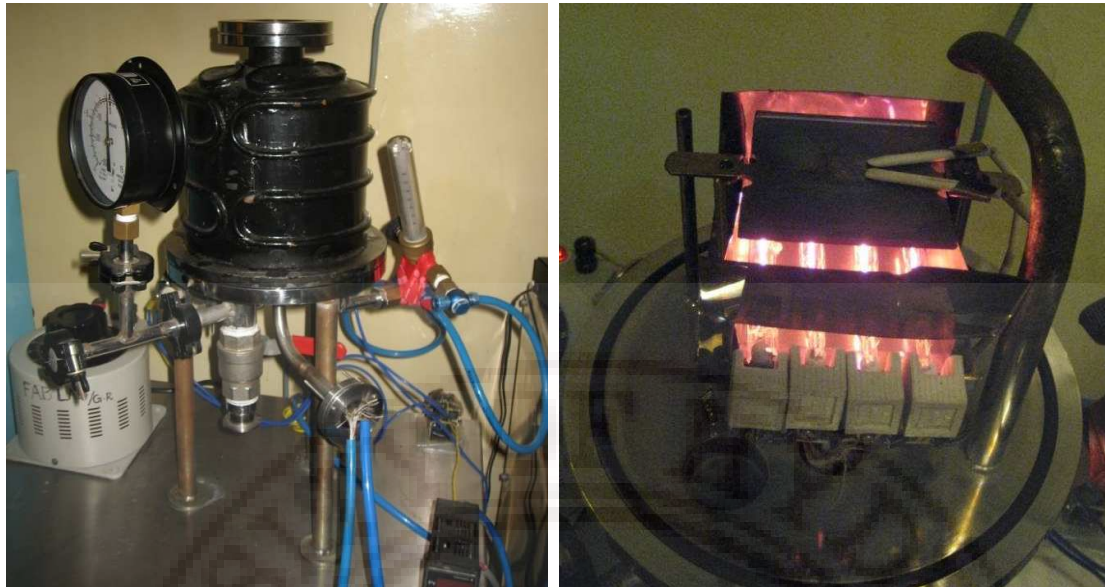


**Figure 2.3.6** Rapid thermal annealing apparatus

The temperature is controlled manually and monitored using the two thermocouples on a symmetrically placed dummy wafer piece during the anneal (Figure 2.3.7). The temperature is logged using a data logger. The wafer is heated from the bottom; i.e., the wafer side. Temperature is ramped from room temperature to  $400^{\circ}\text{C}$  in  $\sim 100$  seconds. Closed loop control is difficult at this ramp rates as the sample holder has a larger mass. A heating rate of  $250^{\circ}\text{C}/\text{min}$  is achieved and a typical time profile of temperature is shown figure 2.3.8.

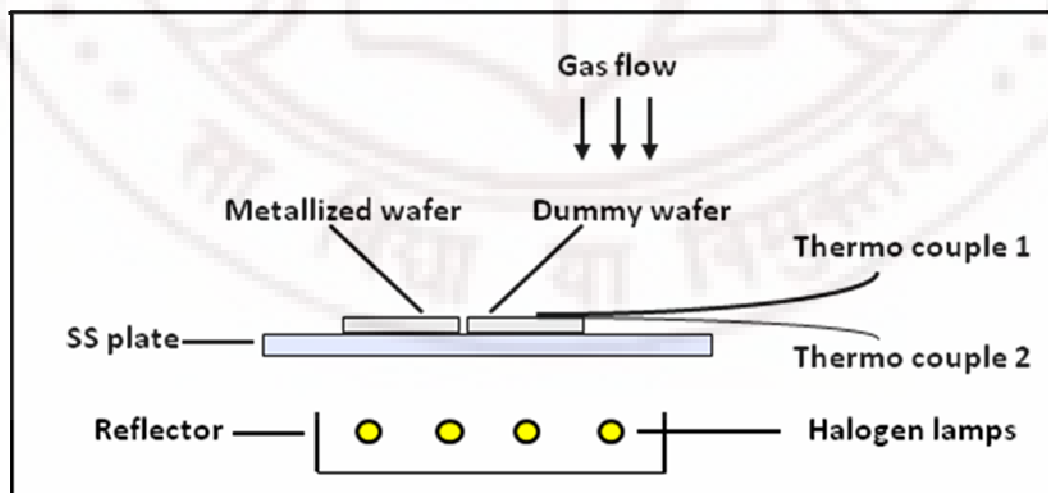


**Figure 2.3.7** RTA heating schematic



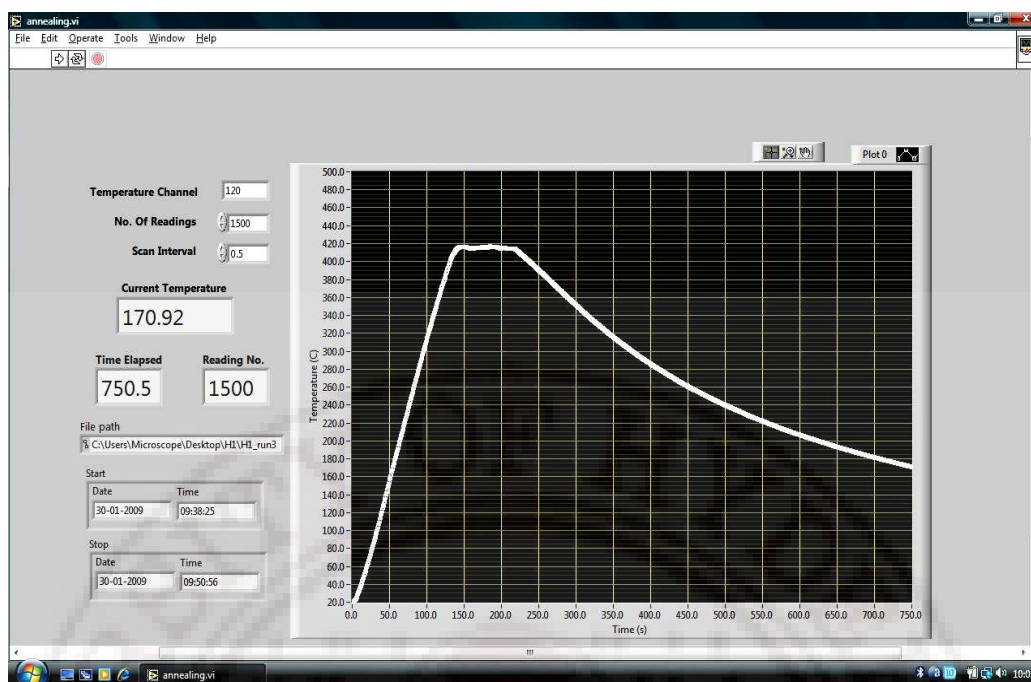


**Figure 2.3.8** Annealing data profile

For AuGe/Ni/Au based contacts, rapid thermal annealing is done between 350°C to 450°C. In the case of Pd/Ge the annealing experiments are done between 200°C to 400°C.

### 2.3.3.6 Probe station

The probe station utilizes manipulators which allow the precise positioning of thin needles on the surface of a semiconductor device. The TLM pattern/device is held by vacuum chuck and the probes are fixed to micro-positioners, enabling fine X, Y, Z movement. In this study, the I-V characteristics at various pads were measured by mounting the TLM device on a wafer-prober (SIGNATONE 1160 series).

### 2.3.3.7 Wire bonding

The TLM device is mounted on a chip holder and pad to chip-holder connections were made using a wire bonder (West bond manual wedge bonder: Model WEST BOND 7476D). Thick (20nm Cr/ 300nm Au) interconnect layers deposited and patterned by lift-off for wire bonding. The bonding parameters are optimized and 25 micron gold wires are ultrasonically bonded.



### 2.3.3.8 Device Analyzer

The I-V characteristics at various TLM pads are measured using an Agilent B1500A semiconductor device analyzer with probe currents in the range  $\pm 0.5\text{mA}$ . This instrument supports IV measurements with a resolution of  $0.1\text{ fA} / 0.5\text{ }\mu\text{V}$  and CV measurements up to  $5\text{ MHz}$  and also at high-voltages.

The micro fabrication facility used for the fabrication of TLM pattern and Hall magnetic field sensors are given in figure 2.3.9.



**Figure 2.3.9** Micro Fabrication facility used for the fabrication of the devices

## 2.4 Electrical Characterization

### 2.4.1. Contact Resistance Measurements by the Transmission Line Model (TLM)

Transmission Line or Transfer length method (TLM) [8-10] is employed for measuring contact resistivity (also described in chapter 1). In this method, measurements of the Voltage - to- Current ratio ( $R_d = V/I$ ) are made between adjacent

pads of an array of alloyed contacts on a semiconductor strip. The sample is first mesa etched to a depth in order to isolate regions of the conductive epitaxial layer thereby restricting current flow within the mesa height. A linear array of metal pads of width 'W', length 'L' are fabricated with various spacing between them. The separation,  $d$ , between adjacent pads varies, typically as  $d_0, 2d_0, 4d_0, \dots, 2nd_0$  etc. A constant current is passed between the pads and second set of probes are used to measure voltage drop using a voltmeter enabling the total resistance between the pads to be obtained. The resistance  $V_n/I = R_n$  is expected to be linear with  $d$  or  $n$  extrapolating to  $2R_c$  at  $n=0$  (i.e.  $d=0$ ), where  $R_c$  is the total contact resistance. The quantity  $R_{TC}=R_c W$  (measured in  $\Omega$ -mm) the contact resistance for unit width normal to current flow, where  $W$  is the pad width on the semiconductor normal to current, is the transfer contact resistance.

A TLM structure with pad size  $l=0.1\text{mm}$ ,  $w = 0.4\text{ mm}$  and varying pad spacing -  $d = 0.025, 0.05, 0.1, 0.2, 0.4\text{ mm}$  is fabricated (figure 2.4.1).

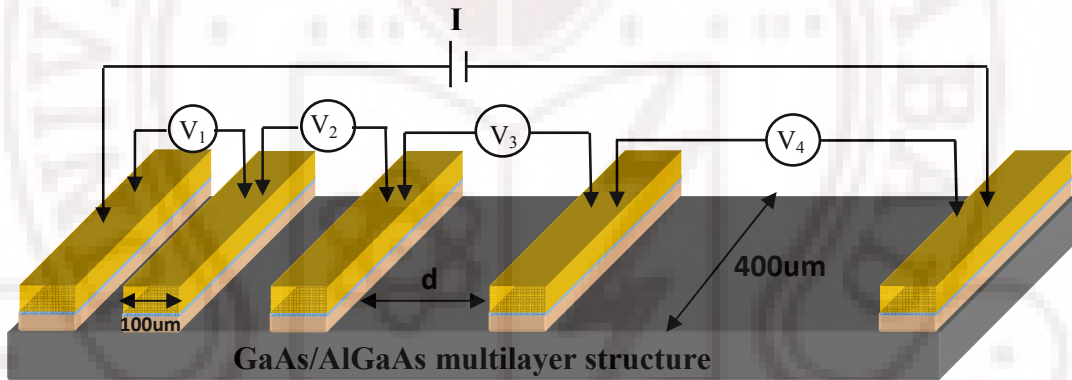


**Figure 2.4.1** Transmission line or transfer length model pattern.

The TLM structures are patterned on photoresist using i-line photolithography. The substrates are sputter cleaned in  $O_2$  plasma and a metal sandwich layer structure AuGe/Ni/Au, is deposited on the GaAs/AlGaAs wafer. This is followed by lift-off of the photoresist. The substrates with the TLM patterns are annealed to a specific anneal temperature  $T_A$ , in  $N_2$  ambient for different durations after ramping up the temperature at a heating rate of  $250^\circ\text{C}/\text{min}$ . I-V characteristics at various pads are measured using a wafer-prober (Signatone 1160 series) and device analyzer (Agilent B-1500A) with probe currents in the range  $\pm 0.5\text{mA}$  (figure 2.4.2a). The total resistance measured as a function of gap spacing  $d$  is as given in figure 2.4.2b. The extrapolation of the resistance versus gap spacing to zero gap spacing gives a value equal to twice the Ohmic contact

resistance  $R_c$ . The slope gives the sheet resistance  $R_s$ . The transfer length ( $L_T$ ) is measured from the intersection of the pad spacing for total resistance equal to zero. The details of the calculation of contact resistance, specific contact resistance, sheet resistance and transfer length are given in Chapter 1.

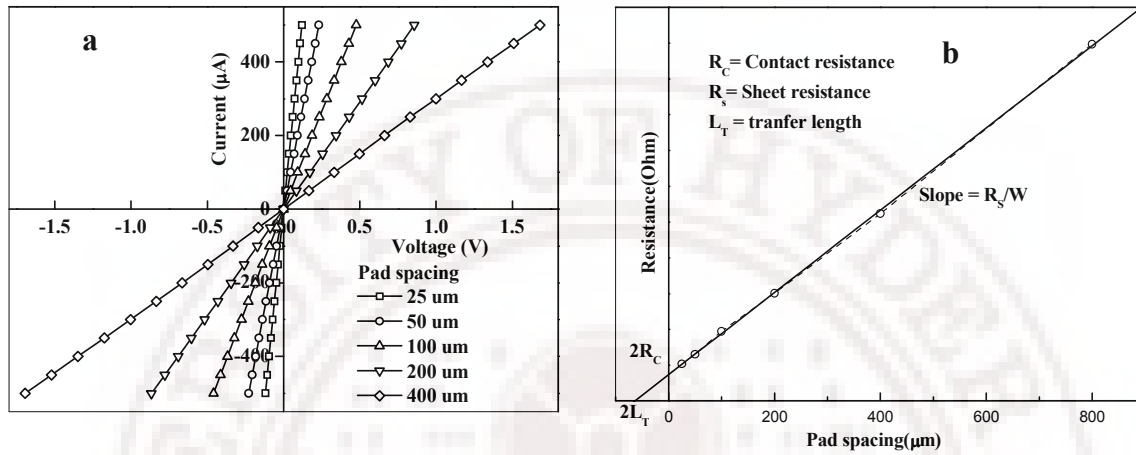


**Figure 2.4.2(a)** Current–voltage (I-V) characteristics at different pad spacing **(b)** Total resistance plotted as a function of contact separation.

### 2.4.2. Temperature dependence of contact resistance measurements

Temperature dependence (4-300K) of the contact resistance is undertaken on a few samples to study the changes in the mechanism of electrical contact conduction. These measurements are also relevant in the context of low-temperature applications of the magnetic field sensor. The measurements were carried out using a closed cycle refrigerator (Sumitomo RDK408D) capable of cooling the sample down to 4K. The temperature dependence of the contact resistance is measured by fixing the TLM pattern/device on a sample holder and the electrical contacts are made by wire bonding (Figure 2.4.3). Then the holder is mounted on the cold head of the closed cycle refrigerator. Pt-resistance and Carbon-glass resistance temperature sensors and a PID temperature controller (Lakeshore 331) are used to measure and control temperature. The TLM measurements for contact resistances were carried between 4K and 300K, at a

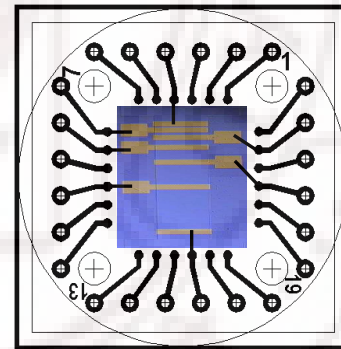


**Figure 2.4.3** TLM pattern mounted on a chip holder and wire bonded.

number of different temperatures on three samples. One was a sample with the eutectic AuGe layer, namely AuGe (88:12 wt %) /Ni (30nm)/Au. The other two samples are the ones in which Ni-layer thickness was increased to 50nm and the other by using an AuGe layer composition of 95:5 wt%.

A heater was used to heat and control the temperature up to 100K and the measurements are carried out for number of times at each temperature after controlling the temperature. The error was calculated after taking the standard deviation at each controlled/fixed temperature. The temperature stability throughout the temperature range is of the order of 0.1K. At temperatures above 100K the temperature was ramped without the heater. The standard deviation in contact resistance is calculated at each temperature. The temperature stability at each of this temperature is of the order of 0.15K. The error was incorporated in the data. The specific contact resistance and sheet resistance are calculated and the errors in the data are obtained.

## **2.5 Magnetic measurements**

### **2.5.1 Vibrating Sample magnetometer**

The magnetization hysteresis loops of the alloy structures are measured using Vibrating Sample Magnetometer (VSM). In VSM, the sample is set to vibrate with a fixed frequency in a uniform magnetic field, which is generated using an electromagnet and the magnetic field is measured using a Hall probe. This sinusoidal vibration of the magnetized sample creates a continuous change in the flux associated with the coil assembly situated near the sample and between the magnetic pole pieces. The change in the magnetic flux,  $\phi$ , associated with the coil induces an emf,  $V(t) = C d\phi(t)/dt$ . This induced signal, proportional to the magnetization of the sample, is amplified and then calibrated with a standard Ni sample.

The measurements are made with a Lake shore VSM system. The system has a magnetic moment resolution of  $10^{-6}$  emu. The electromagnet can generate field upto 2 Tesla. The measurements are typically carried out in sweep mode upto 5 KG in steps of 0.25kG with the magnetic field applied parallel to the film plane. The magnetic field is applied parallel to the film as corrections due to demagnetizing fields are minimal in this configuration. The measurements are carried out on  $4\text{mm}^2$  GaAs/AlGaAs wafers with the

metallization AuGe /Ni/Au at room temperature after RTA annealing them at 100°C, 200°C, 250°C, 300°C, 400°C and 430°C. Background due to a GaAs/AlGaAs sample of similar mass, but without the film structure is measured. The measured magnetization of the alloy metal structure is corrected for the background.

The measured sample area with typical error ~5% is multiplied by sample thickness to obtain the sample volume. The volume is multiplied by the density of Ni (8.9 g/cm<sup>3</sup>) to obtain the mass of the film. The magnetization data is normalized by the mass of Ni film.

## 2.6 Differential Scanning Calorimetry (DSC)

Differential Scanning Calorimetry (DSC) is used in the present work to measure the heat evolved as the AuGe/Ni/Au multilayer film is annealed.

Differential Scanning Calorimetry (DSC) scans are performed on bulk arc melted AuGe eutectic and off-eutectic alloys. The scan spanned from room temperature to 500°C at a heating rate of 100°C/min with the sample in N<sub>2</sub> gas atmosphere. Good homogeneity is obtained as seen by the data on the bulk alloy sample (figure 2.6.1). Each of the original data was subjected to an offset corresponding to its baseline.

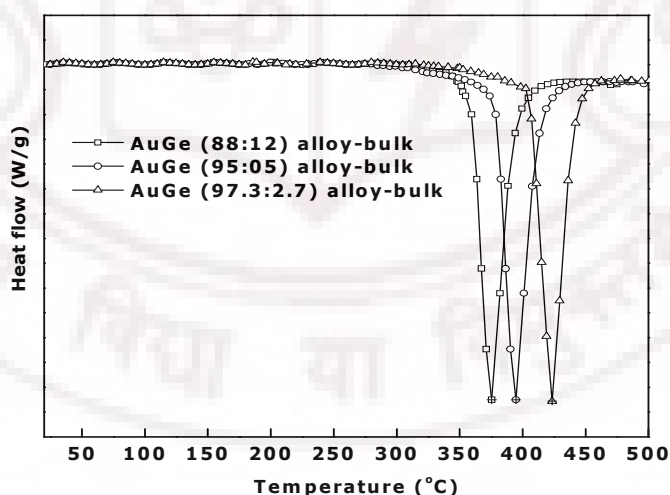


**Figure 2.6.1** Differential Scanning Calorimetry (DSC) of AuGe eutectic and off-eutectic bulk alloy

Temperature scans of DSC are also performed on the metallized substrate, with a bare substrate of similar size as the reference. The scans spanned room temperature to



500°C at a heating rate of 100°C/min. The measurements were carried out at IICT Hyderabad using a METLER TOLEDO DSC-821 system.

## 2.7 Surface Morphology and microstructure analysis

Samples are analyzed for microstructure using grazing incidence X-ray diffraction (GIXRD) and X-ray photo emission spectroscopy (XPS). SEM and AFM were used for measurements of the surface morphology.

### 2.7.1 Grazing Incidence XRD (GIXRD)

In grazing incidence x-ray diffraction technique, grazing incidence and/or grazing exit angles are used to enhance the surface sensitivity. GIXRD combines both diffraction at lattice planes perpendicular to the sample surface with the total external reflection of the incoming beam from the surface. Grazing incidence XRD measurements were carried out to analyze the compound formation when the magnetic to non-magnetic transformation takes place.

GaAs/AlGaAs wafer pieces of 1 cm x 1cm are chemically cleaned and AuGe (100nm)/Ni(25nm)/Au(200nm) layers are deposited. The measurements are carried out on three wafer samples. (i) As-deposited un-annealed sample (ii) annealed at 300°C and then cooled down (structure is non-magnetic) to room temperature (iii) annealed at 400°C for durations of 60s, and then cooled down (the optimized anneal temperature and time for lowest contact resistance).

All the measurements were performed on Bruker D8 Discover diffractometer at Bruker AXS, Germany. The diffractometer configuration used for present study is given below.

Radiation	Cu tube with long fine focus used at 1.6 kW (40kV, 40 mA)
Goniometer diameter	500 mm
Primary optics	40 mm Goebel mirror for Cu radiation
Sample stage	XYZ motorized stage (+) vacuum chuck
Secondary optics	Secondary slit assembly (XRR)
Detector	NaI scintillation counter
Grazing angle	0.35°

### **2.7.2 X-Ray Photoemission spectroscopy (XPS)**

X-Ray photoemission spectroscopy (XPS) is used to examine the chemical composition of the AuGe/Ni/Au metallization deposited on GaAs/AlGaAs wafer before and after alloying. The measurements are performed at the Instrumentation laboratory of Indian Institute of Science, Bangalore. XPS gives information about the chemical composition of the top surface layer up to about few mono-layers, with the X-rays are focused on the surface and the energies of the scattered photoelectrons are recorded. The emitted photoelectrons are detected and analyzed in terms of their kinetic or binding energies. Small shifts in the element specific core or valence band energies signalize changes and can give detailed information about the chemical environment of the atoms.

### **2.7.3 Scanning Electron Microscopy (SEM) and Energy Dispersive Analysis by X-rays (EDAX)**

SEM results presented in this thesis (surface morphology) were recorded using commercial instrument from PHILIPS. In this study the surfaces of the annealed contact pads are examined by scanning electron microscopy (SEM) and energy dispersive x-ray analysis (EDAX) at selected regions of the contact pad. The cross-sectional SEM measurements were carried out at ARCI Hyderabad using a Hitachi make Scanning Electron Microscope with field emission gun.

SEM works by scanning a focused electron beam across the specimen and detecting the emitted secondary electrons. Compositional analysis of the material may also be obtained by monitoring the energy dispersive analysis of secondary X-rays (EDAX).

### **2.7.4 Atomic Force microscopy (AFM)**

Atomic force microscopy (AFM) is used to study the surfaces of the annealed AuGe/Ni/Au contact pads. The surface roughness is computed using the root-mean-square height of the sample over an area of about  $5\mu\text{m} \times 5\mu\text{m}$  of the Dynamic Force Microscopy (DFM) topography data.

In AFM, there are two commonly used scan modes, contact mode and non-contact



mode. In the contact mode the tip makes contact with the surface at a specific contact force (force repulsive). A feed back mechanism moves the tip or sample up or down, to compensate the deformation of the cantilever. In the non contact mode, the distance between tip and the sample is typically 10-100nm (force attractive). The cantilever oscillates at a certain frequency, and when the distance between tip and surface changes, the frequency changes. By keeping the oscillating frequency constant by moving tip or sample, one gets the topographical information through the feedback mechanism.

The measurements have been repeated on several pads of the TLM structure. The RMS is computed using

$$RMS = \sqrt{\frac{\sum_{i=1}^N (x_i^2 - \bar{x}^2)}{N}}$$

' $x_i$ ' is the height measured by AFM on a certain point, ' $\bar{x}$ ' is the average height and  $N$  is the no of points.

### 2.7.5 Conducting Probe Atomic Force Microscopy (C-AFM)

Conducting probe Atomic Force Microscopy (CAFM) is used to map the topography and current distribution on surface of samples with AuGe/Ni/Au metallization. CAFM is equipped with a conducting probe that give topographical properties and conductivity variation in the samples. It is used for variety of material characterization applications[11-13] like, measurement of resistances of individual molecules and nano-particles, to measure oxide thickness in semiconductors, dielectric and ferroelectric thin films, nano tubes, I-V characteristics of organic semiconductors, conductive polymers, measurement of contact resistance across the surface of a metal etc.

The conducting AFM measurements are performed using a commercial system (NT-MDT). The schematic drawing of the conducting AFM set-up is given in figure. 2.7.1. The conducting AFM works at a constant force and constant bias mode with a maximum bias voltage of  $\pm 10V$ . The constant bias voltage was applied between the conducting tip and the sample while the tip scans an area. The measured current as a function of

position gives the map of current distribution. The current range is 200nA.

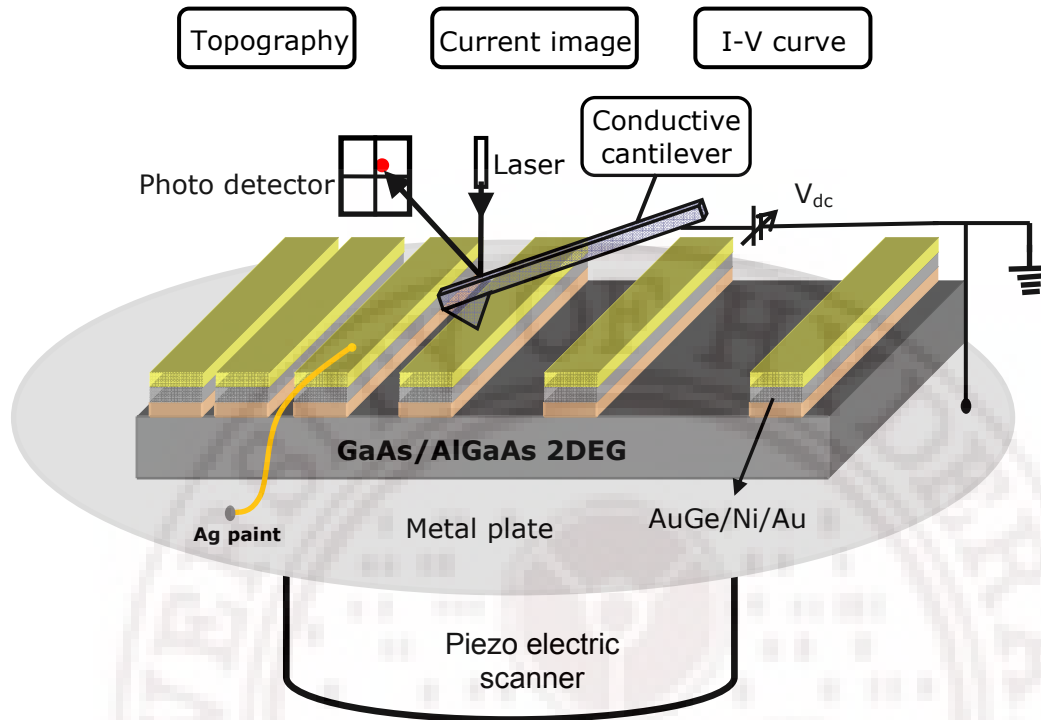


**Figure 2.7.1:** Schematic drawing of the conducting AFM set-up

Gold coated silicon tip with spring constant of 0.16N/m is used as the CAFM cantilevers. The reference force is maintained at 0.1N/m. The electrical contact between sample and sample holder is made by wire bonding gold wire on the sample and attaching to the sample holder using silver paste. A surface area of 10 x 10  $\mu\text{m}$  was scanned. The I-V measurements are performed in the contact mode, at a fixed location, by measuring the current while the voltage is ramped.

## 2.8 Adhesion Characterization

Adhesion is the state in which two surfaces are held together at the interface by adhesive forces. The forces can be Vander wall's force, chemical bonds across the coating substrate interface [14]. Adhesion can be measured in two ways: in terms of force or energy. In terms of forces, the force of adhesion,  $F_{12}$  is defined as the minimum force per unit area required to separate the layer of coating (1) from the substrate (2). In terms of energy, the work of adhesion is the work done in separating the coating from the substrate.

$$W_{AD} = \gamma_1 + \gamma_2 - \gamma_{12}$$

$\gamma_1$ ,  $\gamma_2$  are the specific free energy of coating and the substrate and  $\gamma_{12}$  is the interfacial free energy. An ideal test for adhesion should be non-destructive, easily adaptable, should be simple to perform and interpret, should be reproducible and quantitative. There are a number of tests used to characterize adhesion of thin films like direct pull-off method, laser spallation method, indentation test, abrasion test, scotch tape test, substrate straining test, scratch test etc. Of these indentation and scratch test are the simple techniques and provide consistent data in repeated measurements.

### 2.8.1 Nano scratch test

Scratch test consists of applying an incrementally or continuously increasing load on the coating point by a scratching point while the sample is displaced at constant speed. The lower critical load is taken as the load at which the coating shows the first signs of failure and upper critical load corresponds to the point where the coating is removed in regular way along the whole scratch channel length. Microscopic observation allows the determination of critical load and adhesion quality by examining the nature of failure mode and the extent of damage.

The factors which can affect the scratch testing results are loading rate, scratching speed, indenter tip radius, indenter wear and machine factors. The parameters like substrate hardness, coating thickness, surface roughness and variation in coating hardness can also influence the scratch test. The critical load increases with increasing substrate hardness. The samples must be coated on similar material while comparing adhesion.

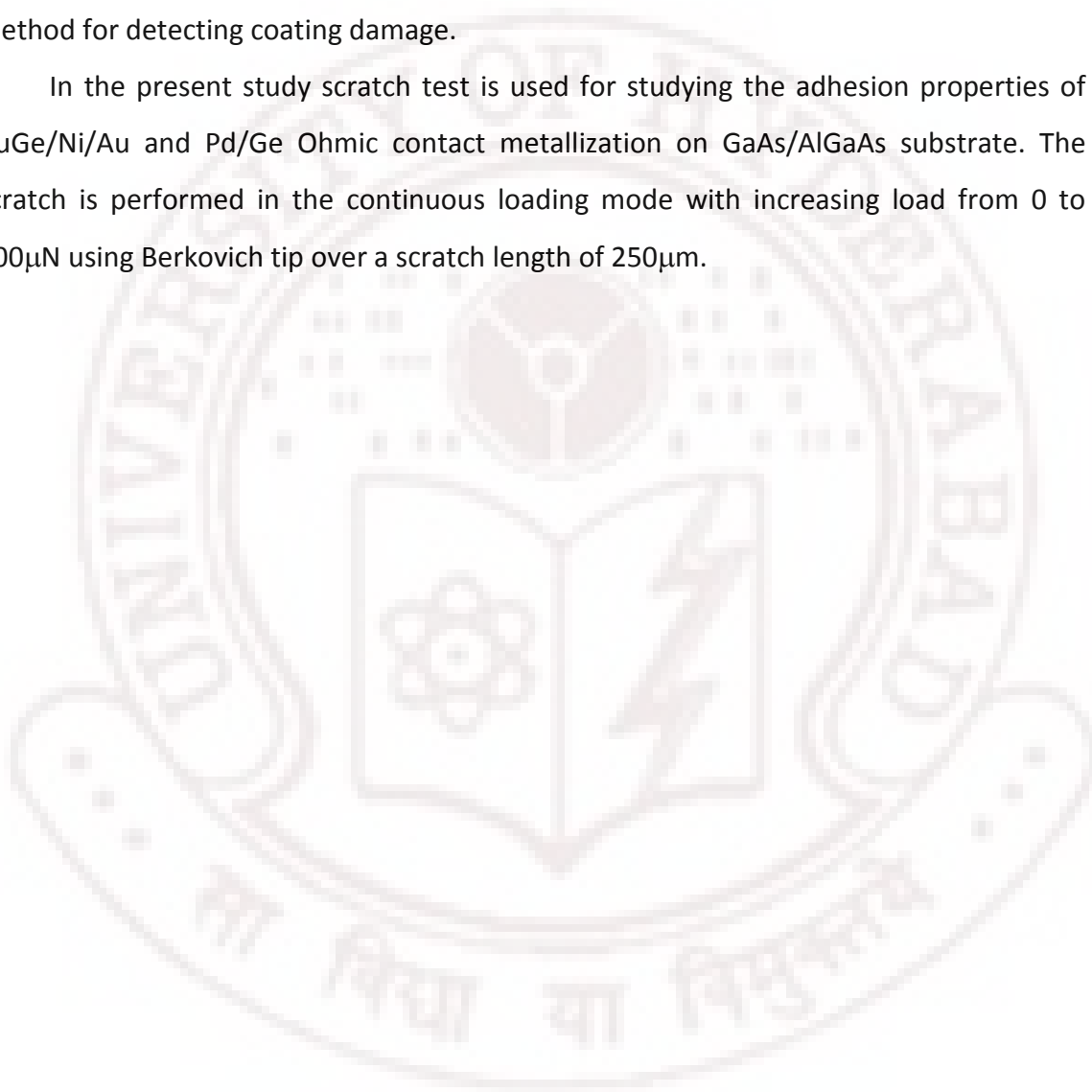
The scratch testing system used for the present study is a Hysitron TriboIndenter. The tribo system is a computer controlled system, with an anti vibration set up and acoustic enclosure to minimize acoustic noise, and to block air currents. The control of the sample and probe positions are controlled by the XYZ staging system and the tribo-scanner is used to provide fine positing of the probe tip ( $\pm 20\text{nm}$ ). A transducer assembly is used to apply the load. The maximum force of  $30\text{mN}$  and a minimum force of  $25\mu\text{N}$  with a resolution of  $1\text{nN}$  can be applied. The thermal drift is  $< 0.05\text{nm/sec}$ .

The sample to be tested is mounted on the sample holder. The diamond tip is brought in contact with the surface. In order to generate scratch, the stylus is moved

over the stationary sample. The scratch test is done in two operational mode (i) continuous loading: the load is increased progressively (ii) constant loading: the load remains constant until scratch length is reaches and the load applied is increased stepwise.

The scratch test can be characterized by microscopic observations, frictional force measurements, profilometry etc. Microscopic method is the simplest and reliable method for detecting coating damage.

In the present study scratch test is used for studying the adhesion properties of AuGe/Ni/Au and Pd/Ge Ohmic contact metallization on GaAs/AlGaAs substrate. The scratch is performed in the continuous loading mode with increasing load from 0 to 500 $\mu$ N using Berkovich tip over a scratch length of 250 $\mu$ m.



## References

1. The wafer is procured from IQE USA. The room temperature (RT) carrier mobility is  $\sim 7800 \text{ cm}^2/\text{V.s.}$  and at 77K is  $\sim 1.4 \times 10^5 \text{ cm}^2/\text{V.s.}$ , sheet carrier density is  $\sim 3.4 \times 10^{11} \text{ cm}^{-2}$  at RT and  $\sim 4.5 \times 10^{11} \text{ cm}^{-2}$  at 77K.
2. R. P. Taylor, P.T. Coleridge, M. Davies, Y. Feng, J. P. McCaffrey, P. A. Marshall, *J. Appl. Phys.* 76 (1994) 7966.
3. M. Kamada, T. Suzuki, F. Nakamura, Y. Mori, M. Arai, *Appl. Phys. Lett.* 49 (1986) 1263.
4. E. D. Marshall, B. Zhang, L. C. Wang, P. F. Jiao, W. X. Chen, T. Sawada and S. S. Lau, *J. Appl. Phys* 62 (1987) 942.
5. Jong- Lam Lee, Yi- Tae Kim, Jung- Woo Oh and Byung- teak Lee, *Jpn. J. Appl. Phys.* 40 (2001) 1188.
6. M. Murakami, *Science and Technology of Advanced Materials* 3 (2002) 1.
7. Kiwamu Tanahashi, H. J. Takata, A. Otuki and Massonori Murakami, *J. Appl. Phys.* 72 (1992), 4183.
8. H.H. Berger, *Solid State Electron.* 15 (1972) 145.
9. H. Murrmann and D. Widmann, *Solid State Electron.*, **12** 879.
10. S.S.Cohen and G.Sh.Gildenblat, *VLSI Electron Microstruct Sci.*, (1986) 101.
11. A. Ando, K. Miki, R. Hasunuma and Y. Nishioka, *Appl. Phys. A*, 72 (2001) S223.
12. S. K. Saha, Y. K. Su, C. L. Lin and D. W. Jaw, *Nanotechnology* 15 (2004) 66.
13. Tommie W. Kelley and C. Daniel Frisbie, *J. Vac. Sci. Technol. B*, 18 (2000) 632.
14. Anthony C. Fischer-Cripps, *Nanoindentation*, Springer-Verlag New York, Inc. 2002.

## Chapter - 3

# Influence of Ni layer thickness on the contact resistance, magnetic properties and surface morphology

### 3.1 Introduction

Recipes based on AuGe/Ni/Au layers have been extensively used for fabricating Ohmic contacts to GaAs [1-3], GaAs/AlGaAs and other heterostructures [4-9]. However, there are many unresolved issues, including those that arise in the context of magnetic field sensor fabrication using the multilayers. These contacts are usually based on the preparation of a metallization structure of evaporated eutectic alloy film of AuGe (88:12 wt%) followed by a rapid-thermal anneal to a temperature of  $\sim 400^{\circ}\text{C}$ . The use of eutectic composition of the AuGe alloy results in low contact resistance, due to enhanced diffusion of Ge into GaAs when the AuGe layer melts, causes a reduction in the width of the depletion layer and forms a tunneling contact. [10-13]. Although this contact has excellent reproducibility, it, however, suffers from poor surface morphology [14-16] as the AuGe alloy is prone to balling-up as it melts (m.p.  $\sim 360^{\circ}\text{C}$ ). The addition of a Ni layer and a thick Au over-layer is found to reduce, to some extent, the surface roughness during alloying [1, 14, 17, 18]. Several studies have shown that, apart from the diffusion of various elemental components into GaAs, significant changes occur in the metal film structure that could potentially influence electrical contact formation. For example, TEM studies have shown the presence of binary and ternary compounds,  $\text{Ni}_3\text{Ge}$ ,  $\text{Ni}_2\text{GeAs}$  and Au-Ga alloys [10, 11, 19-21] in metallization structures cooled down from anneal temperature of  $400\text{-}430^{\circ}\text{C}$ . A correlation is reported between the presence of  $\text{Ni}_2\text{GeAs}$  (interspersed with Au-Ga on GaAs surface) and low contact resistance [11, 19].

Thick Ni layers are beneficial in improving morphology, [22, 23] which in turn influences contact area. The increasing of Ni layer thickness may have other undesirable

consequences: a) un-reacted Ni may make the structure ferromagnetic b) formation of compounds with Ni and Ge may deplete Ge and hence influence contact resistance. In the case of magnetic field sensor fabrication and application, the presence of ferromagnetic material, e.g. Ni, in the proximity of the sensor active area can, potentially, distort the measured field. Thus, reproducible, reliable Ohmic contacts to the 2DEG, that have very low contact resistances, smooth surface, good thermal stability and, for sensor applications, no magnetism, are essential. However, to our knowledge, no systematic studies have been reported on the magnetic properties and its dependence on processing conditions.

In this chapter we report the following studies

1. The possibility of using alternate structures without the ferromagnetic Ni, namely, AuGe/Au, AuGe/Ti/Au and AuGe/Cr/Au. A comparative study of the contact resistance, surface roughness and surface composition in this metallization layers AuGe/Au, AuGe/Ti/Au, AuGe/Cr/Au and AuGe/Ni/Au, after annealing treatments are carried out.
2. AuGe/Ni/Au metallization gives the lowest contact resistance. We report studies undertaken on the dependence of magnetization hysteresis loops, surface roughness and the contact resistance of alloyed AuGe/Ni/Au contacts on the following process parameters: Ni layer thickness (for a fixed AuGe layer thickness of  $\sim 100\text{nm}$ ), anneal temperature ( $T_A$ ) and anneal duration ( $t_A$ ) of post deposition anneal.
3. Similar studies were undertaken on samples with three different AuGe layer thicknesses, after indication emerged that the Ni/AuGe thickness ratio was important in determining the contact characteristics including magnetization.

### **3.2 Effect of Ti, Cr and Ni interlayer on AuGe/TM/Au Ohmic contacts**


Ni layer deposited on AuGe is known to reduce roughness greatly and improve contact resistance [11, 12, 17, 18]. However, the suitability of Ni for fabrication of Hall magnetic sensors needs to be examined in detail, because of its ferromagnetic nature. Cr and Ti are also suitable as interlayer metal. They behave similarly to Ni in the Ohmic contact formation, though no systematic information is available. We have made a comparative



study of the post-anneal contact resistance, surface roughness and other effects in the metallization without any interlayer and with Ti, Cr and Ni as interlayer viz, AuGe/Au, AuGe/Ti/Au, AuGe/Cr/Au and AuGe/Ni/Au [24].

The contact resistance of the alloyed contacts is estimated by micro fabricating a pattern suitable for transmission line or transfer length model (TLM) by i-line lithography and lift-off as explained in chapter 2 [25, 26]. Prior to the deposition of metallization layers, the substrates were sputter cleaned in  $O_2$  plasma. A metallization layer structure such as AuGe (88:12wt %) -100nm/TM -30nm/Au -200nm, (TM = Ti, Cr, Ni or none) was deposited on the GaAs/AlGaAs substrate (table 3.2.1).

**Table 3.2.1** GaAs/AlGaAs wafer and Ohmic contact metallization

Au (200nm)		
TM(30nm), (TM=Ti, Cr, Ni or none)		
AuGe (100nm)		
$n^+$ (Si $1.5 \times 10^{18}$ ) GaAs	20nm	Cap layer
$n^+$ (Si $1.5 \times 10^{18}$ ) $Al_{0.3}GaAs_{0.7}$	30nm	Supply layer
Intrinsic AlGaAs	15nm	Separation layer
Intrinsic GaAs	500nm	<b>2DEG</b> 
SI GaAs Substrate	500 $\mu$ m	

The substrates with the TLM patterns were annealed between 350°C to 450°C in  $N_2$  ambient for different durations using RTA (chapter 2) at a heating rate of 250°C /min. I-V characteristics are measured for estimation of contact resistance ( $R_c$ ). The surfaces of the annealed contact pads are examined for morphology by scanning electron microscopy (SEM), energy dispersive x-ray analysis (EDX) and atomic force microscopy (AFM).

### 3.2.1 Electrical characteristics

The contact resistance,  $R_{TC}$  as a function of anneal temperature for (a) AuGe/Au, (b) AuGe/Ti/Au, (c) AuGe/Cr/Au and (d) AuGe/Ni/Au is shown in figure 3.2.1.

1. The contacts show Ohmic behavior for anneal temperatures  $\geq 350^\circ\text{C}$ . The contact resistance decreases as the interlayer is changed from no interlayer to Ti to Cr to Ni.

2. The lowest, or optimum, contact resistance is observed for anneal temperatures  $\sim 400^\circ\text{C}$  for AuGe/Au, and with Cr, Ti, Ni interlayer. Among these, the lowest contact resistance of  $0.07 \pm 0.005 \Omega\text{-mm}$  is observed for AuGe/Ni /Au for 90 second anneal for the thickness mentioned in table 3.2.2.
3. Increase of anneal temperature results in increase of the contact resistance.

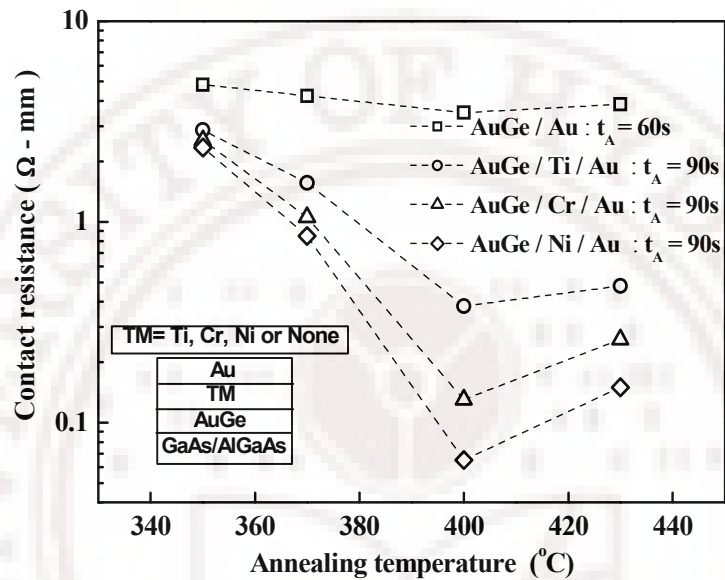


**Figure 3.2.1** Contact resistances as a function of anneal temperature for AuGe/Au, AuGe/Ti/Au, AuGe/Cr/Au and AuGe/Ni/Au. The lines are a guide to the eye.

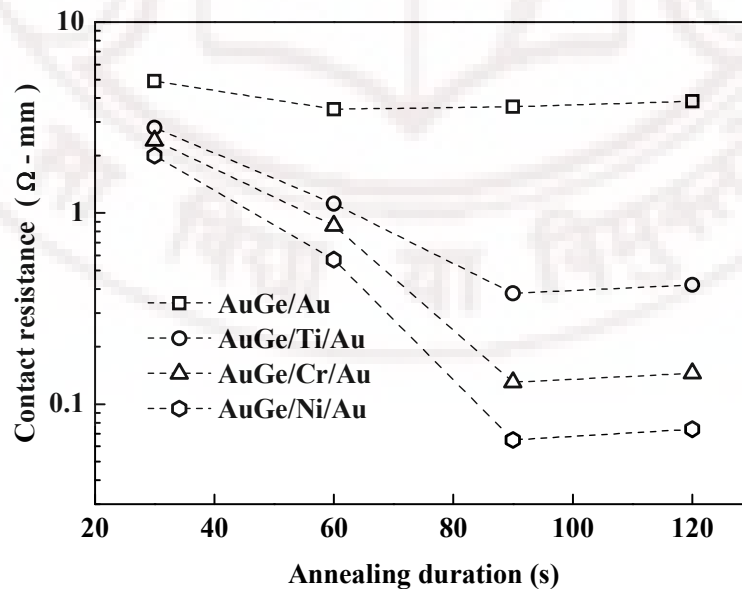


**Figure 3.2.2** Contact resistances as function of anneal durations for AuGe/Au, AuGe/Ti/Au, AuGe/Cr/Au and AuGe/Ni/Au.

The dependence of the contact resistance of AuGe/TM/Au alloyed contacts on anneal durations is shown in figure 3.2.2. Contact resistance at the optimum anneal temperature and durations for various TM are listed in table 3.2.2

**Table 3.2.2** Optimum anneal temperatures and durations, optimum contact resistance and the surface roughness for AuGe/Au, AuGe/Ti/Au, AuGe/Cr/Au and AuGe/Ni/Au.

Metallization	Optimum alloying temperature(°C)	Alloying time (s)	Contact resistance ( $\Omega$ -mm)	Surface roughness (nm)
AuGe -100nm/Au-200nm	400	60	3.5	$44 \pm 4$
AuGe-100nm/Ti-30nm/Au-200nm	400	90	0.38	$40 \pm 3$
AuGe-100nm/Cr-30nm/Au-200nm	400	90	0.13	$26 \pm 3$
AuGe-100nm/Ni-30nm/Au-200nm	400	90	$0.07 \pm 0.005$	$21 \pm 2$

### 3.2.2 Surface morphology

The as-deposited film morphology is shown in the figure 3.2.3. These are SEM and AFM micrographs of a sample with the metallization structure AuGe/Cr/Au. Prior to annealing, the film is uniform with surface roughness  $\sim 2$ nm.

The surface roughness increases by a factor of 10-20 after anneals at 400°C, for durations that gave the lowest contact resistance.

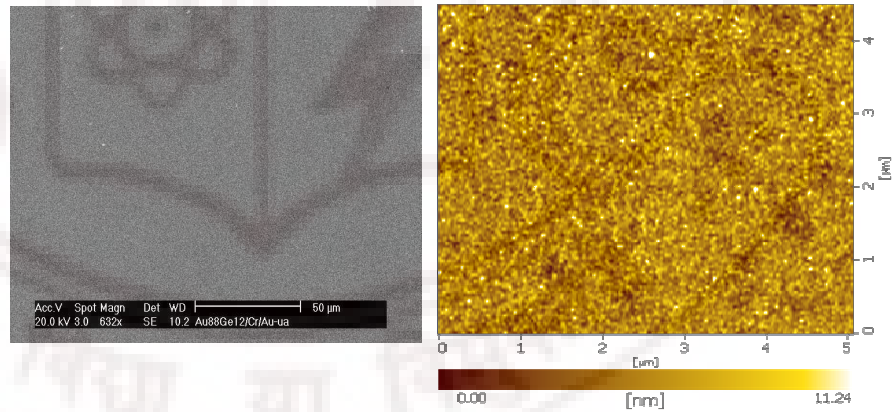


**Figure 3.2.3** SEM & AFM micrographs of the surface of as-deposited un-annealed sample

The rms roughnesses are in the range of 40nm-20nm for AuGe/Au and AuGe/TM/Au as measured by AFM. The SEM micrographs of the sample surface (figure 3.2.4) clearly indicate that the sample roughness decreases systematically as the interlayer is varied from no interlayer Ti to Cr to Ni.

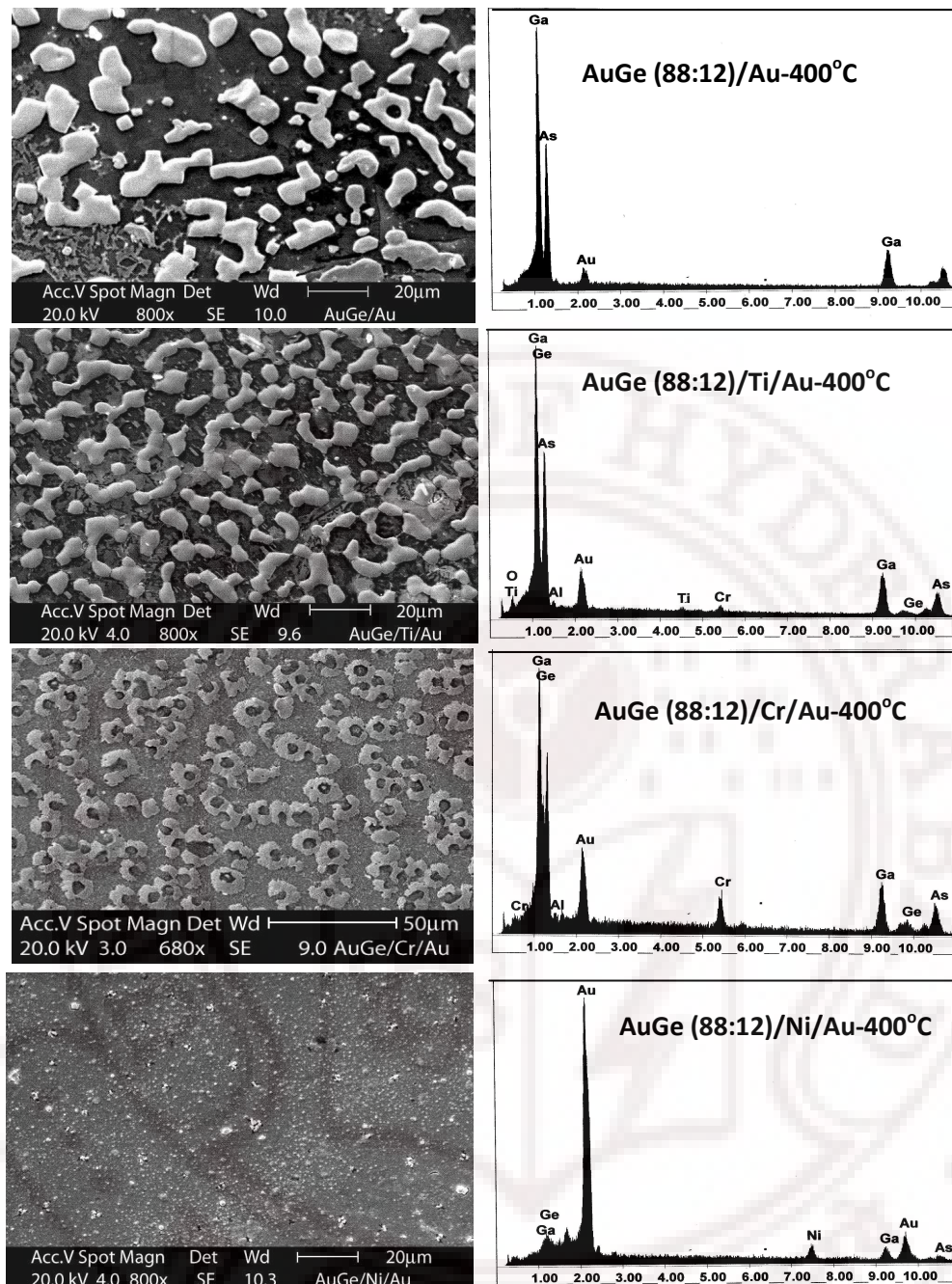


**Figure 3.2.4** SEM Micrographs and EDAX elemental analysis of the surface of AuGe/Au, AuGe/Ti/Au, AuGe/Cr/Au and AuGe/Ni/Au films on GaAs/AlGaAs wafer after RTA at 400°C

When interlayer is not used, the alloy film tends to ball up and formation of blisters/bubbles is observed on the film structure probably due to Ga from the GaAs cap layer, migrating to the surface (figure 3.2.4). The SEM data of the bright portion of the micrographs indicate that these are Au agglomerations and profiler data show that these are 10-20 µm across and 0.5-1 µm high. This roughening could limit the close approach

of the sensor active areas to the surface under examination. For samples with Ni interlayer, coverage by Au is nearly complete, though roughness can still be detected at high magnification.

It is observed from these results that AuGe/Ni/Au gives the lowest contact resistance with smooth surface. However as-deposited Ni is magnetic, and the magnetization of the structure after alloying is of interest, in the context of Hall magnetic field sensor fabrication using GaAs/AlGaAs multilayer. Hence a study of influence of Ni layer and its thickness on magnetic properties, contact resistance and surface roughness is of relevance in the magnetic field sensor fabrication and application.

### 3.3 Influence of Nickel layer thickness on contact resistance, magnetic properties and surface roughness.

The magnetic hysteresis loops, contact resistance and surface morphology are evaluated as functions of Ni layer thickness and anneal temperature. The contact resistance of the alloyed contacts is estimated using TLM [25]. The preparation of the metallization structure is as explained in chapter 2. AuGe (88:12) -100nm/Ni - $x$  nm/Au -200nm, where  $x = 10, 25, 30, 50, 75, 100$  nm, deposited on the GaAs/AlGaAs wafer and rapid thermal annealed between 350-450°C (table 3.3.1). I-V characteristics at various pads are measured using a wafer-prober and device analyzer.

**Table 3.3.1** Ohmic contact metallization structure

Au (200nm)
Ni (10,25,30,50,75,100nm)
AuGe (100nm)
GaAs/AlGaAs Multilayer wafer with $n^+$ -GaAs cap layer

#### 3.3.1 Electrical characteristics

Figure 3.3.1 summarizes the contact resistance,  $R_{TC}$  as a function of anneal temperature for varying Ni layer thicknesses with optimized anneal durations.



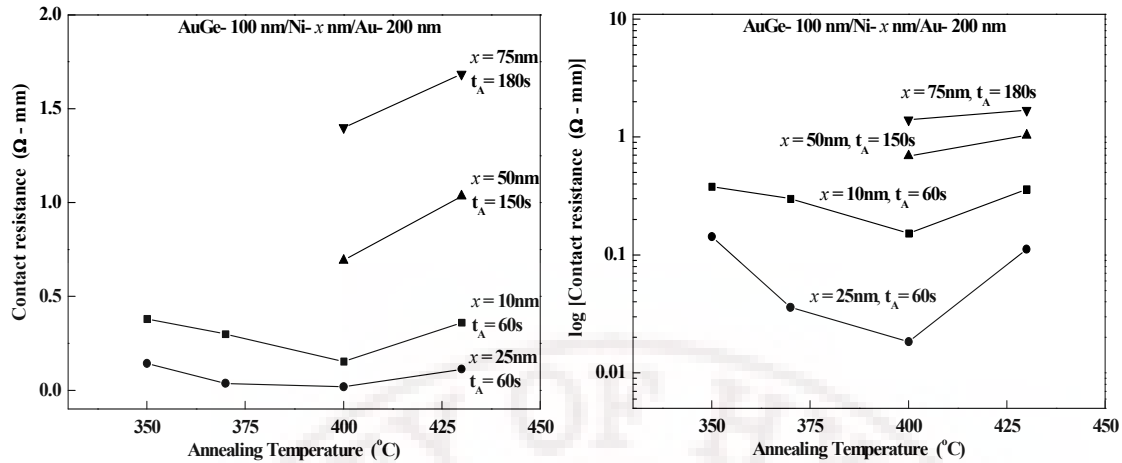


**Figure 3.3.1** Contact resistances as a function of anneal temperature for varying Ni layer thicknesses on linear and log scale

- 1) The contacts with Ni layer thickness, 100 nm, show a non-linear, large resistance ( $\sim 4 \text{ M}\Omega$ ) contacts for long duration anneals ( $\sim 10 \text{ min.}$ ) as shown in figure 3.3.2. Shorter anneals ( $< 4 \text{ min.}$ ) at all temperatures upto  $430^\circ\text{C}$  resulted in a diode-like characteristic similar to those obtained for samples with smaller Ni layer thickness annealed at low temperature (figure 3.3.3).

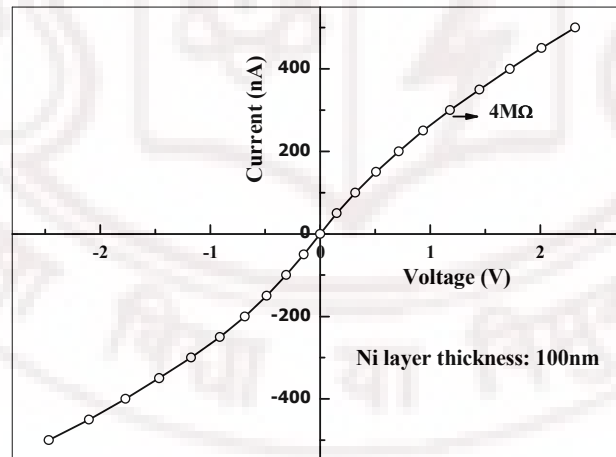


**Figure 3.3.2** I-V curve for AuGe-100nm/Ni-100nm/Au-200nm for anneal duration of 10 minutes

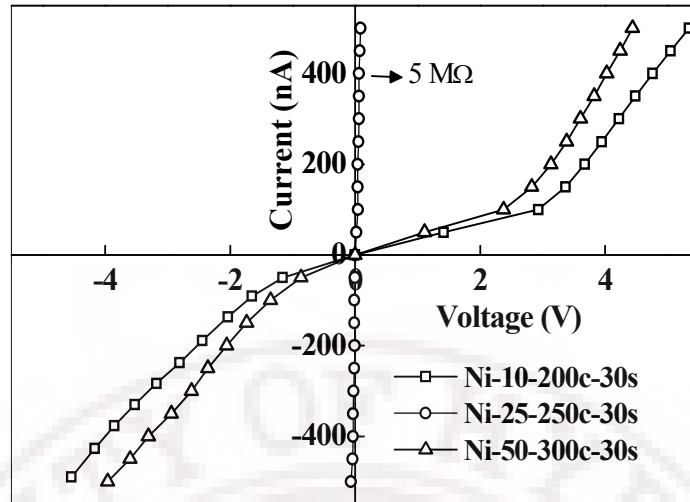


**Figure 3.3.3** I-V curves for low temperature annealed contacts

- 2) The contacts with Nickel layer thicknesses 50nm and 75nm show diode-like behavior when annealed at temperatures below 400°C and Ohmic behavior for anneal temperatures above 400°C.
- 3) The contacts with Ni layer thickness 25nm and 10nm show Ohmic behavior for anneal temperatures above 350°C.
- 4) I-V curves for AuGe/Ni(x nm)/Au with (x=10, 25, 50, 75nm) optimized for low contact resistance are shown in the figure 3.3.4.
- 5) The nature of the contacts for various Ni-layer thicknesses and anneal temperatures are summarized in fig. 3.3.5.

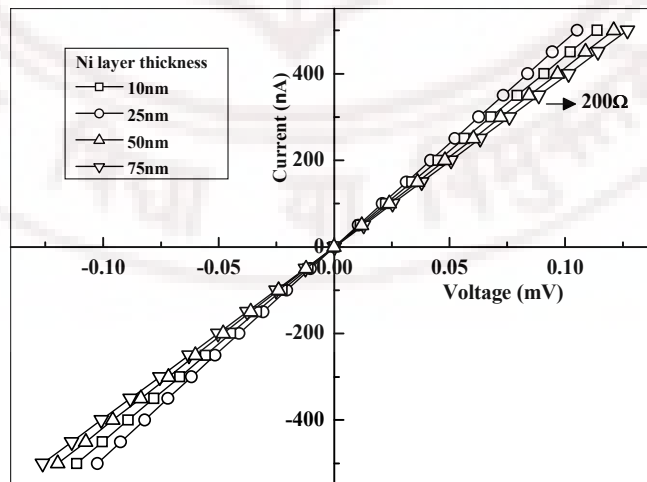


**Figure 3.3.4** shows typical I-V curves for AuGe/Ni/Au with different Ni layer thicknesses.



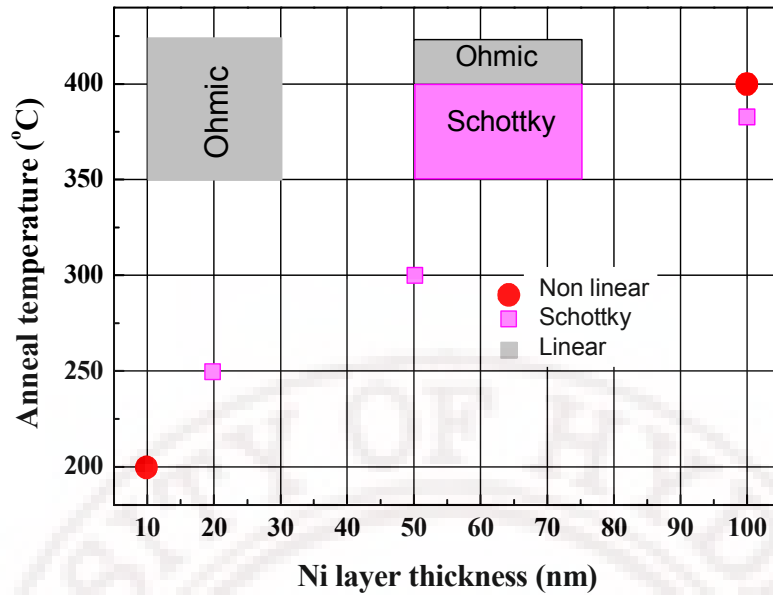


**Figure 3.3.5** Anneal temperature dependence of contact characteristics of AuGe/Ni/Au contacts with varying Ni layer thickness.

Annealing at 430°C is found to increase the contact resistance marginally for Ni layer thicknesses 10, 25, 50 and 75nm. The lowest, or optimum, contact resistance is observed for anneal temperatures  $\sim 400^\circ\text{C}$  for each of the Ni layer thicknesses 10, 25, 50, 75nm (Table 3.3.2). The dependence of the contact resistance of AuGe/Ni/Au alloyed contacts on anneal durations with various Ni layer thicknesses is shown in figure 3.3.6. These results indicate that if the Ni-layer thickness is increased, a larger anneal time is required to optimize the contact resistance.

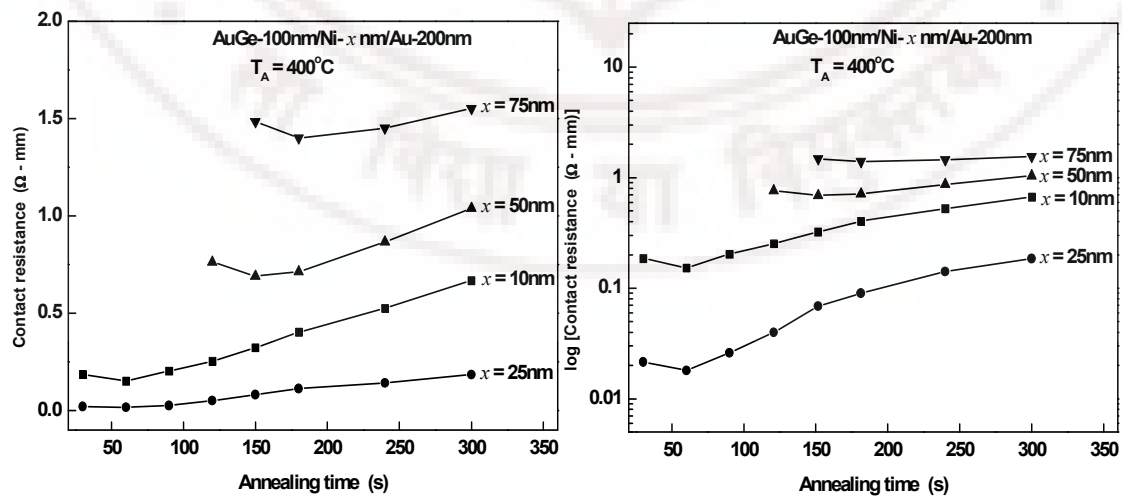


**Figure 3.3.6** Contact resistances as function of anneal time for different Ni layer thicknesses on linear and log scale.

**Table 3.3.2** Optimum anneal temperatures and durations, contact resistance, surface roughness and the magnetic-to-non magnetic transition temperature, for various Ni layer thicknesses

Nickel layer thickness (nm)	Optimum anneal temperature (°C)	Optimum anneal duration(s)	Contact resistance ( $\Omega$ -mm)	Surface Roughness (nm)	Anneal temperature for conversion of magnetic phase to non-magnetic phase (°C)
10	400	60	0.15	$25 \pm 4$	100- 200
25	400	60	$0.05 \pm 0.01$	$21 \pm 3$	200- 250
30	400	90	$0.07 \pm 0.005$	$20 \pm 2$	200- 250
50	400	150	0.90	$11 \pm 1$	250- 300
75	400	180	1.40	$7.5 \pm 0.5$	350- 400
100	400	480	$V(I)$ Non linear	$3 \pm 0.3$	400- 430

Dependence of  $R_{TC}$  on Ni layer thickness, optimized with respect to anneal temperature and time, is shown in figure 3.3.7. Among these, the lowest contact resistance of  $0.05 \pm 0.01 \Omega$ -mm is observed for AuGe (88:12 wt %) /Ni /Au configuration with Ni layer thickness 25nm, for a 60 second anneal. The quoted error (table 3.3.2) is the r.m.s deviation over several separate deposition runs. The best contacts are reproducible.

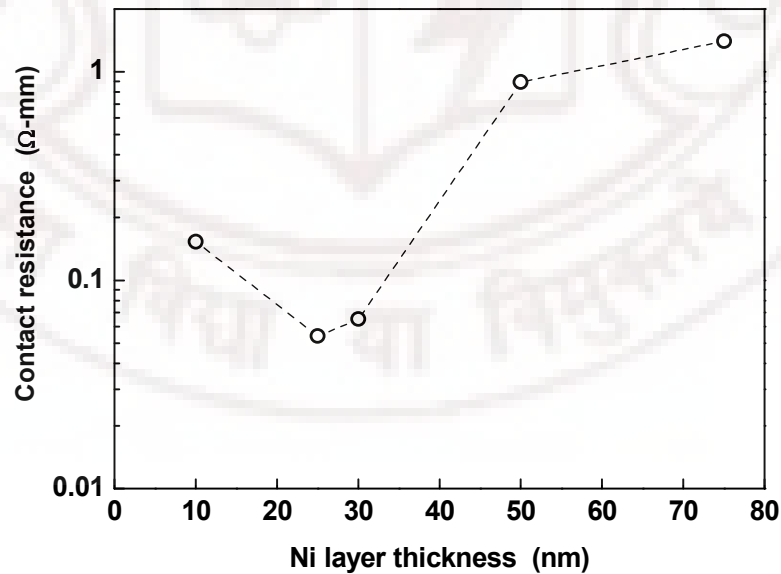


**Figure 3.3.7** Contact resistances at the optimized anneal temperature and time vs. Ni layer thickness.

The optimum Ni layer thickness for a given AuGe layer thickness, in this case 25-30 nm Ni-layer thickness for a 100nm Au-Ge layer thickness (figure 3.3.7), for obtaining the least contact resistance. Moreover under these conditions, the contact resistance variations with the process parameters, Ni layer thickness, anneal temperature and time corresponds to a reasonably shallow minimum which offers good process tolerance.

### 3.3.2 Magnetic properties

The magnetization hysteresis loops of the alloy structures were measured using a Vibrating Sample Magnetometer (VSM), with a magnetic moment resolution of  $10^{-6}$  emu. The measurements were carried out in sweep mode to 5 KG with the magnetic field applied parallel to the film plane. Pieces of GaAs/AlGaAs wafer with area  $4 \text{ mm}^2$ , were metallized with the structure AuGe (100nm)/Ni( $x$  nm)/Au (200nm),  $x=10, 25, 50, 75, 100$ . The pieces were rapid thermal annealed at  $100^\circ\text{C}$ ,  $200^\circ\text{C}$ ,  $250^\circ\text{C}$ ,  $300^\circ\text{C}$ ,  $400^\circ\text{C}$  and  $430^\circ\text{C}$ . They were then subjected to magnetic hysteresis loop measurements using VSM at room temperature. Background due to a sample of the same mass, but without the film structure, was subtracted and the resultant data was normalized by the Ni film mass (see chapter 2).

The magnetization hysteresis loops for AuGe (100nm)/Ni( $x$  nm)/Au (200nm),  $x=10, 25, 50, 75, 100$  and annealed at  $100^\circ\text{C}$ ,  $200^\circ\text{C}$ ,  $250^\circ\text{C}$ ,  $300^\circ\text{C}$ ,  $400^\circ\text{C}$  and  $430^\circ\text{C}$  are shown in figure 3.3.8. These data are typical of the magnetic behaviour of the Ni-containing contact metallization structures. The data show that, while hysteresis loops of the as-deposited film structure are ferromagnetic, the loops become progressively less magnetic after being subjected to anneal at increasing temperatures. Figure 3.3.9 shows the saturation magnetization (measured at an applied field of 5 kG) of samples with the metal film structure, as a function of the anneal temperature. The magnetization data are presented as a percentage of the magnetization of the as-deposited (un-annealed) sample as anneal temperature is increased. Remarkably, substantial decreases in magnetization occur even for anneal temperatures as low as  $100^\circ\text{C}$ . The anneal temperature for which the structure becomes completely non-magnetic, increases with increasing Ni-layer thickness as shown in table 3.3.2.

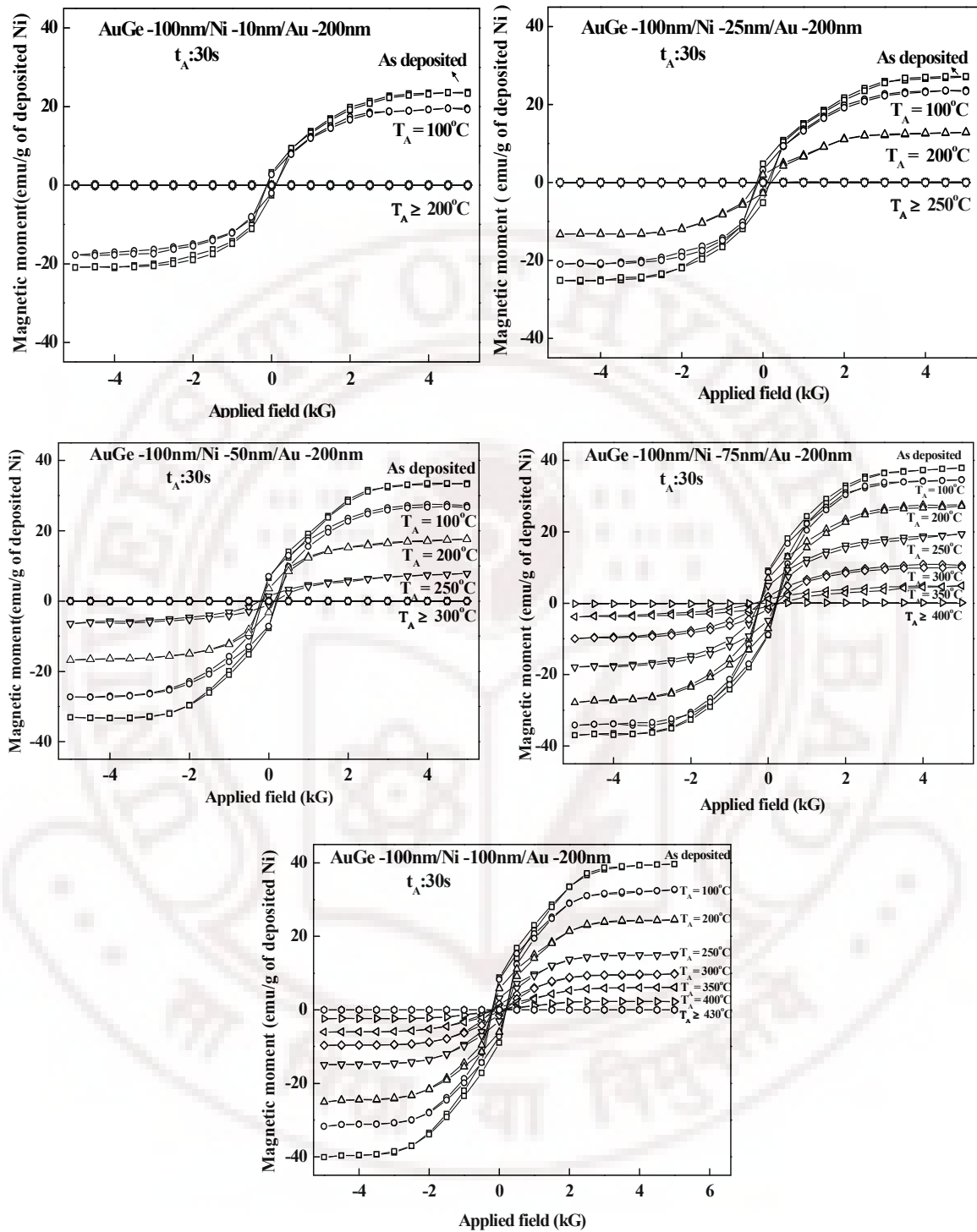


**Figure 3.3.8** Magnetization hysteresis loops for AuGe/Ni (10, 25, 50, 75, 100nm)/Au annealed at various anneal temperatures for 30s.

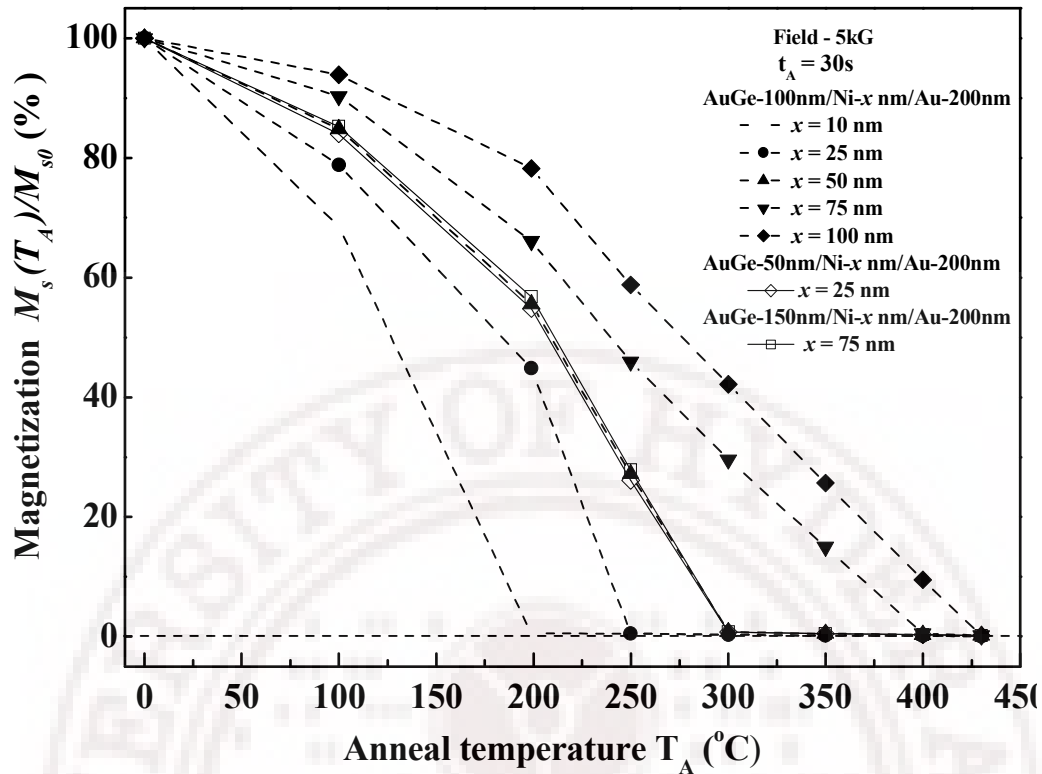


**Figure 3.3.9** Anneal temperature dependence of saturation magnetization of alloyed structures of the form AuGe (100nm) /Ni=x nm/Au (200nm) on GaAs multi-layer, for x= 10 nm, 25 nm, 50 nm, 75 nm, 100 nm. Data for a structure AuGe (50nm)/Ni (25nm)/Au (200nm) and AuGe (150nm) /Ni (75nm)/Au (200nm) are also included.  $M_{s0}$  is saturation magnetization of the as-deposited sample at 5kG.

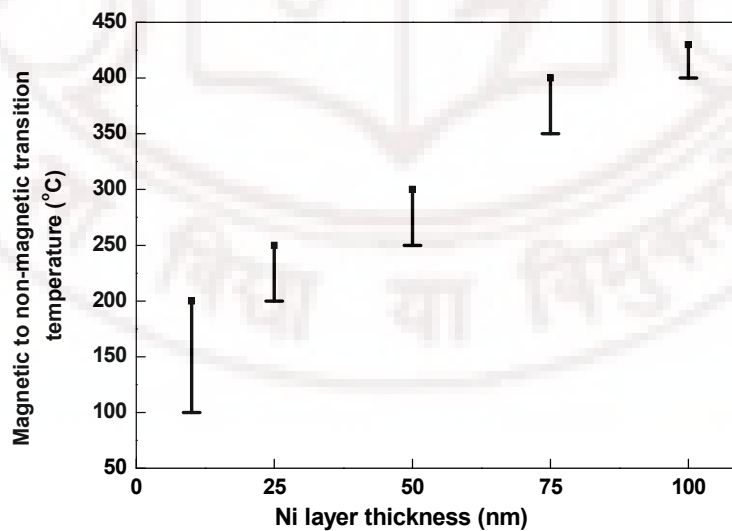


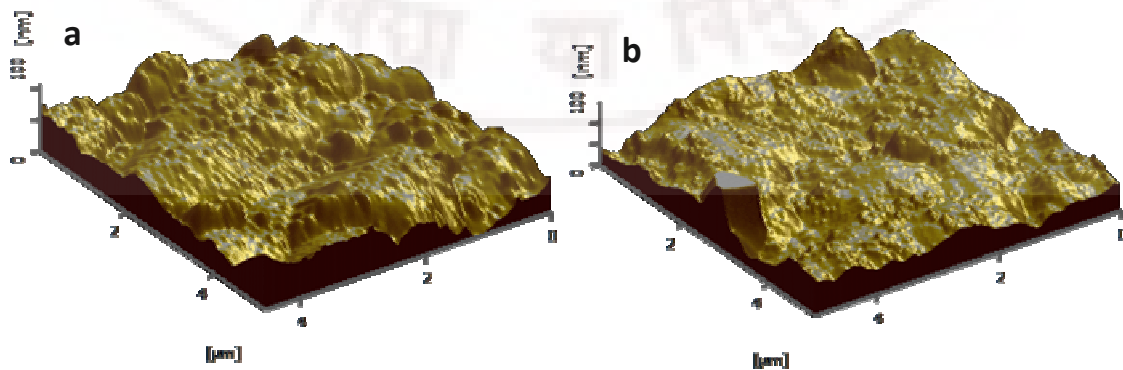
**Figure 3.3.10** Magnetic to non-magnetic transition temperature as a function of Ni layer thickness.

The structure becomes completely non-magnetic on annealing at or above a temperature which varies from 200°C to 430°C as the Ni layer thickness varies from 10nm to 100nm. The minimum anneal temperature required to complete the transformation to a non-magnetic phase is unknown, but lies in the range given in table 3.3.2 and figure 3.3.10. It is to be noted that under conditions normally used for obtaining Ohmic contacts, the structure is non-magnetic for a wide range of Ni layer thicknesses. All the samples with Ni-layer thickness  $\leq 75\text{nm}$  become non-magnetic on annealing at a temperature of 400°C, a commonly used anneal temperature in alloyed Ohmic contact recipes (Table 3.3.2). The structure with 100nm-thick Ni-layer becomes non-magnetic on annealing at 430°C.

### 3.3.3 Surface morphology

The surfaces of the annealed contact pads are examined by scanning electron microscopy (SEM), energy dispersive x-ray analysis (EDAX) and atomic force microscopy (AFM). The roughness is computed using the root-mean-square height of the sample over an area of about  $5\mu\text{m} \times 5\mu\text{m}$  of the Dynamic Force Microscopy (DFM) topography data. The data have been repeated at several pads of the TLM structure.

AFM images of the AuGe/Ni/Au structures on GaAs/AlGaAs wafer corresponding to different Ni layer thicknesses and annealed at 400°C for durations that gave the lowest contact resistance, are shown in figure 3.3.11. The r.m.s. surface roughness calculated are listed in table 3.3.2. They are in the range 24nm-6nm for Ni-layer thickness 10nm-100nm.



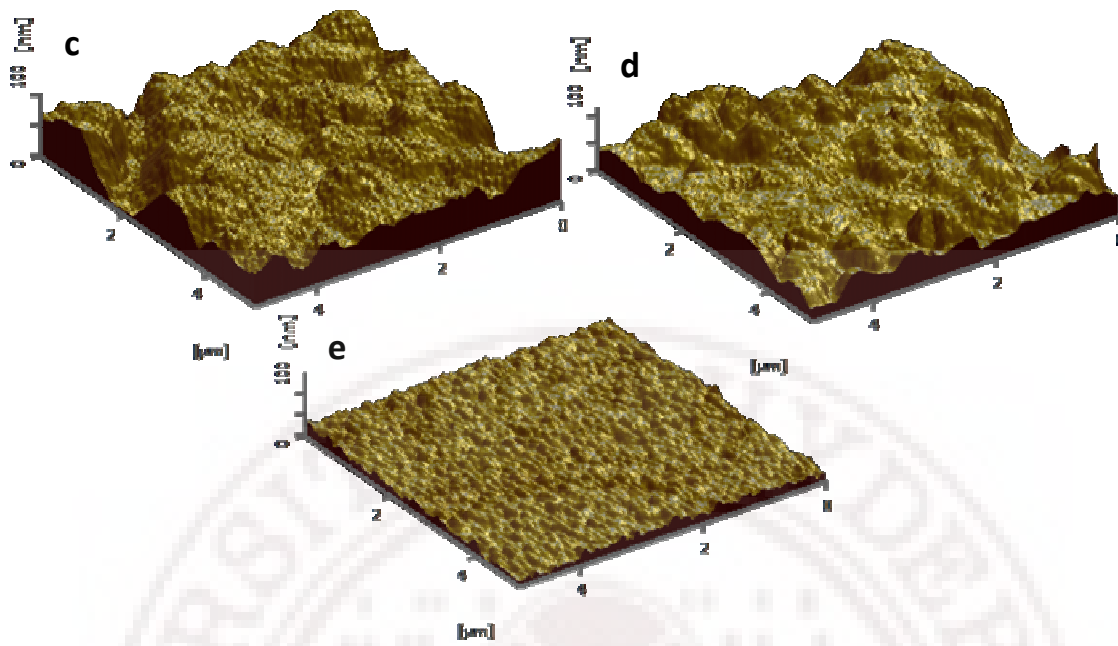


**Figure 3.3.11** AFM micrographs (5 $\mu\text{m}$  x 5 $\mu\text{m}$ ) of the surface of AuGe /Ni(x)/Au, x= 10 nm (a), 25 nm (b), 50 nm (c), 75 nm (d), 100 nm (e), annealed at 400°C for durations that gave the lowest contact resistance (Table 3.3.2).

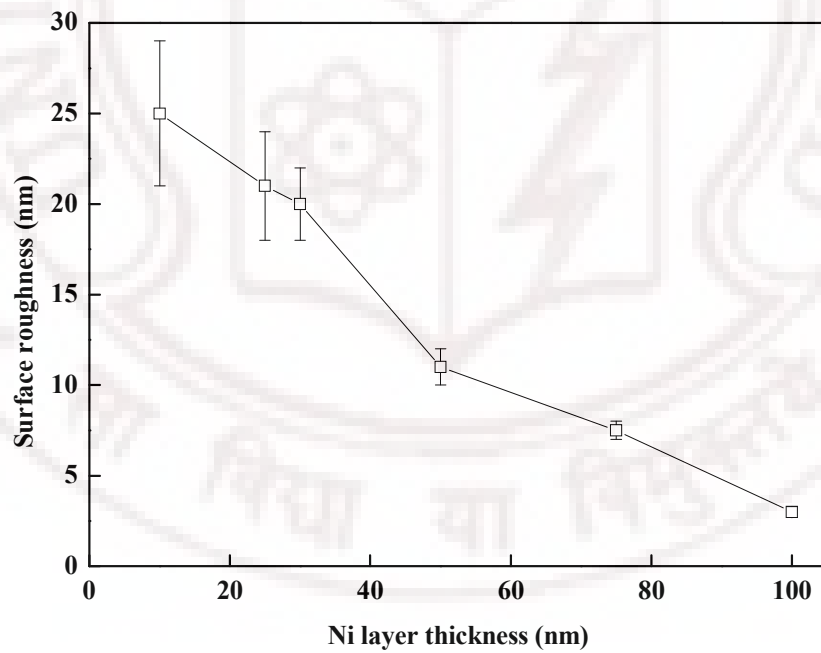


**Figure 3.3.12** Surface roughness as a function of Ni layer thickness



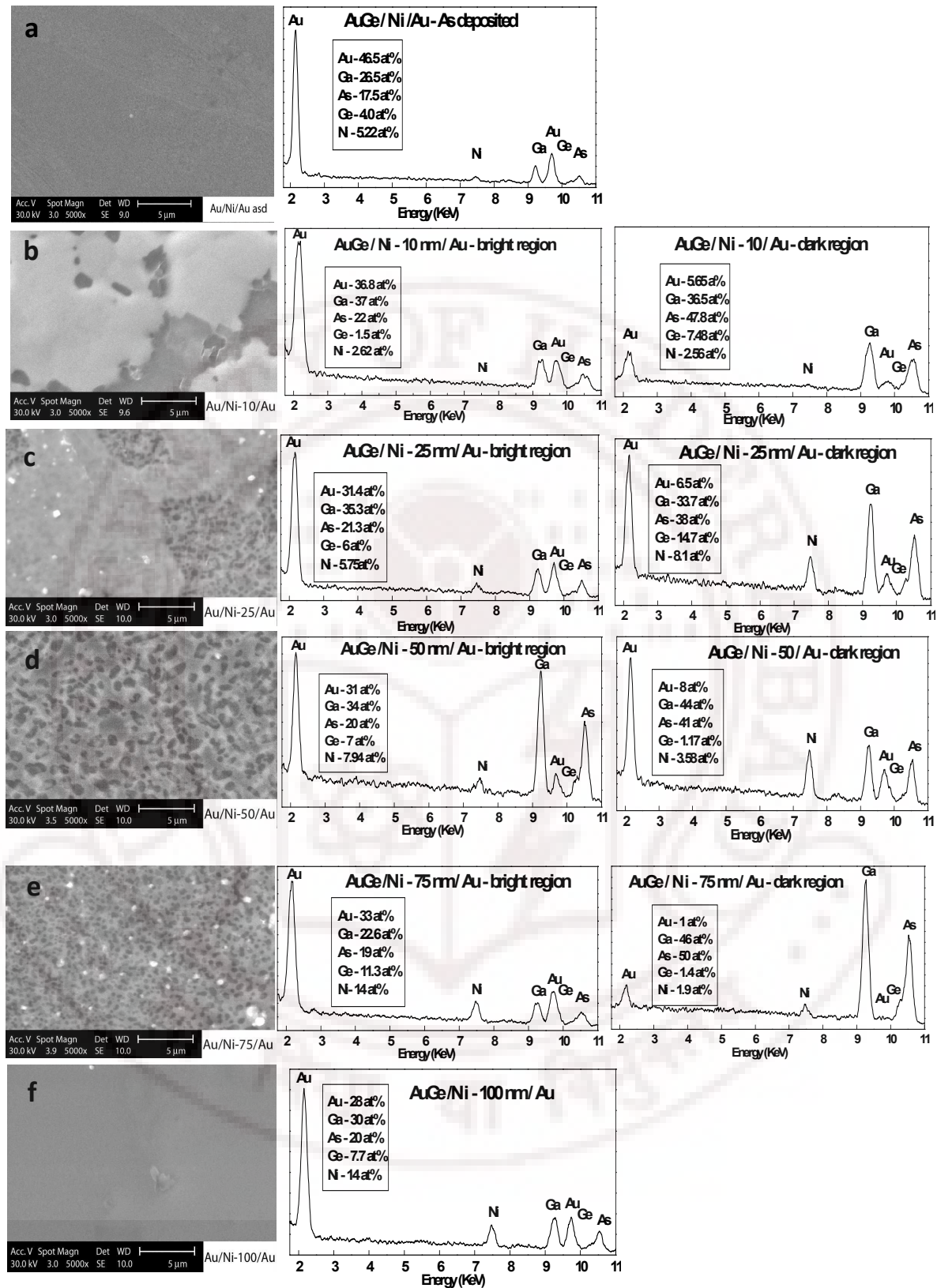


**Figure 3.3.13** SEM micrographs of the surface of AuGe /Ni(x)/Au, (a) as deposited (b)  $x=10$  nm, (c) 25 nm, (d) 50 nm (e) 75 nm and (f) 100 nm annealed at 400°C for durations that gave the lowest contact resistance (Table 3.3.2).

The measured surface roughness as function of Ni layer thickness is shown in figure 3.3.12. Increasing the Ni layer thickness reduces roughness of annealed contacts, but also increases contact resistance. For the structures with the optimum contact resistance the surface roughness is  $\sim 20\text{nm}$ .

SEM micrographs of AuGe/Ni/Au as deposited, un-annealed sample and AuGe/Ni (10, 25, 50, 75, 100)/Au deposited samples and annealed at  $400^\circ\text{C}$  durations that gave low contact resistance (Table 3.3.2) are shown in figure 3.3.13. The metallization is smooth in the case of as deposited and AuGe/Ni-100nm/Au samples and EDAX analysis shows Au, Ga and As rich phases. SEM micrographs of the AuGe/Ni (10, 25, 50, 75)/Au deposited samples (figure 3.3.13) show agglomeration into Au-rich (bright) and Au poor (dark) regions.

EDAX analysis shows the bright regions are rich in Au and Ga and the dark regions are Ga and As. As the Ni layer thickness is increased, agglomerations on much smaller scale are seen in the 'dark' regions which structure eventually covers the entire surface for Ni-layer thickness  $> 50\text{nm}$ .

### 3.3.4 Influence of Ni-to-AuGe layer thickness ratio

The data discussed in the previous section correspond to samples with a fixed AuGe layer thickness of  $100\text{nm}$ . A few measurements were also performed on samples with other AuGe thicknesses- namely  $50\text{ nm}$  and  $150\text{ nm}$ . The motivation was to determine if the Ni-layer thickness to AuGe layer thickness ratio was influential in determining contact resistance (as suggested in some studies [27]), roughness and magnetic properties.

The magnetic hysteresis loops for AuGe (88:12wt%)- $50\text{nm}$ /Ni- $25\text{nm}$ /Au- $200\text{nm}$  and AuGe- $150\text{nm}$ /Ni- $75\text{nm}$ /Au- $200\text{nm}$  (viz. Ni to AuGe thickness ratio constant at 0.5) are shown in figure 3.3.14.

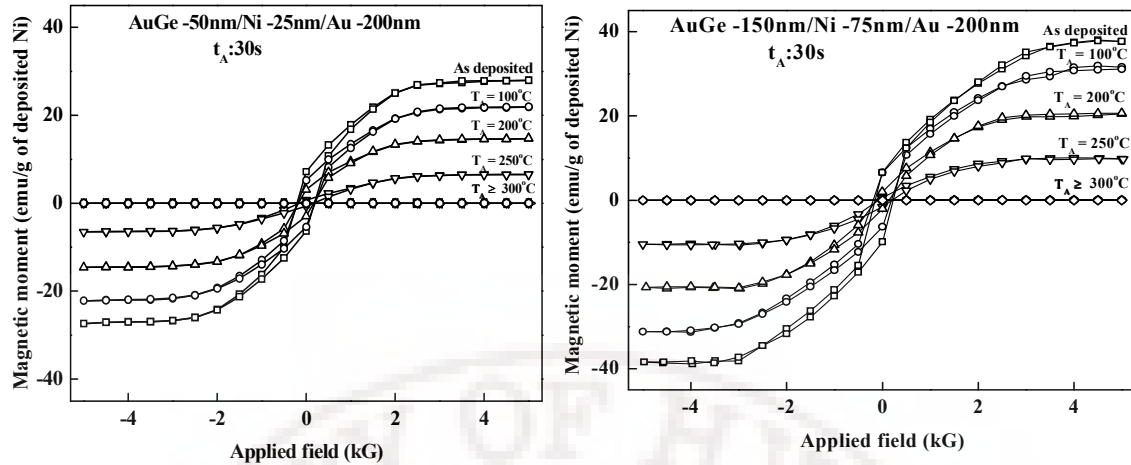


**Figure 3.3.14** Magnetization hysteresis loops for AuGe (50, 150)/Ni (25, 75)/Au (200nm) annealed at various anneal temperatures for durations  $\sim 1$  minute.

Further, as shown in Figure 3.3.15 the magnetic behaviour of the samples with structures AuGe (150nm)/Ni (75nm)/Au (200nm) and AuGe (100nm)/Ni (50nm)/Au (200 nm), AuGe(50nm)/Ni(25nm)/Au(200nm) are virtually identical when the magnetization data, plotted against anneal temperatures, are normalized by the magnetization of as-deposited sample (figure. 3.3.15).

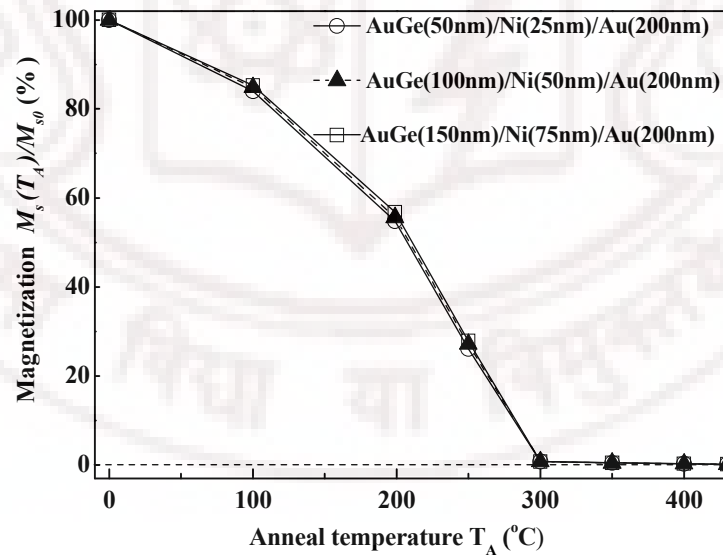


**Figure 3.3.15** Anneal temperature dependence of saturation magnetization of alloyed structures of the form AuGe (50nm)/Ni (25nm)/Au (200nm), AuGe (100nm) /Ni (50nm)/Au (200nm) and AuGe (150nm)/Ni (75nm)/Au(200nm) on GaAs/AlGaAs multi layer.

Figure 3.3.16 and table 3.3.3 shows the contact resistance and surface roughness measurements with AuGe layer thicknesses of 50, 100, 150nm with different Ni/AuGe ratios. The surface roughness appears to depend on the Ni and AuGe layer thicknesses through their ratio.

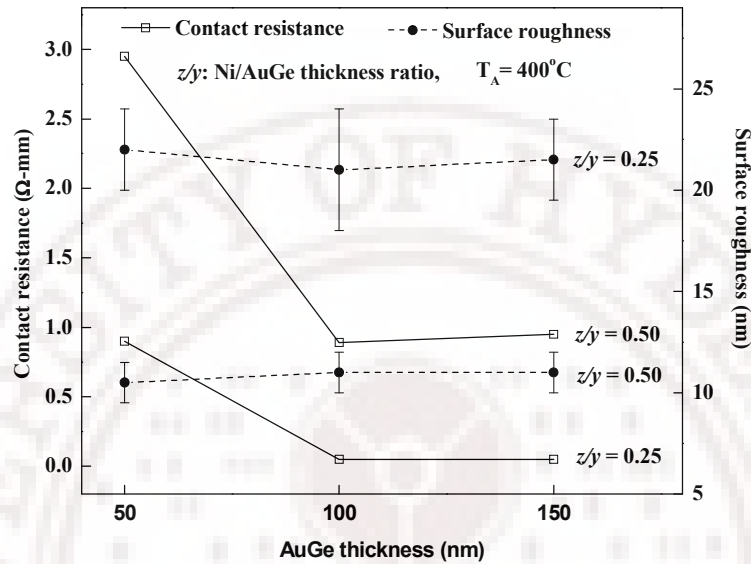


**Figure 3.3.16** Contact resistances and surface roughness of AuGe/Ni/Au contacts with various AuGe layer thicknesses and for Ni/AuGe film thickness ratios 0.25 and 0.5.

**Table 3.3.3** Anneal temperatures and durations optimized for the lowest contact resistance, the contact resistance and surface roughness, for various AuGe thicknesses and different Ni/AuGe ratio.

AuGe thickness ( $y$ nm)	50		100		150		
Ni thickness ( $z$ nm)	12.5	25	25	50	25	37.5	75
Ni/AuGe thickness ratio ( $z/y$ )	0.25	0.5	0.25	0.5	0.167	0.25	0.5
Optimum anneal temperature ( $^{\circ}\text{C}$ )	400	400	400	400	400	400	400
Optimum anneal time (s)	60	180	60	150	60	60	150
Contact resistance ( $\Omega\text{-mm}$ )	0.90	2.95	0.05 $\pm$ 0.01	0.9	0.04	0.05	0.95
Surface roughness (nm)	22 $\pm$ 2	10.5 $\pm$ 1	21 $\pm$ 3	11 $\pm$ 1	24 $\pm$ 3	21.5 $\pm$ 2	11 $\pm$ 1
Anneal temperature for conversion of magnetic phase to non-magnetic phase ( $^{\circ}\text{C}$ )		250-300	200- 250	250- 300			250- 300

Contact resistances close to the optimum are obtained if the Ni to AuGe layer thickness ratio is about 0.25 or less (with the exception of sample with low AuGe thickness  $\sim 50\text{nm}$ ). These results are consistent with previous suggestions on alloyed Ohmic contacts to AlGaAs/GaAs heterostructures [28]. Some published procedures [23]

for Ohmic contacts to GaAs use separate Au, Ge, Ni layers of the form Au (600nm)/Ni (50nm)/Ge (40nm)/Au (100nm). In order to correlate these results, we compute the ratio of the number of atoms per unit area of Ge and to Ni atom ratio per unit area.

For AuGe (100nm)/Ni (25nm)/Au (200nm), the ratio of the number of atoms per unit area of Ge and to Ni atom ratio per unit area at this Ni layer thickness (25nm), for the AuGe thickness of 100nm, comes to approximately 1.

$$x = \frac{t_{Ni}}{t_{AuGe}} \frac{d_{Ni}}{d_{AuGe}} \frac{1.0}{0.12} \frac{M_{Ge}}{M_{Ni}} = \frac{25}{100} \frac{8.908}{19.3} \frac{1.0}{0.12} \frac{72.6}{58.70} = 1.18$$

$t_{Ni}$  and  $t_{AuGe}$  are the thickness of Ni (25nm) and AuGe (100nm),  $d_{Ni}$ ,  $d_{AuGe}$  are the densities of Ni and AuGe, which are  $8.908 \times 10^3 \text{ kg/m}^3$  and  $19.3 \times 10^3 \text{ kg/m}^3$  respectively.  $M_{Ni}$ ,  $M_{Ge}$  are the molecular weight of Ni and Ge, which are 58.7g/mol and 72.6 g/mol respectively.

Procedures utilizing separate Ge, Au and Ni layers [23] find optimum contact resistance formation around 1:1 for the Ge: Ni layer thickness ratio which corresponds to 1:2 for the atom areal density ratio.

$$\text{At } \frac{t_{Ni}}{t_{Ge}} = 1, \frac{Ni}{Ge} (\text{atomic ratio}) = \frac{t_{Ni}}{t_{Ge}} \frac{d_{Ni}}{d_{Ge}} \frac{1.0}{1.0} \frac{M_{Ge}}{M_{Ni}} = 2$$

## Discussions

Process conditions used frequently in practice, viz., 400°C anneal for a minute, result in a non-magnetic contact structure with the contact resistance close to the optimum ( $\sim 0.04 \text{ } \Omega\text{-mm}$ ). This also requires that the AuGe layer thickness should be larger than 50nm, and thickness ratio of Ni/AuGe less than 0.5, conditions that are usually met in practice (table 3.3.3). Total film thickness of  $\sim 450 \text{ nm}$  approaches the maximum suitable for a lift-off patterning process for a typical photoresist thickness of 1  $\mu\text{m}$ .

A significant result of the study is that under conditions normally used for obtaining Ohmic contacts with an AuGe/Ni/Au metallization structure, Ni is rendered non-magnetic after processing. The magnetization data of table 3.3.2 indicates that the samples with Ni layer thickness of  $\sim 10\text{nm}$ -100nm are non-magnetic at room temperature, after the metal film structure is annealed at 430°C for  $x=100\text{nm}$ , and 400°C

for  $x=10-75\text{nm}$ . These are the anneal temperatures most commonly used for Ohmic contact formation. Literature and measured microstructural data is discussed in chapter 5. It is apparent, from the magnetization data presented here, that the transformation of ferromagnetic Ni to a non-magnetic compound or alloy begins at temperatures as low as  $100^\circ\text{C}$  and probably room temperature in all samples. The contact resistance is still quite high at these temperatures as shown in figure 3.3.3.

The electrical contact formation, however, appears to begin at much higher temperatures than  $100^\circ\text{C}$ . Figure 3.3.5 is a summary of the nature of contacts for variation of Ni layer thicknesses and anneal temperature. In any case, experimental data clearly indicates that Ni layer is beneficial at low thickness, for Ohmic contact formation. Our contact resistance data on similar structures but without the Ni-layer are two orders of magnitude higher than ( $3.5\Omega\text{-mm}$ ) for structures with Ni-layers but of low ( $< 50\text{nm}$ ) thicknesses (table 3.2.2). When small Ni-layer- AuGe ( $100\text{nm}$ )/Ni ( $10\text{nm}$ ) thicknesses are used, the contact resistance increases marginally. This may be due to a reduced contact area resulting from the considerable surface roughening coupled with non-conformal coverage of Ni layer.

Further measurements and discussions that provide insights into the contact mechanism are discussed in chapter 5.

### 3.4 Conclusions

1. Systematic studies of the variation of the contact resistance with Ni-layer thickness on a sample with Au-Ge layer thickness of  $100\text{nm}$  indicate that the lowest contact resistance of  $(0.05\pm 0.01\ \Omega\text{-mm})$  is obtained at a Ni layer thickness of  $25\text{nm}$  when annealed at  $400^\circ\text{C}$ .
2. At low Ni layer thickness ( $<25\text{nm}$ ) slight increase in contact resistance is observed relative to the optimum, probably due to a decrease in contact area resulting from the surface roughening.
3. Measurements on samples with other AuGe layer thicknesses suggest that the contact resistances are comparable to this optimum value, if the Ni to AuGe layer thickness ratio is about 0.25 or less.



4. Increasing the Ni layer thickness reduces roughness of annealed contacts, but increases contact resistance.
5. Magnetization hysteresis studies on commonly used metallization of the form AuGe/Ni/Au on GaAs/AlGaAs multilayers indicate that all metallizations are non-magnetic at room temperature after annealing at 400°C (430°C for Ni layer thickness 100nm).
6. Conversion of Ni to non-magnetic phase begins for anneals at temperatures as low as 100°C and is completed at an anneal temperature that increases with Ni layer thickness.
7. The fraction of Ni remaining magnetic as function of anneal temperature is nearly identical for samples with structures AuGe (150 nm)/Ni (75 nm)/Au (200 nm), AuGe (100 nm)/Ni (50 nm)/Au (200 nm) and AuGe (50nm)/Ni (25nm)/Au (200nm).



## References

1. N. Braslau, J. B. Gunn and J. L. Staples, *Solid State Electron.*, **10** (1967) 381.
2. J. B. Gunn, *Trans. IEEE Electron Devices.*, **ED-23** (1976) 705.
3. N. Braslau, *J. Vac.Sci.Technol.*, **19** (1981) 803.
4. Herb. Goronkin, Saied Tehrani, Tom Rimmel, Peter L. Feies and Karl. J. Johnson, *IEEE Trans. Electron Devices.*, **36** (1989) 281.
5. R. P. Taylor, P.T. Coleridge, M. Davies, Y. Feng, J. P. McCaffrey and P. A. Marshall, *J. Appl. Phys.*, **76** (1994) 7966.
6. M. Kamada, T. Suzuki, F. Nakamura, Y. Mori and M. Arai, *Appl. Phys. Lett.*, **49** (1986) 1263.
7. A. Ketterson, F. Ponce, T. Henderson, J. Klem and H. Morkoc, *J. Appl. Phys.*, **57** (1985) 2305.
8. A. K. Rai, A. Ezis, R. J. Graham, R. Sharma and D. W. Langer, *J. Appl. Phys.*, **63** (1988) 4723.
9. G. Sai Saravanan, K. Mahadeva Bhat, K. Muraleedharan, H. P. Vyas, R. Muralidharan and A. P. Pathak, *Semicond. Sci. Technol.*, **23** (2008) 025019.
10. T. C. Shen, G.B. Gao and H. Morkoc, *J. Vac. Sci. Technol.*, **B 10** (1992) 2113.
11. M. Murakami, *Science and Technology of Advanced Materials.*, **3** (2002) 1.
12. M.J.Howes and D.V.Morgan, *GaAs Materials Devices and Circuits.*, Wiley & Sons, (1986).
13. S.M Sze, *Physics of Semiconductor Devices.*, John Wiley, New York (1981).
14. G.Y. Robinson, *Solid State Electron.*, **18** (1975) 331.
15. J. Gyulai, J.W. Mayer, V. Rodriguez, A.Y.C. Yu and H.J.Gopen, *J.Appl.Phys.*, **42** (1971) 3578.
16. L.Y.Zee, Z.A. Munir, *J. Mater.Sci.*, **10** (1975) 1929.
17. W.D. Edwards, W.A. Hartman and A.B.Torrens, *Solid state electron.*, **15** (1972) 387.
18. M.Ostubo, H.Kumabe and H.Miki, *Solid state electron.*, **20** (1977) 617.
19. M. Murakami, K.D. Childs, John. M. Baker and A. Callegari *J. Vac. Sci. Technol.*, **B 4** (1986) 903.

20. T.S. Kuan, P.E. Batson, T.N. Jackson, H. Rupprecht and E. L. Wilkie, *J. Appl. Phys.*, **54** (1983) 6952.
21. A.G. Baca, F. Ren, J. C. Zolper, R. D. Briggs and S. J. Pearton, *Thin Solid Films.*, **308** (1997) 599.
22. Soo-Jin Chua and Seng Hin Lee, *Jpn. J. Appl. Phys.*, **33** (1994) 66.
23. H. Buhlmann and M. Hengemeyer, *J. Electrochem. Soc.*, **138** (1991) 2795.
24. T. S. Abhilash and G. Rajaram, *Proceedings of the DAE Solid State Physics Symposium.*, (2004) p 530.
25. H.H. Berger *Solid State Electron.*, **15** (1972) 145.
26. S.S. Cohen, G.Sh. Gildenblat, *VLSI Electron Microstruct Sci.*, (1986) 101.
27. Hung-Cheng Lin, Sidat Senanayake and Keh-Yung Cheng, *IEEE Trans. Electron Devices.*, **50** (2003) 880.
28. Oktay Goktas, Jochen Weber, Jurgen Weis and Klaus von Klitzing *Physica E.*, **40** (2008) 1579.

## Chapter - 4

### **Dependence of contact resistance, roughness, magnetization and melting on Ge content in the AuGe alloy**

#### **4.1 Introduction**

The eutectic AuGe/Ni/Au Ohmic contact metallization gives low contact resistance of the order of  $\sim 0.03 - 0.1 \Omega\text{-mm}$  [1-10]; however, this is achieved at the expense of increased surface roughness [10]. The optimum Ni layer thickness for a 100nm AuGe layer thickness is  $\sim 25\text{-}30\text{nm}$  (chapter 3) and the surface roughness is  $\sim 25\text{nm}$  [10]. The surface roughness can influence the transistor gate fabrication (HEMT), while fabricating on-chip support circuits with Hall magnetic field sensors for various applications on GaAs/AlGaAs multilayer structures. The surface roughness can be reduced by increasing the Ni layer thickness above the optimum, at the expense of increased contact resistance (chapter 3) and possibly magnetism [10-14].

Alternative to increasing Ni layer thickness, for reducing the surface roughness is reduction of the Ge content below that of the eutectic composition (88:12 wt %). Ge however, is necessary for making the Ohmic contact, indiffusion of Ge dopes device layers forms a low resistance tunneling contact [15-19]. On the other hand, decreasing Ge content from the eutectic composition can increase the alloy melting temperature and could influence the surface roughness. Hence it is relevant to examine the effect of Ge content in the AuGe alloy on the surface roughness and contact formation.

In this chapter the following are studied:

1. The effect of Ge content in the AuGe alloy on the contact resistance and surface roughness using three AuGe compositions.
2. The effect of Ge content in the AuGe alloy on the melting in the metallization.
3. Study the residual magnetization of the processed Ohmic contact metallization (AuGe/Ni/Au) structure in the context of magnetic field sensor applications [20-22].

4. The effect of Ge content in the AuGe alloy layer on the transformation of Ni-layer to the non magnetic phase.
5. Low temperature dependence of contact resistance in the context of application of magnetic field sensor at low temperatures.

## **4.2 Dependence of contact resistance, roughness, magnetization and melting on Ge content in the AuGe alloy and Ni layer thickness.**

In this section, the results of contact resistance, roughness, magnetization and melting in the metallization structure as functions of anneal temperature, Ni layer thickness and three AuGe compositions using annealed AuGe/Ni/Au film structures are presented.

### **4.2.1 Experimental**

Three contacts are investigated with eutectic (88:12 weight %) and off-eutectic (95:5 and 97.3:2.7 wt %) compositions of the AuGe alloy. Temperature scan of Differential Scanning Calorimetry (DSC) are performed on the bulk alloy pieces from room temperature to 500°C at a heating rate of 100°C/min in N<sub>2</sub> gas atmosphere (figure 4.2.1). Each of the original data is subjected to an offset corresponding to its baseline and good homogeneity is obtained as seen by the data on the bulk alloy sample (figure 4.2.1). The melting temperature of AuGe (88:12wt%) alloy is 375.5°C, as shown in figure 4.2.1, and the melting temperature of the bulk alloy increased with decreasing Ge content from 12 wt% to 5wt% to 2.7wt% in the AuGe alloy (figure 4.2.1).

The Ohmic contacts are prepared by evaporating AuGe (100nm)/ Ni (30nm)/Au (200nm) using thermal and e-beam evaporation, onto wafer pieces with multilayer structure as shown in table 4.2.1. The Ni layer thickness of 30nm (close to the optimum for low contact resistance) is used for the Ohmic contact formation (chapter 3). The samples are then subjected to anneal at a temperature  $T_A$  reached at heating rates of 250°C/min, held at  $T_A$  for anneal durations  $t_A$  in N<sub>2</sub> atmosphere.

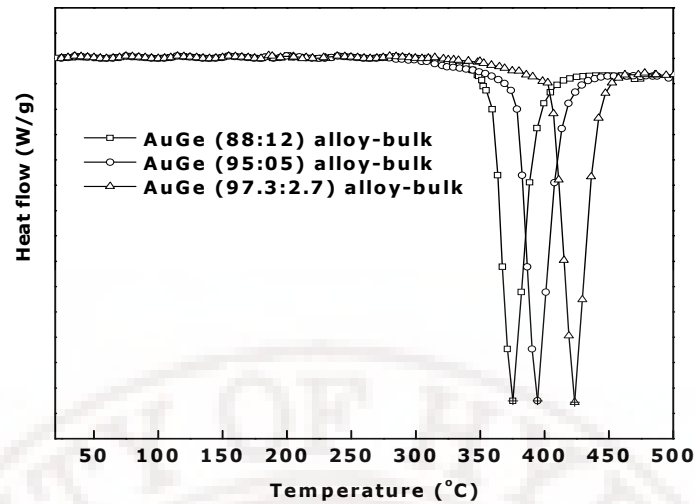


**Figure 4.2.1** Differential Scanning Calorimetry (DSC) of AuGe eutectic and off-eutectic bulk alloy

The contact resistances are measured by lithographically patterning a transmission line pattern as described in [23] chapter 2, and using the Transmission line or Transfer Length Model (TLM) [23, 24]. Magnetization hysteresis loops are measured on samples with the annealed contact structures with several Ni layers thicknesses (25, 30, 50 nm) using Vibrating Sample Magnetometer (VSM). Temperature scans of Differential Scanning Calorimetry (DSC) are performed on the metallized substrate, with a bare substrate as the reference. The scan spanned from room temperature to 500°C at a heating rate of 100°C/min.

**Table 4.2.1** GaAs/AlGaAs wafer layer structure and Ohmic contact metallization

Au (200nm)		
Ni (30nm)		
Eutectic/off-eutectic AuGe alloy (100nm)		
$n^+$ (Si $1.5 \times 10^{18}$ ) GaAs	20nm	Cap layer
$n^+$ (Si $1.5 \times 10^{18}$ ) $\text{Al}_{0.3}\text{GaAs}_{0.7}$	30nm	Supply layer
Intrinsic AlGaAs	15nm	Separation layer
Intrinsic GaAs	500nm	<b>2DEG</b> ➔
SI GaAs Substrate	500μm	

The surface roughness is estimated by measuring the root-mean-square height of the sample profile over an area of about  $5\mu\text{m} \times 5\mu\text{m}$ , at several pads of the TLM structure

using Dynamic Force Microscopy (DFM). Temperature dependence (4-300K) of the contact resistance is undertaken on a few samples to study the changes in the electrical contact conduction mechanism and also in the context of low-temperature applications of the magnetic field sensor.

#### 4.2.2 Electrical characteristics

The contact resistance,  $R_{TC}$  as a function of anneal temperature for three AuGe alloy compositions for optimized anneal durations is shown in figure 4.2.2. The  $R_{TC}$  dependence on Ni layer thickness, optimized with respect to anneal temperature and time, for eutectic AuGe alloy is shown in the inset.

1. The contacts with AuGe (88:12 wt %) /Ni/Au show Ohmic behavior for anneal temperatures ( $T_A$ ) above 350°C and contacts with AuGe (95:5wt %) /Ni/Au show Ohmic behaviour above 370°C (figure 4.2.3). At  $T_A = 350^\circ\text{C}$  the contacts with AuGe (95:5 wt%) /Ni/Au represent characteristics of a back to back reverse biased diodes (figure 4.2.3). AuGe (97.3:2.7 wt%) alloy resulted in a diode-like characteristic at  $T_A$  below 400°C and showed Ohmic characteristic at  $T_A$  above 400°C.

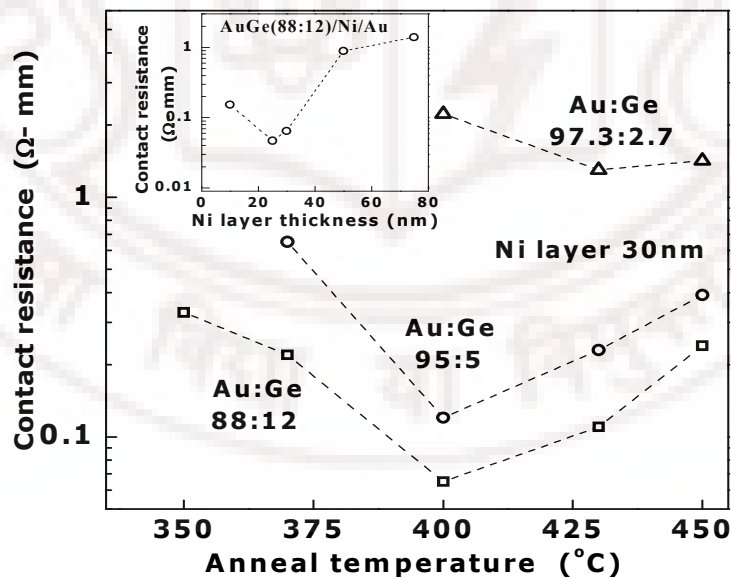


**Figure 4.2.2** Contact resistance ( $R_{TC}$ ) Vs anneal temperature ( $T_A$ ) for eutectic and off-eutectic alloys with Ni layer thickness ( $x_{Ni}$ ) of 30nm.

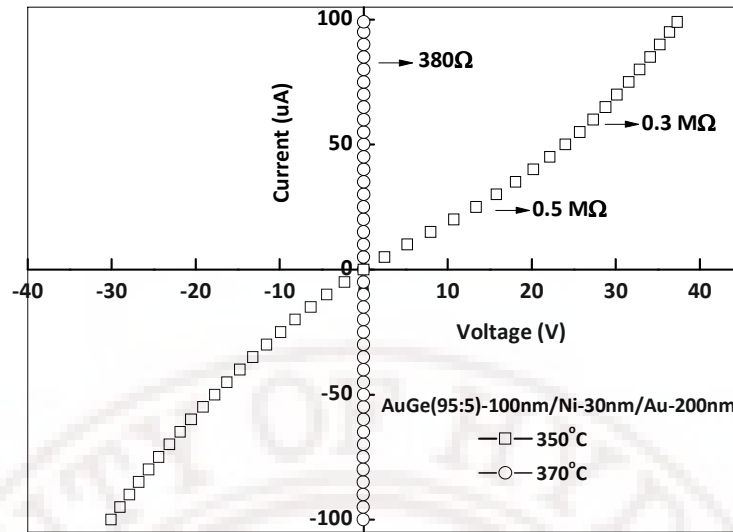


**Figure 4.2.3** I-V characteristics for AuGe (95:5)/Ni-30nm/Au for anneal temperatures of 350°C and 370°C.

2. The lowest contact resistance is observed at  $T_A$  of 400°C for AuGe (88:12 and 95:5 alloy), and a contact resistance ' $R_{TC}$ ' of  $0.07 \pm 0.005 \text{ } \Omega\text{-mm}$  is observed for AuGe (88:12) /Ni-30 nm/Au and  $0.17 \pm 0.02 \text{ } \Omega\text{-mm}$  for AuGe (95:5) /Ni-30 nm/Au configuration for 90 second anneals (table 4.2.2). The quoted errors (table 4.2.2) are r.m.s deviation over several separate deposition runs.
3. The contact resistance increased by a few orders for AuGe (97.3:2.7)-100nm/Ni-30nm/Au-200nm ( $1.3 \text{ } \Omega\text{-mm}$ ) when compared to AuGe (88:12)-100nm/Ni-30nm/Au-200nm ( $0.07 \pm 0.005 \text{ } \Omega\text{-mm}$ ) and AuGe (95:5)-100nm/Ni-30nm/Au-200nm ( $0.17 \pm 0.02 \text{ } \Omega\text{-mm}$ ).
4. Increasing the annealing temperatures increases the contact resistance marginally (figure 4.2.2).
5. The optimum Ni layer thickness for low contact resistance is  $\sim 25\text{-}30 \text{ nm}$  for AuGe layer thickness of 100nm (chapter 3) [10].
6.  $R_{TC}(T_A)$  has a lower value and shallower minimum (better process latitude for  $T_A$ ) for AuGe composition near the eutectic.
7. Increasing the Ni layer thickness and decreasing the Ge content in the alloy from the eutectic increases the contact resistance (table 4.2.2).



The dependence of the contact resistance of AuGe/Ni/Au alloyed contacts on anneal durations with various Ge content in the alloy is shown in figure 4.2.4. The optimum anneal temperature required to minimize contact resistance increases with decreasing Ge content from eutectic (12wt %) to off-eutectic (2.7 wt %) alloy. The data for anneal temperatures and durations optimized for lowest contact resistance, contact resistance for three alloy compositions, for Ni layer thickness of 30nm are summarized in table 4.2.2.

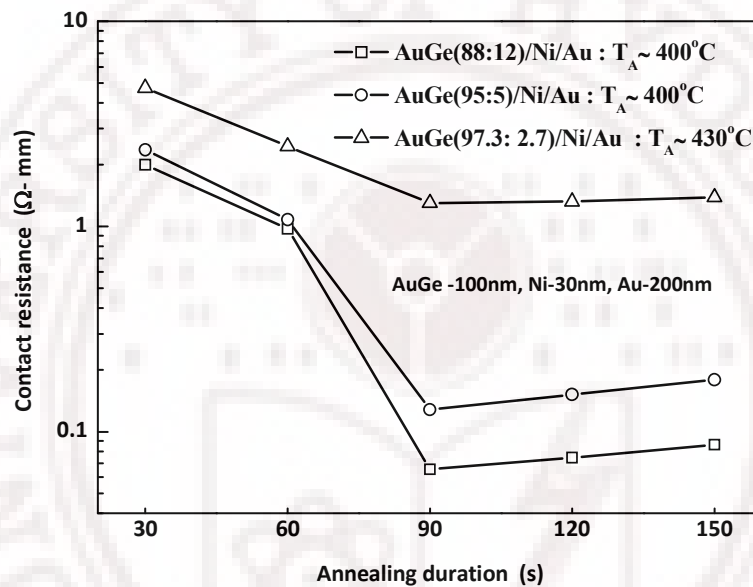


**Figure 4.2.4** Contact resistance ( $R_{TC}$ ) vs. anneal durations ( $t_A$ ) for eutectic and off-eutectic alloys.

**Table 4.2.2** Magnetic-to-non magnetic transition temperatures, surface roughness, contact resistance ( $R_{TC}$ ), anneal temperature ( $T_A$ ) and anneal duration ( $t_A$ ) for three alloy compositions with different Ni layer thicknesses ( $x_{Ni}$ ).

AuGe alloy composition	Nickel layer thickness (nm)	Optimum anneal temperature $T_A(^{\circ}\text{C})$	Optimum anneal duration $t_A(\text{s})$	Optimum contact resistance ( $\Omega\text{-mm}$ )	Magnetic to non magnetic transition anneal temperature ( $^{\circ}\text{C}$ )	Surface roughness (nm)
88:12	25	400	60	$0.05 \pm 0.01$	200-250	$21 \pm 3$
	30	400	90	$0.07 \pm 0.005$	200-250	$20.5 \pm 2$
	50	400	150	0.90	250-300	$11 \pm 1$
95:5	25	-	-	-	250-300	-
	30	400	90	$0.17 \pm 0.02$	250-300	$5.5 \pm 0.5$
	50	-	-	-	350-400	-
97.3:2.7	30	430	120	1.30	400-430	$4.5 \pm 0.5$

The sheet resistance (which may include parallel resistances of multilayers) also can be derived from the contact resistance measurement by the TLM method, for the annealed samples. The sheet resistance increases marginally with anneal temperature and time (figure 4.2.5).

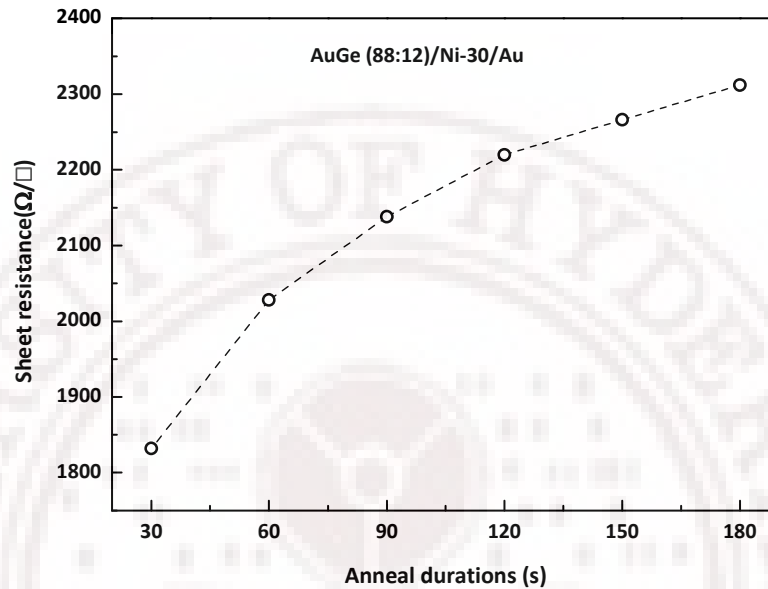


**Figure 4.2.5** Sheet resistance ( $R_s$ ) Vs anneal durations ( $t_A$ ) for eutectic AuGe/Ni/Au.

### 4.2.3 Surface roughness

Atomic Force Microscope (AFM) images for eutectic AuGe(88:12)/Ni/Au, off-eutectic AuGe(95:5)/Ni/Au and AuGe (97.3:2.7)/Ni/Au deposited TLM pattern and annealed for durations that gave the lowest contact resistance are displayed in figure 4.2.6. The R.M.S. surface roughness computed over the scanned surface is given in table 4.2.2.

1. Off-eutectic alloy compositions give lower roughness but increased contact resistances.
2. The surface roughness is quite sensitive to Ni content, decreases steadily with increase of Ni layer thickness.
3. The surface roughness of eutectic AuGe/Ni/Au is  $\sim 20.5 \pm 2$  nm and off-eutectic alloy with AuGe (95:5)/Ni/Au is  $\sim 5.5 \pm 0.5$  nm and AuGe (97.3:2.7)/Ni/Au is  $\sim 4.5 \pm 0.5$  nm.

4. Increasing Ni layer thickness (50nm) above the optimum layer thickness increases the contact resistance  $\sim 10$  times and reduces the roughness by 50%.

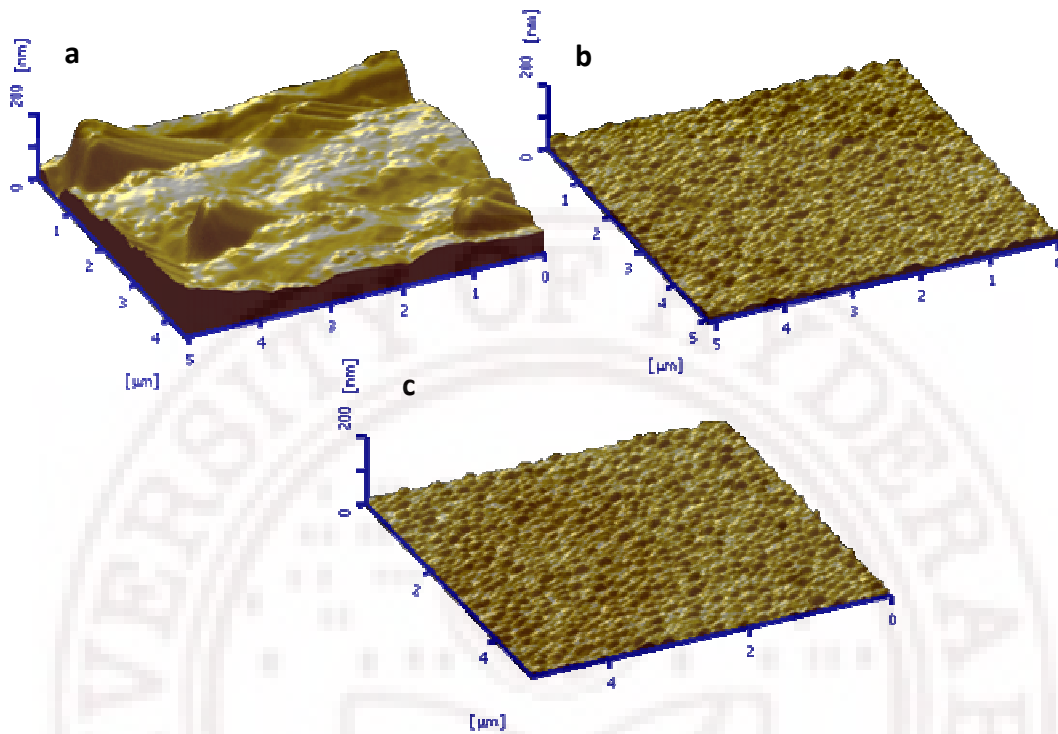


**Figure 4.2.6** AFM micrographs of the surface of samples with (a) AuGe (88:12)/Ni(30nm)/Au(200nm), (b) AuGe(95:5)/Ni(30nm)/Au(200nm), (c) AuGe(97.3:2.7)/Ni(30nm)/Au(200nm) and annealed for durations that gave the lowest  $R_{TC}$ .

5. The use of the off-eutectic alloy with 95:5 wt % results in reduction of surface roughness by 75% and increases contact resistance about twice that of eutectic composition, albeit with a higher sensitivity to anneal temperature.

The use of AuGe (95:5wt %) alloy appears to be a good choice between the contradictory requirements of low surface roughness and low contact resistance, than increasing Ni layer thickness above that of samples which give the least contact resistance.

#### 4.2.4 Magnetic properties

The magnetic hysteresis loops recorded on AuGe (88:12, 95:5, and 97.3:2.7)-100 nm/Ni-30 nm /Au-100 nm for various annealing temperatures are shown in figure 4.2.7.

1. The data show that, while hysteresis loops of the as-deposited film structure are ferromagnetic, the loops become progressively less magnetic after being subjected to anneal at increasing temperatures.
2. The anneal temperature for which the structure becomes completely non-magnetic, increases with decreasing Ge content in the alloy (table 4.2.2).

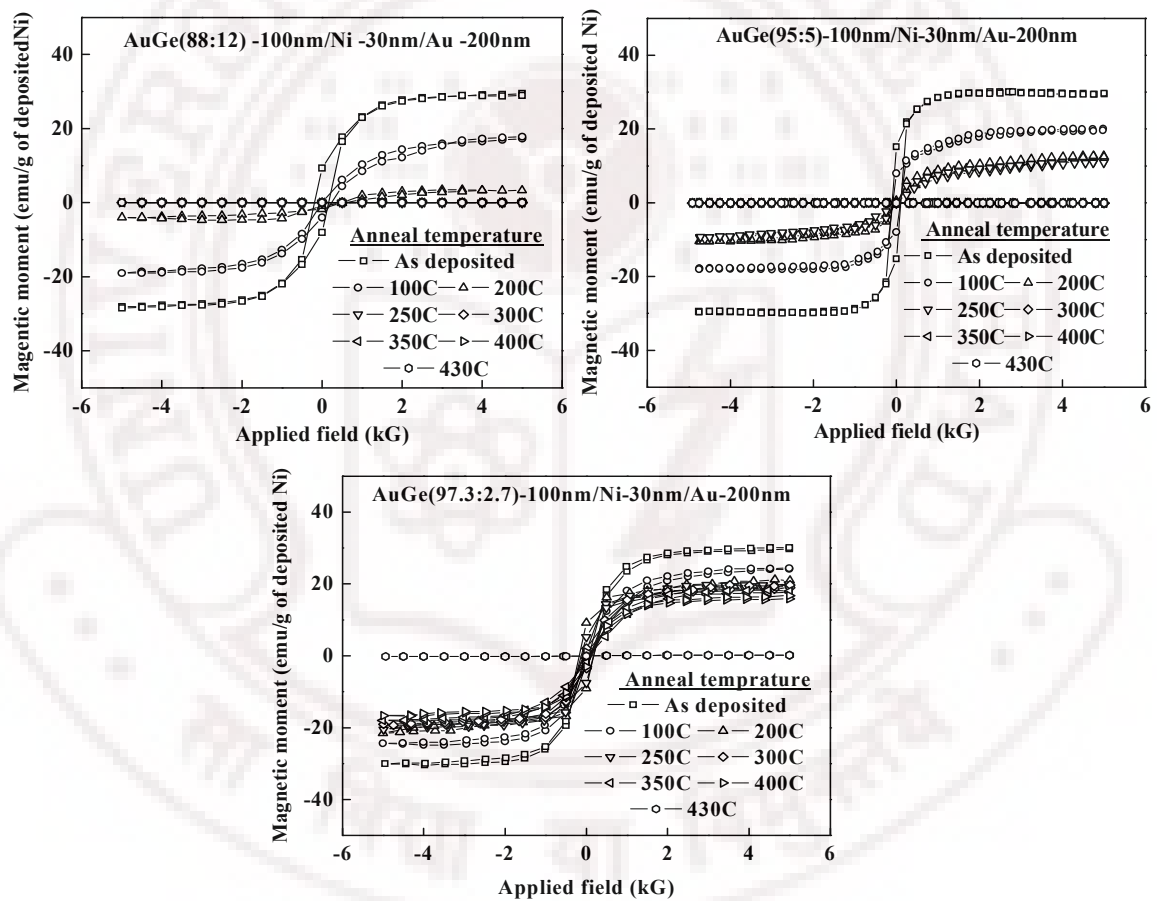


**Figure 4.2.7** Magnetization hysteresis loops for AuGe (88:12)/Ni/Au, AuGe (95:5)/Ni/Au and AuGe (97.3:2.7)/Ni/Au annealed at various anneal temperatures.

Magnetization hysteresis loops of annealed samples collapse as the anneal temperature is increased. The magnetization at 5 kG, as a percentage of that of the un-annealed sample, is shown in figure 4.2.8, as anneal temperature is increased from 100

to 430°C. The results indicate that, the hysteresis loops of the as-deposited film structure are magnetic; the metallization structure becomes completely non-magnetic on annealing at or above a temperature which varies from 250°C to 430°C, as the Ge content is decreased and with increasing Ni-layer thickness (table 4.2.2). Hence, under conditions normally used for obtaining Ohmic contacts, the structure is non-magnetic for a wide range of Ni layer thicknesses. Notably, decrease in magnetization occur even at anneal temperatures as low as 100°C. The minimum anneal temperature required to complete the transformation to a non-magnetic phase is unknown, but lies in the range given in the shaded region.

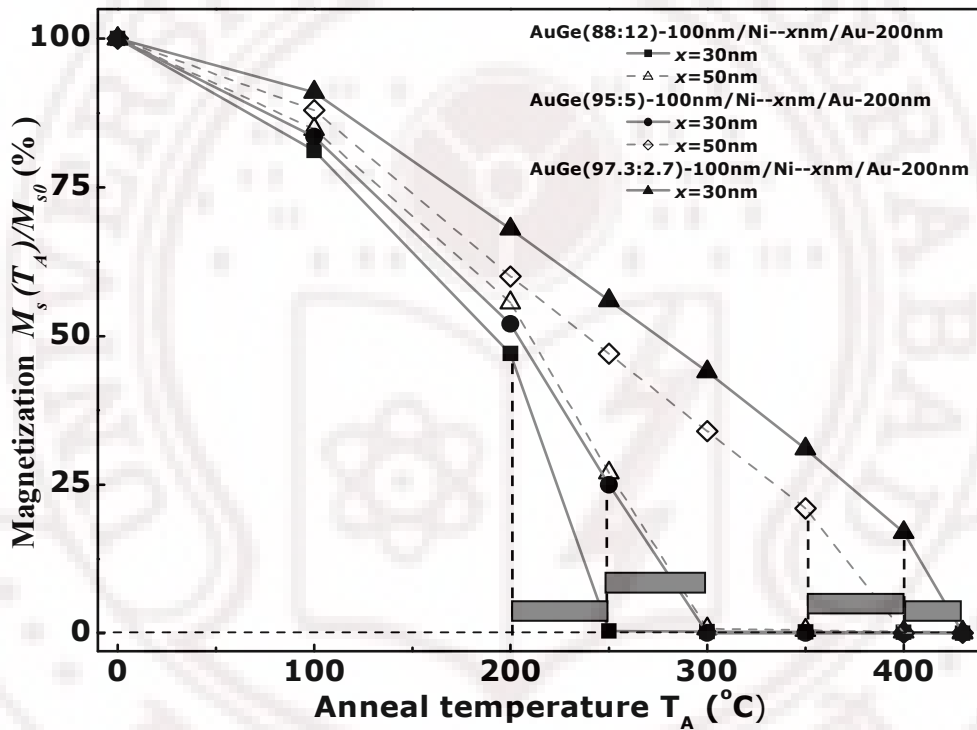


**Figure 4.2.8** Anneal temperature ( $T_A$ ) dependence of the fractional saturation magnetization for samples with three AuGe alloy compositions and two Ni layer thicknesses on GaAs multi-layer.  $M_{s0}$  is the saturation magnetization of the un-annealed sample at 5 kG.

#### 4.2.5 Differential Scanning Calorimetry (DSC)

DSC scans obtained for three AuGe alloy compositions (88:12, 95:5, 97.3:2.7 wt %) with a fixed (30nm) Ni layer thickness is shown in figure 4.2.9. Signatures of melting in the metallization structure occur at higher temperatures when Ge content is reduced.

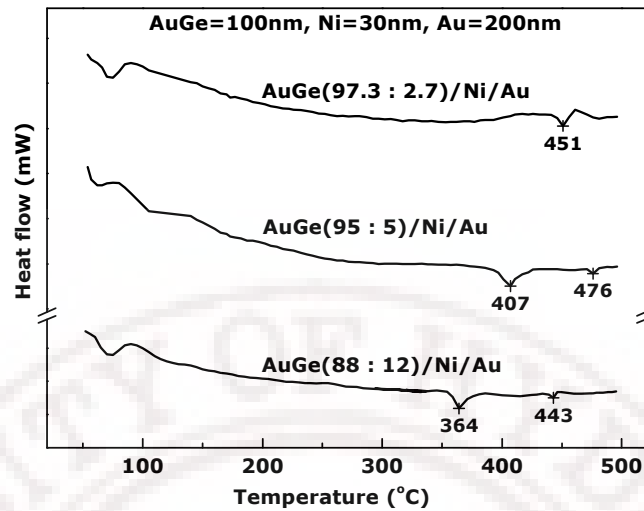


**Figure 4.2.9** DSC scans for samples with eutectic and off-eutectic AuGe alloy with 30nm Ni layer.

The AFM micrographs (figure 4.2.6) of the surface of two samples, one prepared with AuGe at the eutectic composition and the other with off-eutectic composition (95:5 wt %) both annealed at 400°C (at which the contact resistance is close to optimum) show a considerably reduced roughness (table 2) is evident in the latter sample whose anneal temperature is closer to the temperature of ‘melting’ in its metallization structure. Precise quantitative comparisons of temperatures are difficult in view of differences in experimental setup for the DSC and contact anneals, and also the rapid heating rates.

#### 4.2.6 Structural Properties

The X-Ray diffractrogram of the AuGe (88:12 wt %) (100nm)/Ni (30nm)/Au (200nm) films deposited on GaAs/AlGaAs substrate and annealed at 400°C for 90s (optimum contact resistance) is shown in figure 4.2.10. Mainly peaks corresponding to GaAs/AlGaAs substrate and Au are detected in the as deposited un-annealed case.

At 400°C annealed sample the peaks corresponding to AuGa are also detected. The information regarding the inter layers could not be detected, in the either case, as the data was not from grazing incidence XRD.

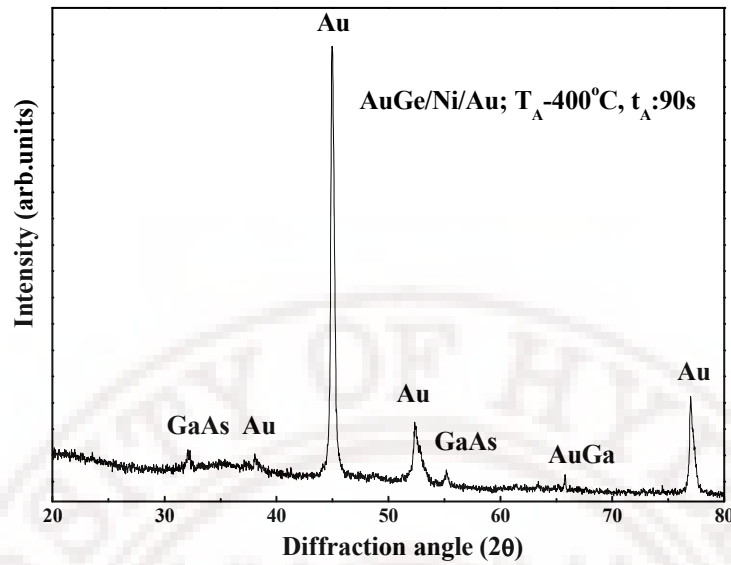


**Figure 4.2.10** XRD analysis of AuGe-100nm/Ni-25nm/Au-200nm annealed at 400°C for 60s.

#### 4.2.7 Temperature dependence of contact resistance

Temperature dependence (4-300K) of the contact resistance is undertaken to study the changes in the electrical conductivity through the Ohmic contacts and also in the context of low-temperature applications of the magnetic field sensor [22]. The TLM measurements for contact resistances are carried out between 4K and 300K, at a number of different temperatures on three samples. One was a sample with the eutectic AuGe layer, namely AuGe (88:12 wt%)/Ni (30nm)/Au whose contact resistance is close to the optimum. The other two samples were those in which the roughness was reduced: one by increasing the Ni-layer thickness to 50nm and the other by using a AuGe layer composition of 95:5 wt%. The current – voltage (I-V) characteristics between the TLM pads at a gap spacing 25μm at several different temperatures for AuGe (95:5)-100nm/Ni-30nm/Au-200nm are given in figure 4.2.11. The I-V curves are linear for all temperatures (300-4K).



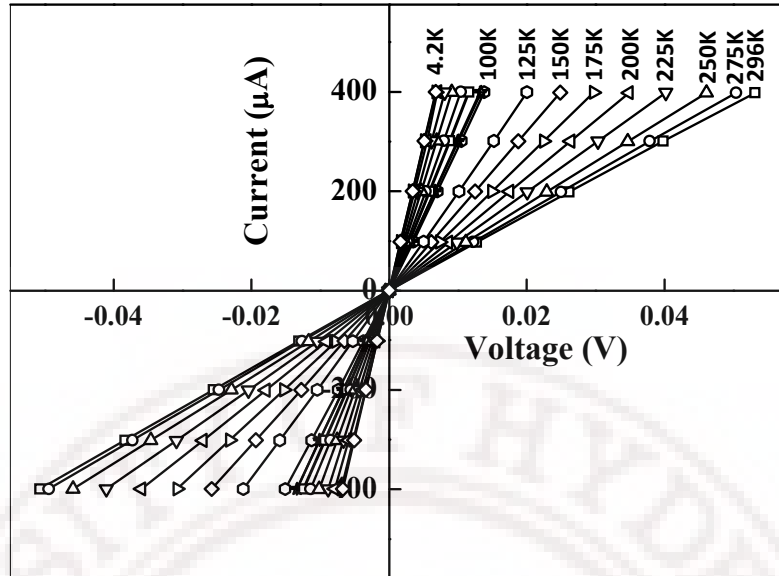


**Figure 4.2.11** Current –voltage (I-V) characteristics at different temperatures.

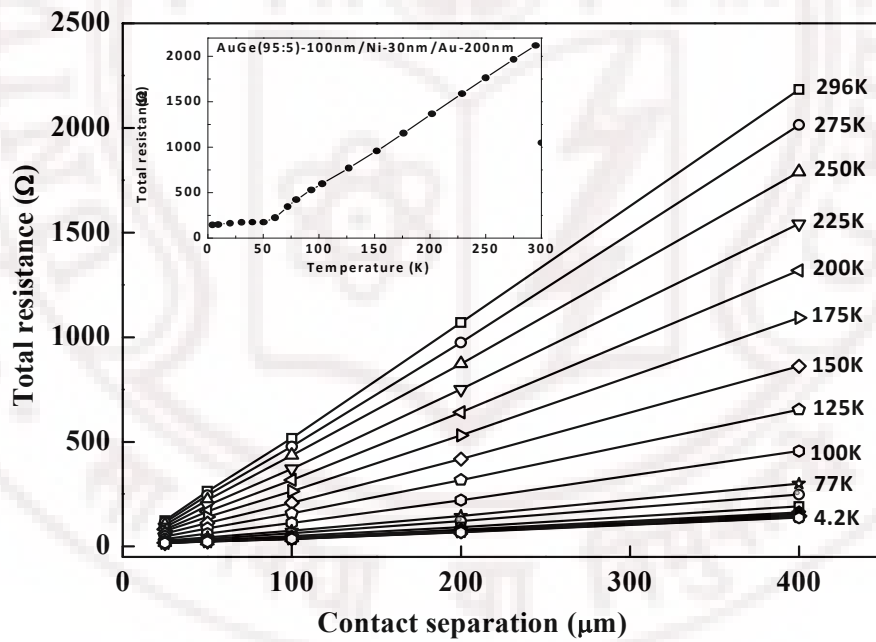


**Figure 4.2.12** Total resistance plotted as a function of contact separation at a number of different temperatures.

The total measured resistance  $R_T$  plotted as a function of contact separation at different temperatures is shown in the figure 4.2.12, which is then extrapolated to zero to calculate  $R_C$ ,  $R_s$  and  $L_T$  as explained in Chapter 1 & 2. The inset shows the total resistance as a function of temperature in the temperature range from 4K to 300K. The

slope and intercept of each line are obtained from the best fits to the data to obtain the sheet resistance  $R_s$  and contact resistance  $R_c$ . The temperature dependence of contact resistance and sheet resistance are plotted in figures 4.2.13 and 4.2.14. The error is calculated by taking the R.M.S deviation at each temperature (details as in chapter 2).

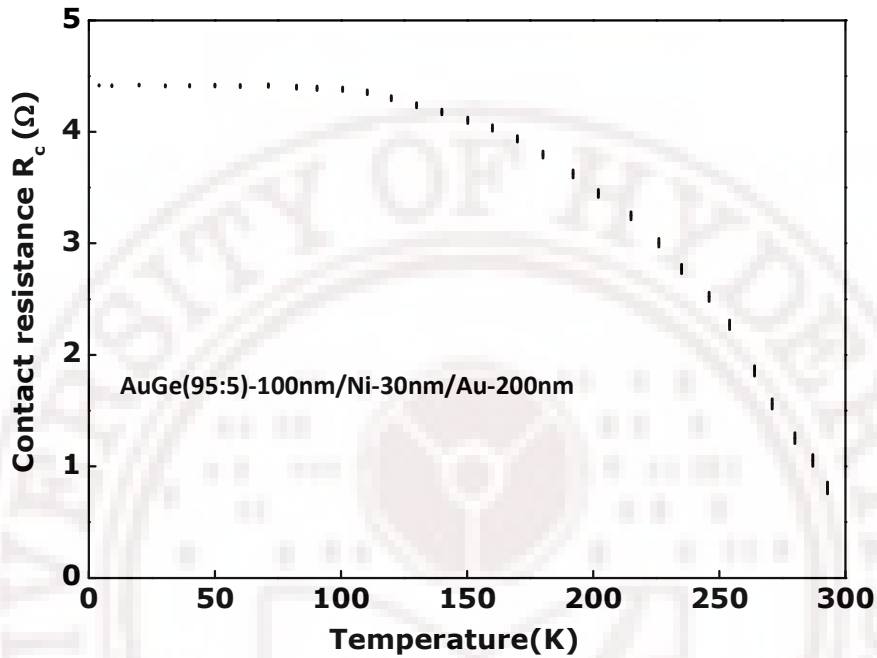


Figure 4.2.13 Total contact resistance  $R_c$  plotted as a function of temperature.

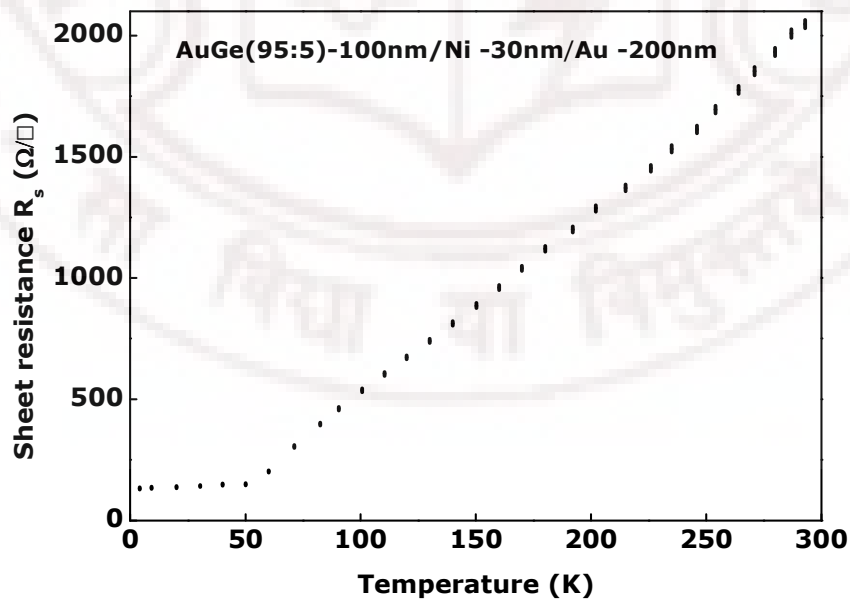
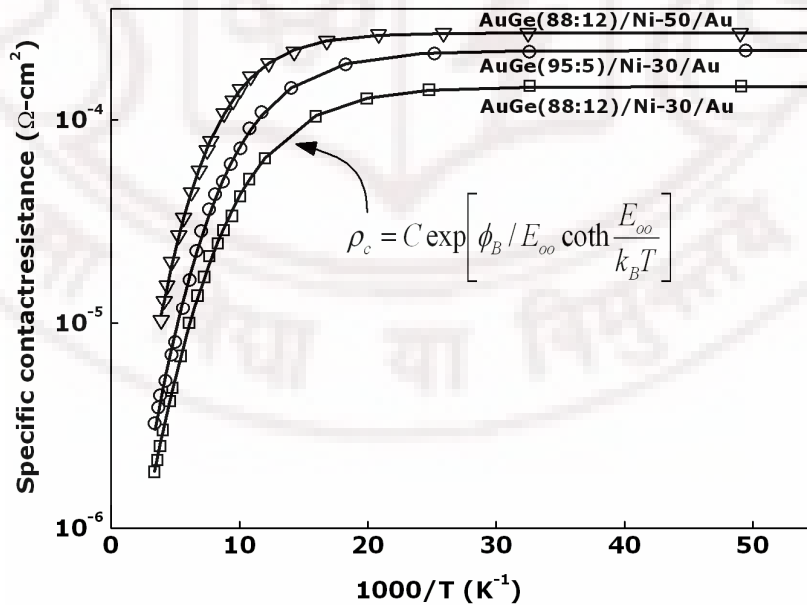


Figure 4.2.13 Measured sheet resistance  $R_s$  plotted as a function of temperature.

The contact resistance increases, and the sheet resistance decreases as the measured temperature is decreased from 300K to 4K (figure 4.2.14 and 4.2.15). The contact resistance,  $R_C$  is related to specific contact resistance  $\rho_c$ , and the contacted material sheet resistance,  $R_s$ , via the concept of transfer length,  $L_T$ . The transfer length characterizes the exponential decrease of current density in a direction perpendicular to the edge of the contact where the current crowding takes place and is given by [23].

$$L_T = \sqrt{\frac{\rho_c}{R_s}}$$

Temperature dependence (4-300K) of the contact resistance was undertaken on three samples to study the changes in the electrical contact mechanism and also in the context of low-temperature applications. One was a sample with the eutectic AuGe layer, namely AuGe (88:12 wt %)/Ni (30nm)/Au whose contact resistance is close to the optimum. The other two samples are those in which the roughness is reduced- one by increasing the Ni-layer thickness to 50nm and the other by using an AuGe layer composition of 95:5 wt%. The specific contact resistivity ( $\rho_c$ ) of these samples as a function of temperature (4-300K) for AuGe (88:12)/Ni/Au with two Ni layer thicknesses (30 and 50nm) and AuGe (95:5)/Ni-30nm/Au are shown in figure 4.2.15.



**Figure 4.2.15** Specific contact resistance  $\rho_c$  plotted as a function of inverse temperature for three AuGe alloy compositions with different  $x_{Ni}$ .

The contact resistivity increases, as the measured temperature is decreased from 300K to 4K (table 4.2.3). The experimental data have been fitted using the expressions of  $\rho_c$  based on the thermionic and tunneling models of current transport through the metal semiconductor contacts [25, 26] (chapter 1, section 1.2). The graph also shows the fitted curve to the equation based on the thermionic field emission.

$$\rho_c = C \exp \left[ \phi_B / E_{oo} \coth \frac{E_{oo}}{k_B T} \right]$$

The specific contact resistance in this case depends on temperature and transmission co-efficient of tunneling  $E_{oo}$ .  $\phi_B$  is the barrier height. The value of  $E_{oo}/k_B$  is the measure of the temperature below which electronic conduction is tunneling dominated and independent of temperature.

Table 4.2.3 shows the temperature dependence of contact resistivity and the value of barrier height, tunneling parameter etc. We observe that

1. The contact resistance shows strong temperature dependence, in the range (4-300K), with indications of both thermionic and tunneling behaviours.
2.  $\rho_c$  decreases with increase of temperature. Figure 4.2.15 shows that the logarithm of  $\rho_c$  increases nearly linearly with  $1000/T$  over temperature range 4K to about 100K and levels off as the temperature decreases to below 100K.
3. The Arrhenius behaviour shown in figure 4.2.16 indicates the presence of a potential barrier and presence of thermionic current transport above 100K.
4. The weak temperature dependence of  $\rho_c$  below 100K indicates a change in the current transport mechanism from thermionic to tunneling.
5. The barrier height for current conduction increases relative to the samples with the eutectic AuGe layer, for increase of Ni and decrease in Ge contents in structure; the increase is less in the latter case relative to the former.

**Table 4.2.3** Temperature dependent contact resistivity for two alloy compositions with different Ni layer thicknesses ( $x_{Ni}$ ).

	Specific contact resistance ( $\Omega\text{-cm}^2$ )			$\phi_B$ (meV)	$E_{oo}$ (meV)	$E_{oo}/k_B$ (K)	log C
	298K	77K	4.2K				
AuGe(88:12)/Ni-30/Au	$1 \times 10^{-6}$	$4.5 \times 10^{-5}$	$1.7 \times 10^{-4}$	$31 \pm 0.5$	$10.3 \pm 0.1$	$116 \pm 1$	$6.8 \pm 0.02$
AuGe(88:12)/Ni-50/Au	$1 \times 10^{-5}$	$1.8 \times 10^{-4}$	$2.7 \times 10^{-4}$	$38 \pm 0.7$	$13.1 \pm 0.1$	$148 \pm 1$	$6.5 \pm 0.03$
AuGe(95:05)/Ni-30/Au	$3.2 \times 10^{-6}$	$7.6 \times 10^{-5}$	$2.4 \times 10^{-4}$	$34.5 \pm 1$	$11 \pm 0.15$	$124 \pm 1.5$	$6.7 \pm 0.04$

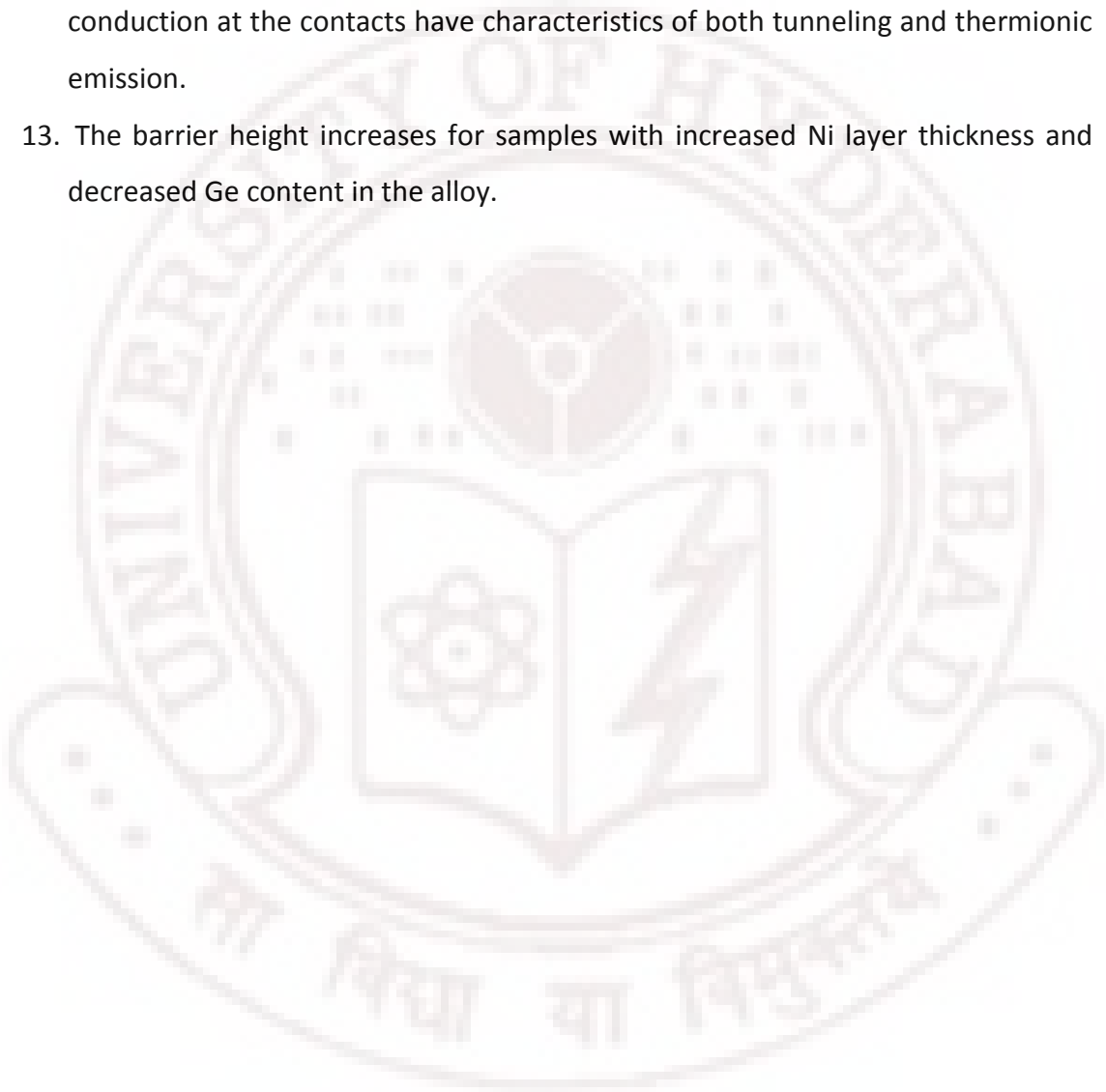
At  $T = 0$ ,  $\rho_c \rightarrow \infty$ , the carriers get localized as they do not have sufficient energy to overcome the barrier.

The enhancement in amount of Ni-Ge compounds formed with increasing Ni layer thicknesses, and less Ge in-diffusion into GaAs with decrease of Ge content in the alloy could be the cause for increase in barrier height with increase of Ni layer thickness and decrease of Ge content in the AuGe alloy.

### 4.3 Conclusions

1. The eutectic AuGe (88:12 wt% alloy)-100nm/Ni-30nm/Au-200nm, gives the lowest contact resistance of  $0.07 \pm 0.005 \Omega\text{-mm}$ , of various AuGe compositions (Ge content).
2. Decreasing the Ge content in the alloy from the eutectic increases the contact resistance.
3. The off-eutectic AuGe (95:5 wt%)-100nm/Ni-30 nm/Au-200nm configuration gives contact resistance of  $\sim 0.17 \pm 0.02 \Omega\text{-mm}$  and AuGe (97.3:2.7 wt%)-100nm/Ni-30nm/Au-200nm gives contact resistance  $\sim 1.3 \Omega\text{-mm}$ .
4. Off-eutectic alloy compositions give lower roughness but increased contact resistances.
5. The surface roughness is quite sensitive to Ge content, decreases steadily with decrease of Ge content.
6. The off eutectic alloy AuGe (95:5) with optimum Ni layer thickness appear to be a good choice between surface roughness and contact resistance than increasing Ni layer thickness above the optimum in the eutectic alloy.
7. The metallization structures are rendered non-magnetic at room temperature after annealing at typically used alloying conditions of temperature (400-430°C).
8. Conversion of Ni to non-magnetic phases, begins at anneal temperatures as low as 100°C and is completed at an anneal temperature that increases with decreasing Ge content in the AuGe alloy (250-430°C).
9. Signatures of melting are seen in Differential Scanning Calorimetry; indicate that the melting temperature increases with decreasing Ge content.

10. Increasing Ni layer thickness increases metallization melting temperature and reduces surface roughness.
11. The structural studies show phases corresponding to Au and substrate in the as deposited case and in the annealed samples formation of AuGa phase is also detected.
12. Low temperature contact resistance measurements indicate that carrier conduction at the contacts have characteristics of both tunneling and thermionic emission.
13. The barrier height increases for samples with increased Ni layer thickness and decreased Ge content in the alloy.

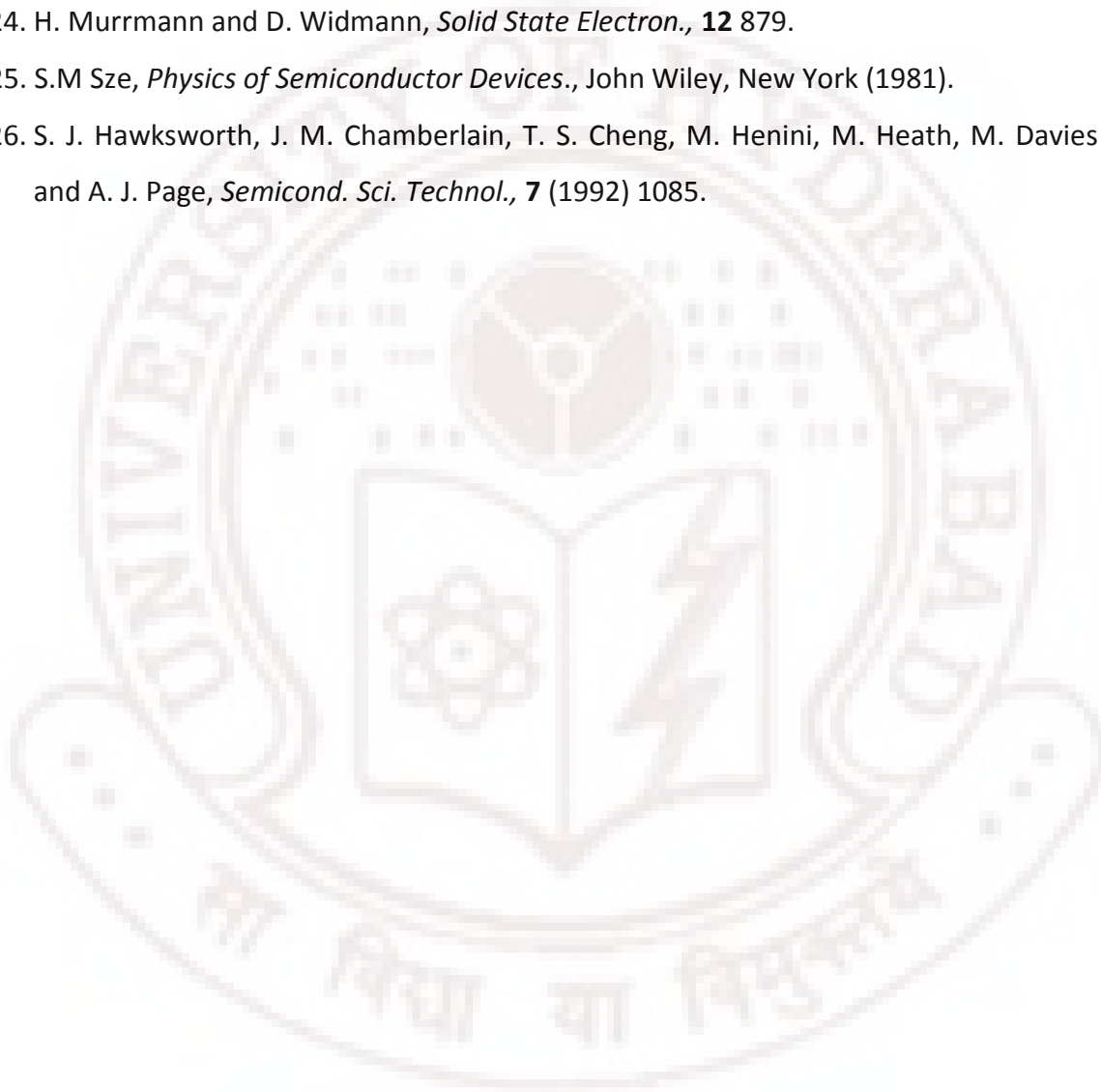


## References

1. N. Braslau, J. B. Gunn and J. L. Staples, *Solid State Electron.*, **10** (1967) 381.
2. N. Braslau, *J. Vac. Sci. Technol.*, **19** (1981) 803.
3. J. B. Gunn, *Trans. IEEE Electron Devices.*, **ED-23** (1976) 705.
4. A. Ketterson, F. Ponce, T. Henderson, J. Klem and H. Morkoc, *J. Appl. Phys.*, **57** (1985) 2305.
5. Herb. Goronkin, Saied Tehrani, Tom Rimmel, Peter L. Feies and Karl. J. Johnson, *IEEE Trans. Electron Devices.*, **36** (1989) 281.
6. R. P. Taylor, P.T. Coleridge, M. Davies, Y. Feng, J. P. McCaffrey and P. A. Marshall, *J. Appl. Phys.*, **76** (1994) 7966.
7. M. Kamada, T. Suzuki, F. Nakamura, Y. Mori and M. Arai, *Appl. Phys. Lett.*, **49** (1986) 1263.
8. G. Sai Saravanan, K. Mahadeva Bhat, K. Muraleedharan, H. P. Vyas, R. Muralidharan and A. P. Pathak, *Semicond. Sci. Technol.*, **23** (2008) 025019.
9. A. K. Rai, A. Ezis, R. J. Graham, R. Sharma and D. W. Langer, *J. Appl. Phys.*, **63** (1988) 4723.
10. T.S. Abhilash, Ch. Ravi Kumar and G. Rajaram, *J. Phys. D: Appl. Phys.*, **42** (2009) 125104.
11. G.Y. Robinson, *Solid State Electron.*, **18** (1975) 33.
12. Soo-Jin Chua and Seng Hin Lee, *Jpn. J. Appl. Phys.*, **33** (1994) 66.
13. A. Iliadis and K.E Singer, *Solid-State Electron.*, **26** (1983) 7.
14. Taeli Kim and D. D.L Chung, *J. Vac. Sci. technol.*, **B 4** (1986) 762.
15. M. Murakami, K.D. Childs, John. M. Baker, A. Callegari, *J. Vac. Sci. Technol.*, **B- 4**, (1986) 903.
16. T. C. Shen, G.B. Gao and H. Morkoc, *J. Vac. Sci. Technol.*, **B 10** (1992) 2113.
17. M. Murakami, *Science and Technology of Advanced Materials.*, **3** (2002) 1.
18. T.S. Kuan, P.E. Batson, T.N. Jakson, H. Rupprecht and E. L. Wilkie, *J. Appl. Phys.*, **54** (1983) 6952.
19. A.G. Baca, F. Ren, J. C. Zolper, R. D. Briggs and S. J. Pearton, *Thin Solid Films.*, **308** (1997) 599.



20. A. Sandhu, A. Okamoto, I. Shibasaki and A. Oral, *Microelectronic Engineering.*, **73-74** (2004) 524.
21. K. Mandal and D. L. Atherton, *J. Phys. D: Appl. Phys.*, **31** (1998) 3211.
22. Y. Yamaguchi, G. Rajaram, N. Shirakawa, A. Mumtaz, H. Obara, T. Nakagawa and H. Bando, *Physical Review.*, **B 63** (2000) 014504.
23. H.H. Berger, *Solid State Electron.*, **15** (1972) 145.
24. H. Murrmann and D. Widmann, *Solid State Electron.*, **12** 879.
25. S.M Sze, *Physics of Semiconductor Devices.*, John Wiley, New York (1981).
26. S. J. Hawksorth, J. M. Chamberlain, T. S. Cheng, M. Henini, M. Heath, M. Davies and A. J. Page, *Semicond. Sci. Technol.*, **7** (1992) 1085.



## Chapter-5

# Ohmic Contact Formation: New Insights from Magnetization Measurements

### 5.1 Introduction

The magnetization hysteresis loops of AuGe/Ni/Au Ohmic contact metallization which are magnetic in the as-deposited state become completely non-magnetic on annealing at or above a temperature which increases from 250°C to 430°C, with increasing Ni-layer thickness or decreasing Ge content from the eutectic AuGe alloy composition (chapter 3 & 4). Partial conversion of the Ni layer to a non-magnetic phase is evident even at the lower anneal temperature, as low as 100°C (figure 3.3.9). These are temperatures well below those at which alloying with the substrate occurs. This study of the magnetism of annealed film structure, together with the contact resistance, surface roughness measurements and metallization melting, gave some interesting insight into the sequence in which the processes involving Ge diffusion and compound formation occur including changes in the metallization structures at temperatures well below the alloying temperature. Ni has generally been described as 'adhesion' or 'barrier layer' [1, 2]. The Ni layer used is not in direct contact with the substrate in the current structure.

Several studies have shown that, apart from the diffusion of various elemental components into GaAs, significant changes occur in the metal film structure itself that could potentially influence electrical contact formation. TEM data reported in the literature [1-7] provide indications regarding Ni compound formation after Ni containing contact structures are annealed and cooled down to room temperature. It is reported that Ni<sub>3</sub>Ge is formed, on cooling down to room temperature (RT) after anneals at temperature of ( $T_A \sim 400^\circ\text{C}$ ), while Ni<sub>2</sub>GeAs is detected after cooling down to RT from anneals at higher temperatures ( $T_A > 400^\circ\text{C}$ ). The presence of Ni<sub>2</sub>GeAs has been correlated with low contact resistance formation.

In-situ X-ray diffraction studies [8] reveal the formation of Au-Ga compounds on annealing with Au or AuGe layers deposited on GaAs. When separate Au and Ge layers,

rather than AuGe alloy films, are used, as in studies of Au/Ge/Ni deposited on SiO<sub>2</sub> and GaAs substrates, Nickel reacts with Germanium to form Ni-Ge (320°C) and Ni<sub>2</sub>Ge (450°C), before and after alloying, with Ni regarded as the 'fast diffusing species' [9, 10].

In this chapter the changes in the metallization prior to alloyed contact formation are discussed in the context of magnetization and DSC results. Grazing Incidence XRD (GIXRD) and cross-sectional SEM measurements are also carried out in an attempt to analyze the compound formation when the magnetic to non-magnetic transformation takes place. X-ray photoemission spectroscopy (XPS) is also attempted to examine the composition of the alloyed Ohmic contact surface. Scratch test is used to study the adhesion properties of the Ohmic contact metallization to the GaAs substrate. The current distributions over the alloyed pads are imaged using a conducting probe-Atomic Force Microscopy (C-AFM) to study the integrity of the layers after contact formation.

## 5.2 Changes in the metallization structure prior to alloying

The magnetic measurements, apart from confirming that the contacts prepared by the conventional recipe are indeed non-magnetic, provide additional insights into changes taking place in the metallization structure before alloying occurs. The first surprising

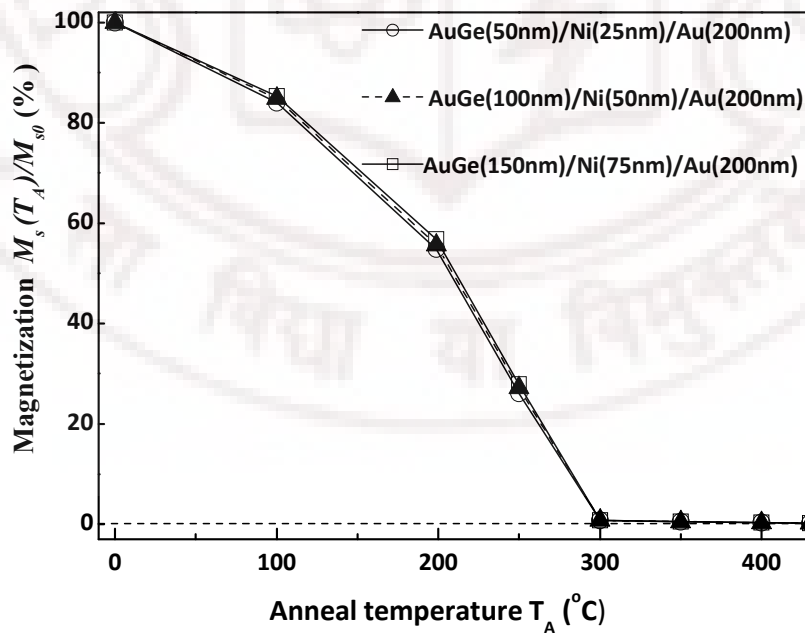


**Figure 5.2.1** Anneal temperature dependence of the fractional decrease in saturation magnetization

result is provided by the magnetization measurements on samples with the same ratio for Ni/AuGe layer thickness. The measurements on samples with structures AuGe (150nm)/Ni (75nm)/Au (200nm), AuGe (100nm)/Ni (50nm)/Au (200 nm) and AuGe(50nm)/Ni(25nm)/Au(200nm), show identical fractional decreases in magnetization (figure 5.2.1) for the eutectic AuGe composition.

These results shows that the *amount of Ni transformed to non-magnetic phase on annealing scales with AuGe layer thickness*, implying that the transformation (of Ni to non- magnetic phase) is not restricted to the interface between Ni and AuGe layers. The entire AuGe layer, and not just the interface, participates in this conversion of Ni layer to a non-magnetic phase, even when this conversion is partial after low temperature anneals. The data also imply that an effective ‘concentration’ of Ni in AuGe does not depend on the initial Ni layer thickness, but only depends on anneal temperature.

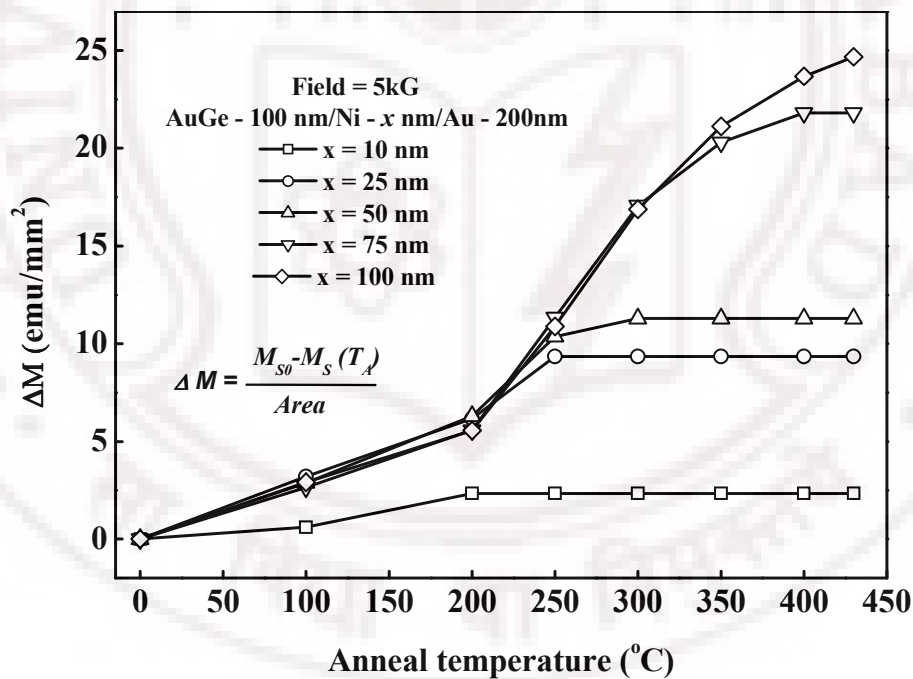


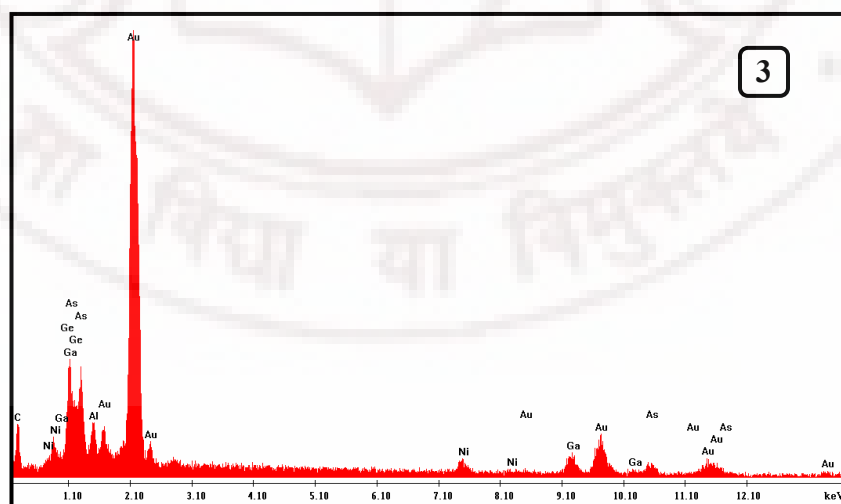
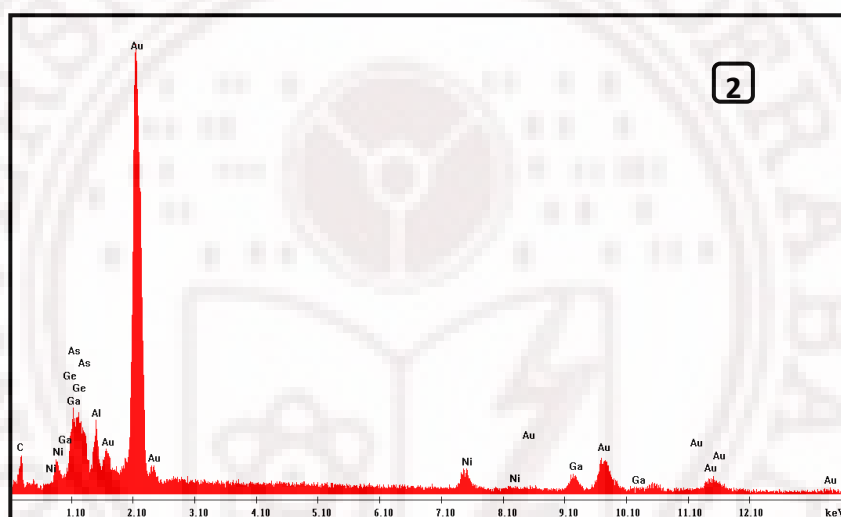
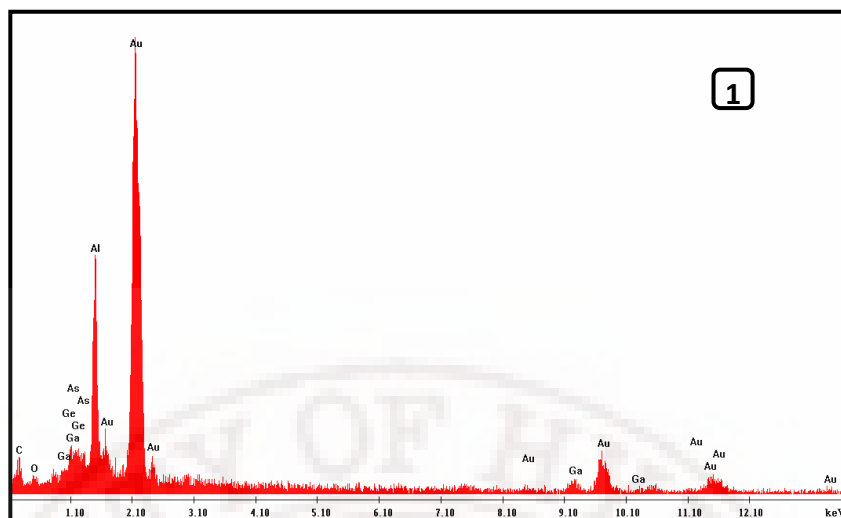
**Figure 5.2.2** Decrease in magnetization per unit area as function of anneal temperature

This is further clarified in figure 5.2.2; where the decrease in magnetization, a quantity proportional to the thickness of the Ni layer transformed to non-magnetic phase, is plotted as a function of anneal temperature. The data has errors arising from determination of sample dimensions. Yet, most of the data independent of initial Ni

layer thickness fall on the same curve for a fixed AuGe layer thickness, and peel off from the curve to a constant value when the entire Ni layer has been transformed. The sample with a 10nm Ni layer thickness is an exception: it is possible that the film's conformal surface coverage may have been affected at this thickness.

Next, this phenomenon of Ni dissolution into AuGe appears to occur in the solid state as shown in the cross sectional SEM (C-SEM) image of figure 5.2.3. The C-SEM image of a GaAs/AlGaAs sample with AuGe/Ni (25nm)/Au deposited and annealed at a temperature of 300°C is shown in figure 5.2.3. Two distinct layers (A and B) are seen at room temperature after anneals at 300°C, the temperature at which the Ni layer transformation to non magnetic phase is complete. The EDAX analysis on four locations on the sample annealed at 300°C, are also given in figure 5.2.3. The spatial resolution in EDAX is about 1 $\mu$ m while the layer thickness has been 0.3 $\mu$ m or less. The top layer (location 1) is Au and higher concentration of Ge and Ni are detected in locations 2 and 3. The presence of Al in portion 1 is from the sample holder since the characteristics X-rays are detected from plume of the order of 1 $\mu$ m. Location 4 is on the GaAs/AlGaAs substrate.





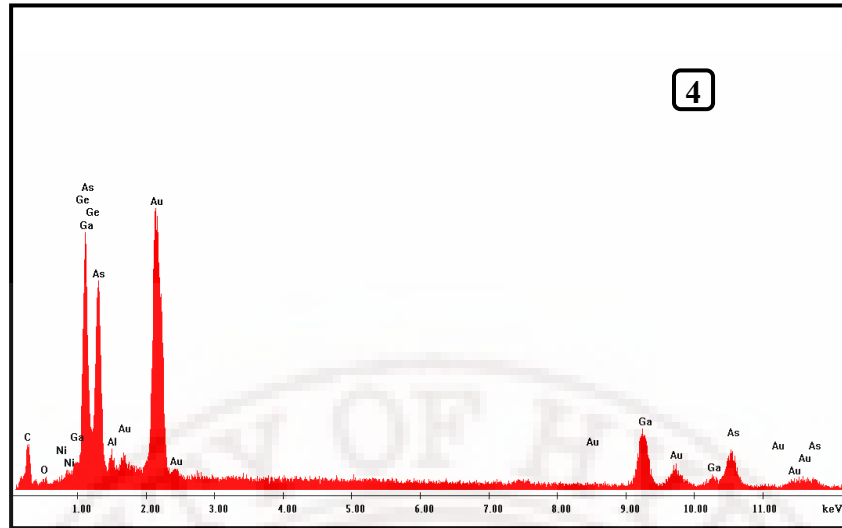


**Figure 5.2.3** Cross sectional SEM and EDAX analysis of AuGe/Ni/Au in a sample annealed at 300°C.

*Is the conversion of Ni to the non-magnetic phase is a simple diffusion into AuGe layer or a dissolution into AuGe with possible compound formation?* To investigate this aspect, magnetization measurements are carried out as a function of anneal durations, on a sample AuGe /Ni (25nm)/Au (magnetic to non-magnetic transformation at 250°C) where the conversion of Ni to non-magnetic phase is partial (200°C) for 60s durations (figure 5.2.4).

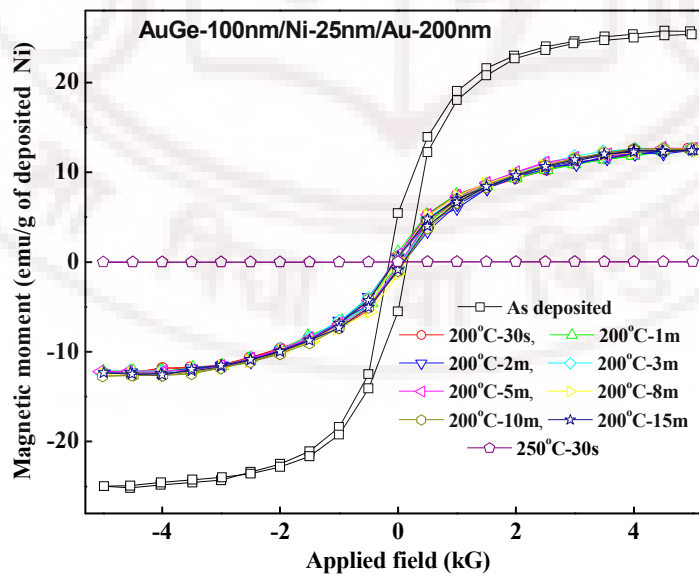


**Figure 5.2.4** Magnetization hysteresis loops for AuGe (88:12)/Ni (25nm)/Au for different anneal durations.



The transformed Ni fraction is independent of time (for time scales  $\sim 15$  minutes) (figure 5.2.5). It depends only on anneal temperature at typically used anneal durations. Therefore, *the transformation involves solid state dissolution of Ni into AuGe, rather than diffusion at these time scales*. Further, the transformation being partial and constant with time imply that further dissolution is limited by solubility of Ni in the AuGe layer. The extent of transformed Ni is a representation of the solubility of Ni in the AuGe.

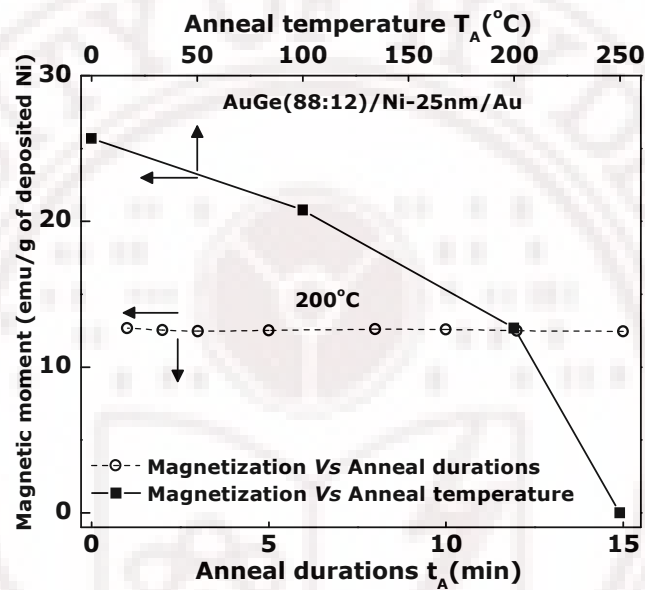


**Figure 5.2.5** Time dependence of saturation magnetization for a sample with 25nm Ni and 100nm AuGe layers annealed at 200°C.

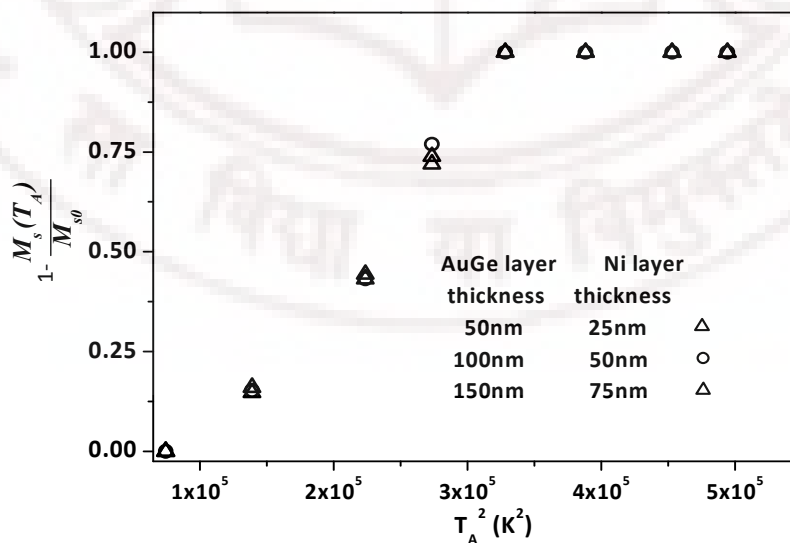


**Figure 5.2.6** The transformed Ni fraction Vs  $T_A^2$  for three AuGe thicknesses with Ni: AuGe thickness ratio at 0.5.

In the partially converted state the decrease in magnetization with increasing anneal temperature is a representation of solubility of Ni in the AuGe. This solubility varies nearly quadratically with temperature as evident from figure 5.2.6.

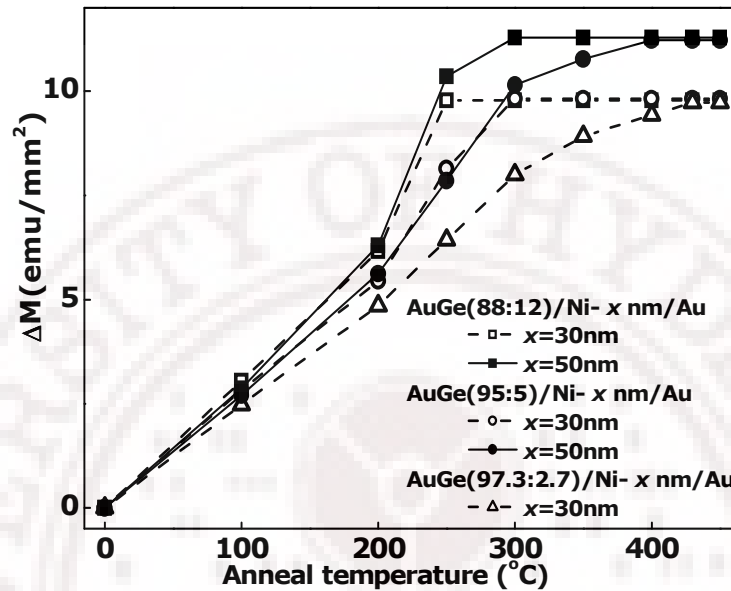


**Figure 5.2.7** Decrease in magnetization per unit area of transformed Ni layer thickness as function of anneal temperature, for three alloy compositions with two Ni layer thicknesses.

Figure 5.2.7 displays the decrease in magnetization per unit sample area for different AuGe compositions (AuGe- 88:12, 95:5, 97.3:2.7 wt %), and for two different Ni layer thicknesses, after anneals at different temperatures. The data indicate that the solubility of Ni in AuGe decreases when the Ge content in the AuGe alloy is reduced from that of the eutectic composition (88:12wt %).

Thus, the Ni-layer appears to dissolve into the AuGe layer to an extent limited by the quadratic temperature dependent solubility of Ni in AuGe, at temperatures well below that at which alloying with GaAs occurs. The dissolution of Ni in AuGe appears to occur between 100~300°C in the solid phase, in the sample with the optimized contact resistance.

This solid state solubility limited dissolution of Ni into AuGe layer is possibly followed by segregation and formation of non-magnetic Ni-Ge compounds on cooling.

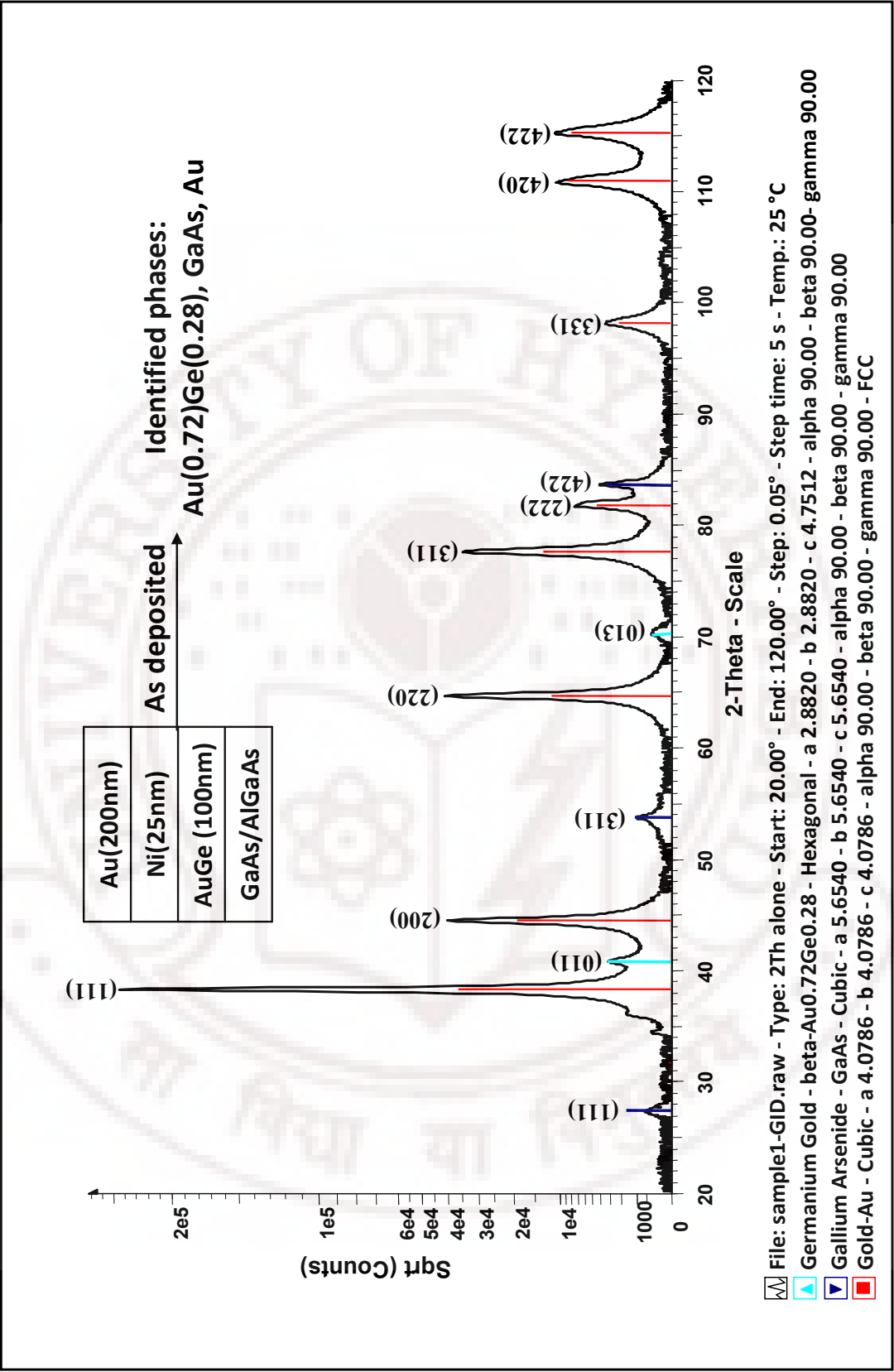


Table 5.2.8 GIXRD measurements on GaAs/AlGaAs substrate with AuGe/Ni/Au metallization layers as deposited and un-annealed.

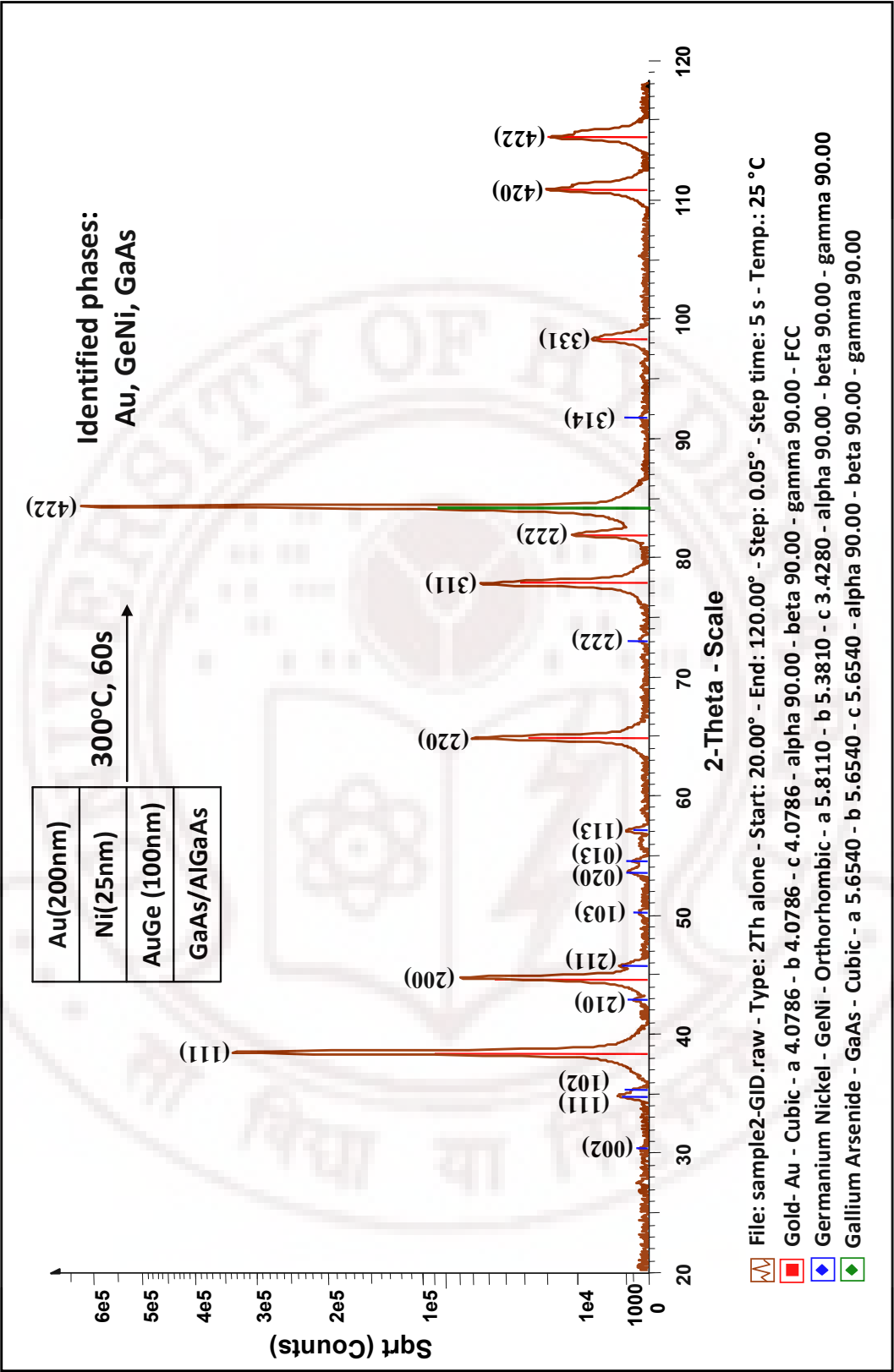


Table 5.2.9 GIXRD measurements on GaAs/AlGaAs substrate with AuGe/Ni/Au metallization layers deposited and annealed at 300°C.

I.No	Peak Position (2θ)	Intensity	Normalized Intensity (%)	$d=\lambda/2\sin\theta$ (Å) $\lambda = 1.5406$	phase	(hkl)	d -literature (Å)
1	27.2	600	0.30	3.2708	GaAs(Cubic)	(111)	3.2640
2	38.2	207612	100	2.3542	Au (Cubic)	(111)	2.3547
3	40.8	2300	1.10	2.2103	Gold Germanium at.%(Au72Ge28), wt.%(Au88Ge12) (Hexagonal)	(011)	2.2082
4	44.4	37123	17.9	2.0405	Au (Cubic)	(200)	2.0393
5	53.8	720	0.35	1.7026	GaAs(Cubic)	(311)	1.7046
6	64.55	38000	18.3	1.4425	Au (Cubic)	(220)	1.4420
7	70.35	340	0.16	1.3373	Gold Germanium at.%(Au72Ge28), wt.%(Au88Ge12) (Hexagonal)	(013)	1.3390
8	77.6	34024	16.4	1.2293	Au (Cubic)	(311)	1.2297
9	81.75	7368	3.5	1.1771	Au (Cubic)	(222)	1.1773
10	83.7	6500	3.15	1.1545	GaAs(Cubic)	(422)	1.1540
11	98.2	5700	2.75	1.0191	Au (Cubic)	(331)	1.0196
12	110.75	10475	5.05	0.9305	Au (Cubic)	(420)	0.9357
13	115.2	10600	5.1	0.9123	Au (Cubic)	(422)	0.9120

Table 5.2.8.a. Peak analysis/phase identification from GIXRD on GaAs/AlGaAs substrate with AuGe/Ni/Au metallization layers as deposited and un-annealed.

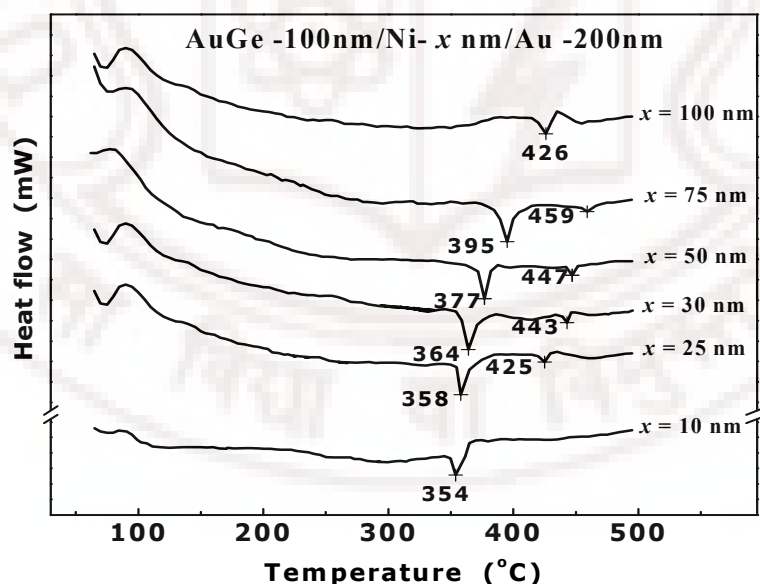
Sl.No	Peak Position (2θ)	Intensity	Normalized Intensity (%)	$d=\lambda/2\sin\theta$ (Å) $\lambda = 1.5406$	phase	(hkl)	d literature (Å)
1	30.8	200	0.04	2.9013	NiGe (Orthorhombic)	(002)	2.9055
2	34.5	1800	0.30	2.5949	NiGe (Orthorhombic)	(111)	2.5884
3	35	1400	0.25	2.5616	NiGe (Orthorhombic)	(102)	2.5566
4	38.2	339821	57.50	2.3542	Au (Cubic)	(111)	2.3547
5	42.6	300	0.05	2.1208	NiGe (Orthorhombic)	(210)	2.1164
6	44.4	66893	11.30	2.0405	Au (Cubic)	(200)	2.0393
7	45.6	1700	0.30	1.9904	NiGe (Orthorhombic)	(211)	1.9886
8	50	200	0.05	1.8227	NiGe (Orthorhombic)	(103)	1.8225
9	53.5	700	0.10	1.7117	NiGe (Orthorhombic)	(020)	1.7140
10	54.45	530	0.09	1.6840	NiGe (Orthorhombic)	(013)	1.6864
11	57.1	940	0.16	1.6174	NiGe (Orthorhombic)	(113)	1.6092
12	64.55	56894	9.6	1.4425	Au (Cubic)	(220)	1.4420
13	73.1	180	0.03	1.2935	NiGe (Orthorhombic)	(222)	1.2942
14	77.6	52785	8.9	1.2293	Au (Cubic)	(311)	1.2297
15	81.75	9967	1.7	1.1771	Au (Cubic)	(222)	1.1773
16	83.9	591000	100	1.1524	GaAs(Cubic)	(422)	1.1540
17	91.7	240	0.04	1.0735	NiGe (Orthorhombic)	(314)	1.0722
18	98.2	6000	1.0	1.0191	Au (Cubic)	(331)	1.0196
19	110.75	18425	3.10	0.9305	Au (Cubic)	(420)	0.9357
20	115.2	17400	2.95	0.9123	Au (Cubic)	(422)	0.9120

Table 5.2.9.a. Peak analysis/phase identification from GIXRD on GaAs/AlGaAs substrate with AuGe/Ni/Au metallization layers deposited and annealed at 300°C.

Since the solubility of Ni increases nearly quadratically *with* the temperature, precipitation of Ni, possibly as compounds with Au, Ge etc. must occur on cooling. Grazing Incidence XRD measurements are carried out on samples with structures AuGe/Ni (25nm)/Au annealed at 300°C, a temperature at which complete conversion of Ni into non-magnetic phase has taken place, but no alloying with the substrate has occurred. This GIXRD data on a sample annealed at 300°C and cooled down to room temperature, shown in figure 5.2.9 indicates the presence of NiGe apart from Au.

Peaks corresponding to AuGe (0.7:0.3) (close to as deposited composition of 72:28 at% or 88:12 wt%) is clearly seen in the as deposited sample (figure 5.2.8), which is absent in the sample annealed at 300°C and cooled down to room temperature (figure 5.2.9).

As mentioned earlier compounds such as Ni<sub>3</sub>Ge and Ni<sub>2</sub>GeAs have been reported to be present in the sample which has been annealed close to the alloying temperature [3-8]. The nature of the Ni dissolution into AuGe, for example whether intermediate compounds are formed, needs investigation. As the AuGe layer is at high temperatures (but below alloying temperatures), a random ternary alloy of Au-Ge-Ni or NiGe compounds present even at these temperatures.



**Figure 5.2.10** DSC scans for samples with eutectic AuGe alloy with different Ni layer thicknesses.

In fact, endothermic peaks are detected in the metallization structure in Differential Scanning Calorimetry (DSC) scans (figure 5.2.10). The melting temperature of the metallization structure systematically increases with initial Ni layer thickness (hence, increased Ni concentration in AuGe before melting).

The increase of roughness that has been observed for anneals close to the temperatures of the peak positions (figure 5.2.11) suggests that the endothermic peaks correspond to melting in the metallization structure. An explanation is that the melting temperature of the ternary Au-Ge-Ni layer is increased with the increase of Ni concentration in this layer. An alternative possibility is that the peaks signify compound formation- e.g. Ni-Ge. For example, in Pd/Ge (figure 6.2.5), as discussed in chapter 6, intermediate peaks are observed in DSC data and correlated with solid state reactions and multiple compound formations [11]. However the fact that only a single significant peak is observed in the case of AuGe/Ni/Au structures as well as the increase of roughness at these temperatures, warrant an alternate explanation. It is likely that the layer that exists at the peak temperature is a solid solution of Ni in AuGe in which melting occurs at progressively increasing temperatures as the Ni concentration increases.

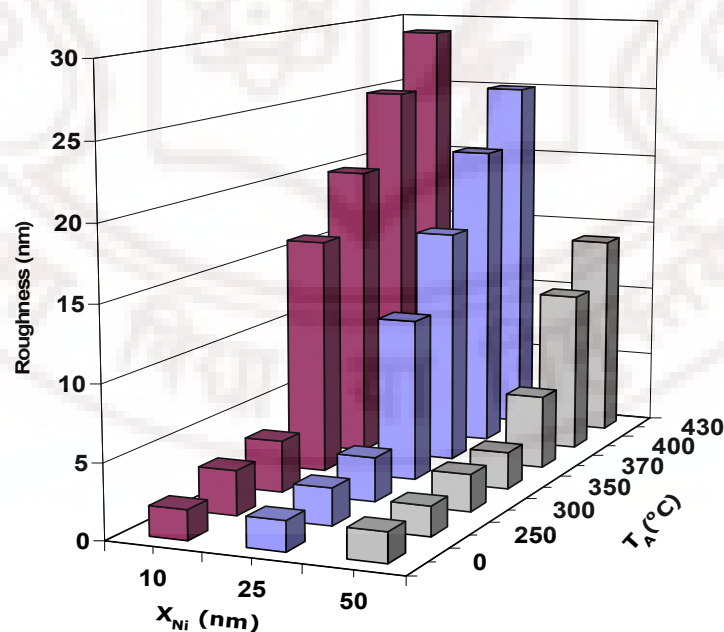


**Figure 5.2.11** Surface roughness of AuGe/Ni/Au contacts with different Ni layer thickness ( $x_{Ni}$ ) as a function of anneal temperature. ( $T_A$ ).



In-situ x-ray diffraction studies also confirm that around these temperatures, signatures of melting such as disappearance of peaks occur and that increase of Ni in the structure significantly increases this melting temperature.

The reductions of surface roughness that are obtained by increasing Ni layer thickness could have a possible origin in the above results. In-situ x-ray diffraction studies [8] reveal the formation of Au-Ga compounds on annealing wafers with Au or AuGe layers deposited on GaAs. The Au-Ga compounds formation is reported to begin at temperatures  $>500^{\circ}\text{C}$  for Au layers on GaAs. In the case of Au-Ge alloy layers deposited on GaAs, the Au-Ga compounds formation appears to form when the Au-Ge alloy layer melts at lower temperatures (table 5.2.1).

**Table 5.2.1** In-situ X-ray diffraction studies of Au and AuGe deposited on GaAs [8].

Metallization Layers	Temperature ( $^{\circ}\text{C}$ )			
	Heating (1 <sup>st</sup> ) Au peaks disappears	Cooling (1 <sup>st</sup> ) Au-Ga peak re-appears	Heating (2 <sup>nd</sup> ) Au-Ga peak disappears	Cooling (2 <sup>nd</sup> ) Au-Ga peak re-appears
GaAs/Au	500-525	400-390	385-410	410-390
GaAs/Au (12wt%Ge)	350-375	350	350-375	375-350
GaAs/Au (12wt %) Ge/Ni (4wt %)	375-400	375-342	350-375	375-350
GaAs/ Au (10wt %) Ge/Ni (17wt %)	400-426	426-402	402-424	424-399

The Au-Ga compounds have low melting temperatures ( $\sim 360^{\circ}\text{C}$ ) [2, 3, 8]. Their formation has been interpreted to be the cause for deterioration of the surface morphology of the contacts.

Ni influence melting temperature and when the alloying takes place, AuGa phase forms in the metallization structure. Ni dissolution into Au-Ge on annealing, as suggested by this study, presumably increases both the melting temperature of Au-Ge layer and that of the Au-Ga compounds after their formation. Because AuGa has low melting temperature, surface roughening affects further alloying through modification of effective surface area. Another contributing factor could be the influence of concentration of Ni in AuGe on nucleation and grain growth of the Ni-Ge phases. A larger Ni-layer thickness could result in higher density of nucleation centers, and consequently, a small grain size, of Ni-Ge.

The decrease of roughness and increase of contact resistance on adding Ni layer could be explained as following: As the structure melts, the film roughens. However the roughness is reduced either due to (i) increased viscosity of the molten film as the 'melting' temperature increases with Ni concentration in the AuGe or (ii) improved adhesion with the substrate prior to alloying or both.

A qualitative evaluation of adhesion of the metallization structure to the substrate or scratch resistance of the upper layers is performed by scratch test in a Nanoindenter. The results of samples annealed at different temperatures are shown below. The figures are optical micrographs of scratch tracks as the force increased from 0 to 500 $\mu$ N from the left to right (figure 5.2.12).

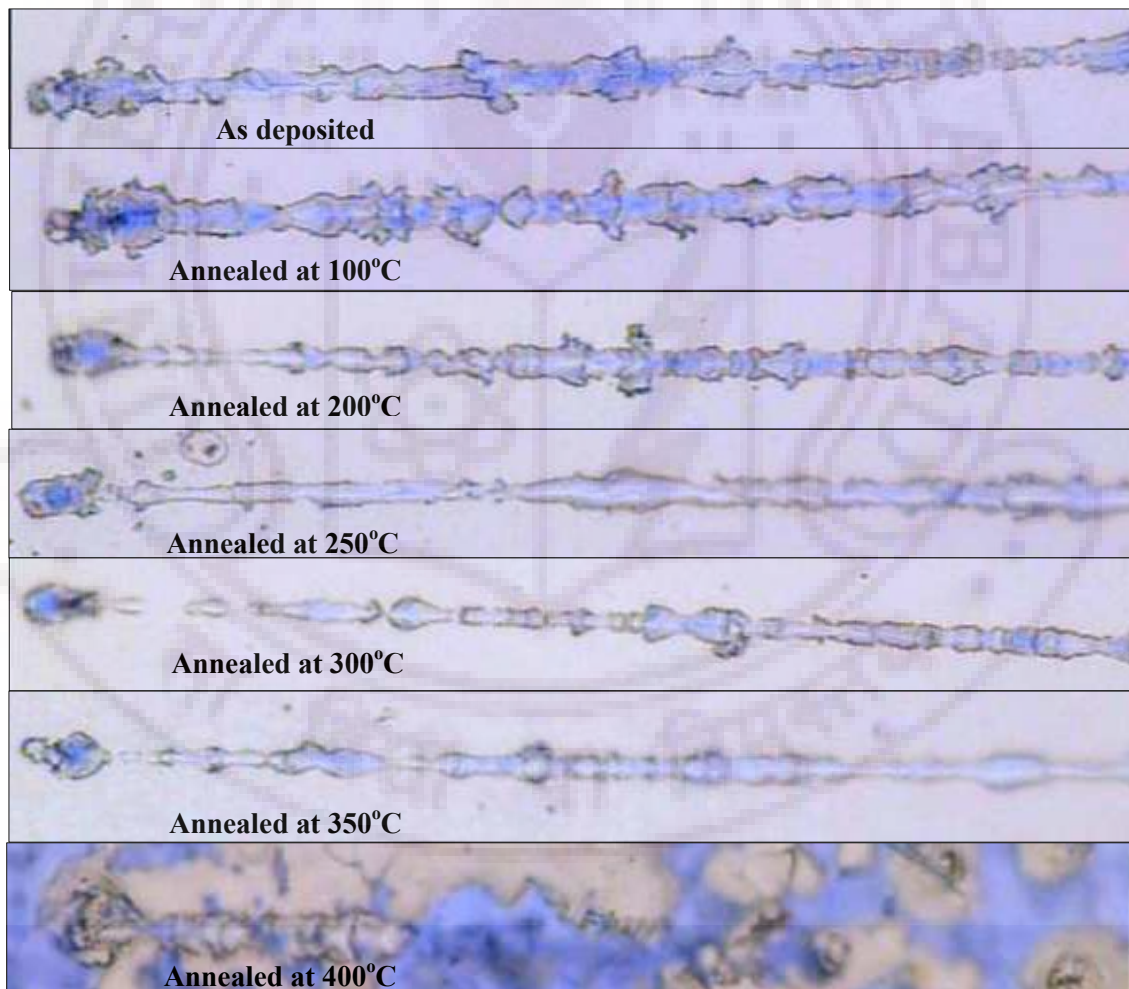


**Figure 5.2.12** Scratch tracks in AuGe-100nm/Ni-25nm/Au-200nm deposited on GaAs/AlGaAs substrate and as a function of anneal temperature.

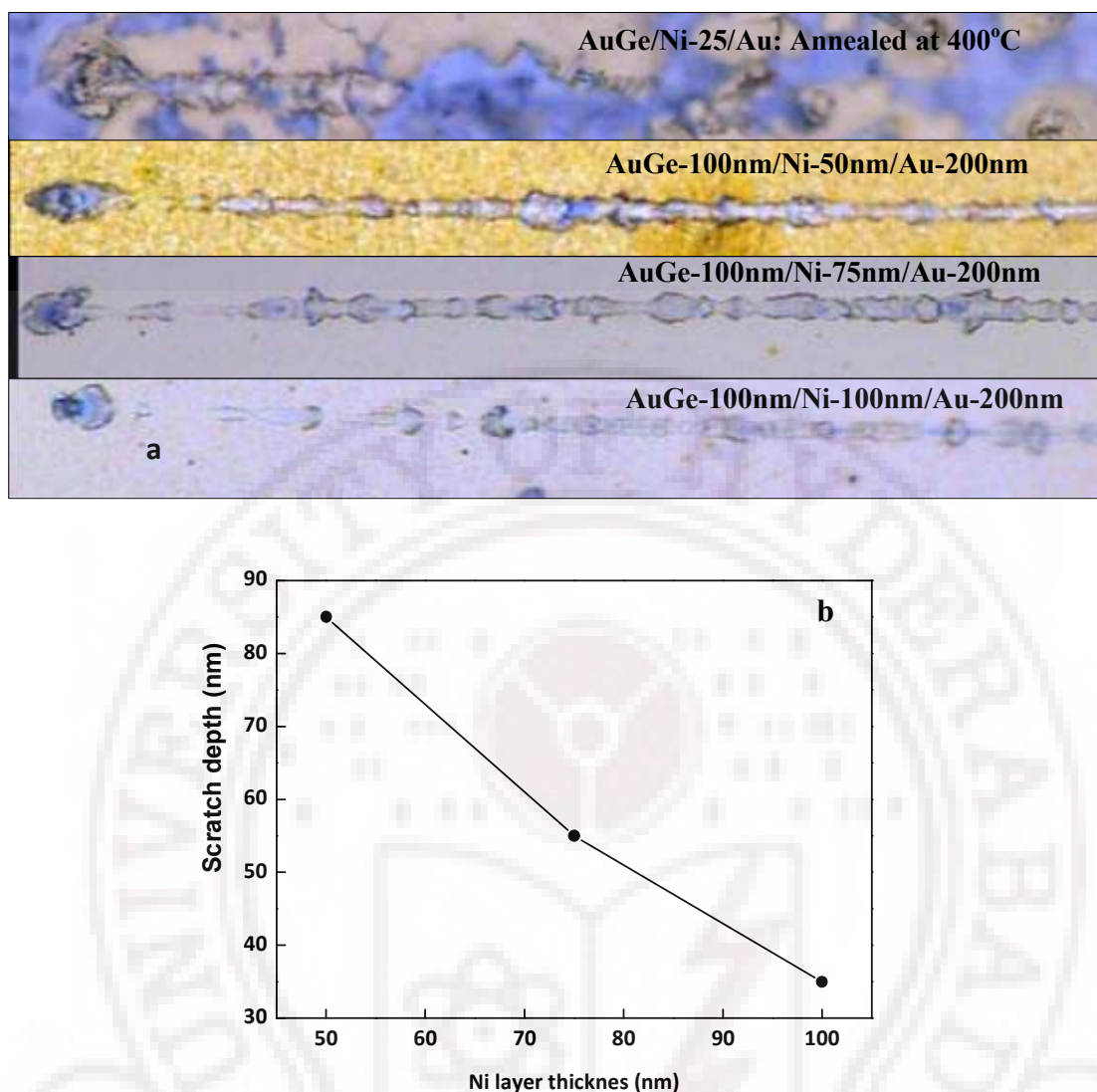


**Figure 5.2.13** (a) Scratch tracks in AuGe-100nm/Ni- $x$  nm ( $x=25, 50, 75, 100$ nm)/Au-200nm deposited on GaAs/AlGaAs substrate and annealed at 400°C (b) Scratch depth Vs Ni layer

The figures (5.2.12 and 5.2.13) allows us to qualitatively conclude that the film scratch resistance or adhesion in the sample improve as the anneal temperature is increased. The hardness of the film increases as Ni content in the AuGe increases due to (i) increase in anneal temperature or (ii) increase of Ni layer thickness and anneals till complete dissolution of Ni in AuGe. This is also apparent in figure 5.2.13b which shows measured scratch depth as a function of initial Ni layer thickness.

Increase of melting temperature appears to be the key factor for reducing roughness. DSC scans obtained for three AuGe alloy compositions (88:12, 95:5, 97.3:2.7 wt %) with a fixed (30nm) Ni layer thickness show that melting in the metallization

structure occurs at higher temperatures when Ge content is reduced (figure 5.2.14). These results are consistent with in-situ XRD results [8] of Au-Ge alloy layers deposited on GaAs, which also demonstrate increase of melting temperatures when thinner Ge-layers are used in Au/Ge/Ni type metallization structures. Hence improvement in the surface morphology with decreasing Ge content in the AuGe alloy.

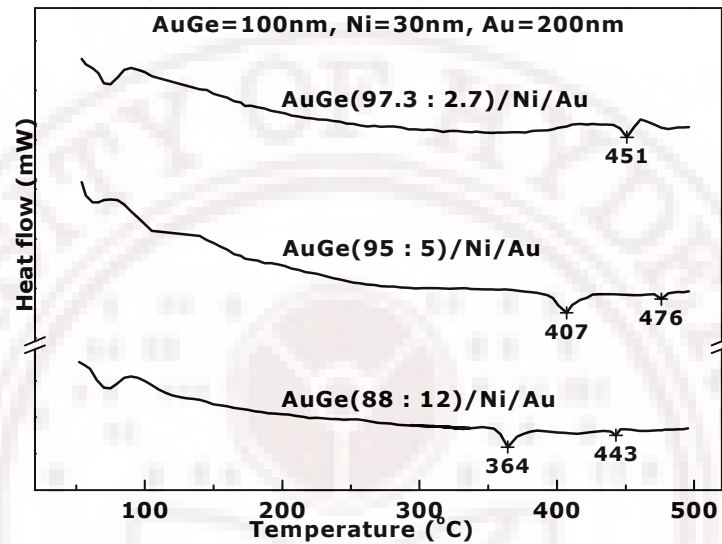


**Figure 5.2.14** Metallization melting temperature Vs Ni layer thickness

Qualitatively, alloying could be understood as a process by which (i) there is a substantial diffusion of Ga into the AuGe (Ni) layer (ii) diffusion of Ge into Ga sites of the substrate. The increase of the melting temperature in the structure could possibly decrease the extent of Ga diffusion resulting in an increased contact resistance. The contact formation at the alloying temperature is a balance between increased contact area due to the process of Ni in AuGe (with consequent improvement of adhesion) and decrease of Ga diffusion into the AuGe (Ni) layer. Hence, the optimum contacts are formed at highest Ni concentration at which melting temperature has not yet begun to show the upward trend (Figure 5.2.15). Low melting temperature and good adhesion are necessary for contact formation. A high melting temperature and good adhesion are necessary for decreasing surface roughness.

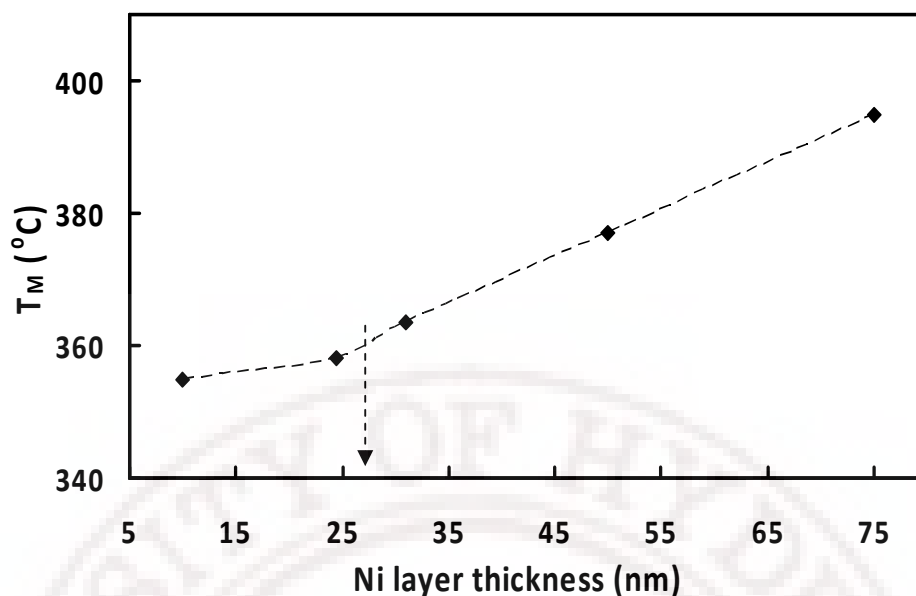


**Figure 5.2.15** Melting temperature Vs Ni layer thickness

Other possible contributions to increasing contact resistance are

1. Differences between contact resistance under the Ni-Ge phase and the AuGe (Ni) phases combined with a Ni-Ge fraction that increases with initial Ni layer thickness.
2. Differences in epitaxial/polycrystalline Ge layer growth on GaAs when the surface is covered with Ni-rich and Ni-poor phases.

In order to examine the above, we have carried out Grazing incidence XRD (GIXRD) on a sample with 25nm Ni layer thickness and annealed at 400°C which showed the lowest contact resistance. The GIXRD is taken at room temperature and the data is given in figure 5.2.16. Peak identification and phase analysis is given in table 5.2.16a. The phases detected are Au, NiGe, GeAs, NiAs, Ni<sub>3</sub>Ge and AuGa etc.

Prior to discussing above results, it may be relevant to examine GIXRD performed on samples annealed at lower temperatures before alloying takes place. Formation of NiGe is observed in GIXRD (figure 5.2.9, table 5.2.9a), on cooling to room temperature after annealing at a temperature at which the structure is rendered non-magnetic. This result is consistent with literature data which show the NiGe is paramagnetic at 300K [12]. It must be emphasized however that at high temperatures, what is present is a saturated solution of Ni in AuGe, formed by solid state dissolution. Formation of NiGe on

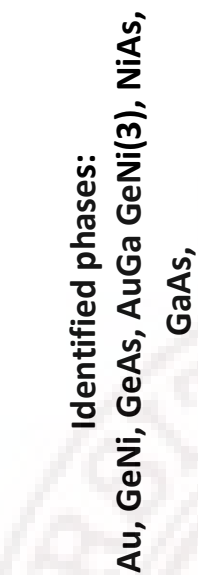


Table 5.2.16 GIXRD measurements on GaAs/AlGaAs substrate with AuGe/Ni/Au metallization layers deposited and annealed at 400°C for 60s.



Sl.No	Peak Position (2 $\theta$ )	Intensity	Normalized Intensity (%)	$d=\lambda/2\sin\theta$ ( $\text{\AA}$ ) $\lambda = 1.5406$	phase	(hkl)	d - literature ( $\text{\AA}$ )
1	34.10	3000	1.62	2.6272	Germanium Arsenide GeAs Tetragonal	(110)	2.6269
2	35.35	740	0.4	2.5363	Germanium Nickel - GeNi3 - Cubic	(110)	2.5222
3	36.85	690	0.38	2.4376	Gallium Gold Au0.79Ga0.21-Hexagonal	(211)	2.4300
4	38.2	185452	100	2.3542	Au (Cubic)	(111)	2.3547
5	41.1	3100	1.68	2.1945	Gallium Gold Au0.79Ga0.21-Hexagonal	(203)	2.1990
6	42.6	530	0.3	2.1208	NiGe (Orthorhombic)	(210)	2.1164
7	43.9	720	0.4	2.0612	Germanium Nickel - GeNi3 - Cubic	(111)	2.0594
8	44.4	34065	18.4	2.0405	Au (Cubic)	(200)	2.0393
9	45.6	600	0.35	1.9904	NiGe (Orthorhombic)	(211)	1.9886
10	46.5	2100	1.15	1.9516	Germanium Arsenide GeAs Tetragonal	(112)	1.9517
11	51.15	800	0.45	1.7843	Germanium Nickel - GeNi3 - Cubic	(200)	1.7835
12	53.8	9000	4.85	1.7026	GaAs(Cubic)	(311)	1.7046
13	54.45	1200	0.65	1.6840	NiGe (Orthorhombic)	(013)	1.6864
14	57.5	6600	3.55	1.5891	Germanium Arsenide GeAs - Tetragonal	(211)	1.5978
15	57.04	800	0.45	1.6135	Gallium Gold Au0.79Ga0.21-Hexagonal	(223)	1.6110
16	61.7	275	0.15	1.5024	Gallium Gold Au0.79Ga0.21-Hexagonal	(321)	1.5050
17	62.8	585	0.32	1.4785	Nickel-arsenide - NiAs - Hexagonal	(103)	1.4838
18	64.55	53226	28.70	1.4425	Au (Cubic)	(220)	1.4420
19	71.5	300	0.17	1.877	NiGe (Orthorhombic)	(401)	1.3105
20	76.25	600	0.32	1.2478	NiGe (Orthorhombic)	(123)	1.2485
21	77.6	42848	23.1	1.2293	Au (Cubic)	(311)	1.2297
22	79.75	884	0.48	1.2015	Gallium Gold Au0.79Ga0.21-Hexagonal	(510)	1.2020
23	81.75	11385	6.15	1.1771	Au (Cubic)	(222)	1.1773
24	83.7	400	0.22	1.1545	GaAs(Cubic)	(422)	1.1540
25	96.85	690	0.38	1.0298	Gallium Gold Au0.79Ga0.21-Hexagonal	(433)	1.0290
26	98.2	7795	4.20	1.0191	Au (Cubic)	(331)	1.0196
27	110.75	13235	7.14	0.9305	Au (Cubic)	(420)	0.9357
28	115.2	8938	4.82	0.9123	Au (Cubic)	(422)	0.9120

Table 5.2.16.a: Peak analysis/phase identification from GIXRD on GaAs/AlGaAs substrate with AuGe/Ni/Au metallization layers deposited and annealed at 400°C for 60s.



cooling indicates that Ni-Ge correlation may possibly be present in this saturated solution. The DSC and adhesion data indicate that the effect of this dissolution is an increase in melting temperature of the metallic structure and also an improvement in adhesion. Both these factors contribute to decreased roughness in the film morphology in the Ohmic contact anneals. The resulting increase in the effective area of the contact due to these factors is proposed to be the possible reason for dramatic improvements in contact resistance when a thin Ni layer is present in the structure. Nevertheless, it is also a fact that use of excessive Ni layer thicknesses deteriorates contact resistance. The reasons for this deterioration are indicated by the GIXRD results on samples annealed at temperature at which alloying take place. NiGe and NiAs phases that are formed on alloying could explain the increase of contact resistance with increase of Ni layer thickness as follows: i) Reduced availability of Ge for doping GaAs, ii) Possibility of out-diffusion of As leading to compensation within GaAs. The formation of NiAs could also explain the increase contact resistances with increase in anneal durations and temperature (figs. 3.3.1 and 3.3.6). An additional factor, namely formation of low-melting AuGa alloy as the alloying with the substrate proceeds ([2] and table 5.2.16a), could also lead to deterioration of surface morphology, and hence contact resistance, at larger values of the anneal temperatures and anneal durations, relative to the optimum values.

### 5.3 Conductive Atomic Force Microscopy (C-AFM) – Characterizing conductivity variations in AuGe/Ni/Au alloyed contacts

The current distributions over the alloyed pads are imaged using a conducting probe-Atomic Force Microscopy (C-AFM) in contact mode on the surface of samples with the lowest contact resistance.

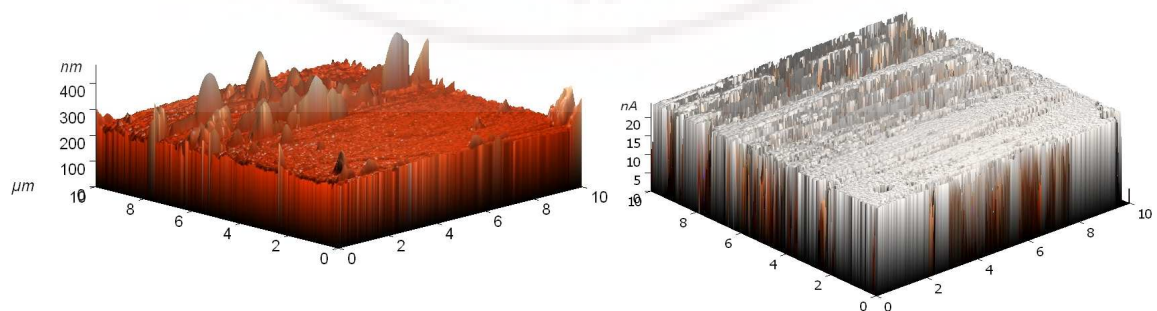


**Figure 5.3.1** Topography (a) and current image (b) of an AuGe/Ni (25nm)/Au as-deposited sample.

Conductive AFM measurements, which can simultaneously map the topography and current distribution of a sample, are performed on the pads of the samples with the TLM pattern used for contact resistance measurements. Typical bias voltage used is 8V. Some measurements of IV characteristics are performed on the relatively smooth unannealed samples and those with 100nm Ni layer thickness.

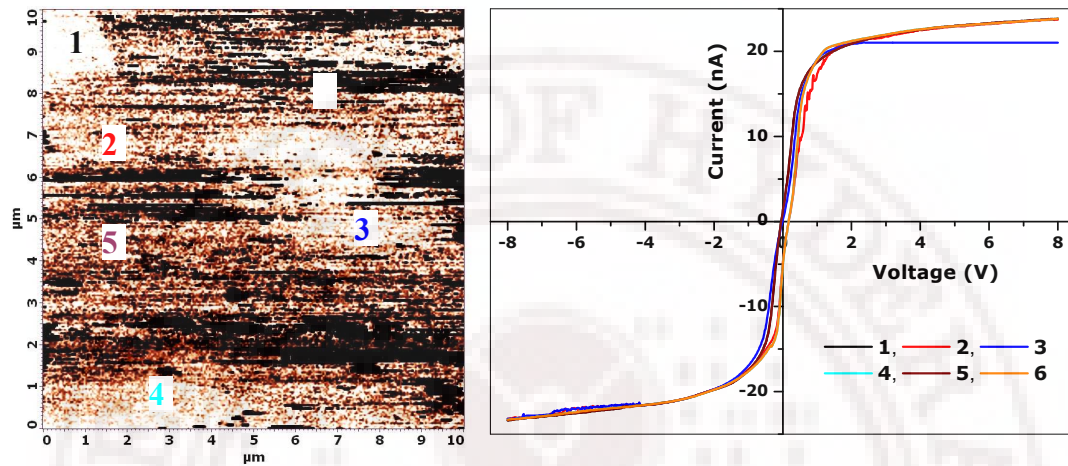


**Figure 5.3.2** Current image (b) of a of a AuGe/Ni (100nm)/Au sample at a bias of 8 volts, Corresponding IV curves (c) recorded at six specific positions from those indicated in 5.6b.

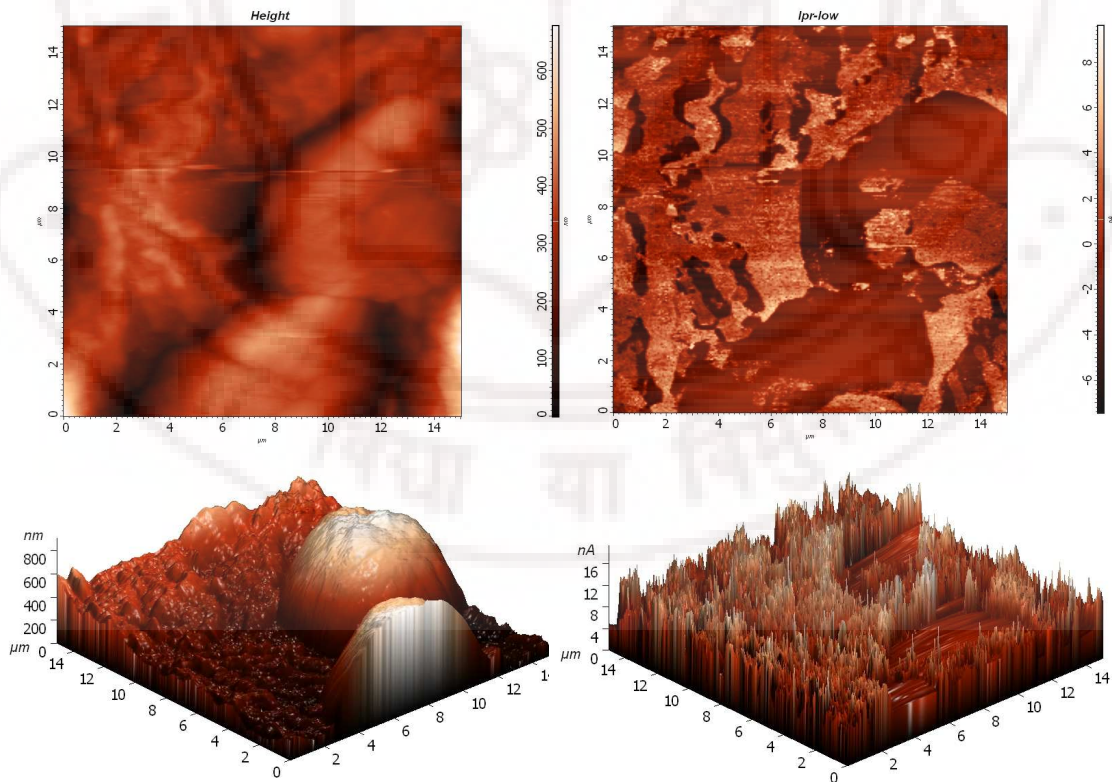


**Figure 5.3.3** (a) Surface topography, (b) Current mapping of AuGe/Ni (25nm)/Au which shows the least contact resistance.

The C-AFM measurements are performed on as-deposited samples for standardization. The sample has a 30nm thick metallization layer and is expected to give a continuous and uniform current distribution. The results of topography and current distribution scans are given in figure 5.3.1a & b. The current distribution is found to be almost uniform as expected. Figure 5.3.2 shows the current distribution and typical I-V curve at several locations for a sample with a 100nm thick Ni layer annealed at 400°C. The IV curves obtained in this sample during the TLM contact resistance measurements are non-linear with high resistance (figure 3.3.2). Voltages used in the data of fig 3.3.2 are 2V, whereas up to 8 volts are used during the C-AFM measurements.

It appears that the 'non-linear' data of figure 3.3.2 could be diode-like when performed in a higher voltage ranges (figure 5.3.2(b)). The data in figure 5.3.2(b) resembles back to back diodes, with a saturation current of 20nA for the AFM tip used. This picture also implies that contacts are not uniform but an agglomeration of smaller contact areas.

The topography and current images obtained for AuGe/Ni (25nm)/Au are shown in figure 5.3.3. The topographic and current images show a spatially non-uniform current distribution. The images in figure 5.3.3 indicate short distance current fluctuations as well as fluctuations correlated with micron-sized surface features. Clearly, the integrity of the Au over-layer is severely affected during the melting/alloying process. The identity of the large features which block the current is not clear.

## 5.4 X-ray photoemission spectroscopy analysis

X-ray photoemission spectroscopy (XPS) is performed to examine the chemical composition of the top layers in alloyed samples after deposition of AuGe/Ni/Au layers and alloying. The measurements are performed on as-deposited un-annealed sample for standardization and sample annealed at 400°C for 60s, which gave the lowest contact resistance, in order to correlate current AFM data with phases present in the annealed structures.

XPS is sensitive to top 1nm of the samples. The diameter of the X-ray beam is ~10nm. The samples examined are TLM patterned. The 'survey' of the as-deposited and annealed sample is given in figure 5.4.1.

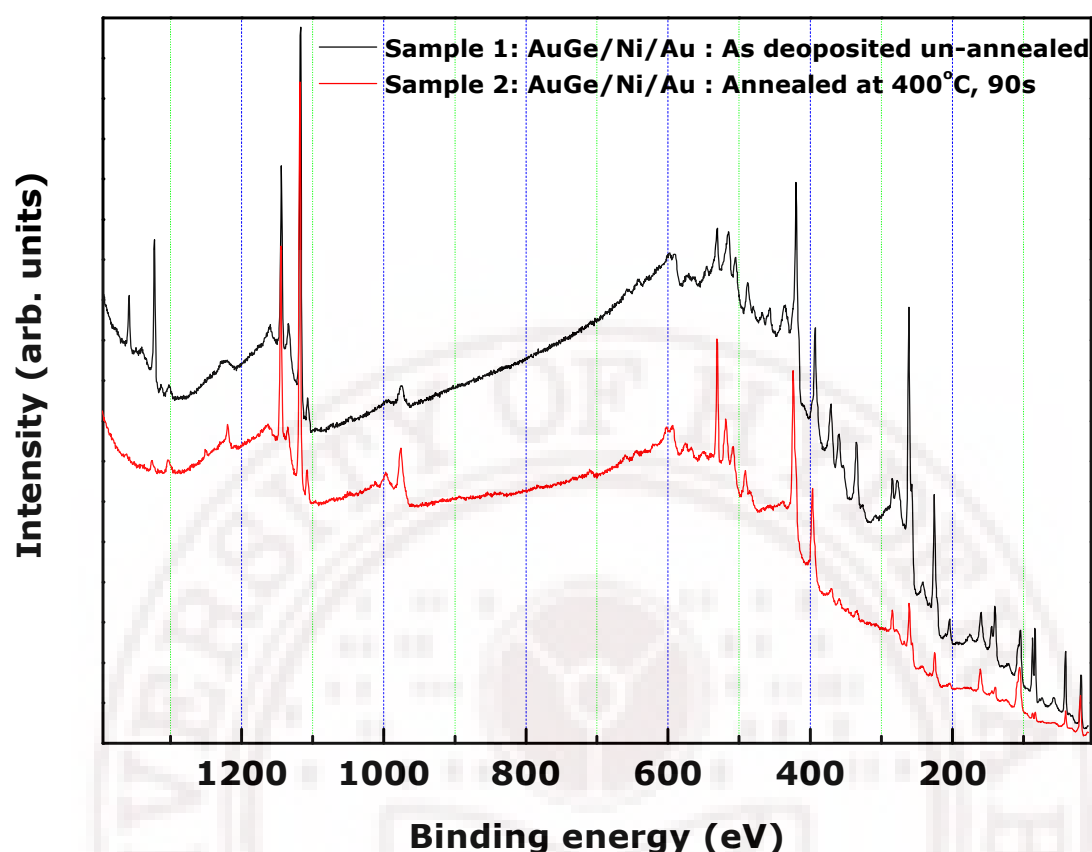


**Figure 5.4.1** XPS survey of the AuGe/Ni/Au metallization on GaAs/AlGaAs before and after annealing.

The as-deposited un-annealed sample composed of Gallium, Germanium, Arsenic and Gold. There is some reduction as well as enhancement in some peaks in the annealed sample (figure 5.4.2). In the sample annealed peaks corresponding to Ga, Ge, Ni, As and Au are detected. Peak corresponding to Ni is detected nearly at the level of noise in the annealed sample (figure 5.4.3). The amount of Ni in the top 1nm is not significantly large. Further investigations are required to determine whether Ni-compounds are distributed close to the semiconductor-metallization interface. The pad sizes of the TLM pattern are smaller than the spot sizes of the X-ray beam in the XPS measurement. This precludes any conclusion about in distribution of Ga in the top Au layer.

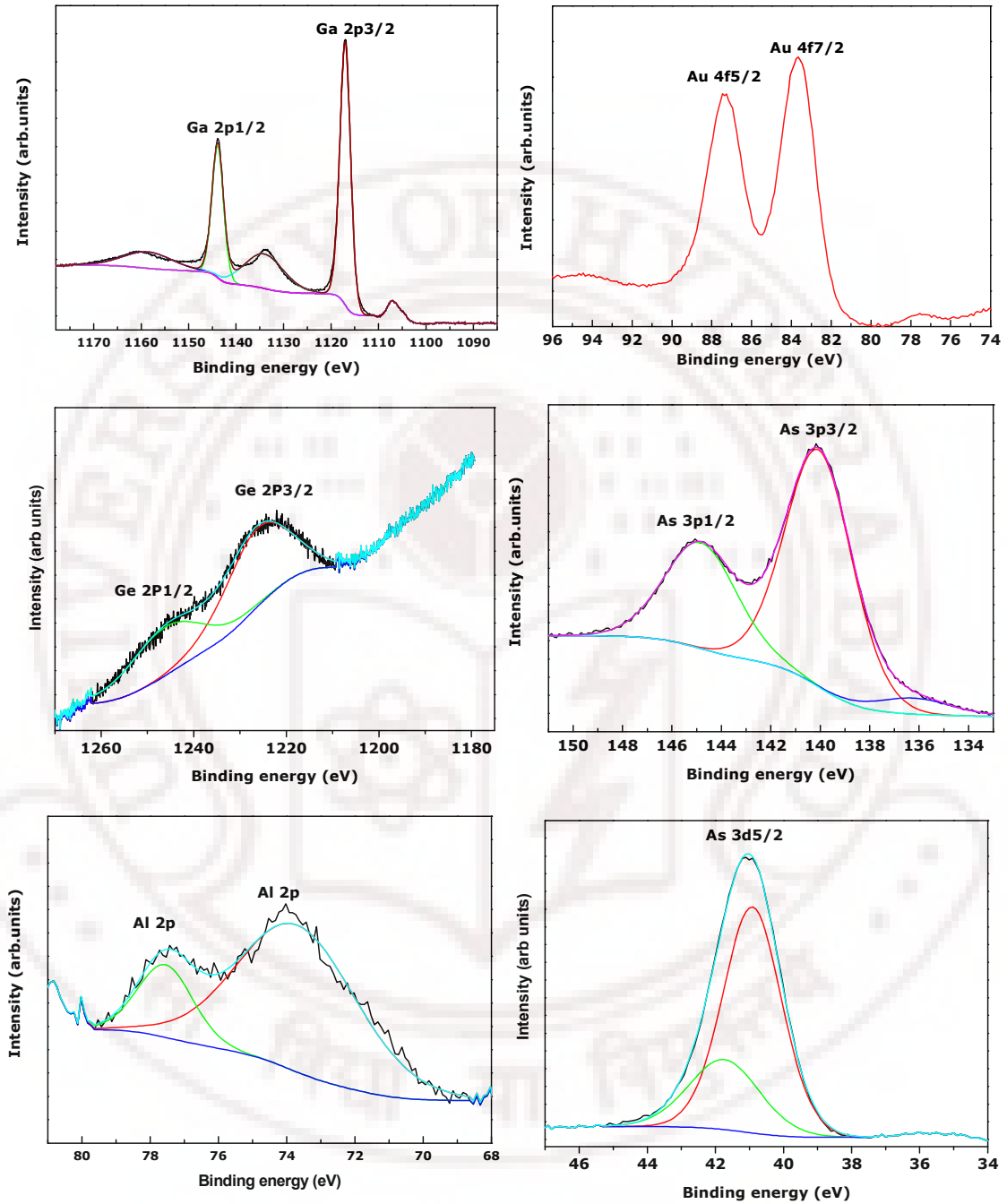


**Figure 5.4.2** XPS spectra of as-deposited AuGe/Ni/Au metallization on GaAs/AlGaAs



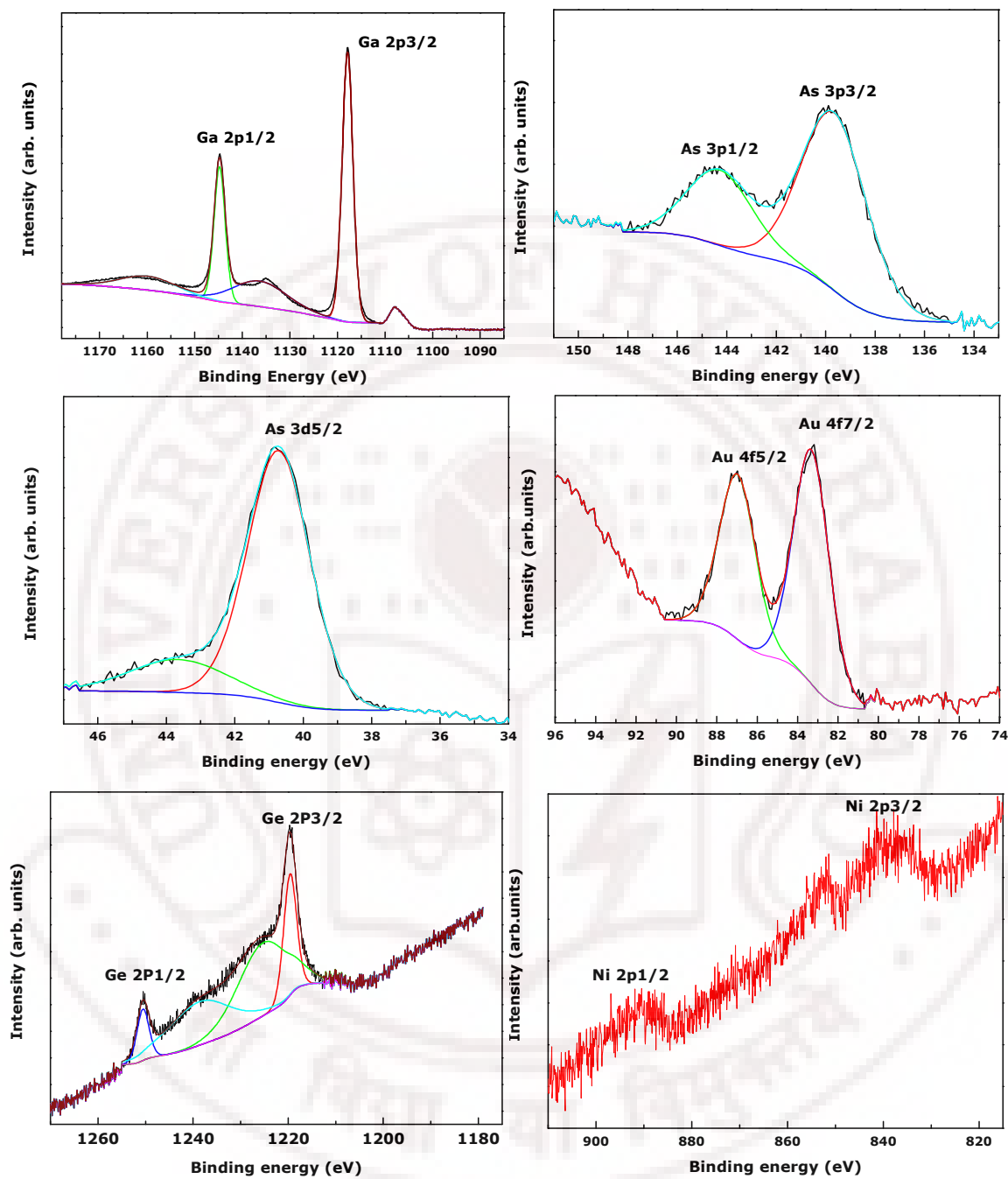


Figure 5.4.3 XPS spectra of AuGe/Ni/Au deposited and annealed at 400°C

## 5.5 Conclusions

1. The amount of Ni transformed to non-magnetic phase on annealing scales with AuGe layer thickness implying that the entire AuGe layer not just the interface, is involved in the conversion of Ni to non-magnetic phase.
2. Au over-layer and AuGe (Ni) layer are seen to be distinct in the cross sectional SEM of a sample annealed at 300°C when Ni has been converted to a non-magnetic phase, but alloying has not yet taken place, also the surface is still relatively smooth. These observations imply that the Ni dissolution/diffusion with AuGe occurs in the solid state. .
3. When the Ni layer is partially converted to non-magnetic phase, the conversion is time independent. This implies that the Ni interaction with AuGe layer not diffusion limited, but solubility limited dissolution.
4. The solubility of Ni in AuGe is quadratic with temperature.
5. The solubility decreases with decreasing Ge content in AuGe alloy.
6. Grazing incident XRD data indicate the presence of Ni-Ge phase in the structure after cooling from anneals at temperatures when the magnetic to non-magnetic transformation is just completed, but alloying has not yet occurred.
7. Signatures of melting (endothermic peak) are seen in Differential Scanning Calorimetry.
8. The melting temperature of the metallization increases with increase in Ni layer thickness and with decreasing Ge content from the eutectic composition of the AuGe alloy layer.
9. Current AFM data on alloyed structures with low contact resistance show short distance current fluctuations, despite an Au over-layer.
10. Peak corresponding to Ni (nearly at the level of noise) is detected in the sample which gave the lowest contact resistance.
11. Adhesion of the metallization structure on the substrate improves as Ni dissolution into the AuGe layer, possibly accounting for morphology favorable for good contact formation, prior to melting and alloying.



**References**

- 1 M. Murakami, K.D. Childs, John. M. Baker, A. Callegari, *J. Vac. Sci. Technol.*, B- **4**, (1986) 903.
- 2 M. Murakami, *Science and Technology of Advanced Materials.*, **3** (2002) 1.
- 3 T. S. Kuan, P. E. Batson, T. N. Jakson, H. Rupprecht and E. L. Wilkie, *J. Appl. Phys.*, **54** (1983) 6952.
- 4 M. Ogawa, *J. Appl. Phys.*, **51** (1980) 406.
- 5 G. Sai Saravanan, K. Mahadeva Bhat, K. Muraleedharan, H. P. Vyas, R. Muralidharan and A. P. Pathak, *Semicond. Sci. Technol.*, **23** (2008) 025019.
- 6 T. C. Shen, G. B. Gao, and H. Morkoc, *J. Vac. Sci. Technol.*, B **10** (1992) 2113.
- 7 Y. C. Shih, M. Murakami, E. L. Wilkie and A. C. Callegari *J. Appl. Phys.*, **62** (1987) 582.
- 8 T. Kim and D. D. L. Chung, *Thin Solid films.*, **147** (1986) 177.
- 9 M. Wittmer, R. Pretorius, J. W. Mayer and M. A. Nicolet, *Solid state electron.*, **20**, (1977) 433.
- 10 T.G. Finstad, *Thin solid films*, 47, (1977) 279.
- 11 F. Radulescu and J. M McCarthy, *J. Appl. Phys.*, **86** (1999) 995.
- 12 Sigurds ARAJS, *Phys. kondens. Materie*, **4** (1965) 15.

## Chapter-6

### Pd/Ge based Ohmic contact

#### 6.1 Introduction

The AuGe alloy based Ohmic contact with Ni layer give low contact resistance with moderate surface roughness and is extensively used in GaAs technology [1-6]. In recent years, since the device dimensions are in the sub-micron regime, the fabrication of Ohmic contacts with smoother surface (a factor that influences the transistor gate fabrication) and low contact resistance has become important. In the case of AuGe based systems, the optimum contacts are obtained by annealing at a temperature of  $\sim 400^{\circ}\text{C}$ , which results in contact resistances of the order of  $\sim 0.03 - 0.1 \Omega\text{-mm}$  [4-8]. However, the contact surface is rough and lateral spreading of the contact material takes place during annealing above the eutectic AuGe alloy melting temperature ( $\sim 360^{\circ}\text{C}$ ).

In addition, low processing temperature  $< 400^{\circ}\text{C}$  may be desirable to avoid unintended modifications to device structures. In such cases, reasonable contact resistances that can be achieved by low temperature processing are desirable. Thus, many investigations have focused on low temperature processed contacts in which contact definition (i.e. avoidable of lateral spreading) is a priority.

A replacement for AuGe/Ni/Au alloy based Ohmic contacts is an Ohmic contact forming at  $\sim 300^{\circ}\text{C}$  through the solid phase reaction is Pd/Ge metallization [9-14].

This contact scheme involves a metallic transport medium Pd, on to which a layer of Ge is grown. The thickness of Pd and Ge is chosen such that upon annealing, the entire Pd is consumed in the formation of a PdGe layer. The remaining amorphous Ge is transported through PdGe to regrow epitaxially on the GaAs substrate. Ge/Pd/GaAs contacts are suitable for shallow junctions without lateral or vertical spiking.

The Pd-Ge based Ohmic contact to GaAs and GaAs/AlGaAs heterostructures have been reported [11-16]. These studies of Pd/Ge on GaAs indicate that the optimum

conditions for lowest contact resistance are with Pd and Ge layer thickness of 50nm and 100nm respectively, and anneal temperature of 300°C and duration of 60s [10].

The melting of the metallization structure plays an important role in the process of contact formation in AuGe/Ni/Au based contact. In the case of Pd/Ge, reactions occur in the solid phase as discussed in detail in chapter 1, section 1.2.4.4 and chapter 6 section 6.2.3. Studies show that the processed structure consists of an epitaxial Ge layer over the GaAs (possibly with Ge doping) occurring during processing with an over-layer consisting of Pd-Ge compounds.

Typical process involved in HEMT after fabrication of the Ohmic contacts are recess etch, gate deposition, passivation, interconnection and encapsulation. Some of these process steps, performed after the Ohmic contacts for gate and interconnect formation using lift-off, can damage (peel-off) the underlying Ohmic contact layer. Therefore, study of adhesion of Pd/Ge contact metallization during and after processing is of interest.

In this chapter the adhesion properties of Pd/Ge metallization structure deposited on GaAs/AlGaAs multilayer structures (with an  $n^+$  cap layer) are examined. The contact resistance and surface roughness have also been measured on samples processed under same condition as the samples used for adhesion studies to aid correlation of the properties of relevance to device fabrication.

## 6.2 Experimental

The Ohmic contacts are prepared by evaporating Pd (50nm)/ Ge (100nm) using e-beam evaporation, onto wafer pieces with multilayer structure as shown in table 6.2.1. The Pd and Ge layer thickness of 50nm and 100nm (optimum thickness for low contact resistance as reported in literature [10] are used. The samples are then subjected to rapid thermal anneal at a temperature  $T_A$  varying between (200 – 400°C), at a rate of 250°C/minute held at  $T_A$  for anneal durations  $t_A$  in  $N_2$  atmosphere, then cooled down to room temperature.

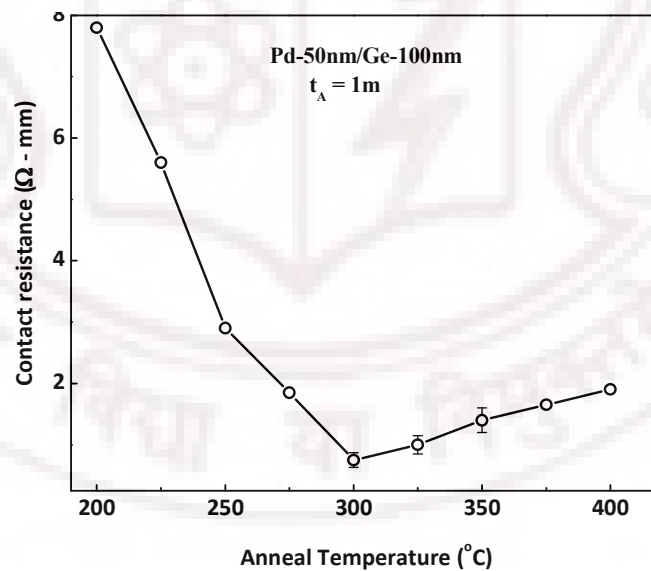
**Table 6.2.1** GaAs/AlGaAs wafer layer structure and Ohmic contact metallization

	Ge (100nm)	
	Pd (50nm)	
$n^+$ (Si $1.5 \times 10^{18}$ ) GaAs	20nm	Cap layer
$n^+$ (Si $1.5 \times 10^{18}$ ) $Al_{0.3}GaAs_{0.7}$	30nm	Supply layer
Intrinsic AlGaAs	15nm	Separation layer
Intrinsic GaAs	500nm	<b>2DEG</b> 
SI GaAs Substrate	500 $\mu$ m	

The contact resistance, film roughness and adhesion using the nano scratch test are described in subsequent sections of this chapter.

### 6.2.1 Electrical properties

The contact resistance,  $R_{TC}$  is shown in figure 6.2.1 as a function of anneal temperature for Pd (50nm)/Ge (100nm) [10] contact structure. The contact resistances are measured by lithographically patterning a transmission line pattern as described in chapter 2, and using the Transfer Length Model (TLM) [17].

**Figure 6.2.1** Contact resistances as a function of anneal temperature

The contact resistances were measured for  $T_A \sim 200-400^\circ\text{C}$ . The contact show Ohmic behaviour for all anneal temperatures used. A minimum is observed in the

contact resistance at an anneal temperatures  $\sim 300^{\circ}\text{C}$  and duration of  $\sim 60$  seconds. The errors calculated are from the rms deviation of the measured contact resistance for different samples. The contact resistances increases marginally and monotonically with anneal durations  $>60$ seconds (figure 6.2.2). The optimum contact resistance is  $\sim 0.75 \pm 0.1 \Omega\text{-mm}$  which is about 15 times larger than that of structures with AuGe/Ni/Au that give the lowest contact resistance. The values of contact resistance are listed in table 6.2.2.

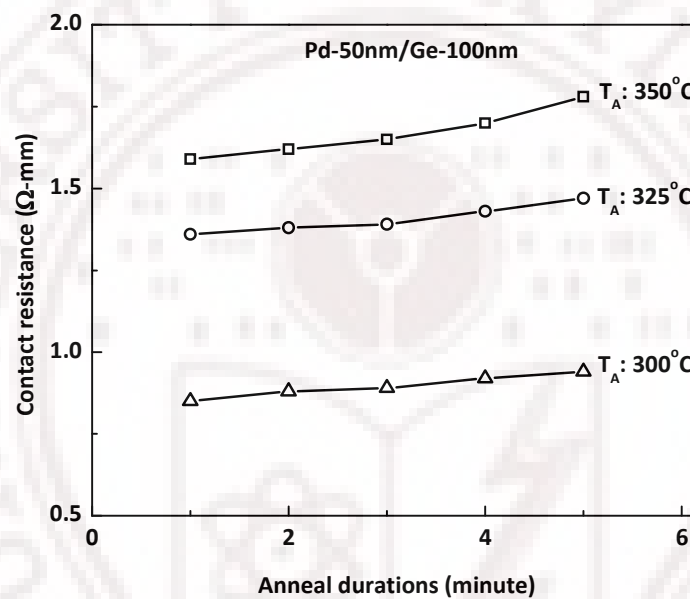


**Figure 6.2.2** Contact resistances as function of anneal duration

**Table 6.2.2** Contact resistances as a function of anneal temperature.

Metallization	Anneal Temperature ( $^{\circ}\text{C}$ )	Alloying time (s)	Contact resistance ( $\Omega\text{-mm}$ )
Pd (50nm) /Ge (100nm)	200	60	7.8
	225	60	5.6
	250	60	2.9
	275	60	1.85
	300	60	$0.75 \pm 0.10$
	325	60	$1 \pm 0.15$
	350	60	$1.4 \pm 0.2$
	375	60	1.65
	400	60	1.90

### 6.2.2 Surface roughness

Atomic Force Microscopy (AFM) is used for examining the surface roughness. AFM image in the region of the TLM pattern deposited with Pd/Ge and annealed at 300°C for 60s is displayed in figure 6.2.3a. The R.M.S. surface roughness is computed over the scanned surface (several pads on TLM pattern). A line scan on the topography of the TLM contact pad performed is shown in figure 6.2.3b.

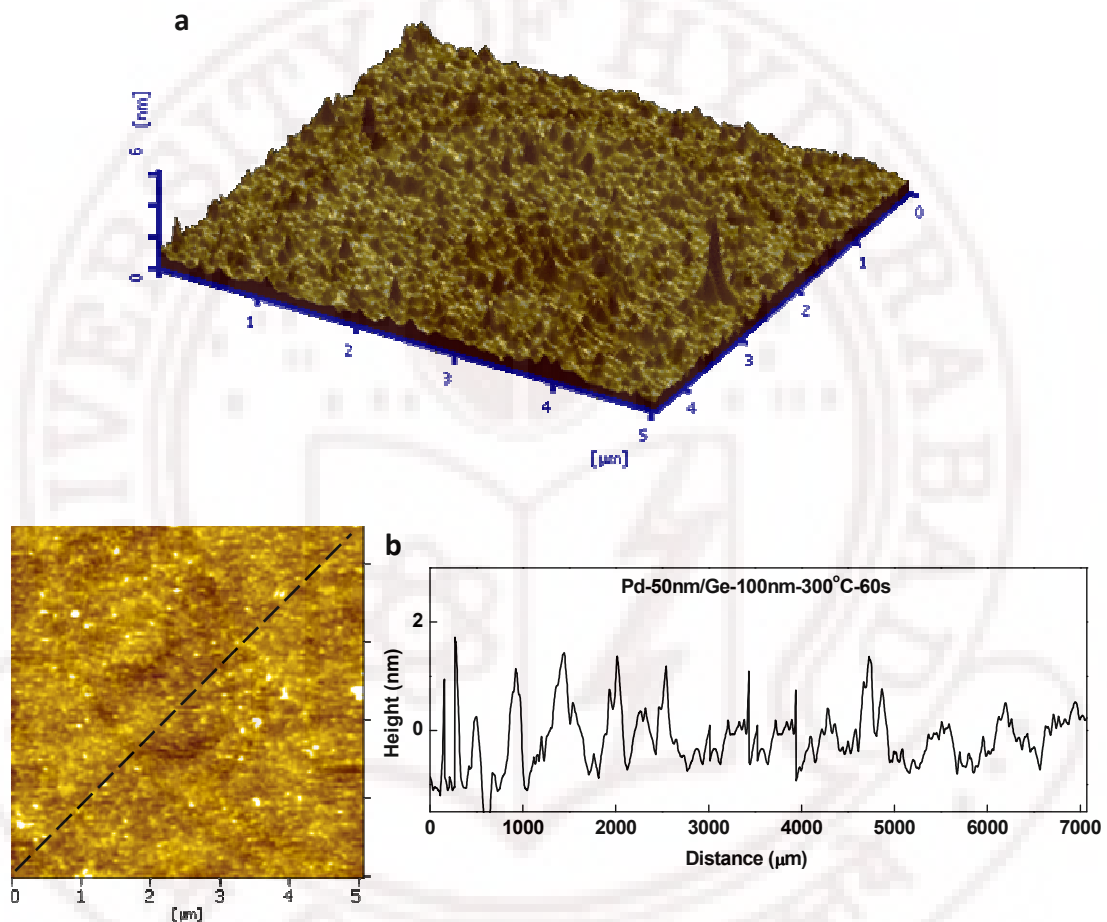


**Figure 6.2.3** AFM micrographs of the surface of samples Pd (50nm)/Ge (100nm) (a) annealed at 300°C for 60s, (b) line scan on the topography of the contact pad

The measured surface roughness is  $\sim 2.0 \pm 0.5$  nm. The surface roughness is 10 times lower than that of AuGe/Ni/Au based contact which gives the lowest contact resistance (25nm Ni layer, anneal temperature ( $T_A$ ): 400°C, anneal duration ( $t_A$ ): 60s).

### 6.2.3 Differential Scanning Calorimetry

DSC scans are performed on the metallized substrate (Pd/Ge), with a bare substrate (GaAs) of similar size as the reference. The scan spanned from room temperature to 500°C at a heating rate of 100°C/min in N<sub>2</sub> gas atmosphere (figure 6.2.4). In DSC scans on Pd/Ge deposited GaAs/AlGaAs, five exothermic peaks are observed.

DSC scans by F. Radulescu et.al. [11] report similar number of peaks at almost similar temperatures in slightly different structure (Pd-20nm/Ge-150nm/Pd-50nm). They also report Cross-sectional TEM results after anneals at temperatures corresponding to each of the peak positions. They have suggested that peaks corresponds to solid state reactions in which various PdGe compounds are formed as mentioned in Chapter1 section 1.2.4.4. Early cross sectional TEM studies reported by Wang et.al. [12, 13] resulted in the suggestion that solid state reaction between various layers and possibly with the substrate occurred as given in table of chapter 1, section 1.2.4.4. The subsequent studies confirm that an epitaxial layer of Ge with an over-layer of PdGe is formed. Alloying with the substrate is not so clear.

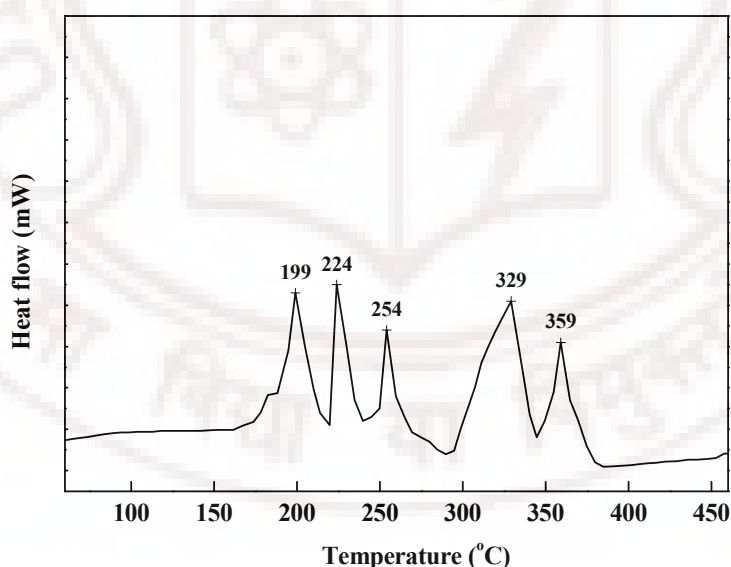


**Figure 6.2.4** DSC scans of Pd (50nm)/Ge (100nm) film deposited on GaAs.



#### 6.2.4 Adhesion studies

Scratch test is employed to study the adhesion properties between the film and underlying film/substrate or wear resistance of the upper layers. Scratch test is performed on samples prepared at various processing conditions.

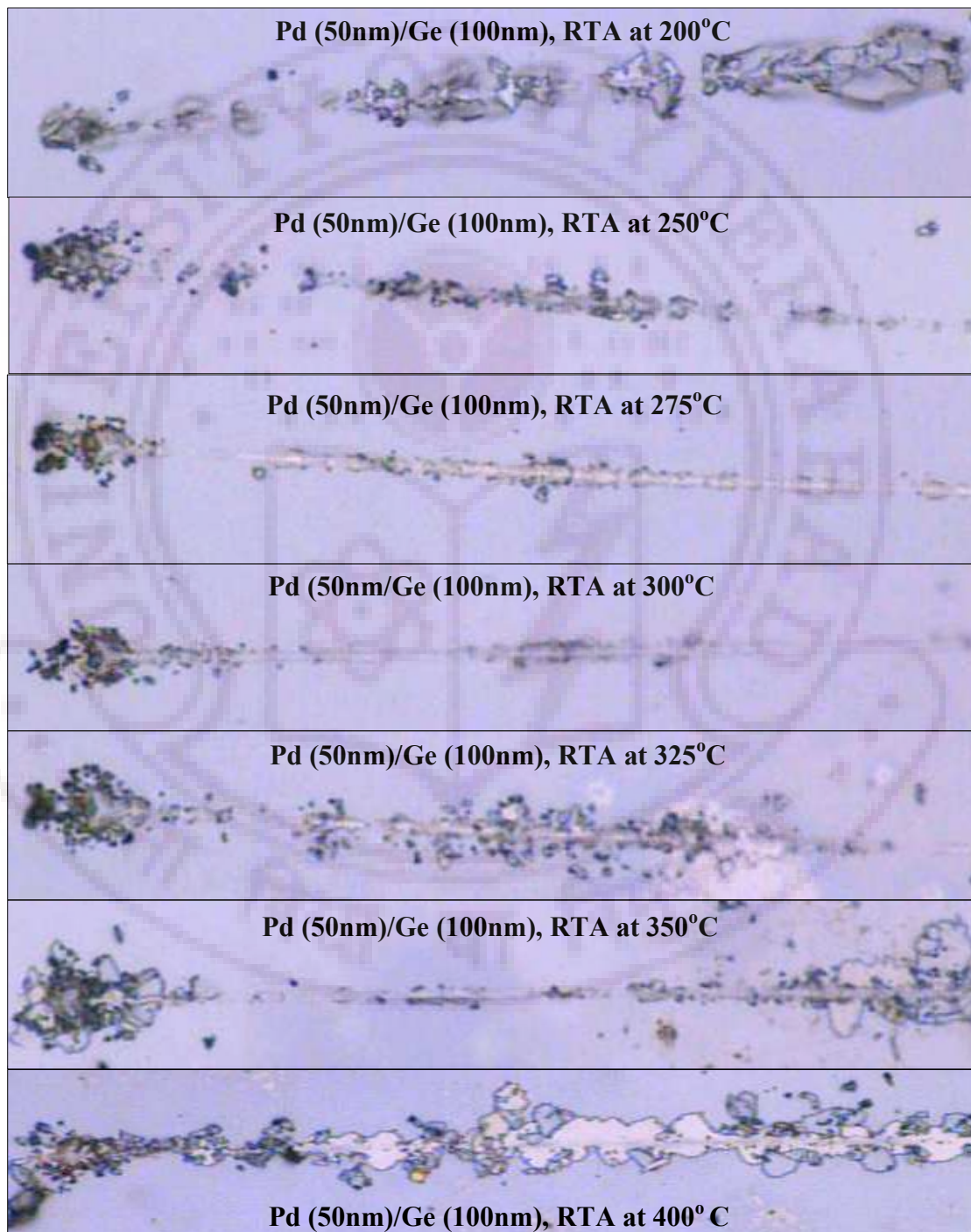


**Figure 6.2.5** Optical microscope image of the scratch track of the Pd/Ge deposited on GaAs

The scratch length is  $250\mu\text{m}$  and the scratch force is ramped from  $0\text{--}500\mu\text{N}$ . The scratch proceeds from left to right. The force is varied continuously from left to right. The optical images of the scratches are given in figure 6.2.5. The force is sufficient to abrade the soft metal. The damage heaps on the left side is from the initial indentation.

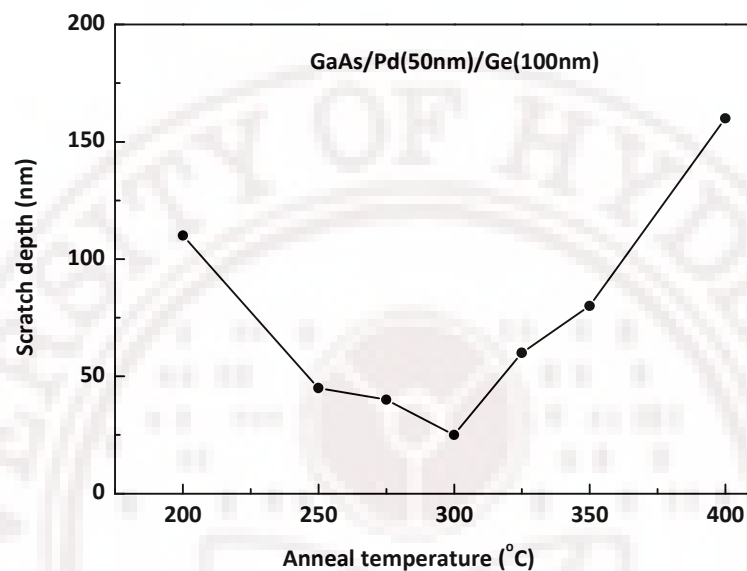


**Figure 6.2.6** Scratch depth Vs anneal temperature

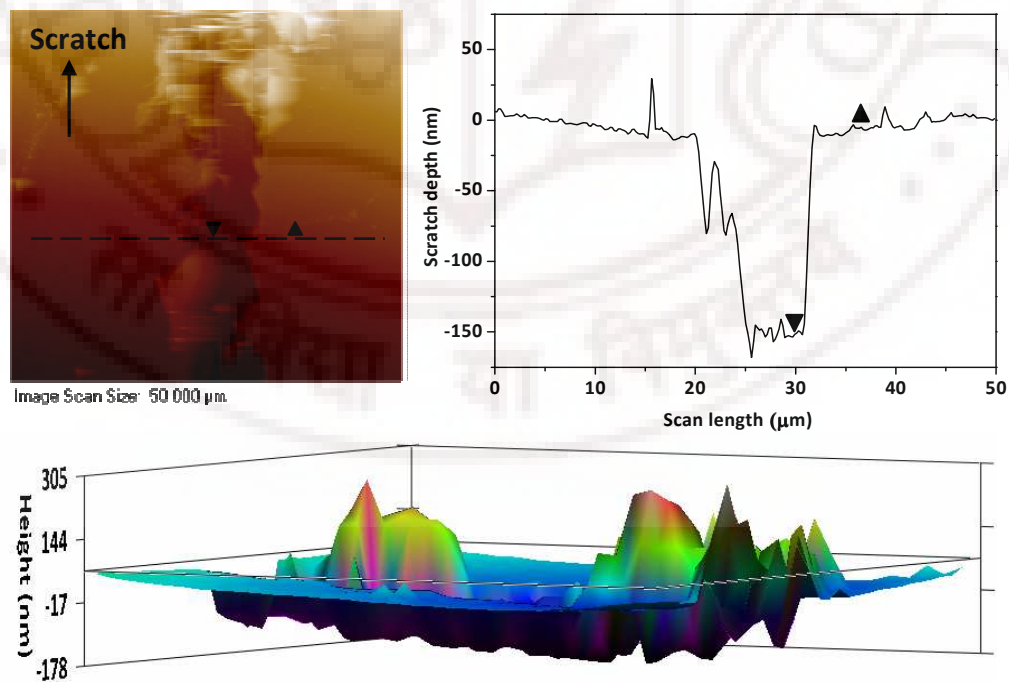


**Figure 6.2.7** AFM analysis and measurement of the scratch track

In addition, experiments were performed at constant force (200 $\mu$ N) to determine scratch depth as a function of anneal temperature. The results are given in figure 6.2.6. The line scan of the topography across scratches is also measured in the AFM mode to determine scratch depth as well as to verify whether scratch extended into the substrate (figure 6.2.7). The results indicate that, for this force, the scratches do not extend into the substrate.

The optical micrographs of the scratch track show least debris at 300°C. The measurement of scratch depth at constant force also show a minimum at 300°C which corresponds to anneal temperature at which lowest contact resistance occurs. The scratch could result in either film abrasion or delamination depending on relative hardness of the films and the adhesion between them. In either case the result lead to an important conclusion. The formation of PdGe as uppermost with epitaxial Ge (indicated by TEM) results in a structure with strong adhesion or wear resistance rather than the opposite.

### 6.3 Conclusions

1. The minimum in the contact resistance for Pd/Ge Ohmic contact scheme is observed at anneal temperature of 300°C.
2. The Optimum contact resistance of Pd/Ge contact ( $0.75 \pm 0.10$ ) is ~15 times larger than those optimized with AuGe/Ni/Au ( $0.05 \pm 0.01$ ) (eutectic AuGe with 25nm Ni layer thickness).
3. The measured surface roughness is  $\sim 2.0 \pm 0.5$ nm and is ~10 times lower than that of AuGe/Ni/Au based contact which gives the lowest contact resistance (25nm Ni layer, anneal temperature ( $T_A$ ): 400°C, anneal duration ( $t_A$ ): 60s).
4. DSC scans are performed on Pd/Ge deposited on GaAs show several peaks.
5. The scratch depth and qualitative estimate of adhesion show the best adhesion/wear resistance at 300°C anneal temperature.

## References

1. N. Braslau, J. B. Gunn and J. L. Staples, *Solid State Electron.*, **10** (1967) 381.
2. M. Murakami, K. D. Childs, J. M. Baker and A. C. Callegari, *J. Vac. Sci. Technol.*, **B 4** (1986) 903.
3. H. Goronkin, S. Tehrani, T. Remmel, P. L. Feies and K. J. Johnson, *IEEE Trans. Electron Devices.*, **36** (1989) 281.
4. A. K. Rai, A. Ezis, R. J. Graham, R. Sharma and D. W. Langer, *J. Appl. Phys.*, **63** (1988) 4723.
5. R. P. Taylor, P. T. Coleridge, M. Davies, Y. Feng, J. P. McCaffrey and P. A. Marshall, *J. Appl. Phys.*, **76** (1994) 7966.
6. A. Ketterson, F. Ponce, T. Henderson, J. Klem and H. Morkoc, *J. Appl. Phys.*, **57** (1985) 2305.
7. G. Sai Saravanan, K. Mahadeva Bhat, K. Muraleedharan, H. P. Vyas, R. Muralidharan and A. P. Pathak, *Semicond. Sci. Technol.*, **23** (2008) 025019.
8. T. S. Abhilash, Ch. Ravi Kumar and G. Rajaram, *J. Phys. D: Appl. Phys.*, **42** (2009) 25104.
9. E. D. Marshall, B. Zhang, L. C. Wang, P. F. Jiao, W. X. Chen, T. Sawada and S. S. Lau, *J. Appl. Phys.*, **62** (1987) 942.
10. Jong-Lam Lee, Yi-tae Kim, Jung-Woo Oh and Byung-Teak lee, *Jpn. J. Appl. Phys.*, **40** (2001) 1188.
11. F. Radulescu and J. M. McCarthy, *J. Appl. Phys.*, **86** (1999) 995.
12. L. C. Wang, S. S. Lau, E. K. Hsieh and J. R. Velebir, *Appl. Phys. Lett.*, **54** (1989) 2677.
13. L.C. Wang, *J. Appl. Phys.*, **77** (1995) 1607.
14. C. J. Palmstrom, S.A. Schwarz, E. Yablonovitch, J. P. Harbison, C. L. Schwartz, L.T. Florez and T. J. Gmitter, *J. Appl. Phys.*, **67** (1990) 334.
15. Jiun-Tsuen Lai and Joseph Ya-Min Lee, *Appl. Phys. Lett.*, **64** (1994) 229.
16. D.A. Ahmari, M.L. Hattendorf, D.F. Lemmerhirt, Q. Yang, Q. J. Hartmann, J.E Baker and G.E Stillman, *Appl. Phys. Lett.*, **72** (1998) 3479.
17. H.H. Berger *Solid State Electron.*, **15** (1972) 145.

## Chapter-7

# Fabrication of Micro Hall Magnetic Sensors

### 7.1 Introduction

GaAs/AlGaAs 2DEG multilayer structures are used in the fabrication of high sensitivity Hall-effect based magnetic field sensors. AuGe/Ni/Au layers are extensively used for fabricating Ohmic contacts to these structures. The goal of the thesis work is to optimize the contact resistance and to study the magnetism of the AuGe/Ni/Au contact metallization that arises in the context of magnetic field sensor fabrication and application using these multilayers.

The optimized non-magnetic AuGe/Ni/Au metallization is used for fabricating the Ohmic contacts in the Hall magnetic sensors. This chapter describes the fabrication, characterization of micro Hall magnetic sensors using the GaAs/AlGaAs 2DEG structures and their application to magnetic flux leakage measurements.

### 7.2 Hall sensors

Semiconductor magnetic sensors based on the Hall Effect are used in several applications. Most of the Hall devices are made of III-V compound semiconductors such as GaAs, InSb, InAs [1-3]. The magnetic sensitivity of the Hall device is inversely proportional to the sheet carrier density ( $n_s$ ). The option to build in increased sensitivity by decreasing  $n_s$  is, however, limited by increasing source resistance, and hence noise, unless carrier mobility,  $\mu$  is also increased. This accounts for the popularity of materials such as GaAs and InSb as Hall sensor materials ( $\mu$  larger than that of Si). The quantum well heterostructure semiconductors with the 2-Dimensional Electron Gas (2DEG) layer, grown by molecular beam epitaxy, are specially suited for fabrication of micro-Hall Sensors and sensor arrays since they consist of a thin carrier sheet of high mobility. They are used for fabricating sensors with high sensitivity, low-temperature operation and low temperature-variation of sensitivity [4]. They are also used in fabrication of high

electron mobility transistors (HEMTs) [5]. GaAs/AlGaAs heterostructures are popular because they are relatively easy to grow in comparison with other HEMT structures.

### 7.2.1 Sensitivity

The sensitivity of the Hall Effect sensor is the figure of merit of the sensor. The Hall Voltage,  $V_H$ , when a film is exposed to a magnetic field  $B$  (Tesla) perpendicular to its plane, is

$$V_H = K_H I B_y$$

Where  $I$  is the excitation current in Ampere.

The sensitivity  $K_H$  (or  $R_H/t$ ,  $t$  is carrier layer thickness and  $R_H$  the Hall constant) is

$$K_H \sim \frac{1}{n_s e}$$

Where  $n_s$  is the surface carrier density in  $m^{-2}$  and  $e$  is the carrier charge.

Though the nominal sensitivity  $K_H$  increases with decreasing carrier density, the eventual resolutions and lowest measurable field will be limited by two factors: (i) the highest excitation current that is useable for a given maximum power dissipation,  $P$ , that will not destroy the device

$$I_{\max} \sim \sqrt{(P/R_l)}$$

$R_l$  is resistance in excitation current path and (ii) white noise which increases as  $R_v$ , the resistance between the Hall voltage leads.

Both  $R_l$  and  $R_v$  increase with decreasing  $n_s$  and improvements in lowest measurable field and signal-to-noise ratio can only be obtained by compensating the effect of decreasing  $n_s$  on  $R$  by choice of materials with large carrier mobilities ( $\mu$ ) [4].

## 7.3 Micro-Hall Sensor fabrication

### 7.3.1 Choice of Material

The chosen material for the fabrication of Hall sensor in this thesis is GaAs/AlGaAs heterostructure with a two-dimensional electron gas (2DEG) layer. This material is desirable because the carrier density of the 2DEG at low temperatures can be set very



small during the heterostructure growth process by tuning the number of dopants. Also, the mobility ( $\mu$ ) is very high, and decreases the resistance of the leads. Hall sensors were fabricated on wafers grown using Molecular beam epitaxy by IQE Europe Ltd. 2DEG lies 65 nm below the wafer surface. The detail of the wafer structure with the 2DEG layer is explained in chapter 2.

### 7.3.2 Hall magnetic sensor design

The Mask layout for the single sensor and Hall sensor array configurations are shown below (figure 7.3.1). The Mask set consists of (i) Deposition of Cr/Au alignment-marks (ii) device isolation by mesa etch (iii) formation of Ohmic contacts (iv) interconnect pads and (v) a protection layer. The details of processing steps are explained in chapter 2.

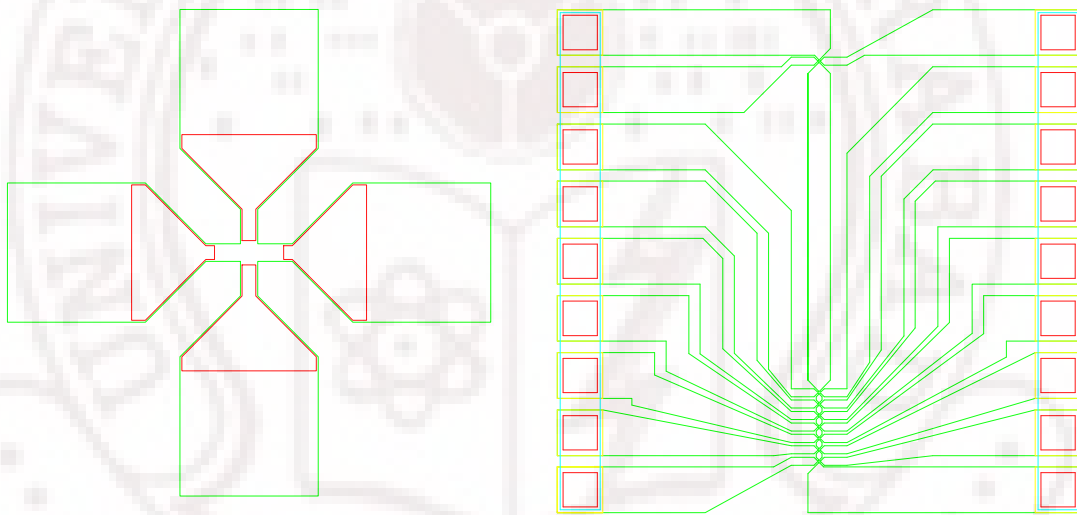


**Figure 7.3.1** Layout of Hall magnetic sensors

### 7.3.3 Hall sensor fabrication

The Hall sensors are fabricated using the Micro-fabrication facility of University of Hyderabad (UoH). The Hall cross active areas ranged from 10 to 500  $\mu\text{m}^2$ . The fabrication consists of three major steps on a wafer piece of 1cm x 1cm. (i) active area definition by UV lithography and wet etching (ii) Ohmic contact definition and metallization (iii) evaporation of interconnect pads. These steps are described in detail below. After the fabrication steps are completed, the sensors are diced and mounted on a chip holder for testing.



The first step in the fabrication of the Hall sensor is to define the Hall cross. This is done by removing the 2DEG with a patterned etch. The etch pattern is designed for use with a positive resist (i-line). Optical lithography with a Karl Suss MJB4 Contact Mask Aligner is used to define these Hall crosses. The pattern defines where the resist will be exposed and subsequently where the wafer will be etched and the 2DEG removed. The etch solutions used are listed in the process steps. The wafers are etched to a depth of  $\sim 80\text{nm}$  and etch depths are measured using an AMBIOS XP-1 profilometer.

The next step in the Hall sensor fabrication is to make Ohmic contacts to the sensors which allow electrical connections to be made. AuGe/Ni/Au metallization structure was used for the metal Ohmics. The Ohmic contact fabrication process is as follows: The Ohmic contact pattern is defined on photoresist using photolithography. The substrates are sputter cleaned in  $\text{O}_2$  plasma and a metal sandwich layer structure of AuGe (100nm)/Ni (25 nm)/Au (200nm), is deposited. After lift-off, the Ohmic contacts are annealed. The annealing is performed at a temperature of  $400^\circ\text{C}$ , in  $\text{N}_2$  ambient for 60s after ramping up at a heating rate of  $250^\circ\text{C}/\text{min}$  in a rapid thermal annealing system (RTA).

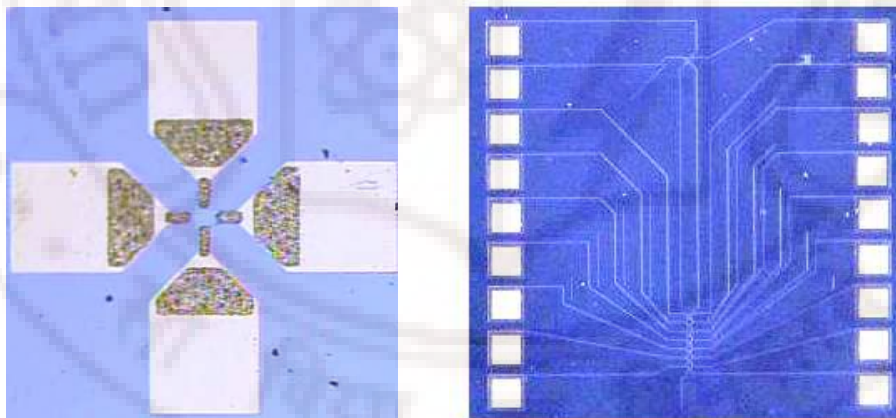


**Figure 7.3.2** Fabricated Hall magnetic single sensor with active area ( $50 \times 50 \mu\text{m}$ ) and  $10 \mu\text{m}$  Hall array

The appearance of the contacts changes from a smooth metal to a bubbly appearance after sufficient annealing. A 20 nm of Cr and 200 nm of Au are deposited for interconnects and contact pads for wire bonding. To protect the multi-layer from a fairly abrasive environment, a layer of photoresist is spun on the die, and patterned to open up windows at the contact pads; the resist is then hard baked and left on the die. The

devices (figure 7.3.2) are then mounted on the sample-holder and wire-bonded [6]. The Hall sensor fabrication processes steps are summarized below.

### 7.3.4 Hall sensor - Process steps

1. Scribe and cleave wafer pieces.
2. Clean wafer, dry, spin-coat with photo-resist, soft bake.
3. Expose with Alignment marks, develop. **Alignment Marks** Mask 1
4. Deposit Cr/Au, Lift-off.
5. Clean wafer, dry, spin-coat photo-resist, bake.
6. Expose wafer with etch mask, develop. **Mesa etch for device isolation** Mask 2
7. Etch with  $\text{H}_3\text{PO}_4 + \text{H}_2\text{O}_2 + \text{H}_2\text{O}$  solution.
8. Strip photo-resist, clean wafer.
9. Spin-coat photoresist, bake.
10. Expose with alloy mask, develop. **Ohmic contacts** Mask 3
11. Deposit AuGe/Ni/Au, lift-off, clean wafer.
12. Rapid thermal anneal.
13. Clean wafer, spin-coat photo-resist, bake.
14. Expose with interconnect mask, develop. **Interconnects and pads** Mask 4
15. Deposit Cr/Au, lift-off.
16. Clean wafer, spin-coat photo-resist, bake.
17. Expose with protection mask, develop. **Protection** Mask 5
18. Hard bake photo-resist.
19. Scribe and cleave to separate devices.
20. Bond to holder and wire bond, test.

## 7.4 Micro Hall magnetic sensor characteristics

The sensors are calibrated against the field, ranges from zero to 90 Oe, with an excitation current of 100  $\mu\text{A}$  derived from a precision current source. The current is reversed to eliminate thermo-emfs and constant offset voltages if any. The voltages are measured using a data acquisition/switch unit. The devices are tested up to a field of

$\sim 8\text{mT}$  using a copper-wire solenoid. Though the testing is restricted to low fields, freedom from hysteresis effects and remnant fields present in electromagnets and superconducting magnets is assured by using a solenoid. These are also typical values of the magnetic fields expected to be measured by the sensors in the envisaged applications. The temperature dependence of the Hall sensor sensitivity is measured in the temperature range 4-300K. The device is mounted on the cold head of a closed cycle refrigerator (Sumitomo RDK408D) capable of cooling down to  $\sim 4\text{K}$ .

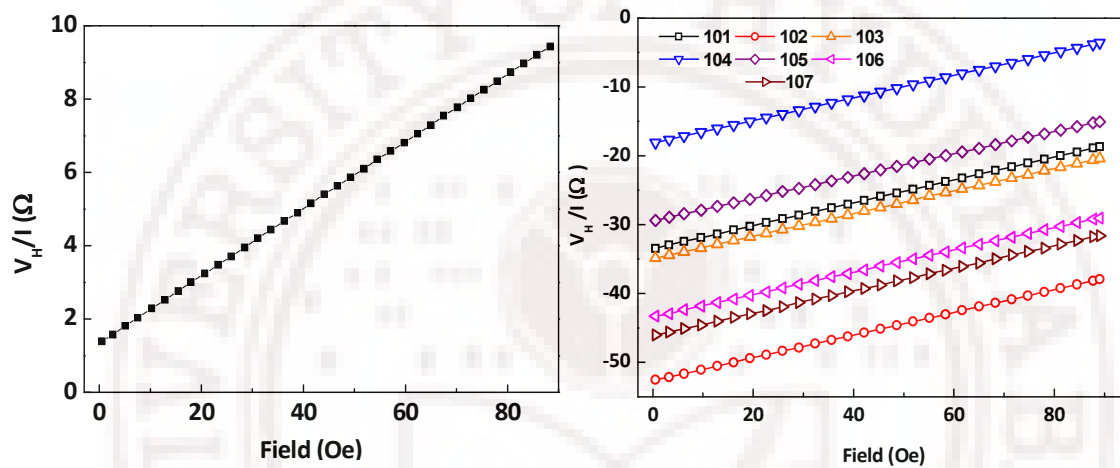


**Figure 7.4.1** Response of single Hall sensor and 7 elements of a Hall sensor array.

The response of the Hall sensor and sensor arrays with increasing magnetic field are given in figure 7.4.1. The sensors have dispersion in offset voltages originating from the material resistance. However, the slopes (i.e. the sensitivity) for different sensors tested agree to within about 1 %. This reflects short range uniformity of the multilayer structure. The sensitivity is calculated to be about  $\sim 1300 \text{ V/AT}$ , in line with expectations of the manufacturer supplied  $n_s$  data.

The sensitivity of the Hall sensor is computed as function of temperature. The data are logged both by fixing temperature and varying the magnetic field (0 to 8 mT) and also as a function of temperature at fixed field as the device is warmed up from 4K-300K at the rate of 1 K/min. The sensitivity, computed as  $K_H(T) = [R_H(B,T) - R_H(0,T)]/B$  from data, is shown in figure 7.4.2. High sensitivity of  $\sim 1300\text{V/AT}$  is obtained. It is observed that the sensitivity slightly increases with decrease of temperature; however it is nearly

constant below 100K. This point is of considerable importance for use of sensors in superconductivity phase diagram application [7].

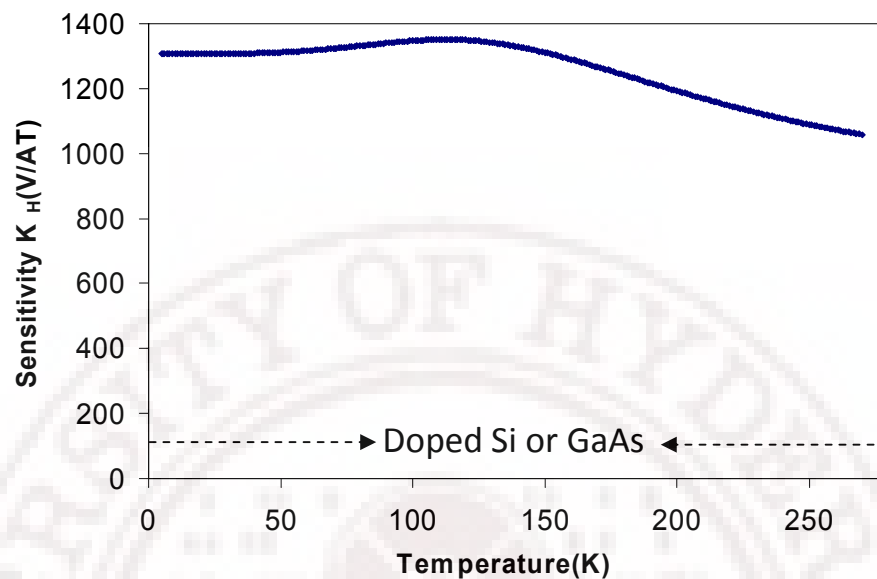


**Figure 7.4.2** Temperature dependence of magnetic sensitivity.

### 7.5 Magnetic non destructive testing (NDT): Flux leakage measurement using 2DEG based Micro Hall Sensors.

Magnetic Flux Leakage method is used to study standardized 'defects' (electro-discharge machined notches) in a mild-steel plate of 6mm thickness in order to assess the sensor's ability to detect defects.

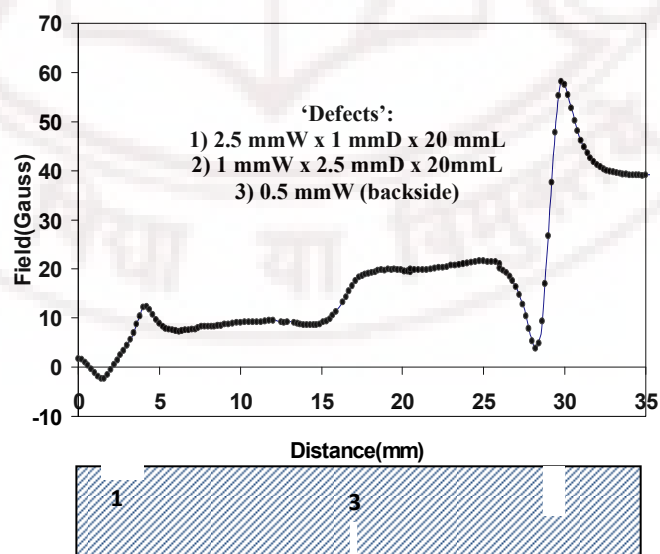
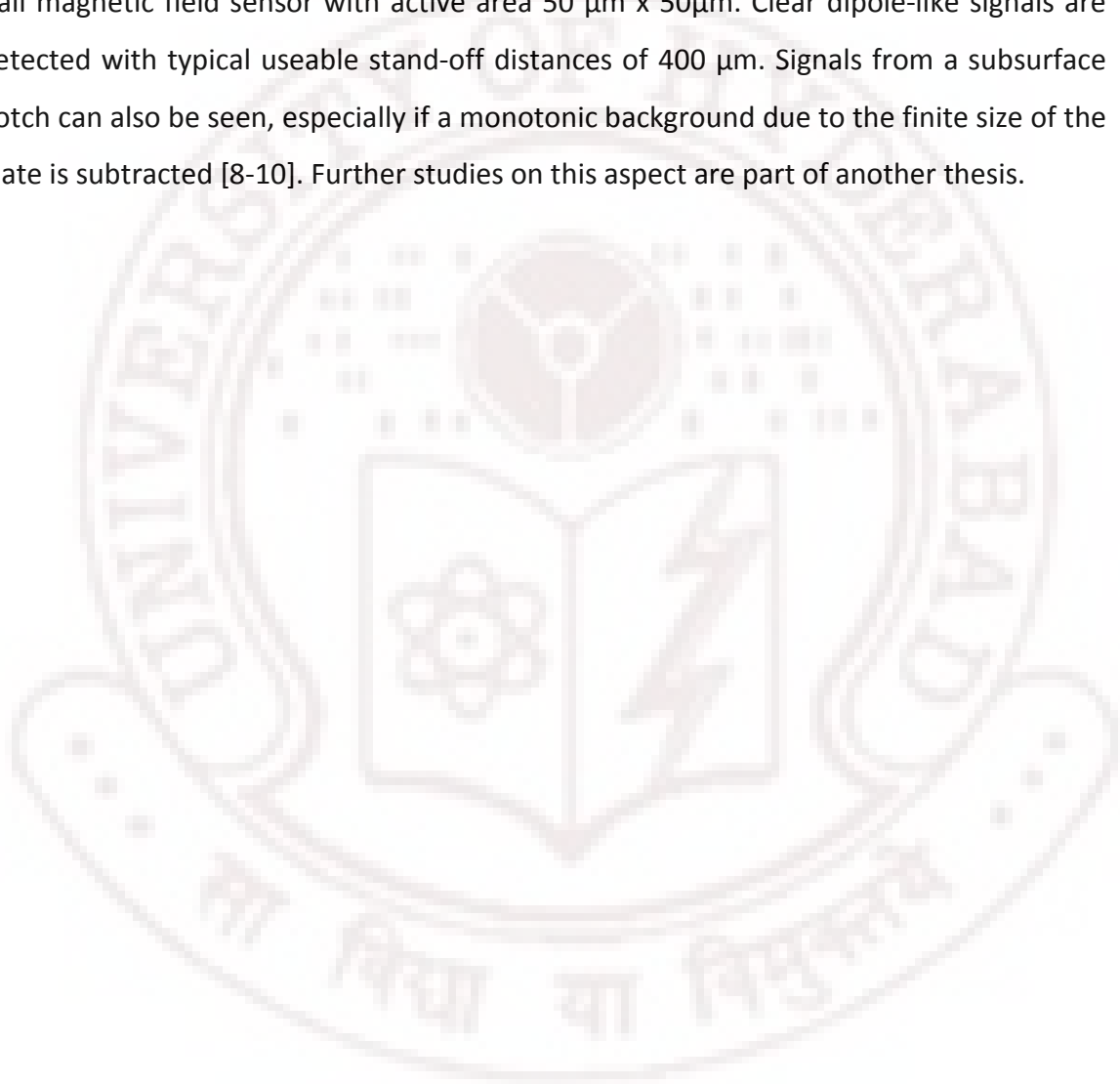


**Figure 7.5.1** Magnetic flux leakage signal of a sample having three defects, including one on the far side of the scan.

The steel plate is mounted on a horse-shoe magnet. The flux lines are closed through the plate. At the defects, however, flux 'leakages occur which results in a finite  $B_z$  that varies from a negative to a positive value when measurements of  $B_z$  are made across the defect. Depending on the plate size/shape and its other properties, a background  $B_z(x)$  occurs. The magnetic field data is logged as the sensor is scanned across notches in Carbon steel plates. Figure 7.5.1 shows such data acquired using 2DEG Hall magnetic field sensor with active area  $50\text{ }\mu\text{m} \times 50\text{ }\mu\text{m}$ . Clear dipole-like signals are detected with typical useable stand-off distances of  $400\text{ }\mu\text{m}$ . Signals from a subsurface notch can also be seen, especially if a monotonic background due to the finite size of the plate is subtracted [8-10]. Further studies on this aspect are part of another thesis.



## References

1. T. R. Lepkowski, G. Shade, S.P. Kwok, M. Peng, L. E. Dickens, D.L Laude and B. Schoendube, *IEEE Electron Device Letters.*, **EDL-7** (1986) 222.
2. A. Sandhu, H. Sanbonsugi, I. Shibasaki, M. Abe and H. Handa, *Jpn. J. Appl. Phys.*, **43** (2004) pp. L868.
3. N. J. Gokemeijer, T.W. Clinton, T.M. Crawford, Mark Johnson, *Journal of Magnetism and Magnetic Materials.*, **290–291** (2005) 254.
4. Y. Sugiyama, *J. Vac. Sci. Technol., B* **13** (1995) 1075.
5. H. Lafontaine, A. M. Haghiri-Gosnet, Y. Jin, P. Crozat, R. Adde, M. Chaker, H. Pepin, F. Rousseaux and H. Lounois, *IEEE Trans. Electron Devices.*, **43** (1996) 175.
6. T. S. Abhilash, Ch. Ravi Kumar, G. Rajaram, Rita Saha, L. S. Vaidhyanathan, K. Gireesan and M. P. Janwadkar, *Proceedings of the 11th National Seminar on Physics and technology of Sensors* (2006), pC37-1.
7. Y. Yamaguchi, G. Rajaram, N. Shirakawa, A. Mumtaz, H. Obara, T. Nakagawa and H. Bando, *Physical Review B* **63** (2000) 014504.
8. Ch. Ravi Kumar, T. S. Abhilash, G. Rajaram B. P. C. Rao, Rita Saha, K. A. Gopal, T. Jayakumar, M. P. Janawadkar, P.V. Kumar and Baldev Raj, *Proceedings of the DAE Solid State Physics Symposium* (2005), p901.
9. Ch. Ravi Kumar, T. S. Abhilash, B. P. C. Rao, S. Thirunavukkarasu, G. Rajaram, T. Jayakumar, and Baldev Raj, *Proceedings of the International conference on Sensors and related networks*, (2007), p-15.
10. G. Rajaram, T. S. Abhilash, Ch. Ravi Kumar, B. P. C. Rao, Rita Saha, L. S. Vaidhyanathan, K. Gireesan, B. Sreedhar, M. P. Janawadkar, T. Jayakumar and Baldev Raj, *Proceedings of the International Workshop on Physics of Semiconductor Devices* (IWPSD- 2009).

## Chapter-8

### Thesis Summary and Future work

In this thesis, Ohmic contacts to GaAs/AlGaAs 2DEG structures are studied with an effort to understand the unresolved issue of magnetism of the AuGe/Ni/Au Ohmic contacts that arise in the context of fabrication of Hall magnetic field sensor using these multilayers. The dependence of contact resistance, surface roughness, magnetization and melting in the metallization on parameters such as Ni layer thickness, anneal temperature and AuGe alloy composition are investigated in the context of Hall magnetic sensors and active devices on GaAs/AlGaAs substrates with  $n^+$  GaAs cap layer. The magnetic measurements provided some interesting insights into the changes taking place in the metallization structure before alloying by examining the early stages of reaction between AuGe/Ni/Au and GaAs.

Chapter 1 discussed the GaAs/AlGaAs 2DEG and the metal/semiconductor contacts. A literature review of various metallization schemes to GaAs and measurements of contact resistance using transmission line model are discussed. Chapter 2 described the experimental techniques employed in this research. Chapter 3 presented the influence of Ni layer thickness on the magnetic properties, contact resistance and surface roughness of AuGe/Ni/Au Ohmic contacts. Chapter 4 described the dependence of melting, surface roughness and contact resistances on Ge and Ni content in the AuGe/Ni/Au. In chapter 5, the insights obtained from changes in the metallization prior to alloyed contact formation are presented. The Ohmic contact using Pd/Ge and the adhesion properties with the substrate are studied in chapter 6, and the fabrication of Hall magnetic sensors using the GaAs/AlGaAs multilayers are described in chapter 7.

#### 8.1 Results Summary

The magnetization hysteresis studies on AuGe/Ni/Au on GaAs/AlGaAs multilayers indicated that the conversion of Ni to non-magnetic phase begins for anneals at



temperatures as low as 100°C and the structure become completely non-magnetic at room temperature after annealing at 400- 430°C with different Ni layer thickness and Ge content in the AuGe alloy. The following results

1. Transformed Ni layer thickness scales with AuGe layer thickness.
2. Transformed Ni layer thickness is independent of Ni layer thickness at a given temperature prior to complete transformation.
3. Transformed Ni layer thickness is time independent at constant anneal temperature.
4. Two distinct layers are observed in cross sectional SEM after complete conversion and before alloying.

imply that the transformation of Ni to non magnetic phase occurs in the solid state.

- (1) A solid state solubility limited dissolution of Ni into AuGe layer occurs starting from anneal temperature <100°C.
- (2) Solubility of Ni layer into AuGe layer increases quadratically with temperature.
- (3) Solubility of Ni layer into AuGe layer decreases with decreasing Ge content in the AuGe alloy.
- (4) The melting temperature of the Ni containing AuGe layer increases with increasing concentration of Ni.
- (5) The adhesion of Ni containing layer improves with increasing Ni layer thickness.

Grazing incident XRD data indicate the presence of Ni-Ge phase in the structure when the magnetic to non-magnetic transformation take place (at 300°C annealed and cooled down to room temperature). Signatures of melting are seen in Differential Scanning Calorimetry and the melting temperature of the metallization increases with increase in Ni layer thickness and decreasing Ge content from the eutectic AuGe alloy. Current AFM data on alloyed structures show spatially non-uniform current distribution.

The contact resistance studies with different Ni-layer thickness on samples with fixed eutectic AuGe alloy layer thickness of 100nm indicate that the lowest contact resistance of  $0.05 \pm 0.01 \text{ } \Omega\text{-mm}$  is obtained at a Ni layer thickness of 25nm when annealed at 400°C. Measurements on samples with different AuGe layer thicknesses suggest that the contact resistances are comparable to this optimum value, if the Ni to AuGe layer thickness ratio is about 0.25 or less. Increasing Ni layer thickness or decreasing the Ge content in the alloy from the eutectic composition increases the

contact resistance. Low temperature contact resistance measurements indicate that the carrier conduction through the contacts have characteristics of both tunneling and thermionic emission. The barrier height increases with increasing Ni layer thickness and decreasing Ge content in the alloy from that of the eutectic composition.

The contacts with the minimum contact resistance (eutectic AuGe-100nm/Ni-25nm)/Au-200nm) show large surface roughness. Increasing Ni layer thickness in the metallization scheme or decreasing Ge content from the alloy reduces surface roughness. The off eutectic AuGe (95:5) alloy with optimum Ni layer thickness appears to be a good choice in trading of contact resistance for surface roughness than increasing Ni layer thickness above the optimum using the eutectic alloy.

The minimum in the contact resistance for Pd/Ge Ohmic contact scheme is observed at anneal temperature of 300°C. The Optimum contact resistance is ~15 times larger than those optimized with AuGe/Ni/Au (eutectic AuGe with 25nm Ni layer thickness), but the reduction in surface roughness ~10 times. The scratch depth and qualitative estimate of adhesion show the maximum adhesion at this temperature.

The results of the Ohmic contact metallization used are summarized in the table given below.

## 8.2 Future work

Although work presented in this thesis has addressed many aspects of Ohmic contacts to GaAs/AlGaAs, it has also lead to several ideas that may be addressed in the future to further our understanding of Ohmic contacts.

Earlier studies on Cross sectional TEM focused on the characterization of the metallization after alloying. The cross sectional TEM studies on the contact metallization structure in the pre alloying stage will help to improve the understanding of the mechanism of contact formation.

Similarly, cross sectional TEM studies on the contact metallization structure, can be used to understand the role of Ge content in the AuGe alloy and the Ni layer thickness in achieving low resistance contact.

Temperature dependent magnetic studies on the alloyed Ohmic contact can give information about the magnetic properties of Ni-Ge compounds which will help in confirming the suitability of the Hall magnetic sensor for low temperature application.

**Table 8.1** Properties of eutectic and off-eutectic AuGe/TM/Au and Pd/Ge based Ohmic Contact

<b>Metallization : AuGe/TM/Au</b>							
<b>AuGe layer thickness (nm)</b>	<b>TM layer thickness (nm)</b>	<b>Au layer thickness (nm)</b>	<b>Optimum alloying temperature (°C)</b>	<b>Alloying time (s)</b>	<b>Contact resistance (<math>\Omega</math>-mm)</b>	<b>Surface roughness (nm)</b>	<b>magnetic to non-magnetic transformation temperature (°C)</b>
100	No TM	200	400	60	3.5	44 $\pm$ 4	-
100	Ti = 30	200	400	90	0.38	40 $\pm$ 3	-
100	Cr = 30	200	400	90	0.13	26 $\pm$ 3	-
100	Ni = 30	200	400	90	0.07 $\pm$ 0.005	21 $\pm$ 2	-
<b>AuGe (88:12wt%)/Ni/Au, TM = Ni</b>							
100	10	200	400	60	0.15	25 $\pm$ 4	100- 200
100	25	200	400	60	0.05 $\pm$ 0.01	21 $\pm$ 3	200- 250
100	30	200	400	90	0.07 $\pm$ 0.005	20 $\pm$ 2	200- 250
100	50	200	400	150	0.90	11 $\pm$ 1	250- 300
100	75	200	400	180	1.40	7.5 $\pm$ 0.5	350- 400
100	100	200	400	480	V(I) Non linear	3 $\pm$ 0.3	400- 430
50	12.5	200	400	60	0.90	22 $\pm$ 2	-
50	25	200	400	180	2.95	10.5 $\pm$ 1	250- 300
150	25	200	400	60	0.04	24 $\pm$ 3	-
150	37.5	200	400	60	0.05	21.5 $\pm$ 2	-
150	75	200	400	150	0.95	11 $\pm$ 1	250- 300
<b>AuGe (95:5 wt%)/Ni/Au, TM = Ni</b>							
100	25	200	-	-	-	-	250-300
100	30	200	400	90	0.17 $\pm$ 0.02	5.5 $\pm$ 0.5	250-300
100	50	200	-	-	-	-	350-400
<b>AuGe (97.3:2.7 wt%)/Ni/Au, TM = Ni</b>							
100	30	200	430	120	1.30	4.5 $\pm$ 0.5	400-430
<b>Pd (50nm)/Ge (100nm)</b>							
-	-	-	300	60	0.75 $\pm$ 0.10	2.0 $\pm$ 0.5	-

### Research Publications: (In referred international journals)

1. T.S. Abhilash, Ch. Ravi Kumar, G. Rajaram, "*Influence of Nickel layer thickness on the magnetic properties and contact resistance of AuGe/Ni/Au Ohmic contacts to GaAs/AlGaAs heterostructures*", **J. Phys. D: Appl. Phys.** **42** (2009) 125104 (8pp).
2. T. S. Abhilash, Ch. Ravi Kumar, B. Sreedhar and G. Rajaram, "*Dependence of melting, roughness and contact resistances on Ge and Ni content in alloyed AuGe/Ni/Au type electrical contacts to GaAs /AlGaAs multilayer structures*", **Semicond. Sci. Technol.** **25** (2010) 035002 (5pp).
3. T. S. Abhilash, Ch. Ravi Kumar, G. Rajaram, "*Nickel dissolution into AuGe in alloyed AuGe/Ni/Au Ohmic contacts on GaAs/AlGaAs multilayer structures*", **Thin Solid Films** **518** (2010) 5576-5578.

### International and National Conferences

4. T.S. Abhilash, Ch. Ravi Kumar and G. Rajaram, "*Magnetism, contact resistance and current conduction distribution in alloyed AuGe/Ni/Au Ohmic contacts on GaAs*", **Proceedings of the International workshop on Physics of Semiconductor devices (IWPSD-2009)**.
5. G. Rajaram, T. S. Abhilash, Ch. Ravi Kumar, B. P. C. Rao, Rita Saha, L. S. Vaidhyanathan, K. Gireesan, B. Sreedhar, M. P. Janawadkar, T. Jayakumar, and Baldev Raj, "*Magnetic field sensor using III-V multilayer structures: New insights into Ohmic contact formation to GaAs from magnetization measurements*", **Proceedings of the International workshop on Physics of Semiconductor devices (IWPSD-2009)**.
6. Ch. Ravi Kumar, T. S. Abhilash, B. P. C. Rao, S. Thirunavukkarasu, G. Rajaram, T. Jayakumar, and Baldev Raj, "*Development of micro Hall sensors for detection of magnetic flux leakage from defects in ferromagnetic materials*", **Proceedings of the International conference on Sensors and related networks (2007)** p-15.
7. T. S. Abhilash and G. Rajaram, "*Comparative study of AuGe/Au, AuGe/Ti/Au, AuGe/Cr/Au, AuGe/Ni/Au Ohmic contacts to GaAs/AlGaAs 2DEG structures*", **Proceedings of the DAE Solid State Physics Symposium (2004)** p- 530.
8. T. S. Abhilash, Ch. Ravi Kumar, G. Rajaram, Rita Saha, L. S. Vaidhyanathan, K. Gireesan and M. P. Janwadkar, "*High sensitivity micro Hall magnetic sensor using GaAs/AlGaAs heterostructures*", **Proceedings of the 11<sup>th</sup> National Seminar on Physics and Technology of Sensors (2006)** p- C 37-1.
9. T.S. Abhilash, Ch. Ravi Kumar and G. Rajaram, "*Optimization of non-magnetic alloyed Ohmic contacts to GaAs/AlGaAs structure for magnetic sensor*",

**Proceedings of the 12<sup>th</sup> National Seminar on Physics and technology of Sensors (2007) p- 191.**

10. T.S. Abhilash, Ch. Ravi Kumar, B. Sreedhar and G. Rajaram, "*Solid state dissolution of Ni into AuGe in AuGe/Ni/Au alloyed contacts to GaAs*", **Proceedings of the DAE Solid State Physics Symposium (2009) p- 651.**
11. T.S. Abhilash, Ch. Ravi Kumar, T. Geetha Kumary and G. Rajaram "*Reduction of surface roughness in AuGe/Ni/Au alloyed Ohmic contacts to GaAs/AlGaAs multilayer structures*", **Proceedings of the DAE Solid State Physics Symposium (2009) p- 959.**

**Other publications**

12. T.S. Abhilash, Ch. Ravi Kumar, P.V. Lajna, R. Tintu and G. Rajaram, "Wet chemical etching characteristics of GaAs and GaAs/AlGaAs using different etch solutions with some process variations", **Proceedings of the DAE Solid State Physics Symposium (2006) p- 359.**
13. Ch. Ravi Kumar, T.S. Abhilash, B. Uday Bhaskar, G. Rajaram, Rita Saha, L. S. Vaidhyanathan and K. Gireesan, "*Temperature correction to the magnetic sensitivity of a Hall magnetic sensor fabricated on implanted GaAs wafer*" **Proceedings of the DAE Solid State Physics Symposium (2004) p- 312.**
14. Ch. Ravi Kumar, T. S. Abhilash, G. Rajaram B. P. C. Rao, Rita Saha, K. A. Gopal, T. Jayakumar, M. P. Janwadkar, P.V. Kumar and Baldev Raj, "*Magnetic flux leakage measurement using 2DEG based Micro-Hall Sensors*", **Proceedings of the DAE Solid State Physics Symposium (2005) p- 901.**
15. Ch. Ravi Kumar, T. S. Abhilash, G. Rajaram B. P. C. Rao, T. Jayakumar and Baldev Raj, "*Development GaAs/AlGaAs micro Hall sensor for magnetic flux leakage measurements*", **Proceedings of the national seminar on Non Destructive Testing (2006).**
16. V. Ramaiah, A. K. Choudary, T. S. Abhilash and S. P. Tiwari, "*Characterization of photo conducting antenna on semi insulating GaAs using femto second laser*", **Proceedings of the National Laser symposium (NLS-2008).**

# Influence of Nickel layer thickness on the magnetic properties and contact resistance of AuGe/Ni/Au Ohmic contacts to GaAs/AlGaAs heterostructures

T S Abhilash<sup>1</sup>, Ch Ravi Kumar<sup>1,2</sup> and G Rajaram<sup>1,2</sup>

<sup>1</sup> School of Physics, University of Hyderabad, Hyderabad 500046, India

<sup>2</sup> Centre for Nanotechnology, University of Hyderabad, Hyderabad 500046, India

E-mail: [grrsp@uohyd.ernet.in](mailto:grrsp@uohyd.ernet.in)

Received 25 February 2009

Published 1 June 2009

Online at [stacks.iop.org/JPhysD/42/125104](http://stacks.iop.org/JPhysD/42/125104)

## Abstract

The magnetization of alloyed Ohmic contact film structures of the form AuGe/Ni/Au deposited on a GaAs/AlGaAs heterostructure substrate are reported as functions of Ni-layer thickness and alloying temperature. The observations are correlated with contact resistance and surface morphology studies. It is found that drops in magnetization, due to conversion of Ni to a non-magnetic phase or alloy, begin at anneal temperatures as low as 100 °C for all Ni-layer thicknesses. The conversion is completed at an anneal temperature,  $T_A$ , that increases with Ni-layer thickness.  $T_A$  varies from 100–200 °C to 400–430 °C as Ni-layer thickness is varied from 10 to 100 nm for an AuGe (88 : 12 wt%) layer thickness of 100 nm. The electrical contact formation, however, appears to begin at much higher temperatures than 100 °C. Lowest contact resistance ( $0.05 \pm 0.01 \, \Omega \, \text{mm}$ ) is obtained when Ni thickness is about 25 nm for 100 nm AuGe layer thickness, anneal temperature is 400 °C and anneal duration is 60 s. This contact is non-magnetic. Measurements on samples with other AuGe layer thicknesses suggest that the contact resistances are comparable to this optimum value, if the ratio of AuGe layer thickness to that of Ni is  $\geq 4$ . Increasing the Ni-layer thickness reduces the roughness of annealed contacts, but also increases contact resistance. The magnetic measurements are suggestive of a transformed Ni-layer thickness proportional to the thickness of the underlying AuGe layer. It is proposed that Ni diffuses into AuGe in a concentration limited diffusive mechanism followed by segregation into  $\text{Ni}_3\text{Ge}$ .

## 1. Introduction

GaAs/AlGaAs heterostructures, with a high mobility two-dimensional electron gas (2DEG) layer, are useful in the fabrication of electronic and optical devices for wireless and optical communication systems [1]. They are also used in the fabrication of Hall-effect based magnetic field sensors [2] in applications such as magnetic phase-diagram determination [3], magnetic microscopy [4] and non-destructive testing (NDT) [5]. Contact resistances to the semiconductor in such devices influence parameters such as the transconductance, power dissipation and sensor-output signal-to-noise ratio. The film roughness influences the minimum gate–drain separation that can be used in electronic devices when maximizing

bandwidth. In magnetic field sensors, the presence of ferromagnetic material, e.g. Ni, in the proximity of the sensor active area can, potentially, distort the measured field. Thus, reproducible, reliable Ohmic contacts to the 2DEG that have very low contact resistances, smooth surface, good thermal stability and, for sensor applications, no magnetism, are essential.

Contacts based on AuGe/Ni sandwich layers have been extensively used for fabricating Ohmic contacts in GaAs MESFETs [6], GaAs/AlGaAs and other heterostructures [7, 8]. These contacts are usually based on the preparation of an evaporated eutectic alloy film of AuGe (88 : 12 wt%) followed by a rapid-thermal anneal to a temperature of  $\sim 400^\circ\text{C}$ . The use of eutectic composition of the AuGe alloy results in low



**Table 1.** GaAs/AlGaAs wafer layer structure and Ohmic contact metallization.

	Au (200 nm)	
	Ni (10–100 nm)	
	AuGe (100 nm)	
n <sup>+</sup> (Si $1.5 \times 10^{18}$ ) GaAs	20 nm	Cap layer
n <sup>+</sup> (Si $1.5 \times 10^{18}$ ) Al <sub>0.3</sub> GaAs <sub>0.7</sub>	30 nm	Supply layer
Intrinsic AlGaAs	15 nm	Separation layer
Intrinsic GaAs	500 nm	(2DEG layer at i-GaAs/i-AlGaAs interface)
SI GaAs Substrate	500 $\mu$ m	

contact resistance, presumably due to enhanced diffusion of Ge into GaAs when the AuGe layer melts. This metallization, however, suffers from poor surface morphology [9]. The addition of a Ni layer and a thick Au overlayer is found to reduce, to some extent, the surface roughness during alloying [10]. Several studies have shown that, apart from the diffusion of various elemental components into GaAs, significant changes occur in the metal film structure itself that could potentially influence electrical contact formation. For example, TEM studies have shown the presence of binary and ternary compounds, Ni<sub>3</sub>Ge, Ni<sub>2</sub>GeAs and Au–Ga alloys. A correlation was reported between the formation of Ni<sub>2</sub>GeAs (between Au–Ga and GaAs) layers and low contact resistance [11].

Thick Ni layers are beneficial in improving morphology [12–14], which in turn, influences contact area. However, increasing the Ni-layer thickness may have other undesirable consequences: (a) unreacted Ni may make the structure ferromagnetic, (b) formation of compounds with Ni and Ge may deplete Ge and hence influence contact resistance. Study of the magnetism of annealed film structure, together with the contact resistance measurements, is not only of interest in magnetic field sensor fabrication but is also expected to give an insight into the sequence in which the processes involving Ge diffusion and compound formation occur. However, to our knowledge, no systematic studies have been reported on the magnetic properties and its dependence on processing conditions. In this paper, we report the dependence of magnetization, surface roughness and the contact resistance of alloyed AuGe/Ni/Au contacts on GaAs/AlGaAs multilayers on the following process parameters: Ni-layer thickness (for a fixed AuGe layer thickness of  $\sim 100$  nm), anneal temperature ( $T_A$ ) and anneal duration ( $t_A$ ) of post-deposition anneal. We also report similar measurements with three different AuGe film thicknesses (and hence AuGe/Ni ratio).

## 2. Experimental details

The GaAs/AlGaAs multilayer structure used in this study is grown by molecular beam epitaxy (MBE) and has the structure given in table 1. The sheet carrier density and electron mobility of the 2DEG are  $\sim 3.4 \times 10^{11} \text{ cm}^{-2}$  and  $\sim 7800 \text{ cm}^2 \text{ V}^{-1} \text{ s}^{-1}$ , respectively, at 300 K. The corresponding values at 77 K are  $\sim 4.5 \times 10^{11} \text{ cm}^{-2}$  and  $\sim 1.4 \times 10^5 \text{ cm}^2 \text{ V}^{-1} \text{ s}^{-1}$ .

The contact resistance of the alloyed contacts is estimated using transmission line model (TLM) [15]. In this method, measurements of the voltage-to-current ratio ( $R_d = V/I$ ) are made between adjacent pads of an array of alloyed contacts on a semiconductor strip. The separation,  $d$ , between adjacent pads varies, typically as  $d_0, 2d_0, 4d_0, \dots, 2nd_0, \dots$ , etc. The resistance  $V_n/I = R_n$  is expected to be linear with  $d$  or  $n$  extrapolating to  $2R_c/w$  at  $n = 0$  (i.e.  $d = 0$ ), where  $R_c$  is the contact resistance (measured in  $\Omega \text{ mm}$ ) for unit width normal to current flow and  $w$  is the pad width on the semiconductor, normal to current flow. A TLM structure with pad size  $l = 0.1 \text{ mm}$ ,  $w = 0.4 \text{ mm}$  and varying pad spacings— $d = 0.025, 0.05, 0.1, 0.2, 0.4 \text{ mm}$ —was fabricated as follows. The GaAs/AlGaAs substrates were chemically cleaned and mesa strips of length 3.0 mm and width 0.4 mm defined by  $\text{H}_3\text{PO}_4 : \text{H}_2\text{O}_2 : \text{H}_2\text{O}$  etch. The TLM structures were patterned on photoresist using i-line photolithography. The substrates were sputter cleaned in  $\text{O}_2$  plasma and a metal sandwich layer structure AuGe (100 nm)/Ni( $x$  nm)/Au (200 nm), where  $x = 10, 25, 30, 50, 75, 100 \text{ nm}$ , deposited on the GaAs/AlGaAs wafer (table 1). AuGe alloy (88 : 12 wt%) is deposited first using thermal evaporation, then Ni using e-beam evaporation and finally Au by thermal evaporation. The thickness and growth rates of AuGe, Ni and Au films were monitored *in situ* by a quartz crystal oscillator and verified using a surface profiler. This was followed by lift-off of the photoresist. The substrates with the TLM patterns were annealed to a specific anneal temperature  $T_A$ , in  $\text{N}_2$  ambient for different durations after ramping up the temperature at a heating rate of  $250^\circ \text{C min}^{-1}$ . The temperature was monitored using a data logger, on a symmetrically placed dummy wafer piece during the anneal. The wafer is heated using lamp-heating from the bottom; i.e. the wafer side.  $I$ – $V$  characteristics at various pads are measured using a wafer-prober and device analyzer with probe currents in the range  $\pm 0.5 \text{ mA}$ . The surfaces of the annealed contact pads are examined by scanning electron microscopy (SEM), energy dispersive x-ray analysis (EDX) and atomic force microscopy (AFM). The roughness is computed using the root-mean-square height of the sample over an area of about  $5 \mu\text{m} \times 5 \mu\text{m}$  of the dynamic force microscopy (DFM) topography data. The data have been repeated at several pads of the TLM structure.

The magnetization hysteresis loops of the alloy structures were measured using a vibrating sample magnetometer (VSM), with a magnetic moment resolution of  $10^{-6} \text{ emu}$ . The



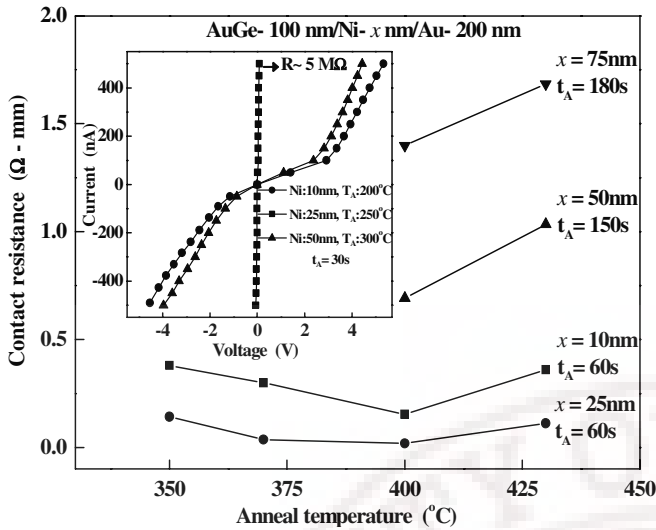


**Figure 1.** Contact resistance as a function of anneal temperature for varying Ni thicknesses. Inset shows typical  $I$ - $V$  curves for low temperature annealed contacts. The lines are a guide to the eye.

measurements were carried out in sweep mode to 5 kG with the magnetic field applied parallel to the film plane. Pieces of GaAs/AlGaAs wafer with area 4 mm<sup>2</sup> were metallized with the structure AuGe (100 nm)/Ni ( $x$  nm)/Au (200 nm),  $x = 10, 25, 50, 75, 100$ . The pieces were rapid thermal annealed at 100, 200, 250, 300, 400 and 430 °C followed by the magnetic hysteresis loop measurements using VSM at room temperature. Background due to a sample of the same mass, but without the film structure, was subtracted and the resultant data was normalized by the magnetization of the as-deposited film structure.

The contact resistance and surface roughness studies were performed on another set of samples with differing AuGe layer thickness. The film layer structure was AuGe ( $y$  nm)/Ni ( $z$  nm)/Au (200 nm), where  $y = 50, 100, 150$  nm and  $z = 37.5$  and 75 nm. Yet another sample with  $y = 150$  nm,  $z = 25$  nm, was also studied. The top Au layer thickness was kept constant at 200 nm, in all the films.

### 3. Experimental results

#### 3.1. Electrical characteristics

Figure 1 summarizes the contact resistance,  $R_c$ , as a function of anneal temperature for varying Ni-layer thicknesses for optimized anneal durations. Some measured  $I$ - $V$  curves for lower anneal temperatures are shown in the inset.

The main results are:

- (1) The contacts with Ni-layer thickness, 100 nm, show a non-linear, large resistance ( $\sim 4$  M $\Omega$ ) for long duration anneals ( $\sim 10$  min). Shorter anneals ( $< 4$  min) at all temperatures up to 430 °C, resulted in a diode-like characteristic similar to those obtained for samples with smaller Ni-layer thickness annealed at low temperature (inset of figure 1).
- (2) The contacts with nickel layer thicknesses 50 and 75 nm show diode-like behaviour when annealed at

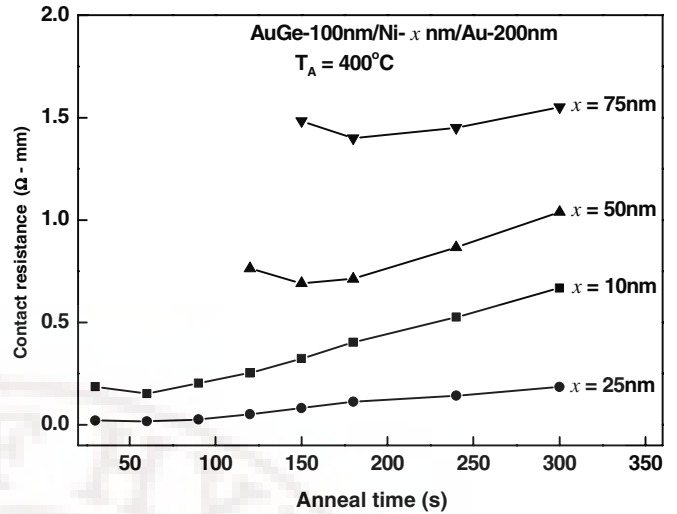


**Figure 2.** Contact resistances as a function of anneal time for different Ni-layer thicknesses.

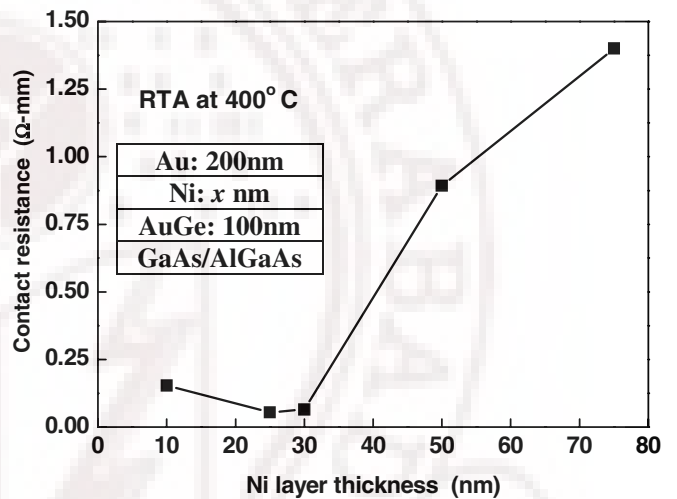


**Figure 3.** Contact resistance at the optimized anneal temperature and time versus Ni layer-thickness.

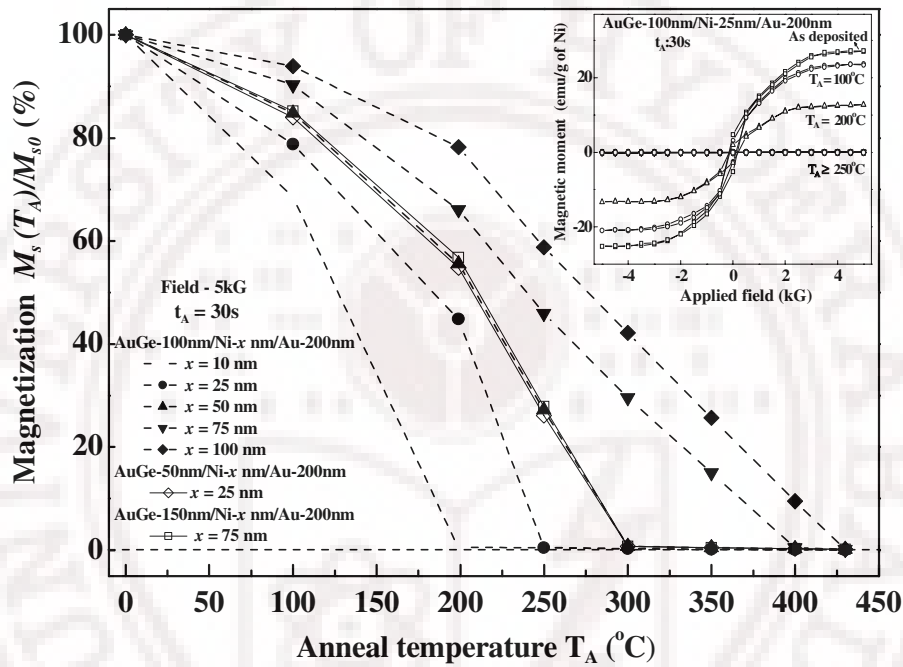
temperatures below 400 °C and Ohmic behaviour for anneal temperatures above 400 °C.

- (3) The contacts with Ni-layer thicknesses 25 and 10 nm show Ohmic behaviour for anneal temperatures above 350 °C

Annealing at 430 °C is found to increase the contact resistance marginally for Ni-layer thicknesses 10, 25, 50 and 75 nm. The lowest, or optimum, contact resistance is observed for anneal temperatures  $\sim 400$  °C for each of the Ni-layer thicknesses 10, 25, 50, 75 nm (table 2). Dependence of  $R_c$  on Ni-layer thickness, optimized with respect to anneal temperature and time, is shown in figure 3. Among these, the lowest contact resistance of  $0.05 \pm 0.01$   $\Omega$  mm is observed for AuGe/Ni/Au configuration with Ni-layer thickness 25 nm, for a 60 s anneal. The quoted error is the rms deviation over several separate deposition runs. The dependence of the contact resistance of AuGe/Ni/Au alloyed contacts on anneal durations with various Ni-layer thicknesses is shown in figure 2. These results indicate that if the Ni-layer thickness is increased, a larger anneal time is required to optimize the

**Table 2.** Optimum anneal temperatures and durations, contact resistance, surface roughness and the magnetic-to-non-magnetic transition temperature, for various Ni-layer thicknesses.

Nickel layer thickness (nm)	Optimum anneal temperature (°C)	Optimum anneal duration (s)	Contact resistance ( $\Omega$ mm)	Surface roughness (nm)	Anneal temperature for conversion of magnetic phase to non-magnetic phase (°C)
10	400	60	0.15	$25 \pm 4$	100–200
25	400	60	$0.05 \pm 0.01$	$21 \pm 3$	200–250
30	400	90	0.065	$20 \pm 2$	200–250
50	400	150	0.90	$11 \pm 1$	250–300
75	400	180	1.40	$7.5 \pm 0.5$	350–400
100	400	480	$V(I)$ Non-linear	$3 \pm 0.3$	400–430

**Figure 4.** Anneal temperature dependence of saturation magnetization of alloyed structures of the form AuGe (100 nm)/Ni =  $x$  nm/Au (200 nm) on GaAs multilayer, for  $x = 10, 25, 50, 75$  and 100 nm. Data for a structure AuGe (50 nm)/Ni (25 nm)/Au (200 nm) and AuGe (150 nm)/Ni (75 nm)/Au (200 nm) are also included.  $M_{s0}$  is the saturation magnetization of the as-deposited sample at 5 kG. The anneal duration is 30 s. Inset shows typical hysteresis loops.

contact resistance. Table 2 summarizes data for processing conditions that optimize contact resistance. The roughness obtained under these processing conditions is also given in table 2.

### 3.2. Magnetic properties

Figure 4 shows the saturation magnetization (measured at an applied field of 5 kG) of samples with the metal film structure, as a function of anneal temperature. The magnetization data are presented as a percentage of the magnetization of the as-deposited (un-annealed) sample. The inset of this figure shows typical evolution of the magnetization hysteresis loops for the sample with 25 nm Ni-layer thickness, on annealing at various temperatures. The results show that the metallization structure becomes progressively less magnetic as the anneal temperature is increased. Remarkably, substantial decreases in magnetization occur even for anneal temperatures as low as 100 °C. The structure becomes completely non-magnetic on

annealing at or above a temperature which varies from 200 to 430 °C as the Ni-layer thickness varies from 10 to 100 nm. The minimum anneal temperature required to complete the transformation to a non-magnetic phase is not known precisely but lies in the range given in table 2. It is noted that all samples with Ni-layer thickness  $\leq 75$  nm become non-magnetic on annealing at a temperature of 400 °C, a commonly used anneal temperature in alloyed Ohmic contact recipes (table 2).

### 3.3. Surface morphology

Figure 5 display typical AFM images of the annealed samples for two different Ni-layer thicknesses (25 and 100 nm). Table 2 gives the rms surface roughness computed over the scanned surface. The surface roughness decreases monotonically with the increase in Ni-layer thickness. They are in the range 30–3 nm for Ni-layer thickness 10–100 nm.

SEM micrographs of alloyed samples are shown in figure 6. EDX analysis indicates that the bright and dark

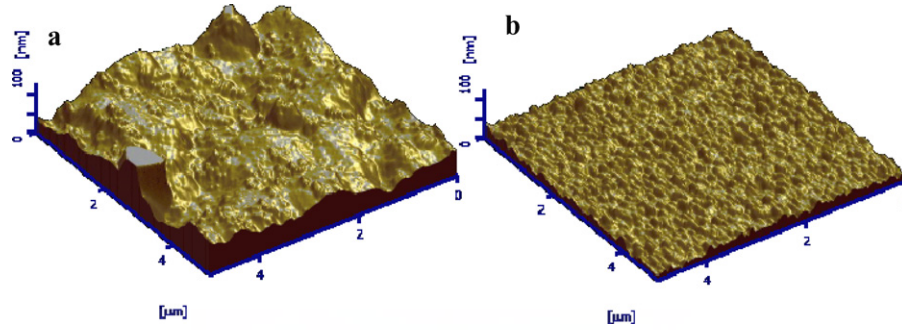


**Figure 5.** AFM micrographs ( $5\ \mu\text{m} \times 5\ \mu\text{m}$ ) of the surface of AuGe/Ni( $x$ )/Au, (a)  $x = 25\ \text{nm}$ , (b)  $100\ \text{nm}$  annealed at  $400\ ^\circ\text{C}$  for durations that gave the lowest contact resistance.

(This figure is in colour only in the electronic version)

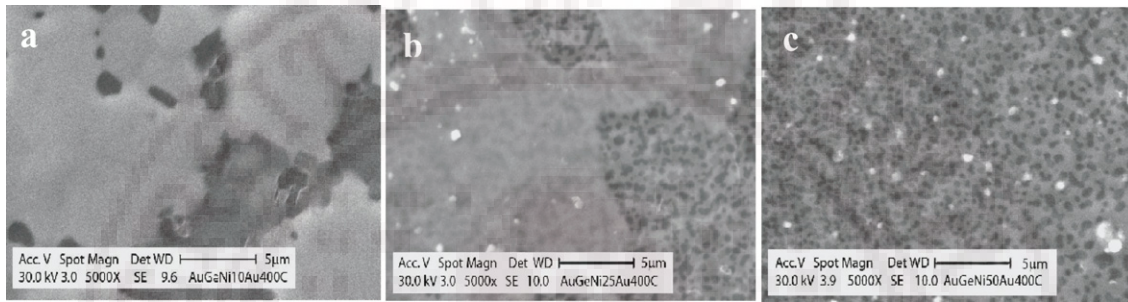


**Figure 6.** SEM micrographs of the surface of AuGe/Ni( $x$ )/Au,  $x = 10\ \text{nm}$  (a),  $25\ \text{nm}$  (b),  $50\ \text{nm}$  (c), annealed at  $400\ ^\circ\text{C}$  for durations that gave the lowest contact resistance.

**Table 3.** Anneal temperatures and durations optimized for the lowest contact resistance, the contact resistance and surface roughness, for various AuGe thicknesses and different Ni/AuGe ratios.

	AuGe thickness (y nm)						
	50		100		150		
Ni thickness (z nm)	12.5	25	25	50	25	37.5	75
Ni/AuGe thickness ratio (z/y)	0.25	0.5	0.25	0.5	0.167	0.25	0.5
Optimum anneal temperature ( $^\circ\text{C}$ )	400	400	400	400	400	400	400
Optimum anneal time (s)	60	180	60	150	60	60	150
Contact resistance ( $\Omega\ \text{mm}$ )	0.90	2.95	$0.05 \pm 0.01$	0.9	0.04	0.05	0.95
Surface roughness (nm)	$22 \pm 2$	$10.5 \pm 1$	$21 \pm 3$	$11 \pm 1$	$24 \pm 3$	$21.5 \pm 2$	$11 \pm 1$
Anneal temperature for conversion of magnetic phase to non-magnetic phase ( $^\circ\text{C}$ )	250–300		200–250		250–300		

regions in these micrographs are Au rich and Au-poor regions, respectively. As the Ni-layer thickness is increased, agglomerations on a much smaller scale are seen in the ‘dark’ regions. This structure eventually covers the entire surface for Ni-layer thickness  $> 50\ \text{nm}$ .

### 3.4. Varying Ni-to-AuGe layer thickness ratios

The data discussed in the previous section correspond to samples with a fixed AuGe layer thickness of  $100\ \text{nm}$ . A few measurements were also performed on samples with other AuGe thicknesses— $50$  and  $150\ \text{nm}$ . The motivation was to determine if the Ni-layer thickness to AuGe layer thickness ratio was influential in determining contact resistance, roughness (as suggested in some studies [16]) and magnetic properties. From the results summarized in table 3, it appears that this indeed is the case. It is found that

the magnetic behaviours of the samples with structures AuGe ( $150\ \text{nm}$ )/Ni ( $75\ \text{nm}$ )/Au ( $200\ \text{nm}$ ), AuGe ( $100\ \text{nm}$ )/Ni ( $50\ \text{nm}$ )/Au ( $200\ \text{nm}$ ) and AuGe ( $50\ \text{nm}$ )/Ni ( $25\ \text{nm}$ )/Au ( $200\ \text{nm}$ ) are virtually identical when the magnetization data, plotted against anneal temperatures, are normalized by the magnetization of as-deposited sample (figure 4). Contact resistances close to the optimum are obtained if the Ni-to-AuGe layer thickness ratio is about  $0.25$  or less (with the exception of samples with low AuGe thickness). The surface roughness too, appears to depend on the Ni and AuGe layer thicknesses through their ratio. Process conditions used frequently in practice, namely,  $400\ ^\circ\text{C}$  anneal for a minute, result in a non-magnetic contact structure with the contact resistance close to the optimum ( $\sim 0.04\ \Omega\ \text{mm}$ ). This also requires that AuGe thickness is larger than  $50\ \text{nm}$ , and thickness ratio of Ni/AuGe less than  $0.5$ , conditions that are usually met in practice. Total film thickness of  $\sim 450\ \text{nm}$  approaches the maximum suitable



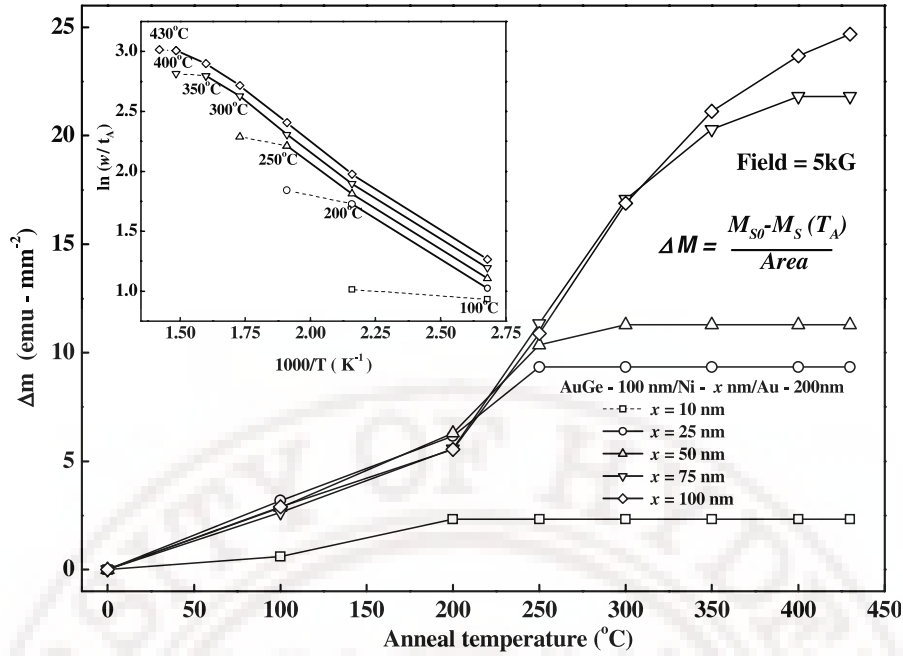


**Figure 7.** Decrease in magnetization per unit area as a function of anneal temperature. The inset shows the logarithmic plots of the Ni-layer conversion rate ( $w/t_A$ ) versus reciprocal of the anneal temperature.  $w$  is the thickness of Ni layer transformed into non-magnetic phase estimated from the magnetization data.

for a lift-off patterning process with a typical photoresist thickness of 1  $\mu\text{m}$ .

#### 4. Discussions

A significant result of the study is that under conditions normally used for obtaining Ohmic contacts with an AuGe/Ni( $x$  nm)/Au metallization structure, Ni is rendered non-magnetic after processing. The magnetization data of table 2 indicates that the samples with Ni-layer thickness of  $\sim 10$ – $100$  nm are non-magnetic at room temperature, after the metal film structure is annealed at  $430^{\circ}\text{C}$  for  $x = 100$  nm and  $400^{\circ}\text{C}$  for  $x = 10$ – $75$  nm. These are the temperatures most commonly used for Ohmic contact formation using AuGe. Use of excessively large Ni-layer thickness for improved surface morphology; however, results in an increase in the contact resistance, apart from requiring higher anneal temperatures to render the film structure non-magnetic. TEM data reported in the literature [12, 17–19] indicate the formation of paramagnetic compounds such as  $\text{Ni}_3\text{Ge}$  and  $\text{Ni}_2\text{GeAs}$  in annealed AuGe/Ni structures. It is apparent, from the magnetization data presented here, that the transformation of ferromagnetic Ni to a non-magnetic compound or alloy begins at temperatures as low as  $100^{\circ}\text{C}$  in all the samples. The contact resistance is still quite high at these temperatures (inset of figure 1).

The magnetization data offer some insight into the changes that occur in the metallization structure during processing. The samples with structures AuGe (50 nm)/Ni (25 nm)/Au (200 nm), AuGe (100 nm)/Ni (50 nm)/Au (200 nm) and AuGe (150 nm)/Ni (75 nm)/Au (200 nm) have nearly identical magnetic behaviours (figure 4). The Ni : AuGe layer thickness ratio, rather than the Ni-layer thickness itself appears to

determine the magnetic fraction remaining after the anneal. This in turn implies that the transformed Ni-layer thickness is proportional to the AuGe layer thickness, independent of the Ni-layer thickness. This is confirmed by figure 7 which displays a quantity proportional to the transformed Ni-layer thickness, after anneals at different temperatures. It shows that the transformed Ni-layer thickness is independent of Ni concentration until all the Ni is transformed to the non-magnetic phase (except the 10 nm Ni layer). These two factors, i.e. the independence of  $\Delta M$  of Ni-layer thickness and its proportionality with AuGe layer thickness, imply that Ni diffuses into solution in AuGe and this process is limited by the concentration of Ni in the AuGe. In this picture, the temperature dependence of transformed layer thickness seen in figure 7 could be a reflection of the temperature dependence of the solubility of Ni in AuGe. Cooling the sample could result in nearly complete segregation of Ni and formation of  $\text{Ni}_3\text{Ge}$ , including at the GaAs surface, as indicated by TEM studies [12].

The rate of transformation of Ni to the non-magnetic phase shows Arrhenius behaviour (inset of figure 7) with a low temperature activation energy ( $\sim 0.12$  eV) that is apparently independent of Ni-layer thickness. In the scenario described above, the activation energy might correspond to that required for Ni diffusion into AuGe. The activation energy changes to a lower value at a temperature that increases with Ni-layer thickness. The cause of this decrease is not clear. One possibility is the phase segregation of  $\text{Ni}_3\text{Ge}$  at the Ni–AuGe interface, at large Ni-layer thicknesses.

As far as electrical contact is concerned, experimental data clearly indicate that Ni layer is beneficial in low thickness, for Ohmic contact formation, i.e. 25–30 nm Ni-layer thickness for a 100 nm Au–Ge layer thickness (figure 3). Moreover,

it is the ratio of thicknesses of the Ni and AuGe layers  $\leq \sim 0.25$  that seem to determine the contact resistance as evidenced by the data on samples with other AuGe layer thicknesses (table 3). (Small increase in contact resistance at very low Ni-layer thickness— $\sim 10$  nm—is probably due to the Ni-layer's non-conformal coverage of the AuGe layer and resulting agglomeration effects on annealing as in figure 6.) This is consistent with previous findings on alloyed Ohmic contacts to AlGaAs/GaAs heterostructures [20]. Our contact resistance data on similar structures but without the Ni-layer are two orders of magnitude higher than for structures with Ni layers but of low ( $< 50$  nm) thicknesses. The ratio of the number of atoms per unit area of Ge to Ni at this Ni-layer thickness (25 nm), for the AuGe thickness of 100 nm, comes to approximately 1. Procedures utilizing separate Ge, Au and Ni layers [13], find optimum contact resistance formation around 1 : 1 for the Ge : Ni-layer thickness ratio which corresponds to 1 : 2 for the atom areal density ratio. Moreover under these conditions, the contact resistance variations with the process parameters, Ni layer thickness, anneal temperature and time corresponds to a reasonably shallow minimum.

The surface roughness is, however, quite sensitive to Ni-layer thicknesses, decreasing steadily with increase in Ni-layer thickness. *In situ* x-ray diffraction studies [21] reveal the formation of Au–Ga compounds on annealing wafers with Au or AuGe layers deposited on GaAs. The Au–Ga compounds formation is reported to begin at temperatures  $> 500^\circ\text{C}$  for Au layers and in the case of Au–Ge alloy layers when the alloy layer melts ( $\sim 360^\circ\text{C}$ ) [12, 21, 22]. Their formation has been interpreted to be the cause for deterioration of the surface morphology of the contacts. This study also reveals that the presence of low thickness Ni layers ( $\sim 10$  nm) does not significantly affect the temperature of formation of Au–Ga compounds nor their melting temperatures determined from the re-heating runs. However, the presence of thicker Ni layers ( $\sim 50$  nm) results in an increase in both these temperatures. Ni dissolution into Au–Ge on annealing, as suggested by this study, presumably increases both the melting temperature of Au–Ge layer and that of the Au–Ga compounds after their formation. This would then explain decrease in surface roughness with increasing Ni-layer thickness. Another contributing factor could be the influence of concentration of Ni in AuGe on nucleation and grain growth of the  $\text{Ni}_3\text{Ge}$  phase. A larger Ni-layer thickness could result in higher density of nucleation centres, and consequently, a small grain size, for a  $\text{Ni}_3\text{Ge}$  phase. This latter effect could also be invoked to explain the increase in contact resistance with increasing Ni-layer thickness. It has been suggested that  $\text{NiAs}(\text{Ge})$  that is observed to form at relatively high temperatures ( $> 400^\circ\text{C}$ ) is essential for Ohmic contact formation in one of two ways: (1) reduction in barrier height between a postulated  $\text{Ge}^{n+}$  layer on GaAs and AuGa layer due to an intervening  $\text{NiAs}(\text{Ge})$  and (2) tunnelling through a narrow depletion barrier due to a structure  $\text{AuGa}/\text{NiAs}(\text{Ge})/n^+\text{GaAs}$  [6, 12, 18, 23]. Formation of  $\text{Ni}_3\text{Ge}$  at the expense of  $\text{NiAs}(\text{Ge})$ , on increasing Ni-layer thickness is a possibility that might result in an increase in contact resistance. The increase in contact resistance over the optimum value with increase in anneal time or anneal temperature has

been attributed to several causes: (i) out diffusion of As from GaAs and change in Ge : As ratio to an As-rich one (ii) increase in area covered by Au–Ga over that by  $\text{NiAs}(\text{Ge})$  [12, 24].

## 5. Conclusions

Magnetization hysteresis studies on commonly used metallization of the form AuGe/Ni/Au on GaAs/AlGaAs multi-layers indicate that all metallizations are non-magnetic at room temperature after annealing at  $400^\circ\text{C}$  ( $430^\circ\text{C}$  for Ni-layer thickness 100 nm). Conversion of Ni to non-magnetic phase, begins for anneals at temperatures as low as  $100^\circ\text{C}$  and is completed at an anneal temperature that increases with Ni-layer thickness. This process precedes the decrease in contact resistance to the sub-M $\Omega$  range. Systematic studies of the variation of the contact resistance with Ni-layer thickness on a sample with Au–Ge layer thickness of 100 nm indicate that the lowest contact resistance of  $(0.05 \pm 0.01 \Omega \text{ mm})$  is obtained at a Ni-layer thickness of 25 nm when annealed at  $400^\circ\text{C}$ . At low Ni-layer thickness ( $< 25$  nm), slight increase in contact resistance is observed relative to the optimum, probably due to a decrease in contact area resulting from the surface roughening. Increasing the Ni-layer thickness reduces roughness of annealed contacts, but increases contact resistance. Measurements on samples with other AuGe layer thicknesses suggest that the contact resistances are comparable to this optimum value, if the Ni-to-AuGe layer thickness ratio is about 0.25 or less. The fraction of Ni remaining magnetic as a function of anneal temperature is nearly identical for samples with structures AuGe (150 nm)/Ni (75 nm)/Au (200 nm), AuGe (100 nm)/Ni (50 nm)/Au (200 nm) and AuGe (50 nm)/Ni (25 nm)/Au (200 nm). The effective thickness of Ni layer converted into non-magnetic phase is independent of Ni-layer thickness for constant AuGe layer thickness, until complete conversion. These results are suggestive of Ni solubility limited diffusion into AuGe layer followed by the possible segregation and formation of  $\text{Ni}_3\text{Ge}$ .

## Acknowledgments

Support of UGC (UPE, CAS programmes), BRNS/DAE, IGCAR, DST (Centre for Nanotechnology) is acknowledged.

## References

- [1] Lafontaine H, Haghiri-Gosnet A M, Jin Y, Crozat P, Adde R, Chaker M, Pepin H, Rousseaux F and Launois H 1996 *IEEE Trans. Electron Devices* **43** 175
- [2] Sugiyama Y 1995 *J. Vac. Sci. Technol. B* **13** 1075
- [3] Yamaguchi Y, Rajaram G, Shirakawa N, Mumtaz A, Obara H, Nakagawa T and Bando H 2000 *Phys. Rev. B* **63** 014504
- [4] Sandhu A, Masuda H, Oral A and Bending S J 2001 *Japan. J. Appl. Phys.* **40** 4321
- [5] Connor S O, Clapham L and Wild P 2002 *Meas. Sci. Technol.* **13** 157
- [6] Braslau N, Gunn J B and Staples J L 1967 *Solid State Electron.* **10** 381
- [7] Goronkin H, Tehrani S, Rimmel T, Feies P L and Johnson K J 1989 *IEEE Trans. Electron Devices* **36** 281

- [8] Rai A K, Ezis A, Graham R J, Sharma R and Langer D W 1988 *J. Appl. Phys.* **63** 4723
- [9] Gyulai J, Mayer J W, Rodriguez V, Yu A Y C and Gopen H J 1971 *J. Appl. Phys.* **42** 3578
- [10] Robinson G Y 1975 *Solid State Electron.* **18** 331
- [11] Murakami M, Childs K D, Baker J M and Callegari A C 1986 *J. Vac. Sci. Technol. B* **4** 903
- [12] Murakami M 2002 *Sci. Technol. Adv. Mater.* **3** 1
- [13] Soo-Jin Chua and Seng Hin Lee 1994 *Japan. J. Appl. Phys.* **33** 66
- [14] Bühlmann H J and Ilegems M 1991 *J. Electrochem. Soc.* **138** 2795
- [15] Berger H H 1972 *Solid State Electron.* **15** 145
- [16] Lin H-C, Senanayake S and Cheng K-Y 2003 *IEEE Trans. Electron Devices* **50** 880
- [17] Kuan T S, Batson P E, Jackson T N, Rupprecht H and Wilkie E L 1983 *J. Appl. Phys.* **54** 6952
- [18] Shen T C, Gao G B and Morkoc H 1992 *J. Vac. Sci. Technol. B* **10** 2113
- [19] Baca A G, Ren F, Zolper J C, Briggs R D and Pearton S J 1997 *Thin Solid Films* **308** 599
- [20] Goktas O, Weber J, Weis J and Klaus von Klitzing 2008 *Physica E* **40** 1579
- [21] T Kim and D D L Chung 1986 *Thin Solid Films* **147** 177
- [22] Ball R K 1989 *Thin Solid Films* **176** 55
- [23] Marshall E D, Zhang B, Wang L C, Jiao P F, Chen W X, Sawada T and Lau S S 1987 *J. Appl. Phys.* **62** 942
- [24] Shih Y C, Murakami M, Wilkie E L and Callegari A C 1987 *J. Appl. Phys.* **62** 582



# Dependence of melting, roughness and contact resistances on Ge and Ni content in alloyed AuGe/Ni/Au-type electrical contacts to GaAs/AlGaAs multilayer structures

T S Abhilash<sup>1</sup>, Ch Ravi Kumar<sup>1</sup>, B Sreedhar<sup>2</sup> and G Rajaram<sup>1</sup>

<sup>1</sup> School of Physics and Centre for Nanotechnology, University of Hyderabad, Hyderabad 500 046, India

<sup>2</sup> Inorganic and Physical Chemistry Division, Indian Institute of Chemical Technology, Hyderabad 500 007, India

E-mail: [grrsp@uohyd.ernet.in](mailto:grrsp@uohyd.ernet.in)

Received 3 October 2009, in final form 19 November 2009

Published 29 January 2010

Online at [stacks.iop.org/SST/25/035002](http://stacks.iop.org/SST/25/035002)

## Abstract

Annealed AuGe/Ni/Au film structures on GaAs/AlGaAs multilayers have been examined for contact resistance, roughness, magnetization and melting as functions of anneal temperature, Ni-layer thickness and three AuGe compositions. Magnetization data indicate that a solid state, solubility-limited dissolution of Ni into AuGe takes place even for low-temperature anneals and that this dissolution is complete when alloying occurs at  $\sim 400^\circ\text{C}$ . An apparent melting temperature, detected in differential scanning calorimetry, increases with increasing Ni-layer thickness and decreasing Ge content in the AuGe alloy. Electrical contact formation and roughening of the surface occur in the range of melting temperatures of the structure. The eutectic alloy with a Ni-layer thickness of  $\sim 25\text{--}30\text{ nm}$  gives the optimum contact resistance. The contact resistance can be traded off for the reduction in roughness by either increasing the Ni-layer thickness or reducing the Ge content, with the latter being the better choice of the two. The temperature dependence ( $4\text{--}300\text{ K}$ ) of the contact resistance shows indications of both thermionic and tunneling behaviors. The barrier height for the current conduction increases with the increase of the Ni-layer thickness and a decrease of the Ge content in the AuGe layer, relative to that of the structure with optimum contact resistance.

(Some figures in this article are in colour only in the electronic version)

## 1. Introduction

III–V compound multilayer structures, such as GaAs/AlGaAs and AlGaAs/InGaAs, incorporating the two-dimensional electron gas (2DEG) layer, are useful for the fabrication of devices [1–3] such as optical devices, high electron mobility transistors (HEMTs) and high sensitivity Hall-effect magnetic field sensors. The structures usually incorporate an  $n^+$  GaAs cap layer that is useful in the formation of ohmic contacts. A widely used recipe for the realization of low-resistance ohmic contacts to these structures is the deposition of AuGe/Ni/Au

multilayer metallization [4–6] followed by a rapid thermal anneal to facilitate alloying. The recipe gives low contact resistances in the region of  $0.03\text{--}0.1\ \Omega\text{ mm}$ ; however, this is achieved at the expense of an increased surface roughness [7], a factor that influences the transistor gate fabrication. The surface roughness can be reduced by increasing the Ni-layer thickness or decreasing the Ge content below that of the eutectic composition (88:12 wt%), albeit at the expense of increasing the contact resistance [8–12].

Residual magnetism, if any, of the processed metallization structure, is relevant to the magnetic field sensor application.



**Table 1.** GaAs/AlGaAs wafer layer structure and ohmic contact metallization.

Au (200 nm)		
Ni (30 nm–75 nm)		
Eutectic/off-eutectic AuGe alloy (100 nm)		
$n^+$ (Si $1.5 \times 10^{18}$ ) GaAs	20 nm	Cap layer
$n^+$ (Si $1.5 \times 10^{18}$ ) $\text{Al}_{0.3}\text{GaAs}_{0.7}$	30 nm	Supply layer
Intrinsic AlGaAs	15 nm	Separation layer
Intrinsic GaAs	500 nm	(2DEG layer)
SI GaAs substrate	500 $\mu\text{m}$	

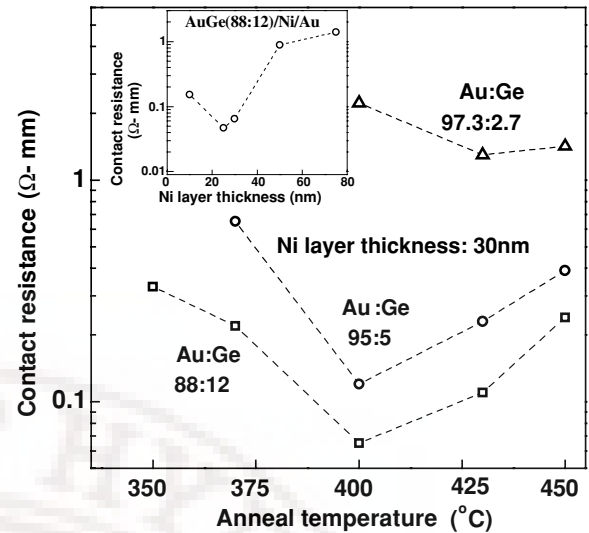
Our efforts to track the contact resistance and magnetism of the structures, while optimizing process parameters such as anneal temperatures and Ni-layer thicknesses, revealed that the solid phase dissolution of Ni into AuGe takes place at temperatures much lower than that at which alloying takes place [12]. In this paper we report the results of magnetization, contact resistance and roughness studies and also of melting in the metallization structure, as the Ge content and Ni-layer thickness are varied. The temperature dependence (4–300 K) of the contact resistance was undertaken on a few samples to study the changes in the electrical contact mechanism and also in the context of low-temperature applications of the magnetic field sensor.

## 2. Experimental details

Three contact metallization structures—with eutectic (88:12 wt%) and off-eutectic (95:5 and 97.3:2.7 wt%) compositions of the AuGe alloy—were investigated. The alloyed contacts were prepared by evaporating AuGe (100 nm)/Ni (30 nm)/Au (200 nm) using thermal and e-beam evaporation, onto wafer pieces with a multilayer structure as shown in table 1. The sheet carrier density and electron mobility of a two-dimensional electron gas are  $\sim 3.4 \times 10^{11} \text{ cm}^{-2}$  and  $\sim 7800 \text{ cm}^2 \text{ V}^{-1} \text{ s}^{-1}$ , respectively, at 300 K and  $\sim 4.5 \times 10^{11} \text{ cm}^{-2}$  and  $\sim 1.4 \times 10^5 \text{ cm}^2 \text{ V}^{-1} \text{ s}^{-1}$  at 77 K.

The samples were then subjected to anneal at a temperature  $T_A$  reached at the heating rates of  $250^\circ\text{C min}^{-1}$ , held at  $T_A$  for durations  $t_A$  in  $\text{N}_2$  atmosphere. Magnetization hysteresis loops of samples with the annealed contact structures with several Ni layers thicknesses were measured using a vibrating sample magnetometer (VSM).

The contact resistances were measured from room temperature to 4 K on samples lithographically patterned for use of the transmission line or transfer length model (TLM) [12, 13]. One was a sample with the eutectic AuGe layer, namely AuGe (88:12 wt%)/Ni (30 nm)/Au whose contact resistance is close to the optimum. The other two samples were those in which the roughness was reduced—one by increasing the Ni-layer thickness to 50 nm and the other by using an AuGe layer composition of 95:5 wt%. Temperature scans of differential scanning calorimetry (DSC) were performed on the metallized substrate, with a bare substrate as the reference. The scan spanned from room temperature to  $500^\circ\text{C}$  at a heating rate of  $100^\circ\text{C min}^{-1}$ . The surface roughness was estimated by measuring the root-mean-square height of the sample over

**Figure 1.** Contact resistances versus anneal temperature for three AuGe alloy compositions.

an area of about  $5 \mu\text{m} \times 5 \mu\text{m}$ , at several pads of the TLM structure using dynamic force microscopy (DFM).

## 3. Results and discussion

Figure 1 summarizes the contact resistance,  $R_C$ , as a function of the anneal temperature,  $T_A$ , for three AuGe alloy compositions for the optimized anneal durations,  $t_A$ . The  $R_C$  dependence on the Ni-layer thickness, optimized with respect to anneal temperature and time, for the eutectic AuGe alloy is shown in the inset.

$R_C(T_A)$  has a lower value and shallower minimum (better process latitude for  $T_A$ ) for the Ni-layer thickness  $\sim 25$ – $30 \text{ nm}$  (AuGe  $\sim 100 \text{ nm}$ ) and AuGe composition near the eutectic [12]. The roughness however is large ( $\sim 20 \text{ nm}$ ). The implications of attempting to reduce the roughness by increasing the Ni-layer thickness or by reducing the Ge content, for the contact resistance and for magnetic properties, can be seen in table 2. Increasing the Ni-layer thickness (50 nm) above the optimum does halve the roughness but increases the contact resistance  $\sim 10$  times, while the use of the off-eutectic alloy with 95:5 wt% results in a reduction of the surface roughness by 75% and increases the contact resistance only about twice that of the eutectic composition, albeit with a higher sensitivity to anneal temperature. Clearly, use of an off-eutectic AuGe alloy with a lower Ge content, such as the AuGe with 95:5 wt% alloy, is a better compromise for trading off the contact resistance for the roughness reduction than increasing the Ni-layer thickness. The reduction in roughness in the sample with AuGe  $\sim 95:5 \text{ wt\%}$  relative to that with the eutectic AuGe  $\sim 88:12 \text{ wt\%}$  alloy is evident in the atomic force microscopy (AFM) images.

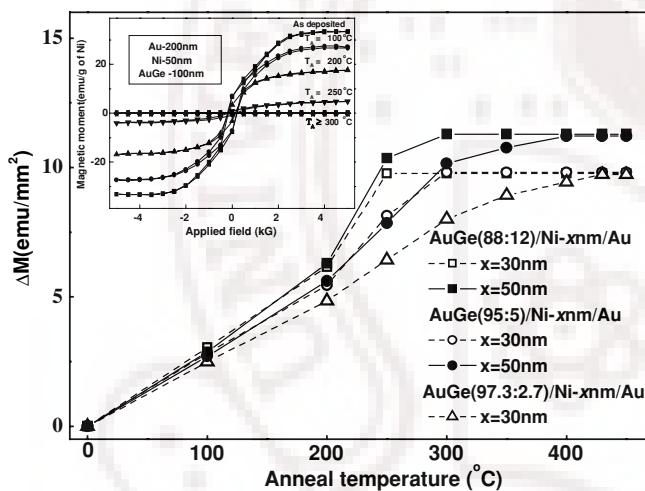
Magnetization hysteresis loops of the film structures, which are magnetic in the as-deposited state, collapse as the anneal temperature is increased. They become completely non-magnetic on annealing at or above a temperature which varies from  $250^\circ\text{C}$  to  $430^\circ\text{C}$ , as the Ge content is decreased

**Table 2.** Magnetic-to-non magnetic transition temperatures, surface roughness,  $R_C$ ,  $T_A$ ,  $t_A$  for three alloy compositions with different Ni-layer thickness.

AuGe alloy composition (wt%)	Nickel layer thickness $x_{Ni}$ (nm)	Optimum anneal temperature $T_A$ (°C)	Optimum anneal duration $t_A$ (s)	Contact resistance $R_C$ ( $\Omega$ mm)	Anneal temperature needed to completely convert Ni to non-magnetic phase (°C)	Surface roughness (nm)
88:12	30	400	90	$0.07 \pm 0.005$	200–250	$20 \pm 2$
	50	400	150	0.90	250–300	$11 \pm 1$
	75	400	180	1.40	350–400	$7.5 \pm 0.5$ [12]
95:5	30	400	90	$0.17 \pm 0.02$	250–300	$5.5 \pm 0.5$
97.3:2.7	30	430	120	1.30	400–430	$4.5 \pm 0.5$

**Table 3.** Fitted parameters for the contact resistance,  $\rho_c(T) = C \exp[\phi_B/E_{\infty} \coth \frac{E_{\infty}}{k_B T}]$ , for three different alloyed contact metal structures to GaAs.

	Specific contact resistance ( $\Omega$ cm <sup>2</sup> )			$\phi_B$ (MeV)	$E_{\infty}$ (MeV)	$E_{\infty}/k_B$ (K)	log C
	298 K	77 K	4.2 K				
AuGe(88:12)/Ni-30/Au	$1 \times 10^{-6}$	$4.5 \times 10^{-5}$	$1.7 \times 10^{-4}$	$31 \pm 0.5$	$10.3 \pm 0.08$	$116 \pm 1$	$6.8 \pm 0.02$
AuGe(88:12)/Ni-50/Au	$1 \times 10^{-5}$	$1.8 \times 10^{-4}$	$2.7 \times 10^{-4}$	$38 \pm 0.7$	$13.1 \pm 0.08$	$148 \pm 1$	$6.5 \pm 0.03$
AuGe(95:05)/Ni-30/Au	$3.2 \times 10^{-6}$	$7.6 \times 10^{-5}$	$2.4 \times 10^{-4}$	$34.5 \pm 1$	$11 \pm 0.14$	$124 \pm 1.5$	$6.7 \pm 0.04$

**Figure 2.** Effective thickness of a Ni layer transformed to non-magnetic phase on annealing at various temperatures. Inset shows typical hysteresis loops.

and as the Ni-layer thickness is increased (table 2). Notably, the decrease in magnetization occurs even after anneals at temperatures as low as 100 °C. The fraction of the Ni layer transformed to the non-magnetic phase scales with the AuGe layer thickness and is independent of time, implying a solid state, solubility-limited dissolution of Ni into the AuGe layer. Ni solubility in the AuGe layer decreases with the decrease in the Ge content in the AuGe alloy layer. This is evident from figure 2 which shows the decrease in magnetization per unit area ( $\Delta M$ ), proportional to the Ni-layer thickness transformed to the magnetic phase, as a function of anneal temperature.

The data are independent of the initial Ni-layer thickness until all the Ni is transformed, for a given AuGe composition. The data demonstrate that the solubility of Ni in AuGe is very sensitive to temperature, in addition to Au–Ge compositions.

The limited solubility for Ni implies a likely precipitation of Ni containing compounds on cooling after the anneals. Grazing incidence XRD indicates the presence of NiGe after cooling from anneals at 300 °C in samples that are found to be non-magnetic at room temperature. TEM [14–16] studies indicate the presence of Ni<sub>3</sub>Ge, Ni<sub>2</sub>GeAs and AuGa after anneals at temperatures close to or greater than temperatures at which alloying with the substrate takes place. A picture consistent with these data is that Ni dissolves into AuGe at temperatures >100 °C to an extent limited by temperature-dependent solubility; phase segregation to non-magnetic NiGe, Ni<sub>3</sub>Ge or Ni<sub>2</sub>GeAs takes place on cooling the structure to room temperature as anneal temperatures are progressively increased.

DSC data (figure 3) and the contact resistance results indicate that the Ni dissolution into AuGe influences the melting and alloying characteristics of the metallization structure. Endothermic peaks typical of melting are seen in DSC data. Additional evidence that these peaks are signatures of melting comes from the surface roughness data as a function of the anneal temperature,  $T_A$ , for the eutectic AuGe alloy with different Ni-layer thicknesses, (figure 4).

The roughness is seen to increase with anneal temperatures that correlate well with observed peak positions in DSC data. It is likely that the increase of the melting temperature with the increase of initial Ni-layer thickness, and hence, the increase of dissolved Ni in AuGe prior to melting and with the decrease of Ge content, is the cause for the reduced roughness. Figure 5 shows AFM micrographs of the surface of two samples, one prepared with AuGe at the eutectic composition and the other with off-eutectic composition (95:5 wt%) both annealed at 400 °C (at which the contact resistance is close to optimum). A considerably reduced roughness (table 2) is evident in the latter sample whose anneal temperature is closer to the temperature of ‘melting’ in its metallization structure. Precise quantitative

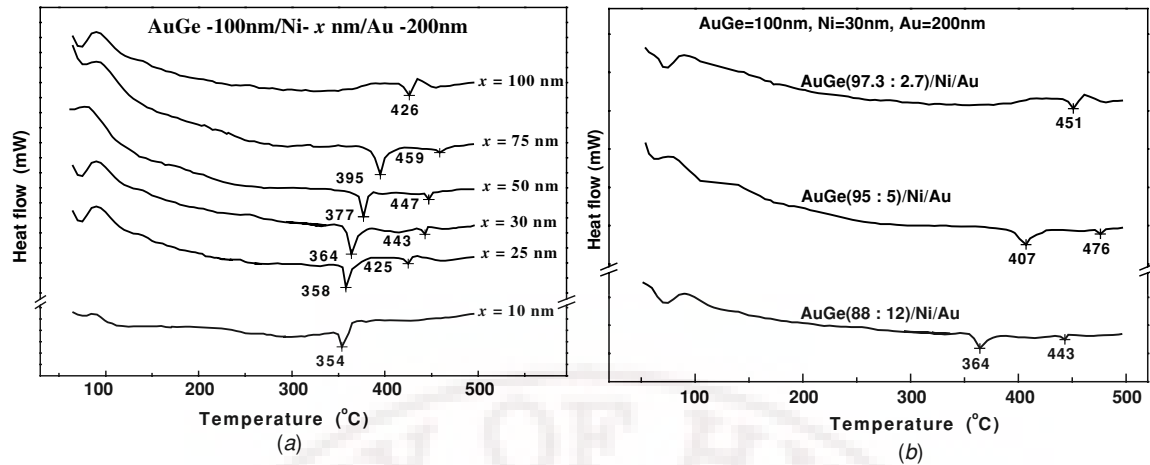


**Figure 3.** DSC scans for samples with (a) eutectic AuGe alloy with different Ni-layer thicknesses, (b) eutectic and off-eutectic AuGe alloys each with a 30 nm Ni layer.

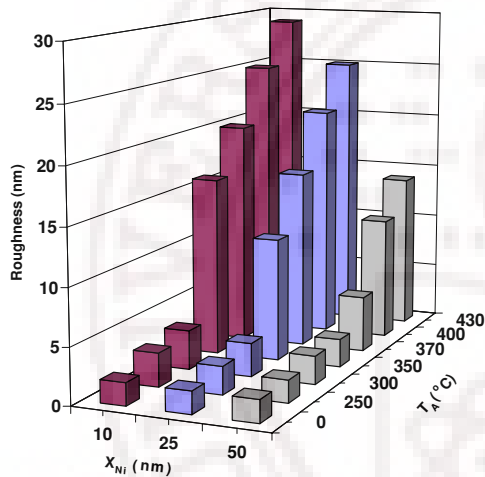


**Figure 4.** Variation of the surface roughness of AuGe (88:12)/Ni/Au contacts with anneal temperature ( $T_A$ ), for three different Ni-layer thicknesses ( $X_{Ni}$ ).

comparisons of temperatures are difficult in view of differences in the experimental setup for the DSC and contact anneals, and also the rapid heating rates. These results are consistent with *in-situ* XRD results [17] of Au–Ge alloy layers deposited

on GaAs, which also demonstrate the increase of melting temperatures when thicker Ni and thinner Ge-layers are used in Au/Ge/Ni-type metallization structures. This study also reveals the formation of low-melting ( $\sim 360^\circ\text{C}$ ) Au–Ga phases when the metallization structure melts, which is believed to contribute to surface roughening [17, 18].

The electrical conduction across the AuGe-based contacts to GaAs has been reported to show both thermionic emission and tunneling characteristics [19]. The specific contact resistivity ( $\rho_c$ ) (determined from the TLM measurements as  $R_s L_T^2$ , where  $L_T$  is the current transfer length in a lateral contact and  $R_s$  is the semiconductor sheet resistance) as a function of temperature (4–300 K) for three samples is shown in figure 6: a sample with the almost optimum contact resistance (eutectic AuGe-88:12 wt% and Ni-layer thickness of 30 nm/Au) and the two other samples, one with increased Ni-layer thicknesses (50 nm) and another with reduced Ge content (Au:Ge::95:5 wt%).

$\rho_c$  increases linearly in the temperature range ( $\geq 100$  K) and levels off as the temperature decreases to below 100 K (table 3). The experimental data have been fitted using the expressions of  $\rho_c$  based on the thermionic and tunneling models of current transport through the metal semiconductor contacts. The line drawn through the contact resistivity points

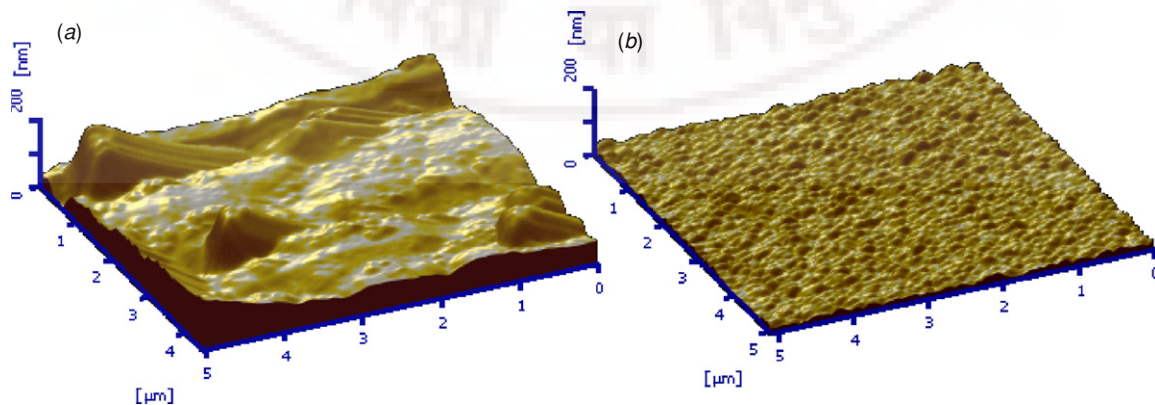


**Figure 5.** AFM micrographs of the surface of samples with (a) eutectic (88:12 w%) and (b) off-eutectic (95:5 w%) AuGe compositions and annealed for durations that gave the lowest  $R_C$ .



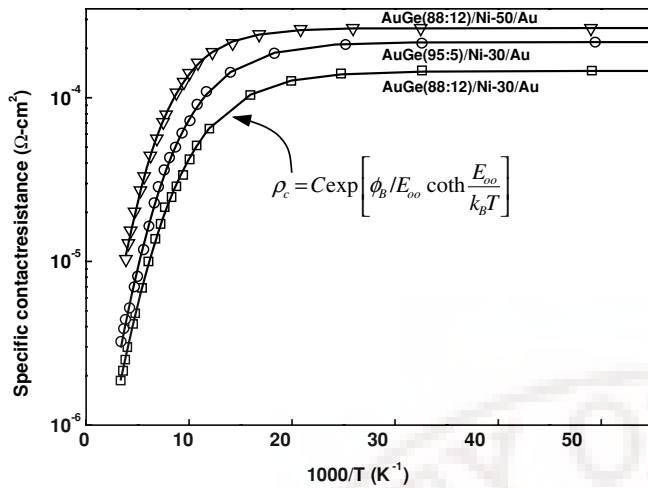


**Figure 6.** Specific contact resistance,  $\rho_c$ , plotted as a function of inverse temperature for eutectic AuGe-88:12 wt%/Ni-30 nm/Au, AuGe-88:12 wt%/Ni-50 nm/Au, and with off-eutectic AuGe-95:5 wt%/Ni-30 nm/Au.

is a fit to the equation based on the thermionic field emission [20].

$$\rho_c = C \exp \left[ \phi_B / E_{oo} \coth \frac{E_{oo}}{k_B T} \right] \quad (1)$$

where  $\phi_B$  is the effective barrier height and  $E_{oo}$  is the tunneling parameter. Arrhenius behavior expected of thermionic current transport dominates  $\rho_c(T)$  above 100 K. The weak temperature dependence of  $\rho_c$  below 100 K indicates a change in the current transport mechanism from thermionic to tunneling. The values of the effective barrier height increase with the increase of the Ni-layer thickness and the decrease of the Ge content (table 3) from that of the structure with the eutectic AuGe alloy and lowest contact resistance. The increase in the barrier height is less in the case of the metallization structure with decreased Ge content than in the case of increased Ni-layer thickness.

#### 4. Conclusions

Ni undergoes a solid-state dissolution into AuGe at relatively low temperature, on the annealing contact metallization structures of the type AuGe (88:12)/Ni/Au. The solubility of Ni in AuGe is reduced when the Ge content in AuGe is decreased. The metallization structure, eutectic AuGe alloy with a Ni-layer thickness of 25–30 nm, results in the lowest contact resistance among the structures studied; the contacts however show morphology with considerable roughness. The roughness can be decreased using a lower Ge content or increasing the Ni thickness; lowering the Ge content however seems a better choice for trading off the contact conductance

for surface smoothness. The structures show signatures of melting with the ‘melting’ temperature increasing with both increase of the Ni-layer thickness and decrease of the Ge content, the possible cause of decreased surface roughness on alloying. The temperature dependence of the specific contact resistance has both thermionic and tunneling characteristics, with barrier heights increasing with the increase of the Ni-layer thickness or the decrease of the Ge content in the structure.

#### Acknowledgments

Support of UGC (UPE, CAS programmes), BRNS/DAE, IGCAR, DST (Centre for Nanotechnology) is acknowledged. The authors thank Dr T. Geetha Kumary, Material Science Group, IGCAR, Kalpakkam, for help in preparation of the alloy.

#### References

- [1] Lim Jong Won, Ahn Ho-Kyun, Ji Hong-Gu, Chang Woo-Jin, Mun Jae-Kyoung and Kim Haecheon 2004 *Semicond. Sci. Technol.* **19** 1416
- [2] Köck A, Gornik E, Abstreiter G, Böhm G, Walther M and Weimann G 1992 *Appl. Phys. Lett.* **60** 2011
- [3] Sugiyama Y 1995 *J. Vac. Sci. Technol. B* **13** 1075
- [4] Taylor R P, Coleridge P T, Davies M, Feng Y, McCaffrey J P and Marshall P A 1994 *J. Appl. Phys.* **76** 7966
- [5] Ketterson A, Ponce F, Henderson T, Klem J and Morkoc H 1985 *J. Appl. Phys.* **57** 2305
- [6] Sai Saravanan G, Mahadeva Bhat K, Muraleedharan K, Vyas H P, Muralidharan R and Pathak A P 2008 *Semicond. Sci. Technol.* **23** 025019
- [7] Robinson G Y 1975 *Solid-State Electron.* **18** 331
- [8] Chua Soo-Jin and Lee Seng Hin 1994 *Japan. J. Appl. Phys.* **33** 66
- [9] Bühlmann H J and Ilegems M 1991 *J. Electrochem. Soc.* **138** 2795
- [10] Goronkin H, Tehrani S, Rimmel T, Feies P L and Johnson K J 1989 *IEEE Trans. Electron Devices* **36** 281
- [11] Kim T and Chung D D L 1986 *J. Vac. Sci. Technol. B* **4** 762
- [12] Abhilash T S, Ravi Kumar Ch and Rajaram G 2009 *J. Phys. D: Appl. Phys.* **42** 125104
- [13] Berger H H 1972 *Solid-State Electron* **15** 145
- [14] Kuan T S, Batson P E, Jackson T N, Rupprecht H and Wilkie E L 1983 *J. Appl. Phys.* **54** 6952
- [15] Ogawa M 1980 *J. Appl. Phys.* **51** 406
- [16] Murakami M, Childs K D, Baker J M and Callegari A 1986 *J. Vac. Sci. Technol. B* **4** 903
- [17] Kim T and Chung D D L 1986 *Thin Solid Films* **147** 177
- [18] Murakami M 2002 *Sci. Technol. Adv. Mater.* **3** 1
- [19] Hawksworth S J, Chamberlain J M, Cheng T S, Henini M, Heath M, Davies M and Page A J 1992 *Semicond. Sci. Technol* **7** 1085
- [20] Shen T C, Gao G B and Morkoc H 1992 *J. Vac. Sci. Technol. B* **10** 2113



# Nickel dissolution into AuGe in alloyed AuGe/Ni/Au Ohmic contacts on GaAs/AlGaAs multilayer structures

T.S. Abhilash, C.H. Ravi Kumar, G. Rajaram\*

School of Physics and Centre for Nanotechnology, University of Hyderabad, Hyderabad 500046, India

## ARTICLE INFO

### Article history:

Received 13 August 2009

Received in revised form 22 April 2010

Accepted 30 April 2010

Available online 12 May 2010

### Keywords:

GaAs/AlGaAs

Multilayer

Ohmic contacts

AuGe/Ni/Au

Semiconductor

Magnetic properties

Sensors

## ABSTRACT

Magnetic properties of alloyed Ohmic contacts of the type AuGe/Ni/Au on GaAs/AlGaAs multilayers with  $n^+$  cap layer with different AuGe compositions and Ni-layer thicknesses are examined. Magnetization data indicate that the annealed structures are non-magnetic, at room temperature for commonly used anneal temperatures ( $\sim 400$ – $430$  °C) and Ni-layer thicknesses (10–100 nm). The transformation of Ni to non-magnetic phase begins at  $\sim 100$  °C, well below temperatures at which extensive alloying with the GaAs substrate takes place. The fraction of Ni transformed to non-magnetic phase on annealing appears to scale with AuGe layer thickness, has a quadratic dependence on anneal temperature and is time independent for time scales of minutes. The data indicate that the Ni layer dissolves into the AuGe layer at temperatures well below that at which alloying between AuGe and GaAs substrate takes place. The dissolved Ni concentration is limited by a solubility that increases with anneal temperature and decreases with decreasing Ge content from that of the AuGe eutectic composition.

© 2010 Elsevier B.V. All rights reserved.

## 1. Introduction

One of the most commonly used recipes for Ohmic contacts in GaAs devices is deposition of the metal structure, AuGe/Ni/Au, followed by alloying with the substrate using rapid thermal anneal [1–3]. The use of eutectic composition for the AuGe alloy layer along with a Ni layer results in low contact resistance [4]. Increase of the Ni-layer thickness results in lower post-anneal film roughness; however, this is at the cost of increasing the contact resistance [5,6]. Moreover, magnetism of the Ni layer can potentially influence device performance; especially so in the case of Hall Magnetic sensors that exploit high magnetic-field sensitivities of multilayers incorporating the 2-dimensional electron gas (2DEG) layer [7]. Use of off-eutectic compositions of the AuGe alloy is an alternative for obtaining lower surface roughness [8] with some increase of the contact resistance. In this context, it is of interest to track changes of Ni in the contact metal structure to non-magnetic phases with anneal temperature and time, along with changes of contact resistances and roughness, as the Ge concentration is decreased and Ni-layer thickness is increased. In this paper we report some interesting results obtained from magnetization studies of annealed structures of the type AuGe/Ni/Au on GaAs/AlGaAs multilayers (with  $n^+$  cap layer) with varying AuGe compositions and Ni-layer thicknesses.

## 2. Experimental details

The wafer used was Si-GaAs with multilayer-structure deposited by Molecular Beam Epitaxy, shown in Table 1. The metallization structure was prepared by evaporating AuGe (100 nm), Ni (25, 30, 50, 75, and 100 nm) and Au (200 nm) using thermal, e-beam and thermal evaporation respectively. Magnetization hysteresis loops of samples with the annealed contact structures with several Ni-layer thicknesses were measured using a Vibrating Sample Magnetometer, with a magnetic moment resolution of  $10^{-6}$  emu. Metallizations with three Au–Ge compositions – eutectic (88:12 weight %) and off-eutectics (95:5 and 97.3:2.7) – were investigated. The samples were subjected to anneals at a temperature  $T_A$ , reached at heating rates of 250 °C/min, held at  $T_A$  for durations,  $t_A$  (typically 1 min), and then cooled down [9]. This was followed by magnetic hysteresis loop measurements at room temperature. The measurements were carried out in sweep mode to 5 kG with the magnetic field applied parallel to the film plane. Background due to a sample of the same mass, but without the film structure, was subtracted and the resultant data was normalized by the magnetization of the as-deposited film structure. Some measurements were also performed with different AuGe film thicknesses, but keeping the ratio of Ni to AuGe film thicknesses at the same value of 0.5.

## 3. Results and discussion

Fig. 1 shows magnetization hysteresis loops for a sample with the AuGe layer with the eutectic composition (88:12 wt.%), and a 30 nm

\* Corresponding author.

E-mail address: [grrsp@uohyd.ernet.in](mailto:grrsp@uohyd.ernet.in) (G. Rajaram).

**Table 1**  
GaAs/AlGaAs wafer and the contact metallization structure.

Au (200 nm)		
Ni (10–100 nm)		
AuGe (100 nm)		
$n^+$ (Si $1.5 \times 10^{18}$ ) GaAs	20 nm	Cap layer
$n^+$ (Si $1.5 \times 10^{18}$ ) $\text{Al}_{0.3}\text{GaAs}_{0.7}$	30 nm	Supply layer
Intrinsic AlGaAs	15 nm	Separation layer
Intrinsic GaAs	500 nm	(2DEG layer at i-GaAs/ i-AlGaAs interface)
Si-GaAs substrate	500 $\mu\text{m}$	

thick Ni layer subjected to anneals at various temperatures. These data are typical of the magnetic behaviour of the Ni-containing contact metallization structures. The results show that, while the as-deposited film structures are ferromagnetic, the metallization structure becomes progressively less magnetic as the anneal temperature is increased and becomes completely non-magnetic at a higher temperature. The minimum anneal temperature required to complete the transformation to a non-magnetic phase, for different Ni and AuGe layer thickness, though not known precisely, lies in the range given in Table 2.

Fig. 2 shows magnetization of annealed samples as a percentage of the magnetization of the un-annealed sample as anneal temperature is increased. The temperature, to which the structure needs to be annealed to render it completely non-magnetic, increases with increasing Ni-layer thickness as seen in Fig. 2. This temperature varies from 250 °C to 430 °C for contact structures with varying Ni-layer thickness and Ge content. Hence, under conditions normally used for obtaining Ohmic contacts, the structure is non-magnetic for a wide range of Ni-layer thicknesses. It is noteworthy that decrease in magnetization occurs at anneal temperatures as low as 100 °C. Motivated by reports [10,11] about the importance of the ratio of Ni to AuGe layer thickness to contact resistance, a few magnetic measurements were also performed on samples with other AuGe (88:12) thicknesses – 50 nm and 150 nm other than 100 nm (viz. Ni to AuGe thickness ratio constant at 0.5). As seen in the inset of Fig. 2, the fractional decrease in magnetization of the samples with structures AuGe (150 nm)/Ni (75 nm)/Au (200 nm), AuGe (50 nm)/Ni (25 nm)/Au (200 nm) and AuGe (100 nm)/Ni (50 nm)/Au (200 nm) are virtually identical. Thus the amount of Ni transformed to non-magnetic phase on annealing appears to scale with AuGe layer thickness, implying that the

**Table 2**

Anneal temperature required to complete magnetic to non-magnetic transition for different Ni and AuGe layer thicknesses and AuGe compositions.

AuGe alloy composition	AuGe layer thickness (nm)	Nickel layer thickness (nm)	Magnetic to non-magnetic transition anneal temperature (°C)
88:12	100	10	100–200
88:12	100	25	200–250
88:12	100	30	200–250
88:12	100	50	250–300
88:12	100	75	350–400
88:12	100	100	400–430
88:12	50	25	250–300
88:12	150	75	250–300
95:5	100	25	250–300
95:5	100	30	250–300
95:5	100	50	350–400
97.3:2.7	100	30	400–430

transformation is not restricted to the interface between the Ni and AuGe layers.

Significantly, also, the extent of Ni transformed to non magnetic phase is independent of time at a given anneal temperature (for time scales  $\sim 15$  min) as shown in Fig. 3. It depends only on anneal temperature at typically used anneal durations. Clearly, the transformation involves fast dissolution of Ni into AuGe, rather than a slow diffusion at these time scales.

Fig. 4 displays the decrease in magnetization per unit sample area (a quantity proportional to the thickness of Ni layer transformed to non magnetic phase) for AuGe layer with the eutectic composition (88:12 wt.%), with varying Ni-layer thickness, after anneals at different temperatures. It shows that, for AuGe layer thickness fixed at 100 nm and eutectic composition, the transformed Ni-layer thickness is independent of Ni concentration until all the Ni is converted to the non-magnetic phase. The sample with a 10 nm Ni layer is an exception – it is possible that the film's conformal surface coverage may have been affected at this thickness. The Ni layer appears to dissolve into the AuGe layer to an extent limited by the temperature dependent solubility of Ni in AuGe, at temperatures well below that at which alloying with GaAs occurs. This solubility limited diffusion of Ni into AuGe layer is possibly followed by segregation and formation of non-magnetic Ni–Ge on cooling [12–17]. This is true of the structures with AuGe at the composition 95:5 wt.% as well as seen in Fig. 5. This figure shows the

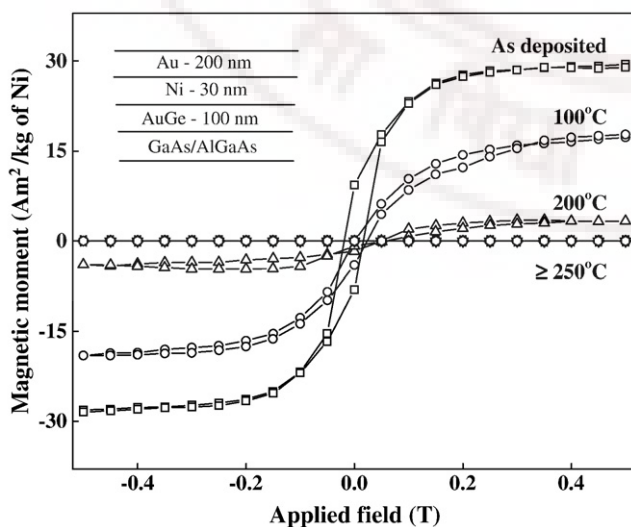


**Fig. 1.** Magnetization hysteresis loops for a GaAs/AlGaAs sample with AuGe/Ni/Au annealed at different temperatures for durations about 1 min.

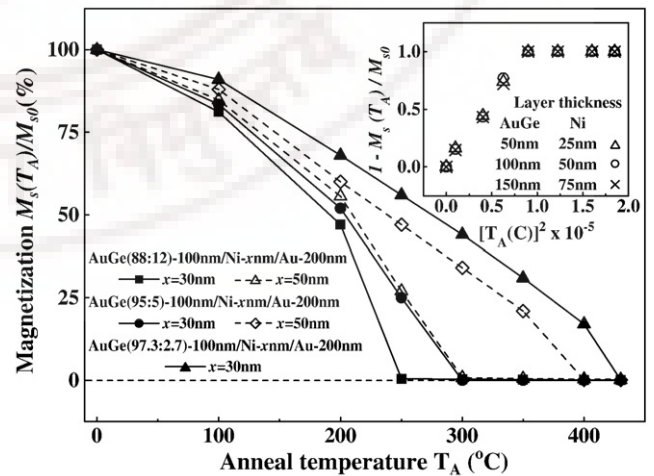


**Fig. 2.** Anneal temperature ( $T_A$ ) dependence of the fractional saturation magnetization for samples with three AuGe alloy compositions and two Ni-layer thicknesses on GaAs multi-layer.  $M_{s0}$  is the saturation magnetization of the un-annealed sample at 5 kG. The inset shows transformed Ni fraction vs  $T_A^2$  for three AuGe thicknesses with Ni: AuGe thickness ratio at 0.5.



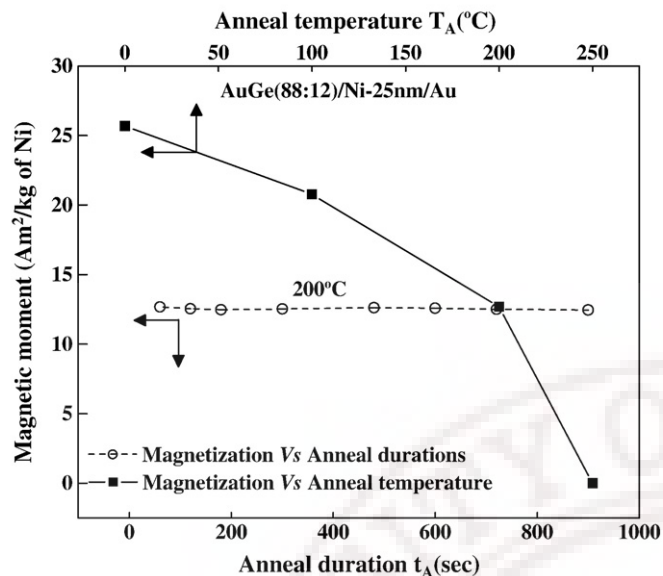


Fig. 3. Time dependence of saturation magnetization for a sample with 25 nm Ni and 100 nm AuGe layers annealed at 200 °C.

transformed Ni-layer thickness as a function of anneal temperature for eutectic and off-eutectic AuGe compositions (88:12, 95:5, and 97.3:2.7 wt.%). The solubility itself is sensitive to Au–Ge composition, decreasing with decreasing Ge content from that of the eutectic composition (88:12). This solubility has increasing dependence on temperature, with an apparent quadratic behaviour in the eutectic AuGe alloy (see inset of Fig. 2).

TEM data reported in the literature [12,13,15,18] provide indications regarding Ni compound formation after Ni containing contact structures are annealed. It is reported that  $\text{Ni}_3\text{Ge}$  is formed after low temperature anneals, while  $\text{Ni}_2\text{GeAs}$  is detected after high temperature anneals. The presence of  $\text{Ni}_2\text{GeAs}$  has been correlated with contact formation. A picture consistent with these data is that the Ni dissolves into AuGe at temperatures  $>100$  °C to an extent limited by temperature dependent solubility, then re-precipitated as  $\text{Ni}_3\text{Ge}$  or  $\text{Ni}_2\text{GeAs}$ , for anneals less than or greater than that of alloying temperatures respectively.

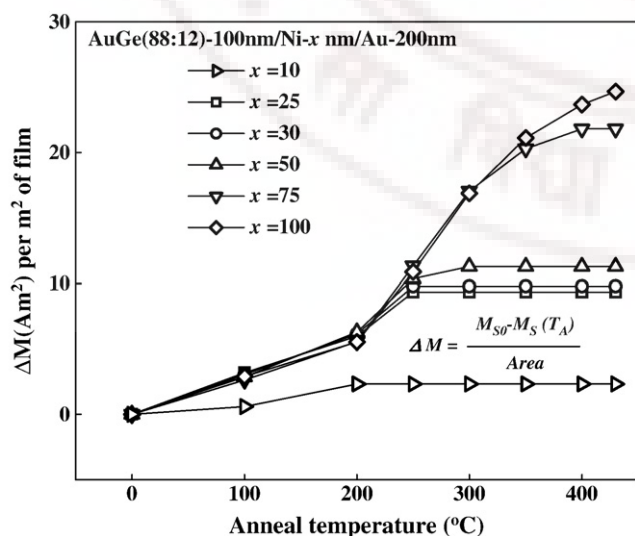


Fig. 4. Variation of the effective thicknesses of Ni layer transformed to non-magnetic phase on annealing at different anneal temperatures ( $\Delta M$  is decrease in magnetization per unit area).

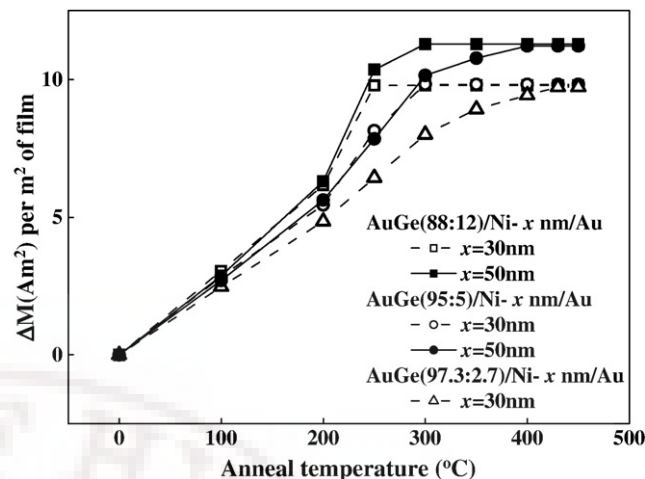


Fig. 5. Decrease in magnetization per unit area of transformed Ni-layer thickness as function of anneal temperature, for three alloy compositions with two Ni-layer thicknesses.

#### 4. Conclusions

In conclusion, we have observed that metallization structures are rendered non-magnetic at room temperature after annealing at typically used alloying conditions of temperature (400–430 °C). Conversion of Ni to non-magnetic phases, begins at anneal temperatures as low as 100 °C and is completed at an anneal temperature that increases with increasing Ni-layer thickness and decreasing Ge content in the AuGe alloy. Three results namely, transformed Ni-layer thickness i) scales with AuGe layer thickness, ii) is independent of Ni-layer thickness at a given temperature prior to complete transformation and iii) is time independent at constant anneal temperature, imply a solubility limited dissolution of Ni into AuGe. This solubility increases quadratically with anneal temperature and decreases with decreasing Ge content in the AuGe alloy.

#### Acknowledgements

We acknowledge the support of UGC (UPE, CAS programmes), BRNS/DAE, IGCAR, and DST (Centre for Nanotechnology).

#### References

- [1] N. Braslau, J.B. Gunn, J.L. Staples, *Solid State Electron.* 10 (1967) 381.
- [2] R.P. Taylor, P.T. Coleridge, M. Davies, Y. Feng, J.P. McCaffrey, P.A. Marshall, *J. Appl. Phys.* 76 (1994) 7966.
- [3] A. Ketterson, F. Ponce, T. Henderson, J. Klem, H. Morkoc, *J. Appl. Phys.* 57 (1985) 2305.
- [4] G.Y. Robinson, *Solid State Electron.* 18 (1975) 331.
- [5] Chua Soo-Jin, Lee Seng Hin, *Jpn. J. Appl. Phys.* 33 (1994) 66.
- [6] H.J. Bühlmann, M. Illegems, *J. Electrochem. Soc.* 138 (1991) 2795.
- [7] Y. Sugiyama, *J. Vac. Sci. Technol. B* 13 (1995) 1075.
- [8] H. Goronkin, S. Tehrani, T. Rimmel, P.L. Fejes, K.J. Johnston, *IEEE Trans. Electron Devices* 36 (1989) 281.
- [9] T.S. Abhilash, Ch. Ravi Kumar, G. Rajaram, *J. Phys. D Appl. Phys.* 42 (2009) 125104.
- [10] Hung-Cheng Lin, Sidat Senanayake, Keh-Yung Cheng, Minghui Hong, J.R. Kwo, Bin Yang, J.P. Mannaerts, *IEEE Trans. Electron Devices* 50 (2003) 880.
- [11] O. Goktas, J. Weber, J. Weis, Klaus von Klitzing, *Phys. E* 40 (2008) 1579.
- [12] M. Murakami, K.D. Childs, J.M. Baker, A. Callegari, *J. Vac. Sci. Technol. B* 4 (1986) 903.
- [13] T.S. Kuan, P.E. Batson, T.N. Jackson, H. Rupprecht, E.L. Wilkie, *J. Appl. Phys.* 54 (1983) 6952.
- [14] T.C. Shen, G.B. Gao, H. Morkoc, *J. Vac. Sci. Technol. B* 10 (1992) 2113.
- [15] M. Murakami, *Sci. Technol. Adv. Mater.* 3 (2002) 1.
- [16] M. Ogawa, *J. Appl. Phys.* 51 (1980) 406.
- [17] A.G. Baca, F. Ren, J.C. Zolper, R.D. Briggs, S.J. Pearton, *Thin Solid Films* 308 (1997) 599.
- [18] Y.C. Shih, M. Murakami, E.L. Wilkie, A.C. Callegari, *J. Appl. Phys.* 62 (1987) 582.

# Magnetic Field Sensor using III-V Multilayer structures: New Insights into Ohmic Contact Formation to GaAs from Magnetization Measurements

G. Rajaram, T. S. Abhilash, Ch. Ravi Kumar, B. P. C. Rao, Rita Saha, L. S. Vaidhyathan, K. Gireesan, B. Sreedhar, M. P. Janawadkar, T. Jayakumar, and Baldev Raj

**Abstract**—The utility of GaAs/AlGaAs multilayers on GaAs substrate with the two dimensional electron Gas (2DEG) layer as materials for Hall effect based magnetic field sensors is discussed. The structures offer useable high sensitivities ( $\sim 1200\text{V/AT}$ ) by combining low carrier density with high mobility. Results of scanning across notches on magnetic steels using Hall magnetic field sensors micro-fabricated for non-destructive testing (NDT) are presented. A process issue arising from the use of Ni in the Ohmic contact metallization, AuGe/Ni/Au is studied in the context of magnetic field sensor application. The dependence of resistance, surface roughness and magnetism of the processed contacts on parameters such as Ni layer thickness, anneal temperature and Au-Ge alloy composition are discussed. The magnetization results indicate that the contacts are rendered non-magnetic for anneals at temperature well below the alloying temperature at which the contact resistance drops. A solubility limited Ni dissolution into AuGe layer appears to take place well below the alloying temperature, increasing the structure's melting temperature. Conductivity map, low temperature contact resistance and other morphological results are also discussed.

**Index Terms**—GaAs/AlGaAs, Hall sensors, Magnetic properties, Ohmic contacts

## I. INTRODUCTION

HALL effect based magnetic field sensors have the advantage of high linearity over a large field range and simplicity of use over other sensors such as GMR based ones and fluxgate magnetometers, albeit with modest sensitivity.

Si-based Hall effect magnetic field sensors that include built-in support circuits are commonly available [1].

The *material* sensitivity of a Hall sensor,  $K_H \sim V_H/iB$ , ( $V_H$  is the Hall voltage for excitation current  $i$  (amps) and magnetic field,  $B$  (Tesla)) varies as  $1/n_s$ , where  $n_s$  is the sheet carrier density perpendicular to the field. The option to build in increased sensitivity by decreasing  $n_s$  is, however, limited by increasing source resistance, and hence noise, unless carrier mobility,  $\mu$  is also increased.

This accounts for the popularity of materials such as GaAs and InSb as Hall sensor materials [2], [3]. Multilayer structures with the 2 dimensional electron gas (2DEG) layer also offer good promise since they consist of a thin carrier sheet with high mobility [4]. *Device* sensitivities will be influenced by the largest useable excitation current for a given maximum power dissipation. These structures have sensitivities five to tens times than that available with doped Si. Other advantages are ability to microfabricate small area sensor ( $\sim 0.3\mu\text{m}$  square [5]) and sensor arrays for magnetic field imaging, low temperature operation (subject to limitations imposed by Quantum Hall Effect). Potential for building on-chip support circuits for varied applications exist since the same structure is suitable for HEMT fabrication [6]. The Hall sensor can be used without flux concentrators for improved spatial resolution. The sensors have potential for application in proximity sensors, Non-destructive testing of cracks and other defects in carbon steel pipes [7] and in research [8].

A structure typical of the wafers used by us is shown in Table 1[9].

G. Rajaram (e-mail: grsrp@uohyd.ernet.in), T. S. Abhilash and Ch. Ravi Kumar are with the School of Physics and Centre for Nanotechnology, University of Hyderabad, Central University P.O., Hyderabad 500046 India.

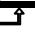
B. P. C. Rao and T. Jayakumar are with the Non Destructive Evaluation Division, Indira Gandhi Centre for Atomic Research, Kalpakkam, 603 102 India.

L. S. Vaidhyathan, K. Gireesan, M. P. Janawadkar and Rita Saha (retired) are with the Material Science Group, Indira Gandhi Centre for Atomic Research, Kalpakkam, 603 102 India

B. Sreedhar is with the Inorganic and Physical Chemistry Division, Indian Institute of Chemical Technology, Hyderabad, 500 007 India

Baldev Raj is the Director, Indira Gandhi Centre for Atomic Research, Kalpakkam, 603 102 India.

TABLE 1. GAAS/ALGAAS WAFER LAYER STRUCTURE.

$n^+$ (Si $1.5 \times 10^{18}$ ) GaAs	20nm	Cap layer
$n^+$ (Si $1.5 \times 10^{18}$ ) $\text{Al}_{0.3}\text{Ga}_{0.7}\text{As}$	30nm	Supply layer
Intrinsic AlGaAs	15nm	Separation layer
Intrinsic GaAs	500nm	(2DEG Layer) 
SI GaAs Substrate	500 $\mu\text{m}$	

The sensors were fabricated into a 'greek-cross' pattern with assorted active areas ranging from  $500 \mu\text{m} \times 500 \mu\text{m}$  to

10  $\mu\text{m}$  x 10  $\mu\text{m}$  for NDT applications and 7-10 member sensor arrays for other applications. A five-mask process principally for isolation-etch, Ohmic contact, interconnection and protection was used with i-line photolithography. Room temperature sensitivity was typically 1200 V/AT and is determined principally by the structure. Typical excitation currents during use were in the range 10-100  $\mu\text{A}$ . Self heating needs to be avoided as there is a small variation of the sensitivity (Fig.1) and offset with temperature.

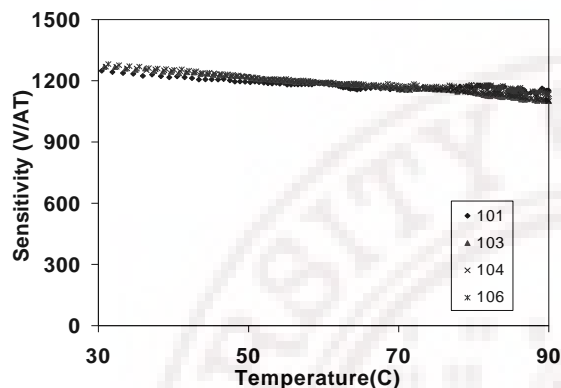


Fig.1. Magnetic sensitivity of 2DEG Hall sensors as function of temperature.

This paper describes application of the 2DEG GaAs/AlGaAs sensors to Non-destructive testing by flux leakage measurements, some Ohmic contact processing and process optimization issues arising in the context of this application and some insights offered by magnetic measurements on the changes taking place in the metallization structure prior to alloying. The Contact resistances were determined using the transmission line (or transfer length) (TLM) model [10].

## II. FLUX LEAKAGE MEASUREMENTS

The sensors were tested for application to Non-destructive testing (NDT) using the flux-leakage technique for magnetic materials, as follows. The magnetic field data was logged as the sensor was scanned across electro-discharge machined (edm) notches in Carbon steel plates. The field profile expected with sensors that measures the tangential component (eg. GMR) or the normal component (eg. Hall sensor) of the leaked flux is shown in fig. 2a and 2b.

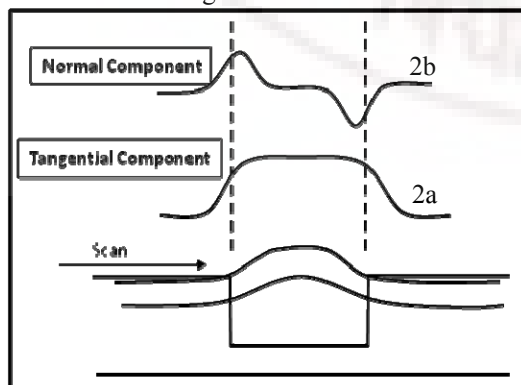


Fig.2. Spatial variation of flux leakage from a crack in a magnetic plate.

Fig. 3 shows such data acquired using 2DEG Hall magnetic field sensor with active area 50  $\mu\text{m}$  x 50  $\mu\text{m}$ . Clear dipole-like signals are detected with typical useable stand-off distances of 400  $\mu\text{m}$ . Signals from a subsurface notch can also be seen, especially if a monotonic background due to the finite size of the plate is subtracted.

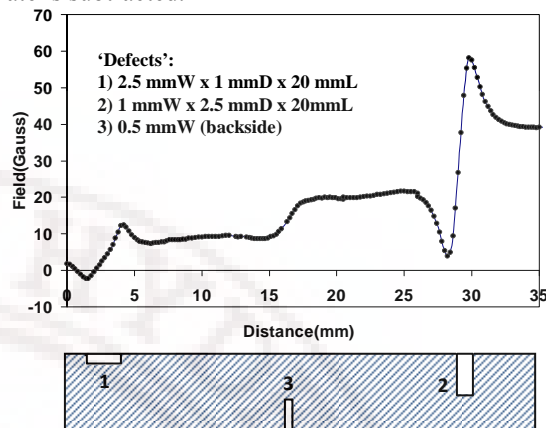


Fig.3. Magnetic flux leakage signal of a sample having three defects, including one on the far side of the scan.

For stand off distances of the order of crack width or less, the distance between the signal maximum and the minimum correlates with the width. Peak height correlates with the crack depth. The crack dimensions can be estimated using the dipole model of the crack [11]. An image of a crack using an x-y scan is shown in Fig. 4.

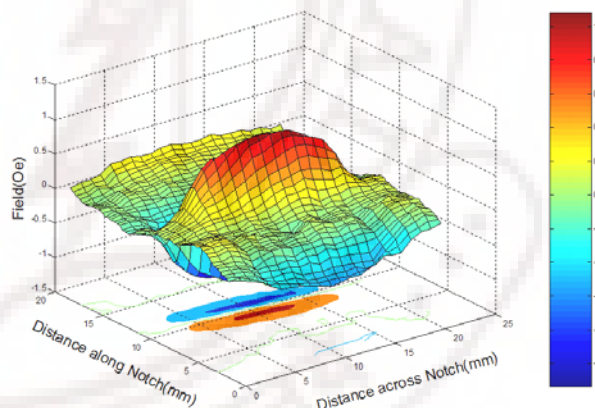


Fig.4. Magnetic flux leakage image of a 0.5mm wide and 2mm deep edm notch on a carbon steel plate.

Some problems with the sensors have been a sizeable and variable offset- probably arising from defects in the wafer and patterning- and possible shorting of the excitation current if the voltage leads are positioned too close to the active area in an effort to reduce source resistance.

## III. OHMIC CONTACT PROCESS OPTIMIZATION

Contact resistance and magnetic properties of the contact are of interest in the context of the Hall-effect based magnetic field sensors and surface roughness in the context of support circuits using FETs integrated into the sensor substrate. A popular recipe for fabricating Ohmic contacts to GaAs is the



deposition of a metallization structure with eutectic AuGe(88:12 wt%)/Ni/Au on a  $n^+$  GaAs cap layer, followed by a rapid thermal anneal (RTA) to about 400°C [12]. Ge diffusion into GaAs and Ga diffusion into the metallization layer occur at the ‘alloying’ temperature, usually in the region of temperatures at which the AuGe melts [13]. The use of Ni, however, could render the structure magnetic and interfere with the local magnetic field measurements. Cr, Ti, Pd, Pt etc are some non-magnetic alternatives to Ni [14]. However, both roughness and contact resistance deteriorate. Fig.5 and 6 show examples of SEM micrographs and contact resistance vs. anneal temperature for Ohmic contact metallization structures with Ti, Cr, Ni and no interlayer between AuGe and Au layers.

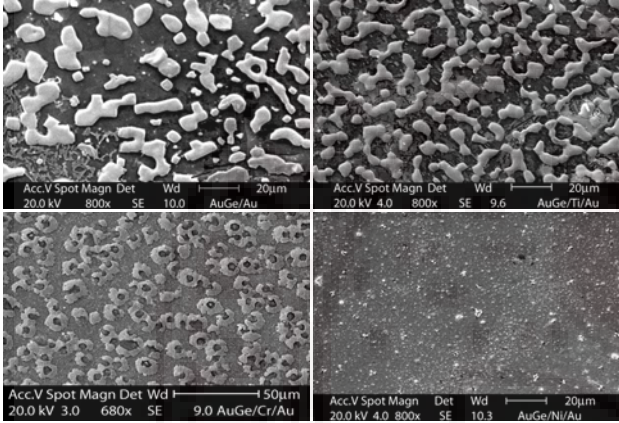


Fig. 5: SEM micrographs of the surface of AuGe /TM/Au contact metallization structures, annealed at 400°C. TM= Ti, Cr and Ni or none.

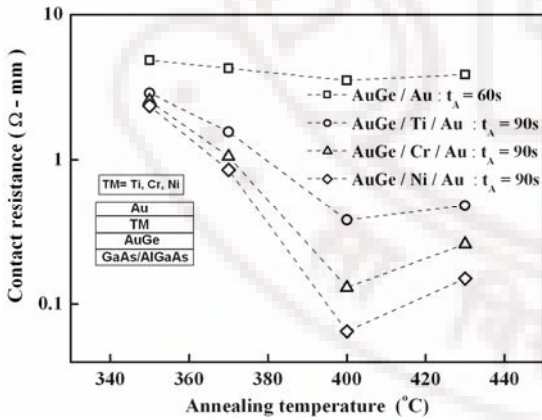


Fig. 6: Contact resistance as a function of anneal temperature for AuGe/TM/Au. TM= Ti, Cr and Ni or none. The lines are a guide to the eye.

Clearly, Ni interlayer is the best choice in terms of contact resistance and surface roughness. An optimization of the Ni layer thickness is, however, in order as thick layers reduce roughness but increase the contact resistance and possibly magnetization. The Ni film thickness, optimized for least contact resistance is ~25-30nm (Fig. 7) for an AuGe layer thickness of 100nm. The least contact resistance is ~0.03-0.05

Ω-mm and the contact resistance as well as roughness and magnetization depend on the Ni-to-AuGe film layer thickness ratio (Table 2) with the ‘optimum’ ratio being 1:4 [15], [16]. Structures with this film thickness ratio have rough surface morphology.

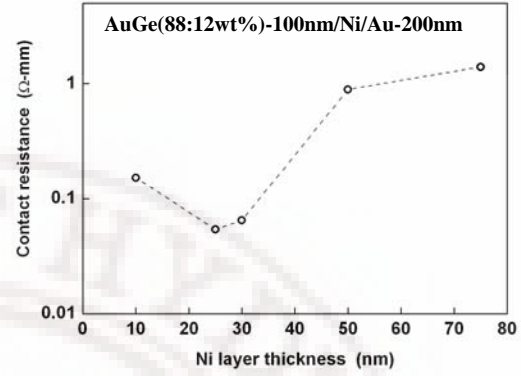


Fig. 7: Contact resistance at the optimized anneal temperature and time vs. Ni layer thickness.

TABLE 2: CONTACT RESISTANCE, SURFACE ROUGHNESS AND THE MAGNETIC-TO-NON MAGNETIC TRANSFORMATION TEMPERATURE, FOR VARIOUS NI LAYER THICKNESSES AND GE CONTENT IN THE AU GE ALLOY.

AuGe alloy composition (wt %)	Ni: AuGe layer thickness ratio	Nickel layer thickness (x nm)	Contact resistance, $R_c$ (Ω-mm)	Surface roughness (nm)	Anneal temperature for Magnetic to non-magnetic transformation (°C)
88:12		10	0.15	$25 \pm 4$	100-200
88:12	1:4	25	$0.05 \pm 0.01$	$21 \pm 3$	200-250
88:12		30	$0.07 \pm 0.005$	$20 \pm 2$	200-250
88:12	1:2	50	0.90	$11 \pm 1$	250-300
88:12		75	1.40	$7.5 \pm 0.5$	350-400
88:12	1:1	100	$V(I)$ Non linear	$3 \pm 0.3$	400-430
88:12	1:2	25	2.95	$10.5 \pm 1$	250-300
88:12	1:2	75	0.95	$11 \pm 1$	250-300
95:5		30	$0.17 \pm 0.02$	$5.5 \pm 0.5$	250-300
97.3:2.7		30	1.30	$4.5 \pm 0.5$	400-430

Smoother films are obtained with higher ratio of Ni: AuGe layer thickness (Fig.8a & 8b), however, contact resistance increases. Moreover, magnetic characterization of the films becomes important. As shown in Fig. 9, the room temperature magnetization of the film structure drops rapidly as the anneal temperature is increased.

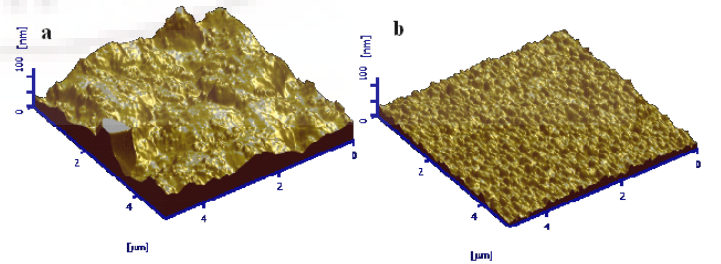


Fig. 8: AFM micrographs (5μm x 5μm) of the surface of AuGe /Ni(x)/Au contacts with (a)  $x = 25$  nm (b)  $x = 100$  nm annealed at 400°C for durations that gave the lowest contact resistance.

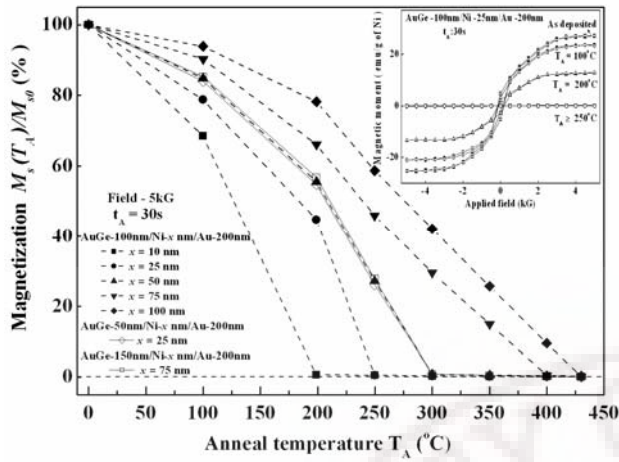


Fig. 9: Anneal temperature dependence of saturation magnetization of alloyed structures of the form AuGe (100nm)/Ni= $x$  nm/Au (200nm) on GaAs multi-layer, for  $x = 10$  nm, 25 nm, 50 nm, 75 nm, 100 nm. Data for structures with AuGe (150nm)/Ni (75nm)/Au (200nm) and AuGe(50nm)/Ni(25nm)/Au(20nm) are also included.  $M_{s0}$  is saturation magnetization of the as-deposited sample at 5 kG. Inset shows typical hysteresis loops

While the contacts with typically used structures (contact resistance optimized) become non-magnetic after anneal at temperatures well below the alloying temperature of  $\sim 400^\circ\text{C}$ , the anneal temperature required to render the contacts non-magnetic increases with Ni layer thickness. 100nm thick Ni layers (Ni: AuGe) ratio 1:1 are rendered non-magnetic at  $\sim 430^\circ\text{C}$ . Despite the contact roughness reductions by an order of magnitude, the electrical characteristics of the contacts are poor (Table 2).

The use of AuGe alloy with reduced Ge content [17], [18] is a better option than increasing the Ni-layer thickness, for reduction in roughness of the processed metallization structure while keeping the structures non-magnetic and conducting with relatively low temperature anneals. The contact resistance with respect to anneal temperature for three different AuGe compositions is displayed in Fig. 10. The contact metallization structure fabricated with 95:5 wt% is smooth and has a contact resistance that is only three times larger than the best contact, but is still an order of magnitude smaller than that of the structure that achieve the same roughness reduction by increasing Ni layer thickness.

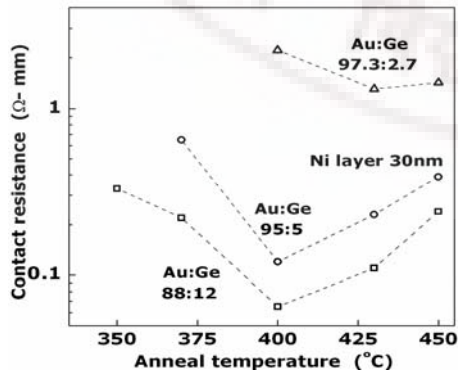


Fig.10: Contact resistances vs. anneal temperature for three AuGe alloy compositions

#### IV. INSIGHTS INTO CHANGES IN THE METALLIZATION STRUCTURE PRIOR TO ALLOYING

The data of Fig. 9 and Table 2 indicate that the amount of Ni converted to non-magnetic phase is proportional to the AuGe layer thickness; clearly the changes are not restricted to Ni-AuGe interface. Further, as the Fig.11 inset shows, at anneal temperatures at which conversion of Ni to non-magnetic phase is still partial, the transformed fraction is independent of time.

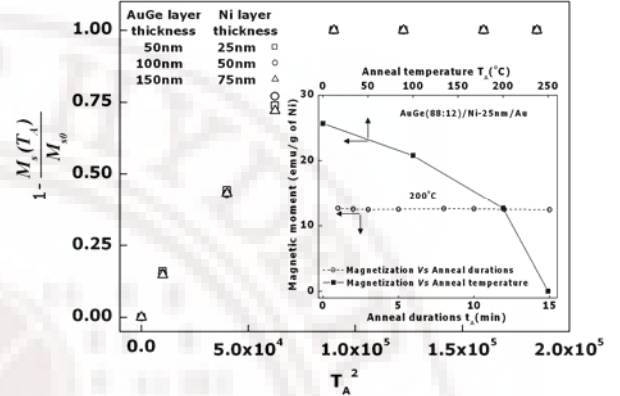


Fig. 11: The transformed Ni fraction vs  $T_A^2$  for three AuGe thicknesses with Ni: AuGe thickness ratio at 0.5. Inset shows magnetization as a function of anneal duration.

Thus the Ni-conversion to non-magnetic phase appears to occur through a solid state *solubility limited dissolution* of Ni into AuGe (starting at temperature  $< 100^\circ\text{C}$ ). This is more apparent in the Fig.12a, which shows a quantity proportional to the transformed Ni layer thickness as a function of anneal temperature.

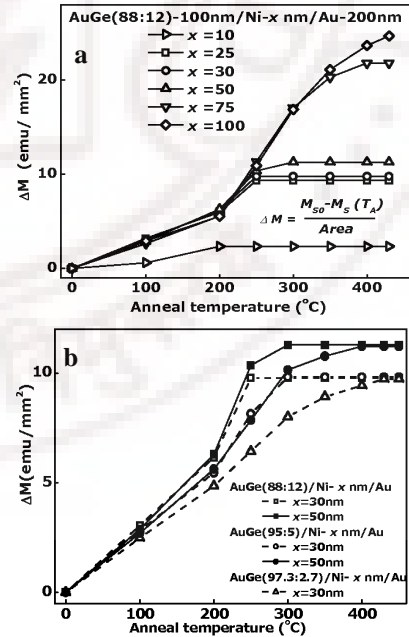


Fig. 12: Effective thickness of Ni layer transformed to non-magnetic phase on annealing at various temperatures. ( $\Delta M$  is the decrease in magnetization per unit area)



The data indicate that 1) the transformed Ni layer thickness depends only on the anneal temperature and is independent of the initial Ni layer thickness, until all the Ni has been transformed into the non-magnetic phase. (The exception is the 10nm Ni layer that may suffer from lack of conformal coverage) 2) The solubility of Ni into AuGe varies quadratically as the temperature (Fig. 11), 3) The solubility of Ni in AuGe decreases with decrease in Ge content of the AuGe alloy layer (Fig. 12b).

Thus, the layer that melts and subsequently alloys with the substrate is AuGe with dissolved Ni. DSC results show that both increase of Ni layer thickness and decrease of Ge content in AuGe, increases the melting temperature of the metallization (Figs.13a & b). Two possible causes for roughness reductions are 1) decreased viscosity of the molten AuGe(Ni) layer as the melting temperature gets closer to the temperature at which alloying is performed. 2) enhanced adhesion to the GaAs surface with larger Ni and smaller Ge content.

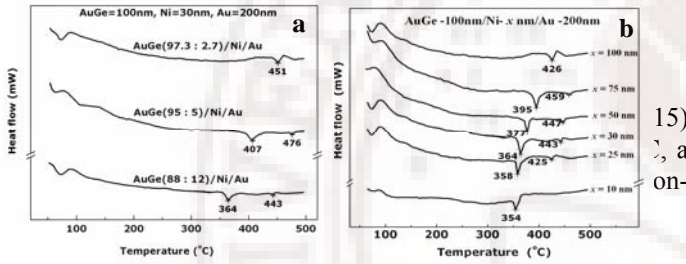


Fig. 13: DSC scans for samples with (a) eutectic and off-eutectic AuGe alloys each with 30nm Ni layer (b) eutectic AuGe alloy with different Ni layer thicknesses.

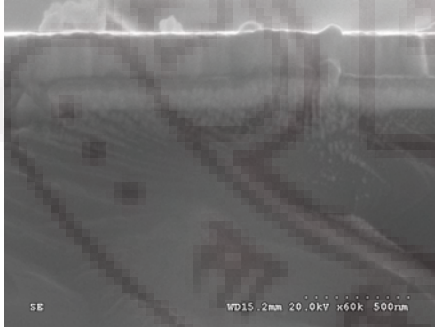


Fig. 14: Cross sectional SEM of AuGe (88:12wt%)-100nm/Ni-25nm/Au-200nm annealed at 300°C and cooled down to room temperature.

Au overlayer and AuGe(Ni) layer are still distinct prior to melting of the AuGe layer and alloying with the substrate (Fig. 14). Grazing incident XRD data indicate the presence of NiGe phase in this structure. Other data in the literature indicate the presence of Ni<sub>3</sub>Ge phase for samples cooled down from higher temperature anneals and larger Ni thickness, finally Ni<sub>2</sub>GeAs and AuGa phases when alloying takes place [19]-[23]. When separate Au and Ge layers, rather than AuGe alloy films are used a propensity for AuGe and Ni-Ge to form,

with Ni as the ‘fast diffusing species’ has been reported from experiments on SiO<sub>2</sub> substrates [24], [25].

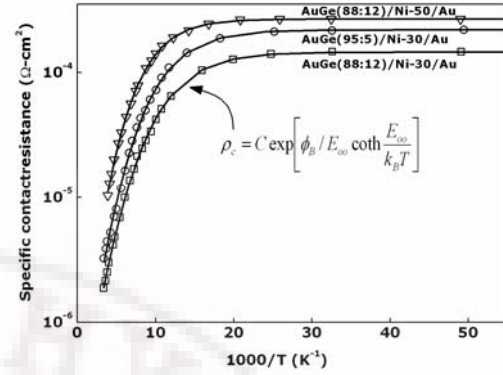


Fig. 15: Specific contact resistance,  $\rho_c$ , plotted as a function of inverse temperature for eutectic AuGe-88:12 wt %/Ni-30nm)/Au), AuGe-88:12/Ni-50nm)/Au), and with off-eutectic AuGe-95:5 wt %/Ni-30nm)/Au).

Low temperature dependence of contact resistance (Fig. 15) displays both tunneling and thermionic emission characteristics. Fits to thermionic field emission model [26] indicate that the effective barrier height in contact structures with enhanced Ni layer thickness or decreased Ge content in the AuGe alloy increases in relation to the optimal structure (eutectic AuGe with 30nm Ni) (Table 3). Current AFM data (Fig. 16a&b) on alloyed structures show short term fluctuations of the conductivity despite the deposited top 200nm Au layer. This could arise from the Ni-Ge or Ni-Ge-As precipitates or from the molten AuGa phases resulting from alloying.

TABLE 3: FITTED PARAMETERS FOR THE CONTACT RESISTANCE, FOR THREE DIFFERENT ALLOYED CONTACT METAL STRUCTURES TO GAAS.

	Specific contact resistance ( $\Omega\text{-cm}^2$ )			$\phi_B$ (meV)	$E_{\infty}$ (meV)	$E_{\infty}/k_B$ (K)
	298K	77K	4.2K			
AuGe(88:12)/ Ni-30/Au	$1 \times 10^{-6}$	$4.5 \times 10^{-5}$	$1.7 \times 10^{-4}$	$31 \pm 0.5$	$10.3 \pm 0.08$	$116 \pm 1$
AuGe(88:12)/ Ni-50/Au	$1 \times 10^{-5}$	$1.8 \times 10^{-4}$	$2.7 \times 10^{-4}$	$38 \pm 0.7$	$13.1 \pm 0.08$	$148 \pm 1$
AuGe(95:05)/ Ni-30/Au	$3.2 \times 10^{-6}$	$7.6 \times 10^{-5}$	$2.4 \times 10^{-4}$	$34.5 \pm 1$	$11 \pm 0.14$	$124 \pm 1.5$

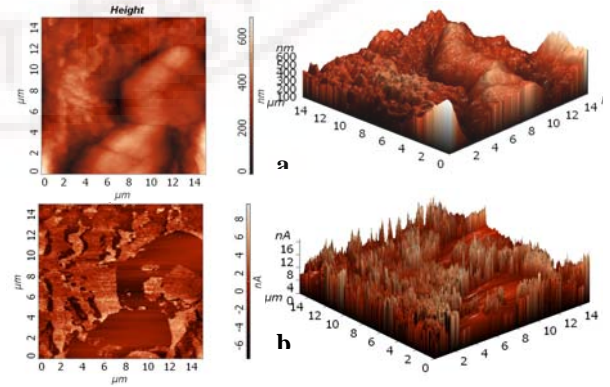


Fig. 16 **a.** Surface topography, **b.** Current mapping of AuGe/Ni/Au contact structures which shows the least contact resistance.



## V. CONCLUSIONS

Contacts of the type AuGe/Ni/Au are rendered non-magnetic (at room temperature) for anneals at temperatures well below the alloying temperature at which the contact resistance drops. A solubility limited Ni dissolution into AuGe layer appears to take place well below the alloying temperature, increasing the structure's melting temperature. Lowering the Ge content is a better option to increasing Ni layer thickness, for roughness reductions from the magnetic and electrical point of view. Temperature dependence of contact resistance shows characteristics of both tunneling and thermionic emission behaviour. Conductivity (x-y) map of the contacts shows short range fluctuations despite the deposition of 200nm thick Au overlayer.

## ACKNOWLEDGMENT

Support of UGC (UPE, CAS programmes), BRNS/DAE, IGCAR, DST (Centre for Nanotechnology, FIST), ACRHEM is acknowledged.

## REFERENCES

- [1] Honeywell Microelectronics and precision sensors, magnetic sensors products, Honeywell.
- [2] T. R. Lepkowski, G. Shade, S. P. Kwok, M. Feng, L. E. Dickens, D. L. Laude, B. Schoendube, "A GaAs integrated Hall sensor/ amplifier", *IEEE Electron Device Letters*, vol. 7, no. 4, pp. 222-224, 2005.
- [3] K. Togawa, H. Sanbonsugi, A. Lapicki, M. Abe, H. Handa and A Sandhu, "High-sensitivity InSb thin-film micro-Hall sensor arrays for simultaneous multiple detection of magnetic beads for biomedical applications" *IEEE Transactions on Magnetics*, vol. 41, no.10, pp. 3661-3663, 2005.
- [4] Yoshinobu Sugiyama, "Recent progress on magnetic sensors with nanostructures and applications", *J. Vac. Sci. Technol. B*, vol. 13, no. 3, pp. 1075-1083, 1995.
- [5] A. Sandhu, A. Okamoto, I. Shibasaki and A. Oral, "Nano and micro Hall-effect sensors for room-temperature scanning Hall probe microscopy", *Microelectronic Engineering*, vol. 73-74, pp. 524-528, 2004.
- [6] N. Haned and M. Missous, "Nano-tesla magnetic field magnetometry using an InGaAs-AlGaAs-GaAs 2DEG Hall sensor", *Sensors and Actuators A*, vol.102, pp. 216, 2003.
- [7] S O'Connor, L Clapham and P Wild, "Magnetic flux leakage inspection of tailor-welded blanks", *Meas. Sci. Technol.*, vol.13 pp.157-162, 2001.
- [8] Adarsh Sandhu, Hiroshi Masuda, Ahmet Oral and Simon J. Bending, "Room Temperature Sub-Micron Magnetic Imaging by Scanning Hall Probe Microscopy", *Jpn. J. Appl. Phys.*, vol. 40, pp. 4321-4324, 2001.
- [9] The wafer is procured from IQE USA. The room temperature(RT) carrier mobility is  $\sim 7800 \text{ cm}^2/\text{V.s.}$  and at 77K is  $\sim 1.4 \times 10^5 \text{ cm}^2/\text{V.s.}$ , sheet carrier density is  $\sim 3.4 \times 10^{11} \text{ cm}^{-2}$  at RT and  $\sim 4.5 \times 10^{11} \text{ cm}^{-2}$  at 77K.
- [10] H. H. Berger, "Models for contacts to planar devices", *Solid State Electron.*, vol. 15, no. 2, pp. 145-158, 1972.
- [11] D. Minkov, Y. Takeda, T. shoji and J. Lee, Estimating the sizes of surface cracks based on model of a crack. *App. Phys. A*, vol. 74, pp. 169-176, 2002.
- [12] A. Ketterson, F. Ponse, T. Henderson, J. Klem and H. Morkoç, "Extremely low contact resistances for AlGaAs/GaAs modulation-doped field-effect transistor structures" *J. Appl. Phys.*, vol. 57, no. 6, pp. 2305-2307, 1985.
- [13] N. Braslau, J. B. Gunn and J. L. Staples, "Metal-semiconductor contacts for GaAs bulk effect devices", *Solid State Electron.* vol.10, pp. 381, 1967.
- [14] C. Lin and C. P. Lee, "Comparison of Au/Ni/Ge, Au/Pd/Ge and Au/Pt/Ge Ohmic contacts to GaAs", *J. Appl. Phys.* vol. 87 no.1, pp.260, 1990.
- [15] T. S. Abhilash, Ch. Ravi Kumar and G. Rajaram, "Influence of Nickel layer thickness on the magnetic properties and contact resistance of AuGe/Ni/Au Ohmic contacts to GaAs/AlGaAs heterostructures", *J. Phys. D: Appl.Phys.*, vol. 42, pp. 125104 (8pp), 2009.
- [16] O. Goktas, J. Weber, J. Weis and Klaus von Klitzing, "Alloyed Ohmic contacts to two-dimensional electron system in AlGaAs/GaAs heterostructures down to submicron length scale", *Physica E*, vol. 40, pp.1579, 2007.
- [17] H. J. Bühlmann and M. Ilegems, "Characterization of AuGe/Ni/Au Contacts on GaAs/AlGaAs Heterostructures for Low-Temperature Applications", *J. Electrochem. Soc.*, vol.138, no.8, pp. 2795- 2798, 1991.
- [18] Herb Goronkin, Saied Tehrani, Tom Rimmel, Peter L. Fejes and Karl J. Johnson "Ohmic contact penetration and encroachment in GaAs/AlGaAs and GaAs FET", *IEEE Trans. Electron Devices*, vol. 36, no. 2, pp. 281-288, 1989.
- [19] T. S. Kuan, P. E. Batson, T. N. Jackson, H. Rupprecht and E. L. Wilkie, "Electron microscope studies of an alloyed Au/Ni/Au-Ge ohmic contact to GaAs", *J. Appl. Phys.*, vol. 54, no. 12, pp. 6952-6957, 1983.
- [20] M. Ogawa, "Alloying behaviour of Ni/Au-Ge films on GaAs," *J. Appl. Phys.*, vol. 51, no. 1, pp. 406-412, 1980.
- [21] G. Sai Saravanan, K. Mahadeva Bhat, K. Muraliedharan, H. P. Vyas, R. Muralidharan and A. P. Pathak, "Ohmic contacts to pseudomorphic HEMTs with low contact resistance due to enhanced Ge penetration through AlGaAs layers", *Semicond. Sci. Technol.*, vol. 23, pp. 025019(6pp), 2008.
- [22] Masanori Murakami, "Development of refractory Ohmic contact materials for gallium arsenide compound semiconductors", *Science and Technology of Advanced Materials*, vol. 3, pp. 1-27, 2002.
- [23] Taeil Kim and D.D.L. Chung, "In situ X-ray diffraction study of the effects of germanium and nickel concentrations on melting in gold-based contacts to gallium arsenide", *Thin Solid films*, vol. 147, no. 2, pp. 177-192, 1986.
- [24] M. Wittmer, R. Pretorius, J. W. Mayer and M. A. Nicolet, "Investigation of the Au-Ge-Ni system used for alloyed contacts to GaAs", *Solid State Electron.*, vol. 20, pp. 433, 1977.
- [25] T.G. Finstad, "The annealing behaviour of Ge-Au-Ni, Ge-Au-Pt and Ge-Au-Pd trilayer films", *Thin solid films*, vol. 47, pp. 279, 1977.
- [26] T. C. Shen, G. B. Gao and H. Morkoc, Recent developments in Ohmic contacts for III-V compound semiconductors", *J. Vac. Sci. Technol. B*, vol. 10, pp. 2113, 1992.